Influence of g-C_3N_4 and metal loading on layered double hydroxides for their improved adsorption and photocatalytic properties

A Thesis
Submitted for the fulfilment of the requirements for the award of the degree of

Doctor of Philosophy

Submitted by

Harpreet Kaur

(Regn. No. 901809014)

THAPAR INSTITUTE
OF ENGINEERING & TECHNOLOGY
(Deemed to be University)

Under the Supervision of

Dr. Bonamali Pal
Professor

Dr. Satnam Singh
Professor and Head

SCHOOL OF CHEMISTRY AND BIOCHEMISTRY
THAPAR INSTITUTE OF ENGINEERING AND TECHNOLOGY
PATIALA-147004
PUNJAB (INDIA)

September-2023

Certificate

This is to certify that the work embodied in this thesis entitled "**Influence of g-C_3N_4 and metal loading on layered double hydroxides for their improved adsorption and photocatalytic properties**" has been carried out by Ms. Harpreet Kaur under my supervision and guidance in the School of Chemistry and Biochemistry, Thapar Institute of Engineering and Technology, Patiala. The candidate completed all the conditions required for the fulfillment of the award of the Degree of Philosophy.

I also certified that the work represented in this thesis is original and has not been submitted in part or full for the award of any degree in any other University or Institute.

Dr. Bonamali Pal

Professor and Supervisor

School of Chemistry and Biochemistry

Thapar Institute of Engineering and Technology

Patiala-147004

Dr. Satnam Singh

Professor, Head and Supervisor

School of Chemistry and Biochemistry

Thapar Institute of Engineering and Technology

Patiala-147004

Candidate's Declaration

I, hereby declare that the work presented in the thesis entitled **"Influence of g-C_3N_4 and metal loading on layered double hydroxides for their improved adsorption and photocatalytic properties"**, in fulfillment of the requirement for the award of the Degree of Doctor of Philosophy, School of Chemistry and Biochemistry, Thapar Institute of Engineering and Technology, Patiala, is an authentic record of my own work carried out under the supervision of Dr. Bonamali Pal (Professor) and Dr. Satnam Singh (Professor and Head), School of Chemistry and Biochemistry, Thapar Institute of Engineering and Technology, Patiala, India. The matter embodied in this thesis has not been submitted in part or full to any other university or institute for the award of any degree in India or Abroad.

Harpreet Kaur

Dr. Bonamali Pal
Professor and Supervisor
School of Chemistry and Biochemistry
Thapar Institute of Engineering and Technology
Patiala-147004

Dr. Satnam Singh
Professor, Head and Supervisor
School of Chemistry and Biochemistry
Thapar Institute of Engineering and Technology
Patiala-147004

Acknowledgement

Without the assistance and encouragement of several special individuals, it would not have been possible to complete this thesis. Hence, I would like to express my appreciation to those who have supported me in a number of ways.

To begin I would like to express my sincere gratitude to my research supervisors **Dr. Bonamali Pal, Professor** and **Dr. Satnam Singh, Professor and Head**. I couldn't have wished for better supervisors who were so kind and supportive. I was always guided in the right direction by their helpful suggestions, and they persuaded me to act professionally. They have provided me with helpful direction, constructive criticism, discussions, and valuable support, and I am deeply grateful. They have always been a constant source of encouragement and support. The objective of this project would not have been accomplished without their persistent help. My sincere thanks also go to **Mr. Chander Thakur** and office staff **Mr. Mayank** for their cooperation, support, and help.

Additionally, I am thankful to **Dr. Rafat Siddique**, Director and Dean (Research and Sponsored Projects), for providing me with the opportunity to carry out this doctoral research. Additionally, I would like to express my gratitude to the members of my doctoral committee, **Dr. Soumen Basu**, **Dr. Debasish Mandal**, and **Dr. Aviniash Chandra**, who participated in the validation survey for this research project. Their insightful suggestions and endless support help me to convey the results of my research in a better way.

I would like to thanks my seniors **Dr. Samriti Thakur, Dr. Aadil Bathla, Dr. Manpreet Kaur, and Dr. Sakshi** for their knowledgeable help and support. I am also thankful to my labmates **Manjusha, Priti, Shikha, Davinder, and Mehak** for their support and cooperation.

I am indebted to my parents, my father, **Sardar. Jaswinder Singh Malhi**, who always supported and encouraged me to fulfill my dreams and desires. I would like to acknowledge my loving mother **Sardarani. Davinder Kaur Malhi**, for all the sacrifices she had made for me throughout her life. I can't put my thoughts or feelings into words to show my heartfelt gratitude to my parents for their unconditional love, endless support, and blessings. My parents are my inspiration.

The help from different institutes and laboratories like SAI Lab TIET, Punjab University Chandigarh, IIT Delhi, etc. are highly acknowledged.

Besides this, I am thankful to the persons who knowingly and unknowingly helped me during the successful completion of this work.

Harpreet Kaur

Harpreet Kaur

DEDICATED

TO

MY

PARENTS

Table of contents

Chapter 2

Adsorption performance of LDH and its g-C_3N_4 loaded composites towards anionic and cationic organic pollutants

Chapter 3

Plasmonic metal (Cu, Ag, Au) loaded composites for efficient degradation of tetracycline under LED light

Chapter 4

Construction of a novel ternary Ag@g-C_3N_4-Co-Al LDH heterostructure for degradation of pharmaceutical drug under LED radiations

Chapter 5

Fabrication of g-C_3N_4 coupled Mg-Al LDH binary heterojunction photocatalyst with boosted photocatalytic degradation of doxycycline under LED irradiations

List of Abbreviations

a.u.	Arbitrary unit
BET	Brunauer-Emmett-Teller
BJH	Barrett-Joyner-Halenda
CB	Conduction band
CN	Graphitic carbon nitride (g-C_3N_4)
CIP	Ciprofloxacin
DI	Deionized water
DRS	Diffuse reflectance spectroscopy
DXC	Doxycycline
EDS	Energy dispersive X-ray spectroscopy
FESEM	Field emission scanning electron microscopy
HRTEM	High resolution transmission electron microscopy
IPA	Isopropyl alcohol
JCPDS	Joint committee on powder diffraction standards
LDH	Layered double hydroxides
nm	Nanometre
NPs	Nanoparticles
PL	Photoluminescence
PPM	Parts per million
RPM	Rotations per minute
SAED	Selected area electron diffraction

SEM	Scanning electron microscopy
SPR	Surface plasmon resonance
TC	Tetracycline hydrochloride
TEM	Transmission electron microscopy
TOC	Total organic carbon
UV	Ultraviolet
VB	Valance band
Vis	Visible
wt%	Weight percentage
XPS	X-ray photoelectron spectroscopy
XRD	X-ray diffraction spectroscopy

List of Symbols

e^-	Electron
h^+	Hole
$O\dot{H}$	Hydroxyl radical
E_g	Band gap
Å	Angstrom
α	Absorption coefficient
A	Absorbance
°	Degree
λ	Wavelength
%	Percentage
μ	Micro
θ	Theta
H	Hour
E_o	Electrode potential
m	Meter
g	Gram
mg	Milligram
E_f	Fermi energy
V	Volt
d	Distance
C	Concentration

v	Frequency
mol	Mole
μmol	Micromol
μl	Microlitre
ml	Millilitre
mM	Millimolar
L	Litre
2D	Two-dimensional

Abstracts

Chapter-1

This chapter includes discussion on structural and chemical composition, adsorptive and photocatalytic behavior of two-dimensional nanostructured layered double hydroxides (LDH). In the context of adsorption and photocatalysis, the behavior and modifications of LDHs have been discussed. Literature review, research gaps, objectives, experimental methods, and characterization techniques are also described in this chapter.

Chapter-2

The traditional positively charged layered double hydroxides generally considered as efficient and low-cost adsorbents for the removal of anionic organic molecules. The g-C_3N_4 loaded Ni-Co LDH composites were prepared through the electrostatic self-assembly method with varying 10, 20, and 30 wt% of g-C_3N_4. The as prepared adsorbents were characterized by XRD, SEM-EDS, Zeta, DLS, and FTIR techniques. Results revealed that the extra peak corresponds to g-C_3N_4 (CN) originating in the XRD patterns, distorted morphology of LDH, reduction in positive surface zeta potential, and enhancement in hydrodynamic size after loading of CN affirmed the successful coupling of LDH with CN. The adsorption performance of as-modified LDH was evaluated by removing the most commonly used salicylic acid and methylene blue as anionic and cationic model pollutant, respectively, from aqueous solution. The adsorption mechanism for both the pollutants by as-synthesized samples followed Langmuir isotherm. The bare LDH had a maximum adsorption efficiency of only 3.66 mg/g for methylene blue and 75.16 mg/g for salicylic acid. The adsorption capacity of methylene blue increased to 25.16 mg/g with 30 wt% of CN loading, which was approximately 6-7 times higher than the adsorption capacity of bare LDH. On the other hand, the adsorption capacity of salicylic acid decreased to 38.37 mg/g, which was approximately half of that of bare LDH. Except for the methylene blue adsorption,

which followed first-order kinetics, the kinetics of the salicylic acid adsorption onto bare LDH followed the second-order model. On the other hand, second-order kinetics was followed in the adsorption of both pollutants onto (10-30) CN-LDH composites.

Chapter-3

This work focused on the enhancement of the photocatalytic activity of solvothermal synthesized $Mg_{0.667}$ $Al_{0.333}$ $(OH)_2$ $(CO_3)_{0.167}$ $(H_2O)_{0.5}$ layered double hydroxides (LDH) by plasmonic metal (Cu, Ag, and Au) photodeposition (1-3 wt%). HRTEM analysis confirmed the successful loading of plasmonic nanoparticles with varying sizes (Au (~ 4-25 nm) > Ag (~ 3-12 nm) > Cu (~2-7 nm)) on the surface of LDH. The effect of different plasmonic metals and their size on the surface structural, optical, electrokinetic, and photocatalytic properties of LDH was investigated. The prepared catalysts were evaluated for the degradation of tetracycline under LED irradiation for 140 min and the photoactivity trend followed the order: pristine LDH < Cu@LDH < Ag@LDH < Au@LDH. The LC-MS studies revealed that the degradation occurred by the attack of various reactive species ($O_2^{\cdot-}$, h^+, $O\dot{H}$) via four paths mainly including hydroxylation, functional group cleavage, and ring-opening reaction. A possible mechanism was proposed for the appreciable enhancement in performance caused by the formation of Schottky barriers and Surface Plasmon resonance of plasmonic nanoparticles. The results of total organic carbon (TOC) indicated the acceptable mineralization of about 84%. Less than a 10% fall in degradation efficiency was observed within four recycle runs.

Chapter-4

Elimination of pharmaceutical drugs from wastewater through photocatalysis is considered an effective and environment-friendly approach to prevent their introduction into the aquatic environment. We constructed ternary Ag deposited g-C_3N_4 loaded Co-Al layered double hydroxide composites through multistep synthesis for wastewater remediation of the pharmaceutical industry. We explored the role of g-C_3N_4 (CN) and Ag nanoparticles in Ag@CN-

LDH heterostructures for improving the photocatalytic performance of LDH. This study revealed that the photoactivity of the ternary composite was significantly affected by the CN and Ag loadings. The visible light-driven ternary composite with 10 wt% of CN and 1 wt% of Ag loadings over LDH exhibited the maximum 97% degradation of commercial ciprofloxacin within 90 minutes, which was highly superior to that noticed for bare LDH. The boosted degradation proficiency was credited to the increased active sites, quick charge move at the CN-LDH interface, and the Surface Plasmon resonance of Ag nanoparticles acting as electron trappers. The ternary composite was highly stable and recyclable upto five cycles with less than a 3% fall in degradation efficiency. Three degradation pathways, including the cleavage of the piperazine ring and the decarboxylation of the quinoline ring, were proposed following the LC-MS analysis. A possible mechanism for efficient charge transfer and photocatalytic degradation was proposed based on the band edge positions calculated from valence band XPS spectra, photoluminescence analysis, and scavenging experiments.

Chapter-5

The Mg-Al LDH is a UV-active photocatalyst with a band gap value greater than 3 eV. The coupling of Mg-Al LDH with visible active g-C_3N_4 came out as an effective strategy to improve the absorbance of light in the visible region, inhibit the rejoining of charge carriers, and enhance its specific surface area. In the current work, we prepared different wt% of g-C_3N_4 coupled Mg-Al LDH composites via the in-situ hydrothermal method. The optimized CN-LDH composite exhibited enhanced 98.5% degradation of doxycycline under LED light within 60 minutes, which was far better than that of bare LDH. The LC-MS studies were performed to determine the intermediates and end products of the doxycylcine degradation. The prepared composite was highly stable and recyclable for up to five cycles.

CHAPTER- 1

1.1 Introduction:

1.1.1. Layered double hydroxides (LDHs):

Layered double hydroxides are inorganic compounds having both natural as well as synthetic origin. Because of their distinctive layered structure, these are generally referred to as hydrotalcite. Hydrotalcite with chemical formula $[Mg_6Al_2\ (OH)_{16}]CO_3.4H_2O$ is a naturally occurring white hydrous mineral with rhombohedral crystallinity and structural properties comparable to those of brucite $Mg(OH)_2$. It consists of assembly of positively charged infinite brucite like layers constituting Mg^{2+} ions partially replaced by Al^{3+} ions octahedrally coordinated to hydroxyl groups (OH^-) and carbonate anions (CO_3^{2-}) intercalated in the interlayer space along with water molecules [1-3]. Inspired from hydrotalcite mineral, the general chemical composition of layered double hydroxides is $[M^{2+}_{(1-x)}\ M^{3+}_{(x)}\ (OH)_2]^{x+}\ (A^{n-})_{x/n}.mH_2O$, where M^{2+} and M^{3+} are metal ions, A^{n-} are the negatively charged ions intercalated between the positively charged metal hydroxide layers, x is the layer charge density or molar ratio of $[M^{3+}/(M^{2+}+M^{3+})]$ generally lies in the range 0.2-0.33, and m is the number of H_2O molecules suited in the region between two brucite like layers alongside anions [4-6]. In their structural arrangement, the M^{2+} ions are uniformly arranged in the brucite layers where some of these are partially substituted by M^{3+} ions having ionic radii smaller than that of M^{2+} ions. For instance, Elhalil *et al*. synthesized ZnAl LDH, where Zn^{2+} ions of ionic radii 0.74 nm in brucite like layers are partially replaced by smaller Al^{3+} ions with ionic radii of 0.53 nm [7]. Both the divalent and trivalent cations are octahedrally surrounded by six OH^- ions forming mixed metal hydroxides. These octahedral units construct infinite metal hydroxide brucite like layers of general composition $[M^{2+}_{(1-x)}M^{3+}_{(x)}\ (OH)_2]^{x+}$ assembling on top of one another by edge-sharing of MO_6 octahedron, and the O-H bond is found at a right angle to the plane of brucite like layers. The fractional substitution of

M^{2+} by M^{3+} ions gives the brucite like layers a positive charge. The negatively charged intercalated anions balance the positive charge of the brucite-like layers to keep the structure electroneutral [8, 9]. A Schematic representation of LDH structure with general composition is shown in **Scheme-1.1**. The structure of LDH acquires stability due to (a) the uniform distribution of M^{2+} and M^{3+} ions in brucite like layers, (b) the electrostatic force of attraction between the brucite like layers and intercalated anions, (c) hydrogen bonding linking the (i) OH^- groups of metal hydroxides and water molecules, (ii) intercalated anions and water molecules, and (iii) hydroxyl group of metal hydroxides and intercalated anions. In brucite, $Mg(OH)_2$ structure, the basal spacing is about 4.8 Å, however, in case of hydrotalcites, the basal spacing is expanded to about 7-10 Å because of intercalated anions and water molecules present in its interlayer region [10-12].

The diversity in LDHs can be employed by their variable chemical composition permitting a variety of cations and anions to participate. Generally, these consist of divalent cations such as Zn^{2+}, Mg^{2+}, Co^{2+}, Ni^{2+}, Cu^{2+}, etc. and trivalent cations such as Fe^{3+}, Al^{3+}, Cr^{3+}, V^{3+}, etc. mostly belonging to the third and fourth period of the periodic table. The commonly found charge adjusting intercalated anions in their composition are CO_3^{2-}, F^-, Cl^-, NO^{3-}, SO_4^{2-}, chromates, dichromates, surfactant anions, carboxylates, poloxymetalates, amino acids anions, etc [13-18].

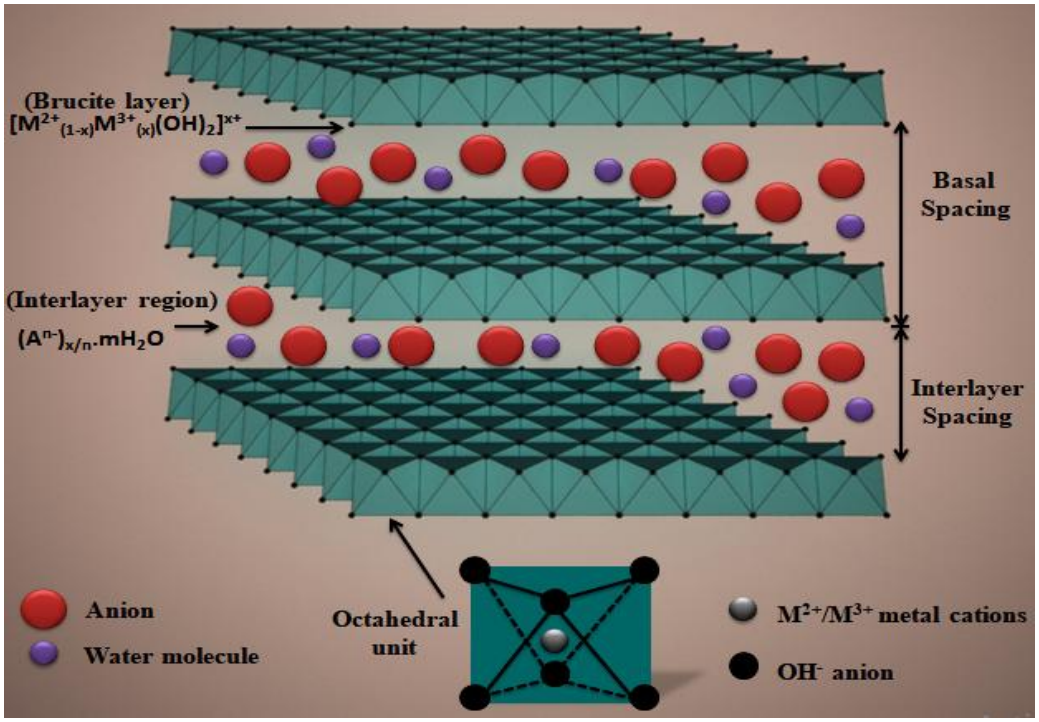

Scheme-1.1. A Schematic representation of three dimensional structure of layered double hydroxides with general chemical composition $[M^{2+}_{(1-x)}M^{3+}_{(x)}(OH)_2]^{x+}(A^{n-})_{x/n} . mH_2O]$.

Their verstality lies in adopting extensive scope of metal cations and anions exhibiting tunable structural and electronic properties with various tremendous features such as easy and low cost synthesis, high thermal and chemical stability, flexible composition, high surface area generally ranges from 20 to 250 m^2g^{-1}, adjustable structural and electronic properties, and porous structure having pore size varies from 2 to 50 nm [19, 20, 24, 25].

One of the most astounding features powered by LDHs is the formation of mixed metal oxides (MMOs) formed upon their calcination at temperature about 400-600^oC. At such high temperature, their layered structure gets destroyed with removal of intercalated anions and water molecules and metal hydroxides get converted into metal oxides. Their exceptionality lies in the fact of reconstruction of layered structure by introducing their calcined compounds to aqueous solution of certain lost or any desired intercalated anions. This special characteristic of LDH is termed as the “memory effect” [21,22]. They possess another prominent characteristic i.e. ability to exchange intercalated anions with other anions in the solution demonstrated as anion

exchangeability. Almost all type of anions can be adjusted into their structural composition with respect to positively charged brucite like layers and interlayer region possessing weak interlayer bonding [23]. On account of various pivotal features, these are raising out as highly potential two-dimensional materials in different fields, for example, catalysis [26], adsorption [27], biomedical science [28], photocatalysis [29], electrochemistry [30], and so on.

Water contamination has become a most serious issue in the public arena causing several medical problems. One of the main reasons is the release of organic pollutants as effluents from industries into water sources. Adsorption and photocatalytic degradation are considered an easy, simple, economic, and highly effective methods that are being extensively adopted worldwide to remove organic pollutants from water [31,32].

1.1.2. LDHs as adsorbents:

Owing to low cost, high surface area, porous structure, non-toxicity, and excellent anion exchange capability, LDHs are served out as efficient adsorbents capable of adsorbing toxic metal cations and anions, harmful organic dyes, pharmaceutical wastes and various other pollution causing compounds [32]. Adsorption is a surface phenomenon that usually occurs due to certain kind of intermolecular interactions between adsorbate and adsorbent. LDHs are generally considered to be powerful candidate for the adsorption of harmful anionic compounds due to their hydrophilic nature and toxic metal cations due to intercalated anions, and shows non-adsorptive behavior towards cationic molecules due to positively charged surface (**Scheme-1.2**).

For instance, Lu *et al*. investigated the highly effective adsorption activity of Ni-Fe LDH towards adsorption of Cr^{6+} heavy metal ion and methyl orange dye [33]. Wu *et al*. synthesized flower-like hierarchical Ni-Co LDH microspheres as a cost-effective promising adsorbent with a high adsorption capacity of methyl orange dye (497 mg/g). The excellent adsorption performance of prepared LDH was credited to its high surface area, porous structure, and

electrostatic interactions between LDH and anionic dye molecules [34].

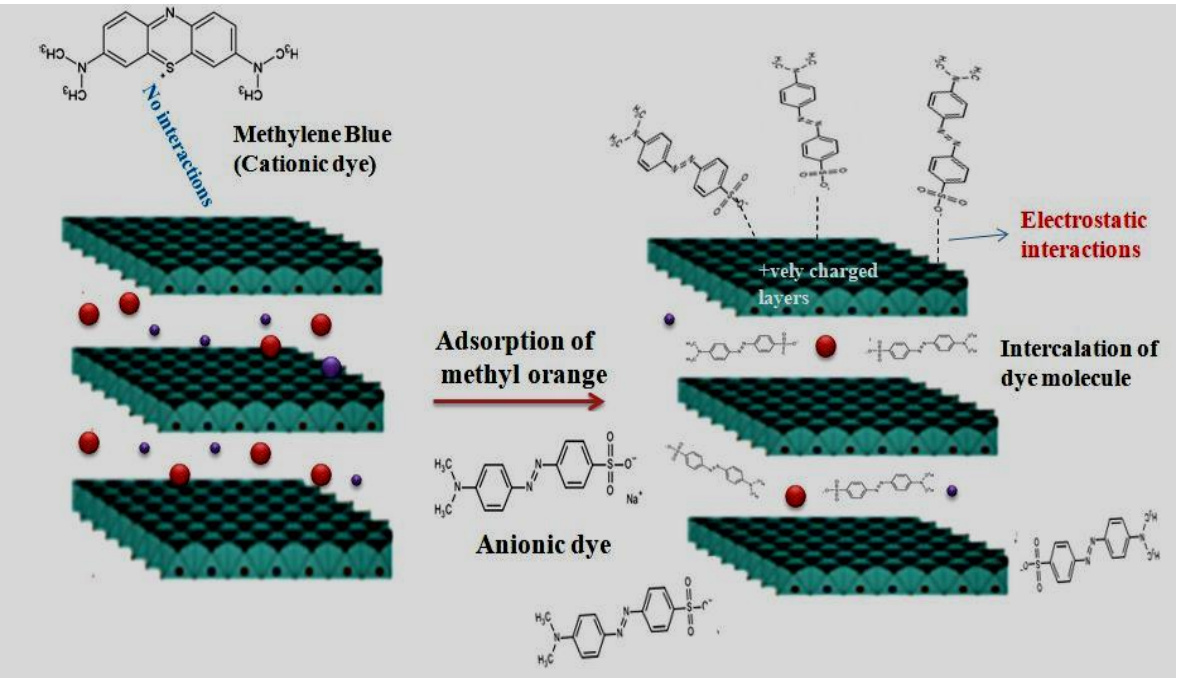

Scheme-1.2. A schematic representation showing the adsorption behavior of LDH towards cationic (e.g. methylene blue) and anionic molecules (e.g. methyl orange).

1.1.3. LDHs as photocatalysts:

Photocatalysis is one of the important fields that hold great concern in solving energy and environmental crises arising due to the rapid development of current human advancement. It is a straightforward procedure that only requires a photoactive catalyst with appropriate band positions and an energy source. The electrons in a photocatalyst's valence band are excited to move into its conduction band when exposed to light with energy greater than or equal to its band gap. The photocatalyst's surface serves as a redox center for the reactions, where electrons in the conduction band (CB) and holes made in the valence band (VB) serve as reduction and oxidation sites, separately (**Scheme-1.3**) [35,36].

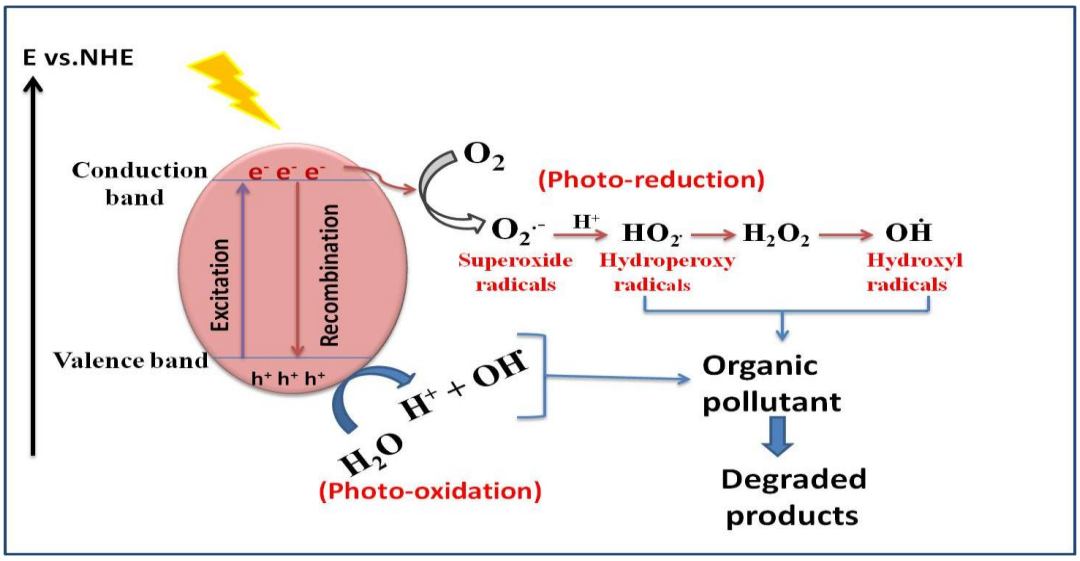

Scheme-1.3. A schematic illustration showing the process of photocatalysis towards degradation of organic pollutants.

Since, most recent couple of years, layered double hydroxides, the unique layered materials are coming out as a group of promising photocatalysts on account of their tremendous features like layered structure possessing semiconductor properties with exceptionally dispersed metals serving as active sites, highly adjustable bandgap, large surface area, low cost, and high reusability. Their exceptionality lies in their tunable chemical composition which allows the incorporation of desired photoactive metals [37,38,39].

The very first report about their photocatalytic behavior was given by Silva *et al*. exploring a series of ZnTi, ZnCe, and ZnCr LDHs for the oxidation of water to produce O_2 gas under visible irradiation. In view of their optical studies through diffuse reflectance spectra, the ZnCe LDH showed a peak at about 280 nm and ZnTi showed a more intense absorption peak at about 380 nm, whereas, the ZnCr LDH showed maximum absorbance at 410 and 570 nm. They also demonstrated the LDHs as "**doped semiconductors**" where the higher valent metal is considered as a dopant [40]. Moreover, the LDHs generally show higher photocatalytic activity than bulk metal oxides or hydroxides. It can be due to their layered structure providing the uniform

dispersion of metal cations (M^{2+} and M^{3+} or M^{4+}) in brucite like layers formed by edge sharing of MO_6 octahedron. Their efficient photoactivity is mainly governed due to the presence of MO_6 octahedron with a high degree of dispersion which consequently permits the rapid transfer and decreased the recombination of charge carriers. The strong evidence of this phenomenon was first given by Zhao *et al*. by dispersing the visible responsive CrO_6 octahedron into the LDH matrix via synthesizing M-Cr LDH (M=Cu, Ni, Zn). In general, chromium hydroxide exhibits significant visible absorption. Despite this, no photoactivity was observed due to the low transfer of excited electrons and high rejoining of electron-hole pairs due to agglomeration of CrO_6 units in $Cr(OH)_3$. However, efficient activity was observed in the case of LDH constituting CrO_6 octahedron units credited to the high dispersion of these octahedron units in layered structure. The Cr 3d orbitals (A_{2g}) as the valence band and Cr 3d orbitals (T_{2g}+T_{1g}) as the conduction band of LDH undergo bandgap transitions, responsible for its photoactivity [41]. Also, Shao *et al*. (2011) found that ZnTi LDH performed significantly better than metal oxides in the photocatalytic degradation of methylene blue [42].

1.1.4. Modification of LDHs:

Layered double hydroxides are mainly known as efficient adsorbents for anionic pollutant molecules due to presence of positively charge brucite like layers. Several modifications such as intercalation of surfactants, coupling of several materials such as graphene oxide, carbon nanotubes, biochar, etc. have been done to improve their adsorption activity towards anions as well as cations. Zhang *et al*. synthesized organo-modified Mg-Al LDHs intercalating three different surfactants (sodium hexanesulfonate, sodium nonanesulfonate, sodium dodocanesulfonate) for efficient adsorption of acid red, disperse orange, and basic yellow dyes. The intercalation of surfactant changed the surface properties of LDH making it hydrophobic and

reversal of charge from positive to negative on increasing the chain length of surfactant [43]. Qian *et al*. fabricated reduced graphene oxide modified Ni-Cr LDH possessing excellent adsorption efficiency towards methyl orange. The adsorption performance was ascribed to the introduction of reduced graphene providing large specific surface area and more interactions of incoming dye molecules with surface of nanocomposite [44]. Various other LDH based materials like MWCNTs-LDH composite [45], carbon dots-LDH [46], Fe_3O_4-LDH [47] etc. have been investigated for improved adsorption performance.

Besides various unique and excellent features, LDHs suffer few limitations like less mobilization and quick recombination of photoinduced charge carriers, limited light response, less surface active sites, etc. responsible for hindering their photocatalytic performance. However, the coupling of LDH with semiconductor-based materials can expect to overcome such constraints through the formation of heterostructure junction leading effective utilization of properties of both the components, rapid transfer of charge carriers, efficient charge separation, increased lifetime of electron and holes, stronger and wider visible light response, and more reactive sites.

Graphitic carbon nitride (g-C_3N_4), a two-dimensional metal free polymer has emerged as a potential low cost, non-toxic, visible light-responsive photocatalyst having a bandgap of about 2.7 eV. The construction of heterojunction of 2D/2D interface by combining LDH with g-C_3N_4 through its delocalized conjugated π structure is one of the successful strategies to enhance absorbance response in visible light and separation of photoinduced charges during the photocatalytic process [48].

Ramesh and co-workers constructed g-C_3N_4/Ni-Al LDH composite for enhanced water splitting to produce hydrogen. The H_2 evolution rate of 30% g-C_3N_4/Ni-Al LDH was found to be about 1000 times than that of pristine LDH. This can be due to the fact of strong synergetic effect

between oppositely charged Ni-Al LDH and g-C_3N_4 providing effective inhibition of electron-hole pair rejoining at the heterojunction interface [49]. Yazdani *et al*. prepared g-C_3N_4/Ni-Ti LDH heterojunction film which exhibited better performance than bare g-C_3N_4 and Ni-Ti LDH film for photodegradation of methyl orange. The heterojunction system attributed high redox ability and migration of charge carriers in opposite direction across the interface enabling efficient charge separation [50]. Li *et al*. successfully modified photo inactive Zn-Al LDH with various loading of g-C_3N_4 (2, 7, and 8 wt %) and explored towards the photodegradation of methylene blue. As Zn-Al LDH was not excited by UV light, by virtue of g-C_3N_4/Zn-Al heterostructure, the electrons were injected into conduction band of Zn-Al LDH from progressively negative CB of g-C_3N_4 and hence promoted the photocatalytic action [51]. A p-n type heterostructure including n-type P25 nanoparticles uniformly dispersed inside the p-type Co-Al LDH network was prepared by Kumar *et al*. via one-pot hydrothermal synthesis for enhanced reduction of carbon-dioxide. The movement of electrons from Co-Al LDH to neighbouring P25 and movement of holes in its contrary course from P25 to Co-Al LDH empower their successful separation bringing about the enhanced conversion of CO_2 to CO [52]. Recently numerous heterojunctions based materials have been synthesized like CdS-LDH [53, 54], Ag_2CO_3-LDH [55], etc.

One of the ideal approaches to increment the absorption of solar light by a semiconductor is the loading of plasmonic metals onto its surface. In the field of photocatalysis, plasmonic metal-loaded semiconductors have recently received more attention. The Surface Plasmon Resonance, a resonance-frequency collective oscillation of conduction electrons, is thought to be initiated by these metallic nanoparticles. The absorption of visible light is significantly enhanced as a result of this phenomenon. If the Fermi level of the metal is located between its VB and CB, the

photoinduced electrons from the semiconductor's CB immediately move to the metal nanoparticles. The Schottky barriers formed at the metal-semiconductor interface allow these metal nanoparticles to serve as electron sinks. The photoinduced electrons of metal nanoparticles are captured by suitable reactive species. Thus, metal loaded on the surface of the semiconductor is responsible for shortening the charge transfer distance, suppressing the electron-hole pairs rejoining, and enhancing the response of the photocatalyst in visible region [56, 57]. Wang *et al*. fabricated Ag/Ni-Co LDH with varying Ag loading through the photo-deposition method on the surface of flower-like Ni-Co LDH. They discovered their performance to be better than bare LDH towards the degradation of tetracycline. The Ag nanoparticle-induced surface plasmon resonance led to a stronger visible light response and effective charge carrier separation favorable for enhanced photoactivity. The sample with 15% of Ag loading showed the highest activity as further surface coverage of LDH by Ag nanoparticles reduces their approach towards the light [58]. Katsumata *et al*. demonstrated the conversion of CO_2 to CO in the presence of different Pt, Pd, and Au loaded ZnCr LDHs fabricated via photo-deposition of metals. Among them, Pt loaded ZnCr LDH exhibited the best activity due to its smaller size providing more reactive sites inducing enhanced electron-hole separation and two-electron reduction of CO_2 molecule to CO [59]. Various other metal loaded LDHs and its composites such as Pt or Pt-Ag loaded Zn-Al and Zn-FeAl LDHs [60], Au-Ag loaded Mg-Al LDH [61], Au/Zn-Al MMO [62], Ag@Ni-Al LDH/g-C_3N_4 [63], etc. have been successfully fabricated.

1.2. Research Gaps:

Literature survey reveals that various LDHs have been extensively investigated for adsorption and photocatalytic activities. Due to positively charged brucite like layers, LDHs are well known for adsorption of only anionic compounds. But several modifications such as intercalation of

surfactants, coupling of adsorbing materials such as graphene oxide, multiwalled carbon nanotubes, biochar etc. have been done to improve their adsorption activity towards anionic as well as cationic species.

Graphitic carbon nitride (g-C_3N_4) is a non-toxic, environment friendly and most stable allotrope of carbon having high surface area. It consists of uniformly arranged tri-s-triazine (C_6H_7) units containing π-π interactions and could be used as an efficient adsorbent for various toxic metal cations and organic molecules. The coupling of LDHs with graphitic nitride can be expected to increase their adsorption capability towards different organic pollutants due to their strong synergetic effect, larger surface area, increased porosity, and more active sites. But, the adsorption performance of LDHs modified with g-C_3N_4 has not been explored well. There is a lack of reports demonstrating the impact of g-C_3N_4 loading on the adsorption behavior of LDH towards both the anionic and cationic pollutants.

Similarly, coupling of LDH with g-C_3N_4 has came out as a powerful phenomenon to improve its photocatalytic property through the formation of heterojunction leading stronger and wider visible light response, more reactive sites, rapid transfer of charge carriers, efficient charge separation increasing lifetime of electron and holes. Among different LDH photocatalysts reported in the literature, the Mg-Al LDH showed the advantages of easy and low-cost synthesis, durable structure, and high sustainability [7-8]. But due to its wide bandgap (>3 eV), its photocatalytic performance has not been explored well. Only a few reports for the photocatalytic decomposition of pollutants using highly stable and durable Mg-Al LDH are available. In this manner, it is essential to research such LDH in the interest of photocatalysis. However, the challenge is to adjust its wide band gap in the visible region and decreases the rejoining of charge carriers.

According to literature reports, the photoactivity of Co-Al LDH with band gap value ~ 2.1 eV having suitable redox potentials and excellent visible light response has not been surveyed accordingly. As a consequence, there is need to explore the photoactivity of such highly capable photocatalyst. The introduction of g-C_3N_4 (E_g ~ 2.7 eV) to Co-Al LDH (E_g ~ 2.1 eV) can be significantly promotes its photoactivity. Construction of 2D/2D g-C_3N_4/LDH composite can make an efficient photocatalyst as it possess (1) efficient migration of electron and holes across the interface of heterojunction causing electron-hole pairs separation (2) enhanced surface area with more reactive sites.

As reported in literature, coupling of semiconductors with plasmonic nanoparticles is a promising way to achieve dual advantages of improved light absorption response and enhanced generation and enahanced separation of photogenerated electron and holes. Moreover, the photoactivity of LDHs and g-C_3N_4 coupled LDH nanocomposites can be further improved via deposition of plasmonic metals on their surface. But, very few reports are available in literature regarding metal loaded LDHs and ternary metal loaded g-C_3N_4 coupled LDH composites. Thus, there is a need to explore the influence of g-C_3N_4 and metal deposition on LDHs to improve their adsorption and photocatalytic performance. In order to overcome the above mentioned facts, following objectives were designed for the preparation of various LDHs to study their adsorption and photocatalytic properties. The research focused on investigating the influence of plasmonic metal nanoparticles and g-C_3N_4 loading over LDHs to improve their adsorption and photocatalytic performance for environment remediation.

1.3. Objectives:

1. Preparation and characterization of different metal (M_1^{2+}, M_2^{3+}) layered double hydroxides (e.g. Ni-Co, Co-Al etc.) nanostructures.
2. Study the effect of graphitic carbon nitride (g-C_3N_4) and metal (Ag, Cu, and Au) loading on the surface structure and physicochemical properties of as-prepared LDH nanostructure.
3. Evaluate the adsorption and photocatalytic properties using model toxic pollutants by these prepared metal loaded g-C_3N_4/LDH hybrid nanocomposites.

1.4. Methodology:

1.4.1. Synthesis of LDHs:

(a) Direct co-precipitation method:

It involved the direct hydrolysis of metal cations by strong base in the presence of solution containing interlayer anions. The desired LDH was obtained by mixing solutions of M^{2+} and M^{3+} metal salts, with further addition of strong base (such as NaOH and NH_4OH) and solution containing anions to be intercalated. The base was used to maintain the appropriate pH required to precipitate metal hydroxides. The mixture was aged for several hours and then washed with distilled water and ethanol and dried.

(b) Solvothermal method:

This method included the chemical reaction taking place in an organic solvent at a particular temperature higher than the solvent's boiling point. In this process, the metal precursors along with a base were mixed in an organic solvent. The mixture was then transferred to an auto clave

to get hydrothermally treated at a particular temperature for certain hours.

(c) Urea hydrolysis method:

This method involved the precipitation of metal hydroxides using urea as a precipitating agent instead of strong bases like NaOH and KOH. Urea is a very weak Bronsted base (pK_b = 13.8) that hydrolyzes slowly in aqueous solutions (as shown below) providing a low degree of supersaturation as compared to strong bases.

$NH_2\text{-}CO\text{-}NH_2 \longrightarrow NH_4^+ + NCO^-$

$NCO^- + H_2O \longrightarrow NH_4^+ + CO_3^{2-}$

$NCO^- + 2H^+ + 2H_2O \longrightarrow NH_4^+ + H_2CO_3$

The ammonium carbonate forming at the end of the process leads to the precipitation of mixed metal hydroxide layers with carbonate ions as an intercalated anion. The metallic solution containing a particular amount of urea was hydrothermally treated at a required temperature for certain period of time.

1.4.2. Synthesis of g-C_3N_4 (CN):

Melamine was used as a precursor to synthesize graphitic carbon nitride. About 5.0 g of melamine was heated in a muffle furnace at 550^{o}C for 4 hours with a heating rate of 5^{o}C/min. The obtained yellow-colored product was crushed into powder and further calcined for two hours at 530^{o}C at a heating rate of 5^{o}C/min in order to create g-C_3N_4 nanosheets.

1.4.3. Preparation of CN-LDH composites:

The CN-LDH composites were fabricated through the electrostatic self-assembly method. This method involved mixing CN and LDH suspensions under continuous stirring for about 12 hours. The electrostatic forces generated between negatively charged CN and positively charged brucite like layers of LDH were the driving forces in the formation of CN-LDH composites.

1.4.4. Preparation of metal loaded composites:

The photo-reduction method was approached to deposit plasmonic nanoparticles on LDH and CN-LDH composites. This method depends on the metal ion reduction potential and CB edge potential of the catalyst. About 100 mg of catalyst was dispersed in an aqueous solution of sacrificial agent in flask. A predetermined amount of metal salt solution was added to the aforementioned dispersion and the prepared flask was purged with argon to remove excess oxygen and prevent oxidation. A rubber septum was used to seal the prepared flask, which was then exposed to ultraviolet light for some time. The obtained composite was centrifuged, washed, and dried.

1.5. Characterization Techniques:

Different modified synthetic procedures were applied for the fabrication of pure LDHs and CN-LDH, M@LDH, and M@CN-LDH nanocomposites (experimental details are provided in the respective chapters). The as-prepared catalysts were further analyzed using various characterization techniques to investigate their surface, structural, and physicochemical properties.

1.5.1. X-ray powder diffraction:

The crystallographic diffraction patterns were recorded on (i) an X-ray diffractometer (XRD, Xpert pro) equipped with Cu-Kα radiation (1.54 Å), operating at 45 kV over a diffraction angle in the range of $10° \leq 2\theta \leq 80°$ and (ii) an X-ray diffractometer (BRUKER) using Cu-Kα radiation ($\lambda = 1.5403$ Å) in the 2θ range of 5-80^{o}.

1.5.2. Fourier transform infrared spectroscopy:

To determine the structural information of the catalysts, the Fourier transform infrared spectra

were recorded on an Agilent FTIR spectrometer.

1.5.3. Dynamic light scattering and Zeta potential:

The electrokinetic properties of all the catalysts were demonstrated through the dynamic light scattering technique and zeta potential analysis. The dispersions containing 2 mg of catalysts in 5 ml of distilled water in a disposable cuvette (for DLS analysis) and folded capillary cell (for zeta potential analysis) were analyzed using a Zeta potential analyzer (Light source: He : Ne laser, Detector: Avalanche photodiode).

1.5.4. Morphological analysis:

The structural and morphological properties were analyzed with (i) Scanning electron microscopy (SEM-EDS, JEOL JSM-7600 F, 01 operating at 30 kV), (ii) Field emission scanning electron microscopy (Carl-Zeiss Sigma 500 FEG-SEM with Bruker EDS), and (iii) High resolution electron microscopy, (HRTEM, TALOS F200S G2 (200 KV, FEG, CMOS Camera 4K x 4K).

1.5.5. Surface area and porosity determination:

The surface area and pore size distribution of samples were analyzed with the BET (Brunauer-Emmett-Teller) and BJH (Barrett-Joyner-Halenda) methods, respectively, using Quanta Chrome Nova 2200 Surface Area & Pore Size Analyzer (Outgas Time: 6.0 hrs, Outgas temperature: 200℃, Analysis gas: Nitrogen, and Bath Temp: 77.3 K).

1.5.6. Optical studies:

The UV-visible diffuse reflectance spectra were obtained on a diffuse reflectance spectrophotometer (Avantes) using $BaSO_4$ as a reference. The Halogen lamp and AvaSpec-2048 was used a light source and detector, respectively. The photoluminescence spectra were recorded on PL-spectrophotometer (RF-5301) (scan range: 300.0 nm to 900.0 nm, and slit width:

Excitation: 10.0 nm, Emission: 10.0 nm).

1.5.7. X-ray photoelectron spectroscopy:

The elemental composition was demonstrated by X-ray photon spectroscopy using XPS, Shimadzu-165, U.K. Al k-alpha was used as an X-ray source at a photon energy of 1486.6 eV and a hemispherical analyzer was used. The pass energy of the survey spectrum and core levels spectrum was 160 eV and 20 eV, respectively. The samples were mounted using carbon tape (stick on stub) and the surface charge was mitigated using a flood gun.

1.6. Adsorption and Photocatalytic studies:

During adsorption and photodegradation studies, a required amount of catalyst was added to the test tube containing aqueous solution of certain pollutant and placed under dark and light illumination, respectively, for some time. At definite time intervals, the catalyst was removed from the pollutant solution via centrifugation and remaining pollutant concentration was analyzed using UV-visible spectrophotometer (Shimadzu UV-2600 spectrophotometer).

The two important Langmuir and Freundlich models were investigated to predict the mechanism of adsorption on the surface of catalyst. In order to predict the reaction kinetics in case of adsorption and photodegradation, pseudo first and second order kinetic models were studied. The detailed procedures and equations are explained in respective chapters.

Further, the mineralization of the pollutant during degradation was determined by measuring the total oxygen chemical demand (TOC) using the chemical method. The degradation products and intermediates were investigated using the LC-MS (Waters, SYNAPT-XS HDMS MASS Spectrometer, U.K). The C18 column (2.1 mm × 100 mm; 1.7 µm) was used at a temperature of 35^{o}C. The mobile phase consists of 0.1% formic acid water & 0.1% acetonitrile with a flow rate of 0.3ml/min.

References:

[1] C. Forano, U. Costantino, V. Pre, Layered Double Hydroxides, 2013. https://doi.org/10.1016/B978-0-08-098258-8.00025-0.

[2] N. Chubar, R. Gilmour, V. Gerda, M. Mi, M. Omastova, K. Heister, P. Man, J. Fraissard, V. Zaitsev, Layered double hydroxides as the next generation inorganic anion exchangers : Synthetic methods versus applicability, 245 (2017) 62–80. https://doi.org/10.1016/j.cis.2017.04.013.

[3] L. Mohapatra, K. Parida, A review on the recent progress , challenges and perspective of layered double hydroxides as promising photocatalysts, J. Mater. Chem. A Mater. Energy Sustain. 4 (2016) 10744–10766. https://doi.org/10.1039/C6TA01668E.

[4] O. Aberdeen, Segregation and cation-ordering in sj6grenite and pyroaurite, 37.

[5] G. Arrabito, A. Bonasera, G. Prestopino, A. Orsini, A. Mattoccia, E. Martinelli, B. Pignataro, P.G. Medaglia, Layered Double Hydroxides : A Toolbox for Chemistry and Biology, (2019).

[6] Z. Peng, Y. Xin, X. Dong, Z. Quan, Facile synthesis of CoAl-LDH/MnO_2 hierarchical nanocomposites for high-performance supercapacitors, Ceram. Int. 40 (2014) 2115–2120. https://doi.org/10.1016/j.ceramint.2013.07.127.

[7] M. Farnane, A. Machrouhi, F.Z. Mahjoubi, R. Elmoubarki, H. Tounsadi, M. Abdennouri, N. Barka, Effects of molar ratio and calcination temperature on the adsorption performance of Zn/Al layered double hydroxide nanoparticles in the removal of pharmaceutical pollutants Ala a, 3 (2018) 188–195. https://doi.org/10.1016/j.jsamd.2018.03.005.

[8] H. Jiang, K. Katsumata, J. Hong, A. Yamaguchi, K. Nakata, C. Terashima, N. Matsushita, M. Miyauchi, A. Fujishima, Photocatalytic reduction of CO_2 on Cu_2O-loaded Zn-Cr layered double hydroxides, "Applied Catal. B, Environ. (2017). https://doi.org/10.1016/j.apcatb.2017.11.011.

[9] N. Baig, M. Sajid, Applications of layered double hydroxides based electrochemical sensors for determination of environmental pollutants : A review, Trends Environ. Anal. Chem. 16 (2017) 1–15. https://doi.org/10.1016/j.teac.2017.10.003.

[10] A. Grover, I. Mohiuddin, A. Kumar, J. Singh, K. Kim, Zn-Al layered double hydroxides intercalated with surfactant : Synthesis and applications for efficient removal of organic dyes, J. Clean. Prod. 240 (2019) 118090. https://doi.org/10.1016/j.jclepro.2019.118090.

[11] H.N. Tran, C. Lin, H. Chao, Amino acids-intercalated Mg/Al layered double hydroxides as dual-electronic adsorbent for effective removal of cationic and oxyanionic metal ions, Sep. Purif. Technol. (2017). https://doi.org/10.1016/j.seppur.2017.09.060.

[12] I. Jean, B. Fr, D. Lorraine, J. Lamour, Nomenclature of the hydrotalcite supergroup : natural layered double hydroxides, 76 (2012) 1289–1336. https://doi.org/10.1180/minmag.2012.076.5.10.

[13] M. Aghazadeh, S. Mohammad, R. Paran, G. Naderi, D. Puglia, Progress in Organic Coatings Epoxy/layered double hydroxide (LDH) nanocomposites: Synthesis, characterization, and excellent cure feature of nitrate anion intercalated Zn-Al LDH, Prog. Org. Coatings. 136 (2019) 105218. https://doi.org/10.1016/j.porgcoat.2019.105218.

[14] Z. Yang, J. Wei, G. Zeng, H. Zhang, X. Tan, C. Ma, A review on strategies to LDH-based materials to improve adsorption capacity and photoreduction efficiency for CO_2, Coord. Chem. Rev. 386 (2019) 154–182. https://doi.org/10.1016/j.ccr.2019.01.018.

[15] A. Guzmán-vargas, E. Lima, G.A. Uriostegui-ortega, M.A. Oliver-tolentino, E.E. Rodríguez, Adsorption and subsequent partial photodegradation of methyl violet 2B on Cu/Al layered double hydroxides, Appl. Surf. Sci. 363 (2016) 372–380. https://doi.org/10.1016/j.apsusc.2015.12.050.

[16] M. Ogawa, S. Asai, Hydrothermal Synthesis of Layered Double Hydroxide- Deoxycholate Intercalation, (2000) 3253–3255.

[17] M. Xu, B. Bi, B. Xu, Z. Sun, L. Xu, Polyoxometalate-intercalated ZnAlFe-layered double hydroxides for adsorbing removal and photocatalytic degradation of cationic dye, 157 (2018) 86–91. https://doi.org/10.1016/j.clay.2018.02.023.

[18] Z. Huang, P. Wu, X. Zhang, X. Wang, N. Zhu, Intercalation of Fe(III) complexes into layered double hydroxides: Synthesis and structural preservation, Appl. Clay Sci. 65–66 (2012) 87–94. https://doi.org/10.1016/j.clay.2012.05.007.

[19] E. Article, NiTi-Layered double hydroxides nanosheets as efficient photocatalysts for oxygen evolution from water using visible light, (2014) 951–958. https://doi.org/10.1039/c3sc52546e.

[20] H. Lyu, K. Hu, J. Fan, Y. Ling, Z. Xie, J. Li, 3D hierarchical layered double hydroxide/carbon spheres composite with hollow structure for high adsorption of dye, Appl. Surf. Sci. 500 (2020) 144037. https://doi.org/10.1016/j.apsusc.2019.144037.

[21] A. Tsujimura, M. Uchida, A. Okuwaki, Synthesis and sulfate ion-exchange properties of a hydrotalcite-like compound intercalated by chloride ions, 143 (2007) 582–586. https://doi.org/10.1016/j.jhazmat.2006.09.073.

[22] S. Miyata, Anion-exchange properties of hydrot alcite-like compounds, 31 (1983) 305–311.

[23] S. V Prasanna, P.V. Kamath, Anion-Exchange Reactions of Layered Double Hydroxides : Interplay between Coulombic and H-Bonding Interactions, (2009) 6315–6320.

[24] B. Valim, L.P. Cardoso, Study of acids herbicides removal by calcined Mg - Al - CO_3 - LDH, 67 (2006) 987–993. https://doi.org/10.1016/j.jpcs.2006.01.015.

[25] M. Hu, X. Yan, X. Hu, R. Feng, M. Zhou, High-capacity adsorption of benzotriazole from aqueous solution by calcined Zn-Al layered double hydroxides, Colloids Surfaces A. 540 (2018) 207–214. https://doi.org/10.1016/j.colsurfa.2018.01.009.

[26] M.L. Kantam, B. Neelima, C.V. Reddy, A recyclable protocol for aza-Michael addition of amines to α,β-unsaturated compounds using Cu-Al hydrotalcite, 241 (2005) 147–150. https://doi.org/10.1016/j.molcata.2005.06.061.

[27] V. Veselsk, J. Filip, S. Cíhalov, M. Kom, Sorption mechanisms of arsenate on Mg-Fe layered double hydroxides : A combination of adsorption modeling and solid state analysis Barbora Hudcov a, (2016) 1–10. https://doi.org/10.1016/j.chemosphere.2016.11.031.

[28] Y. Kuthati, R.K. Kankala, C. Lee, Layered double hydroxide nanoparticles for biomedical applications : Current status and recent prospects, Appl. Clay Sci. 112–113 (2015) 100–116. https://doi.org/10.1016/j.clay.2015.04.018.

[29] K.M. Parida, L. Mohapatra, Carbonate intercalated Zn/Fe layered double hydroxide : A novel photocatalyst for the enhanced photo degradation of azo dyes, Chem. Eng. J. 179 (2012) 131–139. https://doi.org/10.1016/j.cej.2011.10.070.

[30] L. Su, X. Zhang, C. Mi, Y. Liu, Insights into the electrochemistry of layered double hydroxide containing cobalt and aluminum elements in lithium hydroxide aqueous solution, 179 (2008) 388–394. https://doi.org/10.1016/j.jpowsour.2007.12.087.

[31] D. Xiaolong, H. Jinzhao, W. Hao, C. Fashen, L. Yifan, X. Xijin, M. Renzhi, T. Sasaki,

Recent progress in functionalized layered double hydroxides and their application in efficient electrocatalytic water oxidation, J. Energy Chem. (2018). https://doi.org/10.1016/j.jechem.2018.07.007.

[32] M. Zubair, M. Daud, G. Mckay, F. Shehzad, M.A. Al-harthi, Recent progress in layered double hydroxides (LDH)-containing hybrids as adsorbents for water remediation, Appl. Clay Sci. 143 (2017) 279–292. https://doi.org/10.1016/j.clay.2017.04.002.

[33] Y. Lu, B. Jiang, L. Fang, F. Ling, J. Gao, F. Wu, High performance NiFe layered double hydroxide for methyl orange dye and Cr (VI) adsorption, 152 (2016) 415–422. https://doi.org/10.1016/j.chemosphere.2016.03.015.

[34] T. Guan, L. Fang, Y. Lu, F. Wu, F.Ling, J. Gao, B. Hu, F. Meng, X. Jin, A facile approach to synthesize 3D flower-like hierarchical NiCo layered double hydroxide microspheres and their enhanced adsorption capability, (2017). https://doi.org/10.1016/j.colsurfa.2017.06.049.

[35] N. Kaur, S.K. Shahi, V. Singh, Anomalous behavior of visible light active TiO_2 for the photocatalytic degradation of different reactive dyes, Photochem. Photobiol. Sci. 14 (2015) 2024-2034. https://doi.org/10.1039/c5pp00165j

[36] D. Zhu, Q. Zhou, Action and mechanism of semiconductor photocatalysis on degradation of organic pollutants in water treatment : A review, Environ. Nanotechnology, Monit. Manag. 12 (2019) 100255. https://doi.org/10.1016/j.enmm.2019.100255.

[37] Y. Li, C. Gao, R. Long, Y. Xiong, Photocatalyst design based on two-dimensional materials, 11 (2019). https://doi.org/10.1016/j.mtchem.2018.11.002.

[38] B. Sriram, J. N. Baby, S.F. Wang, R.R. M., M. Govindasamy, M. George, Eutectic Solvent-Mediated Synthesis of NiFe-LDH/Sulfur-Doped Carbon Nitride Arrays: Investigation of Electrocatalytic Activity for the Dimetridazole Sensor in Human Sustenance, ACS Sustainable

Chem. Eng. 8, 48, (2020) 17772–17782. https://doi.org/10.1021/acssuschemeng.0c06070.

[39] P. Rosaiah, N. G. Prakash, P. Divya, S. Sambasivam, M. Shkir, H. Algarni, T.J. Ko, One pot synthesis of flower-like Ni-Co/ reduced graphene oxide layered double hydroxide nanocomposites as advanced electrodes for high-performance asymmetric supercapacitors 56, (2022) 106133. https://doi.org/10.1016/j.est.2022.106133.

[40] V. Forne, Layered double hydroxides as highly efficient photocatalysts for visible light oxygen generation from water, (2009) 13833–13839.

[41] C. Octahedra, H. Matrix, Y. Zhao, S. Zhang, B. Li, H. Yan, S. He, L. Tian, A family of visible-light responsive photocatalysts obtained by dispersing CrO_6 octahedra into a hydrotalcite matrix, (2011) 13175–13181. https://doi.org/10.1002/chem.201101874.

[42] M. Shao, J. Han, M. Wei, D.G. Evans, X. Duan, The synthesis of hierarchical Zn-Ti layered double hydroxide for efficient visible-light photocatalysis, Chem. Eng. J. 168 (2011) 519–524. https://doi.org/10.1016/j.cej.2011.01.016.

[43] B. Zhang, Z. Dong, D. Sun, T. Wu, Y. Li, Enhanced adsorption capacity of dyes by surfactant-modified layered double hydroxides from aqueous solution, J. Ind. Eng. Chem. (2017) 1–11. https://doi.org/10.1016/j.jiec.2017.01.029.

[44] X. Ruan, Y. Chen, H. Chen, G. Qian, R.L. Frost, Sorption behavior of methyl orange from aqueous solution on organic matter and reduced graphene oxides modified Ni-Cr layered double hydroxides, Chem. Eng. J. (2016). https://doi.org/10.1016/j.cej.2016.01.041.

[45] Y. Long, J. Yu, F. Jiao, W. Yang, Preparation and characterization of MWCNTs/LDHs nanohybrids for removal of Congo red from aqueous solution, Trans. Nonferrous Met. Soc. China. 26 (2016) 2701–2710. https://doi.org/10.1016/S1003-6326(16)64398-4.

[46] M. Zhang, Q. Yao, C. Lu, Z. Li, W. Wang, Layered double hydroxide-carbon dot

composite: High-performance adsorbent for removal of anionic organic dye, 6 (2014) 20225-20233. https://.doi.org/10.1021/am505765e.

[47] D. Chen, Y. Li, J. Zhang, W. Li, J. Zhou, L. Shao, G. Qian, Efficient removal of dyes by a novel magnetic Fe_3O_4/ZnCr-layered double hydroxide adsorbent from heavy metal wastewater, J. Hazard. Mater. 243 (2012) 152–160. https://doi.org/10.1016/j.jhazmat.2012.10.014.

[48] M.S. Nasir, G. Yang, I. Ayub, S. Wang, L. Wang, X. Wang, W. Yan, S. Peng, S. Ramakarishna, Recent development in graphitic carbon nitride based photocatalysis for hydrogen generation, Appl. Catal. B Environ. 257 (2019) 117855. https://doi.org/10.1016/j.apcatb.2019.117855.

[49] S. Megala, M. Sathish, S. Harish, M. Navaneethan, S. Sohila, B. Liang, R. Ramesh, Enhancement of photocatalytic H_2 evolution from water splitting by construction of two dimensional g-C_3N_4/NiAl layered double hydroxides, Appl. Surf. Sci. 509 (2020) 144656. https://doi.org/10.1016/j.apsusc.2019.144656.

[50] D. Yazdani, A.A. Zinatizadeh, M. Joshaghani, Organic–inorganic Z-scheme g-C_3N_4-NiTi-layered double hydroxide films for photocatalytic applications in a fixed-bed reactor Authors:, J. Ind. Eng. Chem. (2018). https://doi.org/10.1016/j.jiec.2018.01.041.

[51] X. Li, Z. Yu, L. Shao, H. Zeng, Y. Liu, X. Feng, A novel strategy to construct a visible-light-driven Z-scheme (ZnAl-LDH with active phase/g-C_3N_4) heterojunction catalyst via polydopamine bridge (a similar “bridge” structure), J. Hazard. Mater. 386 (2020) 121650. https://doi.org/10.1016/j.jhazmat.2019.121650.

[52] S. Kumar, M.A. Isaacs, R. Trofimovaite, L. Durndell, C.M.A. Parlett, R.E. Douthwaite, B. Coulson, M.C.R. Cockett, K. Wilson, A.F. Lee, Environmental P25@CoAl layered double

hydroxide heterojunction nanocomposites for CO_2 photocatalytic reduction, "Applied Catal. B, Environ. 209 (2017) 394–404. https://doi.org/10.1016/j.apcatb.2017.03.006.

[53] S. Mancipe, F. Tzompantzi, R. Gómez, Synthesis of CdS/MgAl layered double hydroxides for hydrogen production from methanol-water decomposition, Appl. Clay Sci. 136 (2017) 67–74. https://doi.org/10.1016/j.clay.2016.11.013.

[54] Y. Qiu, B. Lin, F. Jia, Y. Chen, B. Gao, P. Liu, CdS-pillared CoAl-layered double hydroxide nanosheets with superior photocatalytic activity, Mater. Res. Bull. (2015). https://doi.org/10.1016/j.materresbull.2015.07.026.

[55] Y. Ao, D. Wang, P. Wang, C. Wang, J. Hou, J. Qian, Enhanced photocatalytic properties of the 3D flower-like Mg-Al layered double hydroxides decorated with Ag_2CO_3 under visible light illumination, Mater. Res. Bull. (2016). https://doi.org/10.1016/j.materresbull.2016.03.033.

[56] R.A. Rather, D. Pooja, P. Kumar, S. Singh, B. Pal, Plasmonic stimulated photocatalytic/electrochemical hydrogen evolution from water by (001) faceted and bimetallic loaded titania nanosheets under sunlight irradiation, J. Clean. Prod. 175 (2018) 394–401. https://doi.org/10.1016/j.jclepro.2017.12.083.

[57] R.A. Rather, S. Singh, B. Pal, Visible and direct sunlight induced H_2 production from water by plasmonic Ag-TiO_2 nanorods hybrid interface, Sol. Energy Mater. Sol. Cells. 160 (2017) 463–469. https://doi.org/10.1016/j.solmat.2016.11.017.

[58] T. Wang, X. Liu, C. Ma, Y. Liu, H. Dong, W. Ma, 3D Ag/NiCo-layered double hydroxide with adsorptive and photocatalytic performance, J. Taiwan Inst. Chem. Eng. 0 (2018) 1–8. https://doi.org/10.1016/j.jtice.2018.07.031.

[59] K. Katsumata, K. Sakai, K. Ikeda, G. Carja, N. Matsushita, Preparation and photocatalytic

reduction of CO_2 on noble metal (Pt, Pd, Au) loaded Zn-Cr layered double hydroxides, Mater. Lett. 107 (2013) 138–140. https://doi.org/10.1016/j.matlet.2013.05.132.

[60] M. Darie, E.M. Seftel, M. Mertens, R.G. Ciocarlan, P. Cool, G. Carja, Harvesting solar light on a tandem of Pt or Pt-Ag nanoparticles on layered double hydroxides photocatalysts for p-nitrophenol degradation in water, Appl. Clay Sci. 182 (2019) 105250. https://doi.org/10.1016/j.clay.2019.105250.

[61] N. Arora, A. Mehta, A. Mishra, S. Basu, 4-Nitrophenol reduction catalysed by Au-Ag bimetallic nanoparticles supported on LDH : Homogeneous vs. heterogeneous catalysis, Appl. Clay Sci. 151 (2018) 1–9. https://doi.org/10.1016/j.clay.2017.10.015.

[62] Y.X. Zhang, X.D. Hao, M. Kuang, H. Zhao, Z.Q. Wen, Preparation, characterization and dye adsorption of Au nanoparticles/ZnAl layered double oxides nanocomposites, Appl. Surf. Sci. (2013). https://doi.org/10.1016/j.apsusc.2013.06.136.

[63] S. Tonda, W.K. Jo, Plasmonic Ag nanoparticles decorated NiAl-layered double hydroxide/graphitic carbon nitride nanocomposites for efficient visible-light-driven photocatalytic removal of aqueous organic pollutants, Catal. Today. 315 (2018) 213–222. https://doi.org/10.1016/j.cattod.2017.12.019.

CHAPTER- 2

Adsorption performance of LDH and its g-C_3N_4 loaded composites towards anionic and cationic organic pollutants

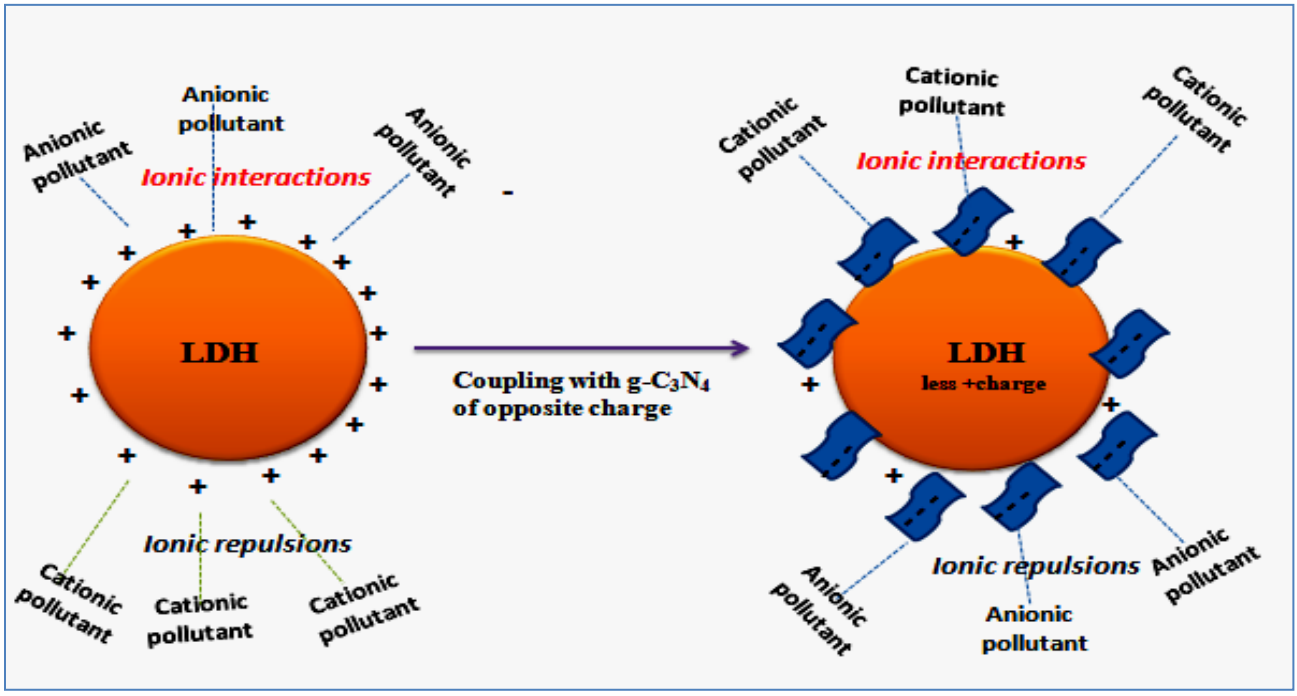

Schematic outline:

The LDHs possessing positively charged surfaces generally show efficient adsorption towards anionic pollutants due to the ionic interactions between the LDH surface and pollutant molecule. On the other hand, repulsive forces between cationic pollutant molecules and LDH's surface inhibit their adsorption towards cationic pollutants. After loading g-C_3N_4 onto LDH, the positive surface charge of LDH gets reduced leading to efficient adsorption of anionic pollutant molecules.

2.1. Introduction:

Water contamination has become a serious problem in the public arena that causes several medical issues. One of the main reasons is the release of organic pollutants as effluents from industries into water sources [1-3]. To get rid of such kinds of pollution, various techniques like ion exchange [4], photocatalytic degradation [5], coagulation [6], adsorption [7], and membrane separation [8] are used for water purification. Among them, adsorption is an easy, simple, economical, and highly efficient method extensively adopted worldwide to remove organic pollutants from water.

For the last few years, layered double hydroxides have received incredible consideration in the adsorption research field [9-11]. Owing to their low cost, high surface area, porous structure, non-toxicity, and excellent anion exchange capability, serving as efficient adsorbents capable of adsorbing toxic metal cations and anions, harmful organic dyes, herbicides, pesticides, toxic gases, pharmaceutical wastes, and various other pollution causing compounds [3,12,13]. Because of the positively charged surface, LDHs are highly effective adsorbents for the adsorption of harmful anionic organic compounds, whereas having a low affinity towards cationic organic species due to ionic repulsions. Several modifications such as the intercalation of surfactants into their interlayer gallery [14], coupling with other adsorbing materials (graphene oxide [15], multiwalled carbon nanotubes [16], biochar [17], etc.) are being adapted to LDHs for improving their adsorption activity towards anionic as well as cationic organic compounds.

Recently, Zhang *et al*. fabricated a Ni-Fe LDH/montmorillonite composite consisting of the positively charged LDH nanoflakes supported on the negatively charged surface of montmorillonite. They investigated the adsorption performance of the composite towards both the anionic and cationic dyes [18]. Li *et al*. modified the surface of Mg-Al LDH from

hydrophilic to hydrophobic by intercalating organic surfactants to effectively adsorb non-ionic, anionic, and cationic dyes [19]. However, cost-effective, easily synthesized, and non-toxic materials as adsorbents are of concern nowadays.

Graphitic carbon nitride is a non-toxic, easily synthesized, and environment-friendly compound having surface area. It is used as an effective adsorbent for a variety of toxic metal cations and organic molecules as it is made up of uniformly arranged tri-s-triazine (C_6N_7) units containing hydrophobic and Π-Π interactions. Due to the lone pair of electrons on nitrogen atoms in tri-s-triazine units, the surface of g-C_3N_4 has a negative charge [20-22]. The formation of composite constituting LDH and g-C_3N_4 can be an effective adsorbent towards organic pollutants owing to their environment-friendly nature, non-toxicity, and synergic effect.

In this work, positively charged Ni-Co LDH was coupled with negatively charged g-C_3N_4 nanosheets via self-assembly method. The effect of g-C_3N_4 loading onto LDH was demonstrated towards adsorption of anionic and cationic pollutants. Salicylic acid having the chemical formula $C_7H_6O_3$ is an anionic organic compound generally utilized in dyestuff and pharmaceutical industries as a key ingredient in numerous skincare products. A large amount of salicylic acid as waste is generated due to poor separation of products causing various health issues like headaches, gastric irritation, and diarrhea, and can even bring about death if consumed in high concentrations [23,24]. On the other hand, methylene blue having the chemical formula $C_{16}H_{18}ClN_3S$ is a cationic organic compound broadly utilized in numerous industries such as pharmaceuticals, textiles, paper, and cosmetics. The waste dye discharged from industries into the environment can cause genuine health problems like hypertension, abdominal pain, bladder irritation, and nausea [25, 26]. Thus, these harmful pollution-causing compounds need to remove from the environment.

This work evaluated the adsorption performance of Ni-Co LDH itself and the impact of g-C_3N_4 loading on its adsorption behavior towards salicylic acid and methylene blue chosen as model pollutants. Parameters like adsorbent dosage, initial pollutant concentration, and adsorption time were optimized using bare LDH. The adsorption performance of bare LDH, different 10-30 wt% g-C_3N_4 loaded LDH composites were then analyzed and compared under optimum conditions.

2.2. Experimental Section:

2.2.1. Chemical and Reagents:

Nickel nitrate hexahydrate ($Ni(NO_3)_2 \cdot 6H_2O$), Cobalt nitrate hexahydrate ($Co(NO_3)_2 \cdot 6H_2O$), Ammonium Chloride (NH_4Cl), Sodium Hydroxide (NaOH), Melamine ($C_3H_6N_6$), Salicylic acid ($C_7H_6O_3$), and Methylene blue ($C_{16}H_{18}ClN_3S$) were obtained from Loba Chemie, India. Distilled water was obtained using Milli-Q, Millipore an ultrafiltration system.

2.2.2. Synthesis of Ni-Co LDH:

Ni-Co LDH was synthesized by a simple and easy co-precipitation method [27]. The metallic salt of Ni^{2+} (0.45 mmol) and Co^{3+} (0.30 mmol) were dissolved in 20 ml of distilled water to prepare a metallic solution. Then, 4 mmol of NH_4Cl and 2.06 mmol of NaOH were added simultaneously to the above prepared metallic solution and stirred at 600 rpm for about half an hour. The mixture was then transferred to an oven and aged at 55^{o}C for 15h. After cooling to room temperature, the solution was centrifuged at 6000 rpm for five minutes to collect the precipitates, which were then washed several times with ethanol and distilled water. The sample was then dried for 12h at 60^{o} C. The as-prepared Ni-Co LDH sample was abbreviated as bare LDH.

2.2.3. Synthesis of g-C_3N_4 nanosheets (CN):

First, bulk graphitic carbon nitride was prepared by placing about 5 g of melamine in a silica crucible, covered, and heated in a muffle furnace at 550^oC for 4 hours with a heating rate of 5^oC/min. The bulk g-C_3N_4 yellow powder was collected until it cooled to room temperature and was crushed into a fine powder using a mortar pestle.

To prepare the g-C_3N_4 nanosheets, the obtained bulk g-C_3N_4 yellow powder was further calcined for another 2 hours at 530^oC with a heating rate of 5^oC/min. The obtained pale yellow product was g-C_3N_4 nanosheet powder [28, 29]. The prepared g-C_3N_4 nanosheet sample was abbreviated as CN.

2.2.4. Preparation of CN-LDH composites:

An appropriate amount of g-C_3N_4 powder (10, 20, and 30 wt%) was added into a beaker containing water and sonicated for 60 minutes to completely disperse the g-C_3N_4 particles. The LDH powder was taken in another water-containing beaker and sonicated for 60 minutes to completely disperse the LDH particles. Both the g-C_3N_4 and LDH suspensions were mixed and magnetically stirred at 600 rpm for about 12 hours [30]. The different 10, 20, and 30 wt% g-C_3N_4@LDH composites were abbreviated as 10CN-LDH, 20CN-LDH, and 30CN-LDH, respectively.

2.2.5. Adsorption activity:

The adsorption behavior of adsorbents (bare LDH and different (10-30) CN-LDH composites) was observed using a 30 ml solution of pollutants. The parameters such as the concentration of pollutants (5-55 mg/L for salicylic acid and 2-50 mg/L for methylene blue), amount of adsorbent (2-20 mg), and contact time (2-30 min for salicylic acid and 15-210 min for methylene blue) were investigated. A set of beakers, each beaker containing 30 ml of pollutant solution of a

particular concentration and the appropriate amount of adsorbent was prepared and stirred at 600 rpm using a magnetic stirrer under the dark for different time intervals. After stirring for a fixed time, each beaker was removed and the adsorbent was separated from the solution using centrifugation. The concentration of adsorbate in the supernatant was measured using a UV-Visible spectrophotometer at maximum absorbance (λ_{max}= 296 and 664 nm for salicylic acid and methylene blue, respectively). The adsorption capacities (adsorbed mass per unit mass, mg/g) of the adsorbents were determined using the following equation:

$$Q_e = (C_o - C_e)\frac{V}{W} \quad \text{..... (2.1)}$$

where C_o signifies the initial concentration of pollutant (mg/L), C_e is the concentration of the pollutant in the solution at equilibrium (mg/L), V is the volume of solution (L), W is the amount of adsorbent (g), and Q_e is the adsorption efficiency of the adsorbent (mg/g) at equilibrium. The percentage (R%) of salicylic acid and methylene blue adsorbed onto adsorbents was determined using the following equation:

$$R\% = \frac{(C_o - C_e)}{C_o} \times 100 \quad \text{..... (2.2)}$$

where C_o is the concentration of pollutant at time, t = 0 min and C_e is concentration of pollutant at equilibrium [47, 48].

2.3. Results and discussion:

2.3.1. Crystallographic and structural studies

The XRD spectra of bare Ni-Co LDH, g-C_3N_4 (CN), and CN-LDH composites were studied (**Fig. 2.1)**. The peaks observed at 2θ value of 11.0^o, 22.2^o, 34.1^o, and 60.6^o in LDH spectrum corresponds to (003), (006), (009), and (110) planes, respectively, of pure LDH (JCPDS No. 38-0486) [27, 31]. The peak at 2θ value of 27.5^o in CN spectrum indexed to pure g-C_3N_4 [20]. In the case of CN-LDH composites, all the peaks related to pure LDH were present along an additional

peak originating at about 2θ= 27.5° corresponding to g-C_3N_4 which confirmed its presence in composites. This peak intensity increased with an increase in the wt% loading of g-C_3N_4 in the LDH sample demonstrating the successful formation of the composites. Moreover, after modification with g-C_3N_4, a very slight change was observed in diffraction peak positions of pure LDH confirming the preservation of its crystal structure phase and successful coupling of LDH with CN.

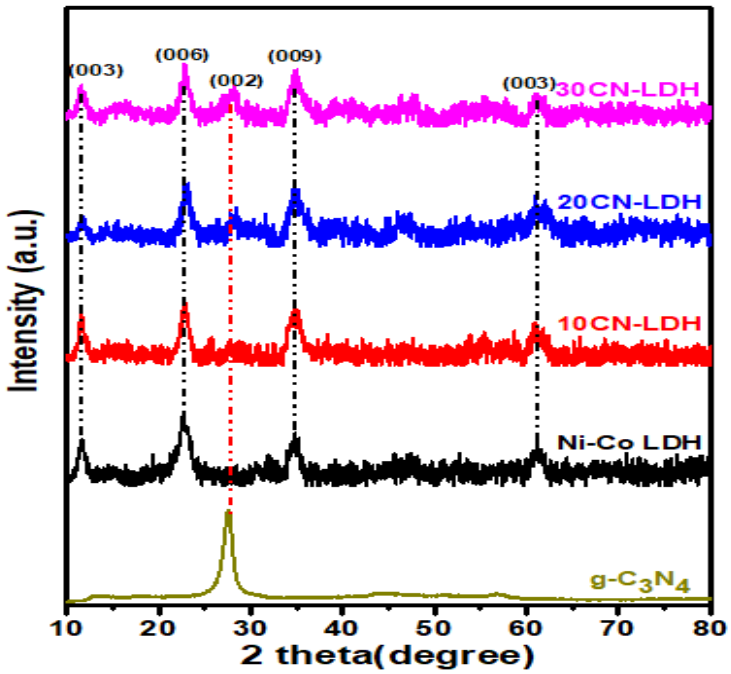

Fig.2.1. X-ray diffraction patterns of g-C_3N_4, Ni-Co LDH, and different CN-LDH composites.

Fig.2.2 shows the FTIR spectrum of bare LDH and 30CN-LDH composite. The spectrum of LDH revealed the presence of hydroxyl groups, intercalated anions, and metal ions in the brucite like layers. A broad absorption band appeared at about 3400 cm^{-1} is the O-H stretching band corresponding to metal hydroxyl groups and interlayer water molecules. A band at 1622 cm^{-1} originated due to the vibrations of water molecules in the interlayer region. The band positioned at 1350 cm^{-1} accredited to the nitrate anions in the interlayer spacing [33, 34]. The bands that

appeared in the region 500-900 cm^{-1} correspond to metal-oxygen (Ni-O and Co-O) and metal-oxo-bridge linkage (Ni-O-Co) bands [30, 35]. In the case of the 30CN-LDH composite, the additional band originating at about 3500 cm^{-1} credited to the stretching of uncondensed N-H groups of CN [29]. The presence of CN credited to the sharpness of bands appearing in the region 1350 to 1650 cm^{-1} credited to stretching vibration modes of sp^2 C-N and out-of-plane bending vibrations of sp^3 C-N bonds. A peak originated at 834 cm^{-1} corresponds to the bending vibrations of s-triazine units [36, 20]. Moreover, after the addition of g-C_3N_4, the bands representing the pure LDH phase in CN-LDH composite spectrum show little shift from that in bare LDH spectrum. These results indicated the effect and deposition of g-C_3N_4 on LDH through interfacial electrostatic interactions [29].

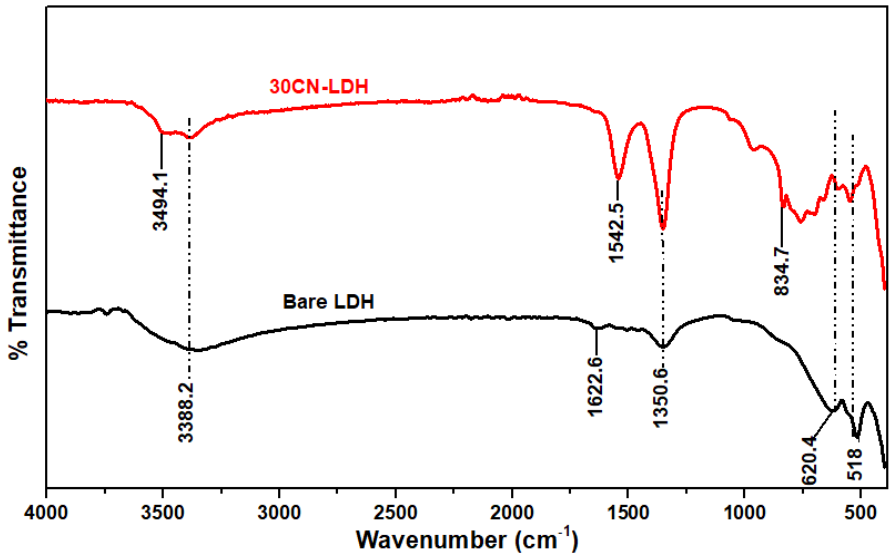

Fig.2.2. The FTIR spectrum of bare LDH and 30CN-LDH composite.

2.3.2. Morphological studies:

The surface morphology of bare LDH and CN-LDH composites was examined using SEM analysis. The SEM image (**Fig.2.3 (a and b)**) of bare LDH shows the petal-like morphology comprising sharp petals oriented and interconnected in certain directions. Such morphology provides more contact area and space for the reaction to take place on the surface [27, 32]. On

the other hand, in the case of the 30CN-LDH composite (**Fig.2.3 (c and d)**), a significant change in morphology than bare LDH was observed. The sharp petals were missing and the petal-like surface morphology was distorted due to the stacking of negatively charged CN onto the positively charged LDH.

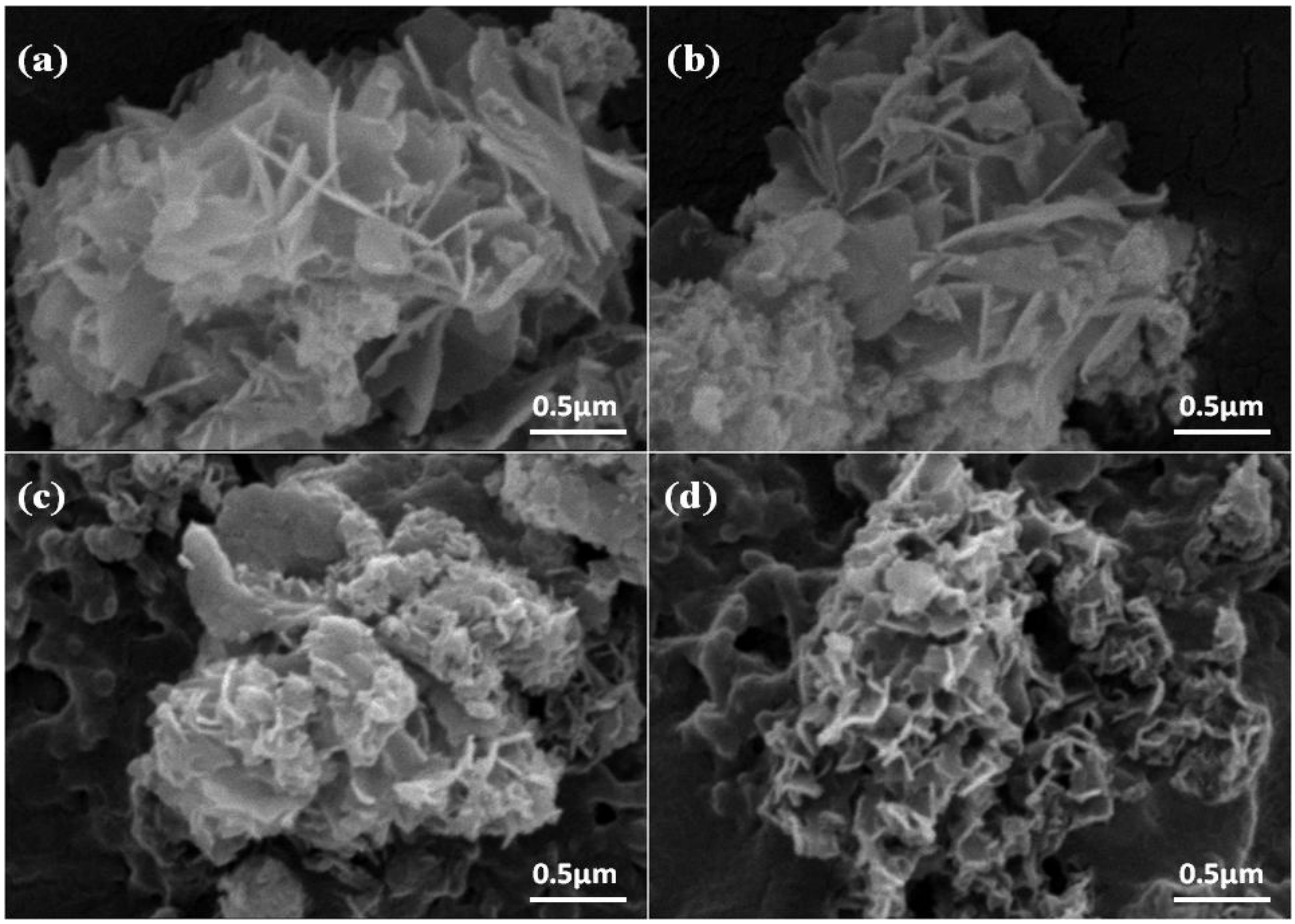

Fig.2.3. SEM images of Ni-Co LDH (a and b) and 30CN-LDH composite (c and d).

The EDS spectrum and elemental dot mapping for the 30CN-LDH composite are shown in **Fig.2.4**. The EDS spectrum showed the signals corresponding to elemental composition of the CN-LDH composite. The wt% distribution of elements was as 17.51, 23.67, 33.36, 2.81, 10.33, and 12.32 % for C, N, O, Cl, Co, and Ni, respectively. Similarly, the elemental mapping showed the distribution of Ni, Co, O, Cl, C, and N elements appearing in purple, blue, green, sky-blue, red, and yellow regions, respectively.

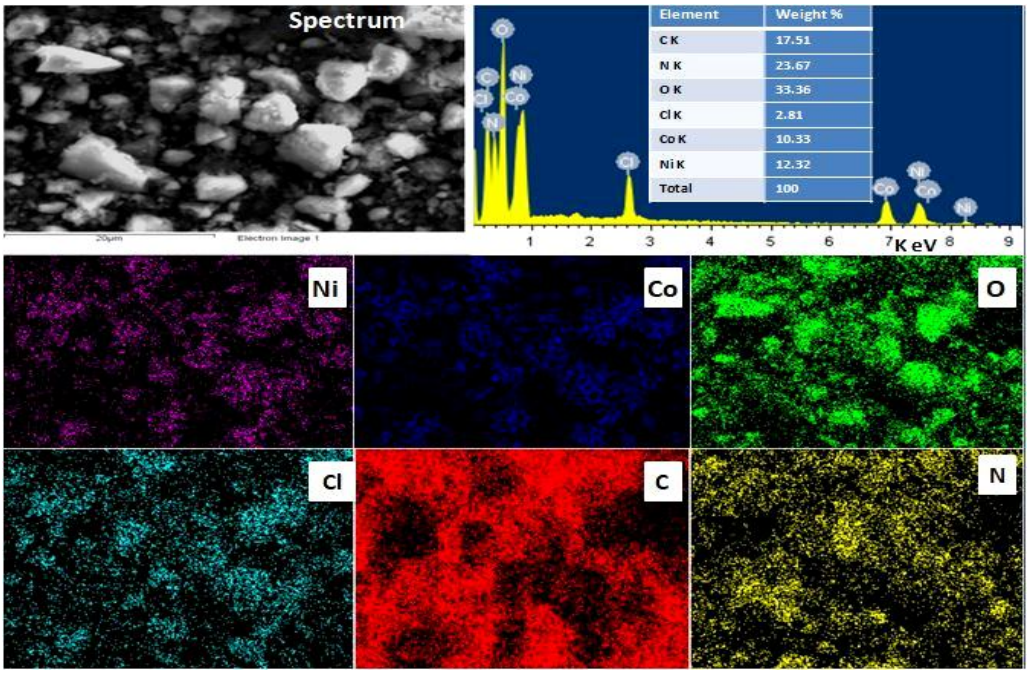

Fig.2.4. The EDS spectrum showing elemental composition and elemental dot mapping showing elemental distribution of 30CN-LDH composite.

2.3.3. Electrokinetic studies:

The electrokinetic studies of as-synthesized samples were examined using Zeta and DLS analysis. Due to the positive charge of brucite-like layers that resulted from the partial substitution of Ni^{2+} by Co^{3+} ions during the formation of double hydroxide layers, the zeta potential of bare LDH was found to be +27.7 mV as shown in **Fig.2.5 (a)**. The zeta potential value of pure g-C_3N_4 was observed as -19.3 mV ascribed to tri-s-triazine units containing nitrogen pots having a lone pair of electrons responsible for negatively charged surface. For composites, the zeta potential value was observed at +10.6, +6.69, and +3.36 mV for 10CN-LDH, 20CN-LDH, and 30CN-LDH composite, respectively. The decrease in the zeta potential with an increase in the wt% loading of g-C_3N_4 credited to the ionic interactions between LDH and g-C_3N_4 that neutralized the positive charge on the LDH surface [30].

As per the dynamic light scattering technique, a variation in the hydrodynamic particle size of

LDH was observed with variable wt% stacking of CN (**Fig.2.5 (b)**). The particle size of bare LDH was 1057 nm, which increased to 1251, 1488, and 1681 nm in the case of 10CN-LDH, 20CN-LDH, and 30CN-LDH composites, respectively. The expansion in the particle size of CN-LDH composites could be due to the deposition of g-C_3N_4 nanosheets onto the surface of LDH.

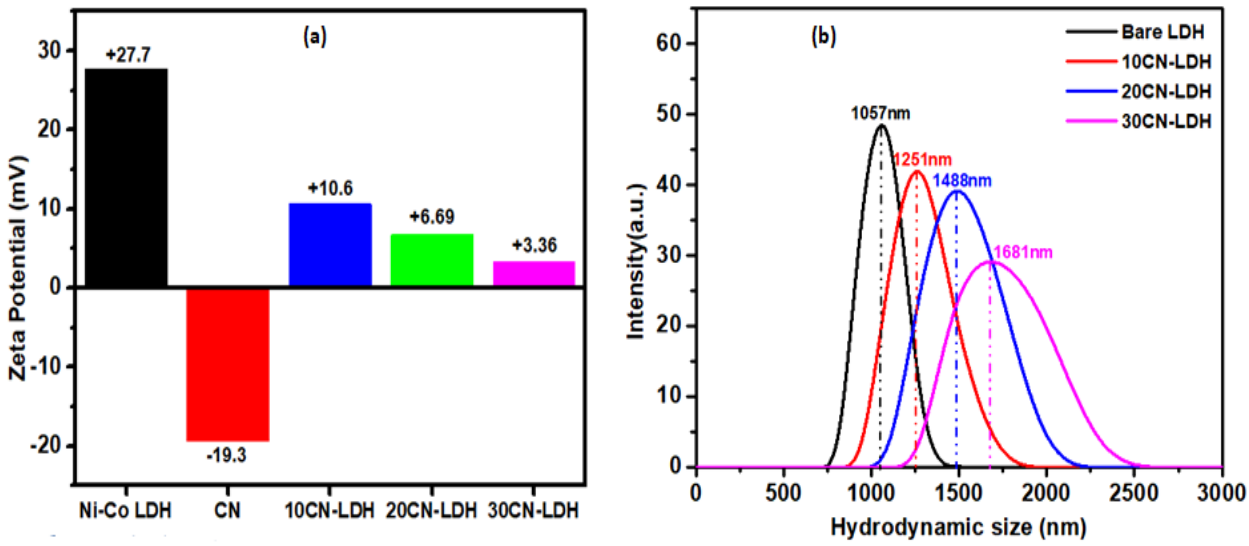

Fig.2.5. The Zeta potential variation (a) and hydrodynamic particle size (b) of Ni-Co LDH, CN, and different CN-LDH composites.

Adsorption Studies

2.3.4. Effect of adsorbent dosage:

The adsorption of adsorbate at the surface of the adsorbent varies directly with its dosage. It is because the number of adsorption sites increases with an increment in the dose of adsorbent until saturation [37]. The influence of the dosage of bare LDH on the removal of negatively charged salicylic acid (40 mg/L) and positively charged methylene blue (10 mg/L) is represented in **Fig.2.6 (a)**. According to the observation, 0.012 g of LDH removed about 73.8% of salicylic acid. No significant change in the adsorption efficiency of LDH was noticed with further

increasing its dosage due to reaching saturation. On the other hand, 0.012 g of LDH dosage exhibited the maximum of only 12.5% removal of methylene blue dye showing saturation with more amount of LDH dosage. Here, no rise in adsorption efficiency was found by further increasing the concentration of LDH, which indicated the saturation of active sites. Therefore, 0.012 g of LDH dosage was optimized for adsorption of both the pollutants.

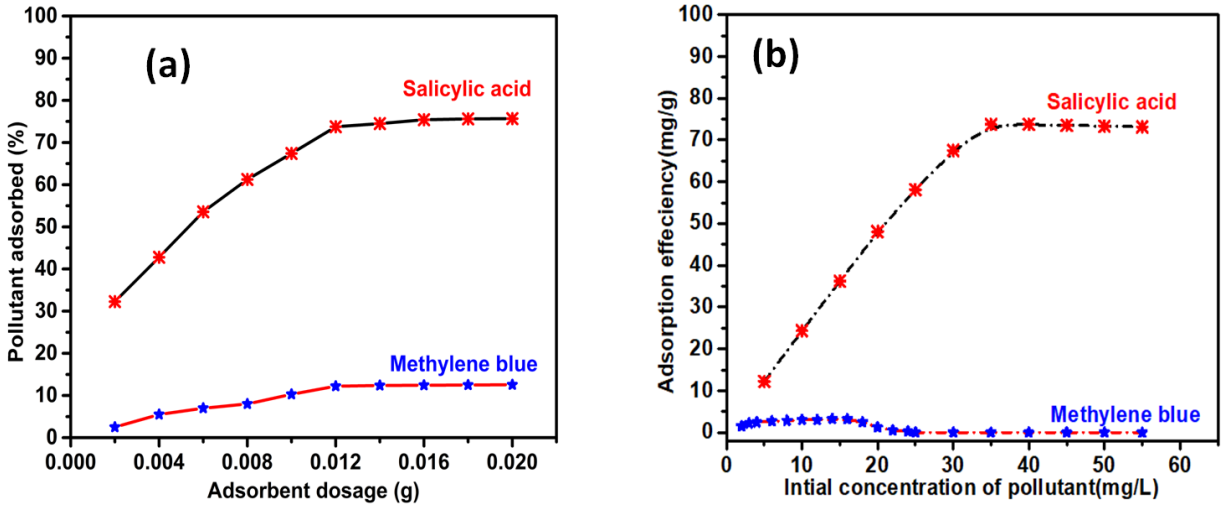

Fig.2.6. Effect of dosage of LDH (a) and effect of initial concentration of pollutants (b) on adsorptive removal of pollutants from aqueous solution.

2.3.5. Effect of initial concentration:

The influence of the concentration of pollutants (dosage- 0.012g) was investigated via varying the concentration of salicylic acid and methylene blue by 5-55 mg/L and 2-50 mg/L, respectively. As illustrated in **Fig.2.6 (b)**, the highest adsorption efficiency of 73.7 mg/g was observed at 35 mg/L initial concentration of salicylic acid and a plateau at higher concentrations representing the saturation of adsorption sites [38, 39]. On the other hand, for methylene blue, the adsorption efficiency was a maximum of 3.03 mg/g at 10 mg/L of its initial concentration. It then decreased with a further increase in concentration and became even zero at higher

concentrations showing no adsorption.

2.3.6. Effect of contact time:

The contact time between adsorbate and adsorbent plays a crucial role in the adsorption process as the adsorption increases with an increase in contact time until the reach of the equilibrium state [37, 39]. As shown in **Fig.2.7 (a)**, more than 60% of salicylic acid was rapidly adsorbed in the first 2 minutes on the surface of bare LDH and then adsorbed slowly with time. The maximum adsorption of about 84% of salicylic occurred within only 20 minutes with no further increment as the equilibrium state was achieved. For methylene blue (**Fig.2.7 (b)**), the equilibrium was achieved in 150 minutes with only 12.5% of dye adsorbed. The adsorption of salicylic acid was efficiently high on the surface of LDH. It could be due to (i) its petal-like morphology that provides a large contact area and (ii) electrostatic interactions between its surface and salicylic acid molecules. On the other hand, the ionic repulsions between the brucite-like layers of LDH and methylene dye molecules were responsible for the lesser adsorption of methylene blue.

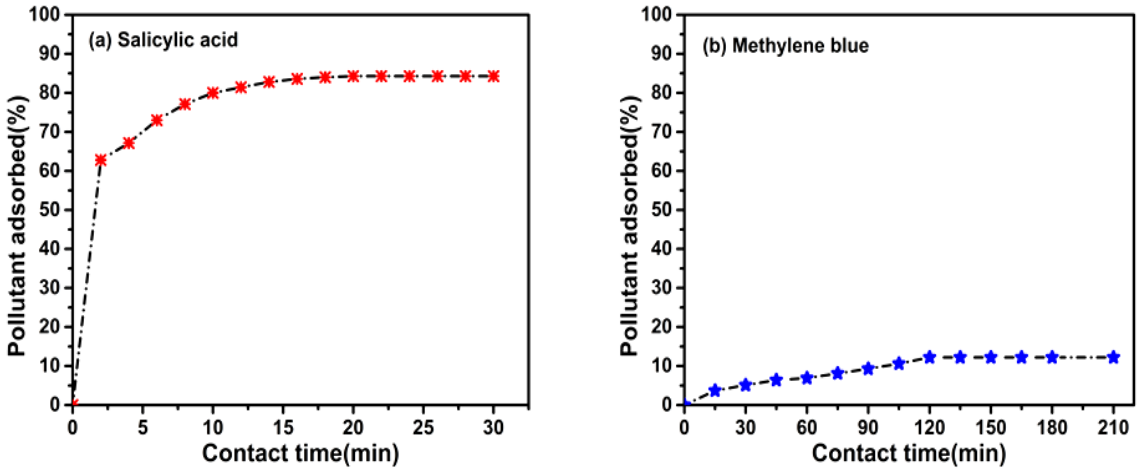

Fig.2.7. Effect of contact time on adsorption behavior of bare LDH towards salicylic acid (a) and methylene blue (b). Adsorbent dosage- 0.012g, Salicylic acid concentration- 35mg/L, methylene

blue concentration-10mg/L.

2.3.7. Influence of g-C_3N_4 loading:

As represented in **Scheme-2.1**, the loading of g-C_3N_4 nanosheets onto LDH brought an adverse change in its adsorption behavior by decreasing its positive charge. The decrease in the positive charge of LDH with the loading of g-C_3N_4 onto its surface improved its adsorption efficiency towards methylene blue, whereas showed the opposite behavior for salicylic acid. As shown in **Fig.2.8**, when the wt% loading of g-C_3N_4 on LDH was increased, the adsorption efficiency of LDH decreased towards salicylic acid, whereas increased towards methylene blue. The 30CN-LDH composite with the highest 30 wt% g-C_3N_4 loading exhibited maximum adsorption efficiency of 79% for methylene blue that was 6-7 times higher than that of bare LDH. It could be to the deposition of g-C_3N_4 on the surface of LDH that decreased its surface charge and provided adsorption sites for methylene blue. For salicylic acid, in the case of 30CN-LDH composite, the adsorption efficiency decreased to 43.75% which was about two times less than bare LDH.

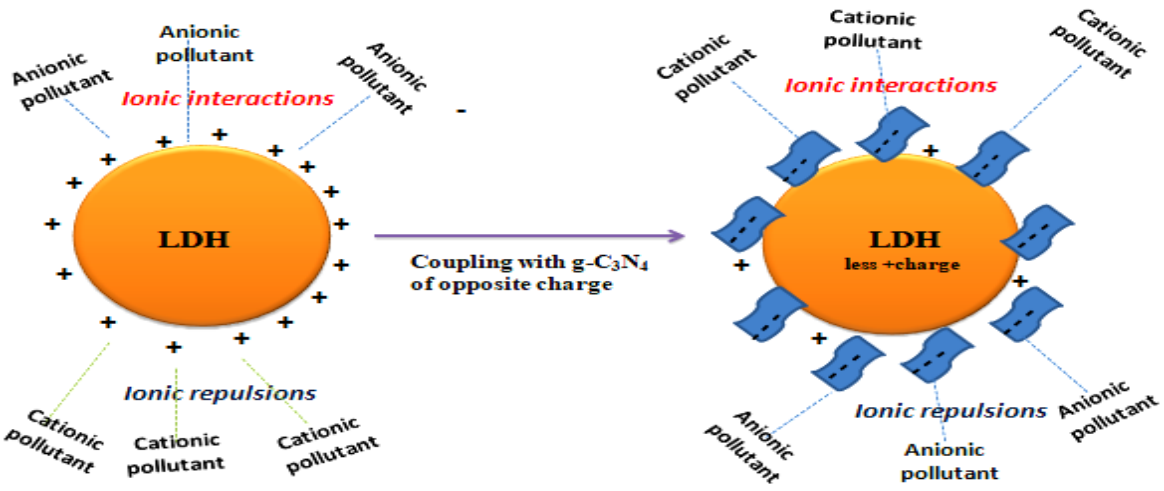

Scheme-2.1. A schematic representation of surface modification of LDH with loading of g-C_3N_4 and adsorption mechanism of cationic and anionic pollutants.

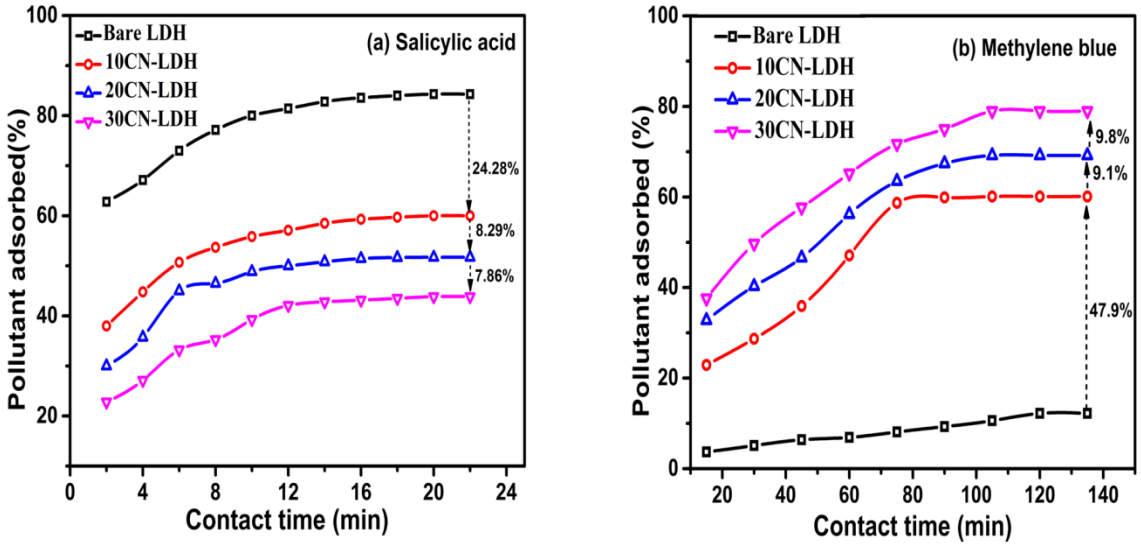

Fig.2.8. Influence of g-C_3N_4 loading on adsorption behavior of bare LDH towards salicylic acid (a) and methylene blue (b); Adsorbent dosage- 0.012g, Salicylic acid concentration- 35mg/L, methylene blue concentration-10mg/L.

2.3.8. Adsorption Isotherms:

To confirm the adsorption phenomenon, 30 ml of solutions of salicylic acid and methylene blue with an initial pollutant concentration of 35 mg/L and 10 mg/L, respectively, were stirred in the presence of 0.012g of adsorbent under dark for 12 hours. As shown in **Fig.2.9** and **Fig.2.10**, no significant change in the absorbance value was observed with 12 hours of contact time than 150 and 20 min for salicylic acid (S.A) and methylene blue (M.B), respectively. It confirmed that there was no intercalation of molecules in the interlayer gallery of LDH during the adsorption of pollutants. **Fig.2.11 (a,b)** shows the graph between C_e vs Q_e representing the adsorption of salicylic acid and methylene blue over bare LDH and (10-30) CN-LDH composites. The adsorption capacity initially increased with an increase in the concentration and then reached a plateau due to the saturation of active sites.

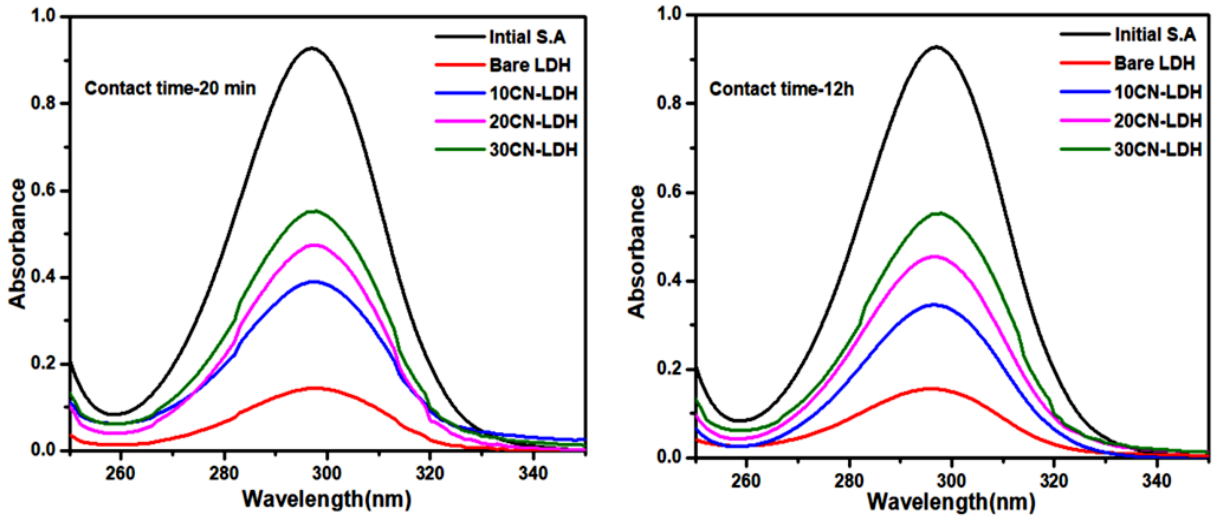

Fig.2.9. Absorbance spectra of adsorption of salicylic acid over bare LDH and (10-30) CN-LDH composites in 20 min (left) and 12 hours (right).

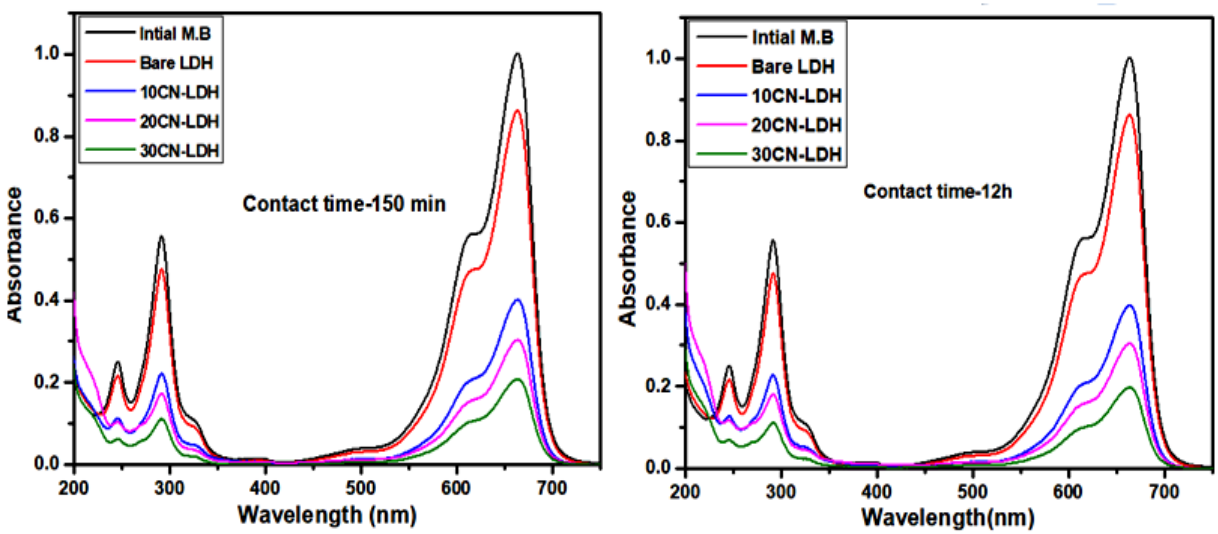

Fig.2.10. Absorbance spectra of adsorption of methylene blue over bare LDH and (10-30) CN-LDH composites in 150 min (left) and 12 hours (right).

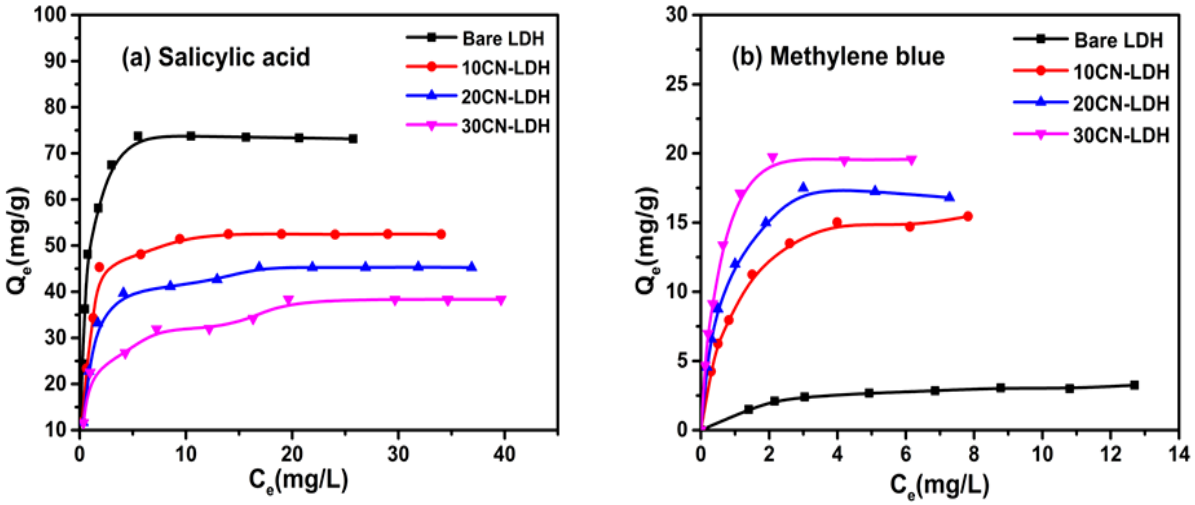

Fig.2.11. The adsorption of salicylic acid (a) and methylene blue (b) over bare LDH and (10-30) CN-LDH composites.

The two most common Langmuir and Freundlich adsorption isotherm models were employed to analyze the adsorption process of the adsorbate at equilibrium. With a specific amount (0.012g) of the adsorbent, the initial concentration of pollutants was changed (5-55 mg/L for salicylic acid and 2-10 mg/L for methylene blue).

The Langmuir isotherm is based on homogenous adsorption, which occurs when a monolayer of adsorbate is formed on the surface of the adsorbent with identical adsorption sites having equivalent energy. It is also assumed that there are no interactions between the adjacent adsorbed molecules as one molecule adsorbs on one adsorption site. The expression of Langmuir adsorption isotherm is expressed as:

$$Q_e = \frac{Q_{max} K_L C_e}{1+K_L C_e} \quad \ldots\ldots\ldots\ldots\ldots\ldots \quad (2.3)$$

The Langmuir isotherm equation in linear form is described as:

$$\frac{C_e}{Qe} = \frac{1}{Q_{max} K_L} + \frac{C_e}{Q_{max}} \quad \ldots\ldots\ldots\ldots\ldots \quad (2.4)$$

where k_L (L/mg) is Langmuir constant demonstrates the affinity of adsorbate towards adsorbent,

C_e (mg/L) is the concentration of adsorbate at equilibrium, Q_e (mg/g) is the adsorption capacity of adsorbent at equilibrium, Q_{max} (mg/g) is the maximum adsorption capacity of adsorbent upto complete monolayer formation. The graph was plotted between C_e/Q_e vs C_e (**Fig. 2.12**) and intercept and slope were used to determine the k_L and Q_{max} values. The nature of adsorption whether the process is favorable or unfavorable was concluded through a dimensionless constant, R_L expressed as:

$$R_L = \frac{1}{1+K_L C_o} \quad \text{..... (2.5)}$$

The value of R_L suggests the adsorption nature, Irreversible ($R_L = 0$), favorable ($0 < R_L < 1$), linear ($R_L = 1$) or non-favorable ($R_L > 1$) [40].

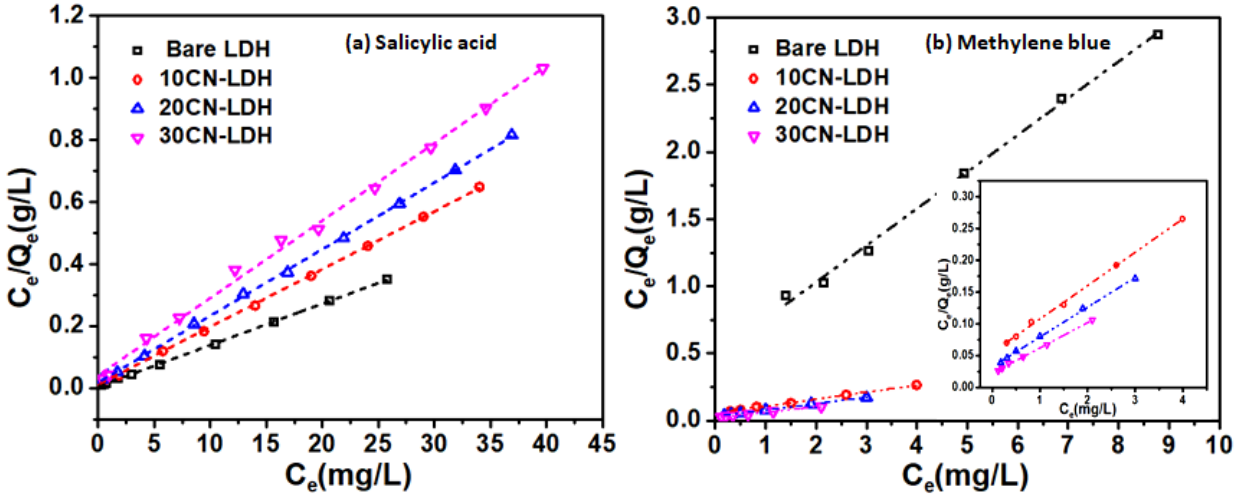

Fig.2.12. Modeling of adsorption equilibria by Langmuir isotherm; salicylic acid (a) and methylene blue (b) by Ni-Co LDH and (10-30) CN-LDH composites.

Freundlich isotherm is based on the idea that the surface of the adsorbent is heterogeneous and strong interactions occur between the adsorbate molecules. The adsorption occurs through the multilayer formation of the adsorbate molecules at adsorbent. The equation of the Freundlich isotherm is represented as follows:

$Q_e = k_F C_e^{1/n}$……. (2.6)

The linear form of Freundlich model is described by the following equation:

$\log Q_e = \frac{1}{n} \times \log C_e + \log k_F$ ……. (2.7)

where k_F is the Freundlich constant, 1/n is the heterogeneity factor that represents the favorability of adsorption, Q_e (mg/g) is the amount of pollutant adsorbed at equilibrium, C_e (mg/L) is the concentration of the pollutant at equilibrium. The values of n greater than unity indicate the favorability of the process [41, 42]. The plot of $\log Q_e$ vs $\log C_e$ for both pollutants is shown in **Fig.2.13**.

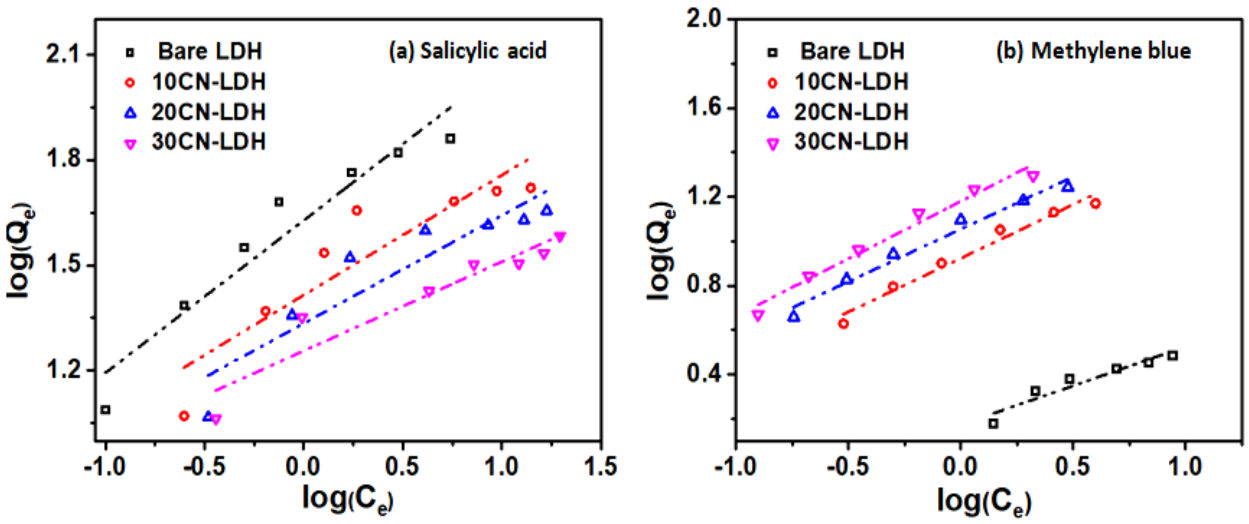

Fig.2.13. Modeling of adsorption equilibria by Freundlich isotherm; salicylic acid (a) and methylene blue (b) by Ni-Co LDH and (10-30) CN-LDH composites.

Both the adsorption models fitted the experimental data. Their corresponding calculated parameters using the slope and intercept obtained from their respective graphs are mentioned in **Table-2.1.**

Table-2.1. The calculated parameters of Langmuir and Freundlich models for adsorption of salicylic acid over bare LDH and CN-LDH composites are as follows:

(a) Salicylic acid

	Langmuir model				Freundlich model		
Adsorbent	**Q_{max}**	**K_L**	**R_L**	**R^2**	**K_F**	**1/n**	**R^2**
Bare LDH	75.18	2.56	0.008	0.9996	42.4	0.4338	0.9094
10CN-LDH	53.76	1.63	0.013	0.9995	26.0	0.3413	0.7987
20CN-LDH	46.50	1.20	0.018	0.9990	21.6	0.3073	0.8221
30CN-LDH	40.08	0.613	0.036	0.9992	18.0	0.2537	0.8803

(b) Methylene blue

	Langmuir model				Freundlich model		
Adsorbent	**Q_{max}**	**K_L**	**R_L**	**R^2**	**K_F**	**1/n**	**R^2**
Bare LDH	3.66	0.566	0.150	0.9957	1.48	0.3514	0.8924
10CN-LDH	19.02	3.827	0.025	0.9981	8.37	0.4833	0.9648
20CN-LDH	21.34	1.444	0.067	0.9984	11.33	0.4721	0.9694
30CN-LDH	25.07	1.819	0.052	0.9984	15.12	0.5164	0.9688

The Langmuir model's R^2 (correlation coefficient) values were in the range 0.9957-0.9996, higher and closer to unity than the Freundlich model's R^2 values, which were in the range 0.7987-0.9694. Therefore, a better fit was observed for Langmuir as compared to Freundlich model suggesting the adsorption of pollutants through monolayer formation at the surface of adsorbents. Also, the adsorption capacities of the adsorbents calculated using the Langmuir model equation were found closer to that obtained from experimental data. Hence, the adsorption of pollutants followed the Langmuir model and took place at a homogenous surface of the adsorbent where each pollutant molecule was fairly distributed on its surface. Moreover, the calculated R_L values using the Langmuir model equation fall within the range of 0-1 suggesting the favorable adsorption of both pollutants. The favorability of adsorption was deduced from the Freundlich parameter (n), which was found more than unity (1.936-3.941).

2.3.9. Kinetic Studies:

The rate of adsorption of salicylic acid and methylene blue over bare LDH and CN-LDH composites were analyzed using pseudo first order and pseudo second order kinetic models. The pseudo first order kinetic equation in linear form is written as:

$$\log(Q_e - Q_t) = \log Q_e - \frac{k_1}{2.303} t \quad \ldots\ldots\ldots\ldots (2.8)$$

where Q_t and Q_e are termed as adsorption efficiencies (mg/g) at time t (min) and equilibrium respectively, k_1 is the first order rate constant (min^{-1}) [43, 44]. The plots of $\log(Q_e-Q_t)$ vs t for both the pollutants salicylic acid and methylene blue are shown in **Fig.2.14**.

The pseudo second order kinetic equation in linear form is expressed as follows:

$$\frac{t}{Q_t} = \frac{1}{k_2 Q_e^2} + \frac{t}{Q_e} \quad \ldots\ldots\ldots\ldots\ldots (2.9)$$

where, k_2 is the second order rate constant, Q_t and Q_e represents the amount of adsorbate adsorbed per unit mass of the adsorbent (mg/g) at time t (min) and equilibrium, respectively [45, 46]. The second-order kinetic model is based on the assumption that the rate-limiting step is chemisorption that involves share or exchange of electrons between the adsorbate and adsorbent. The plots of t/Q_t vs t for both the pollutants are shown in **Fig.2.15**.

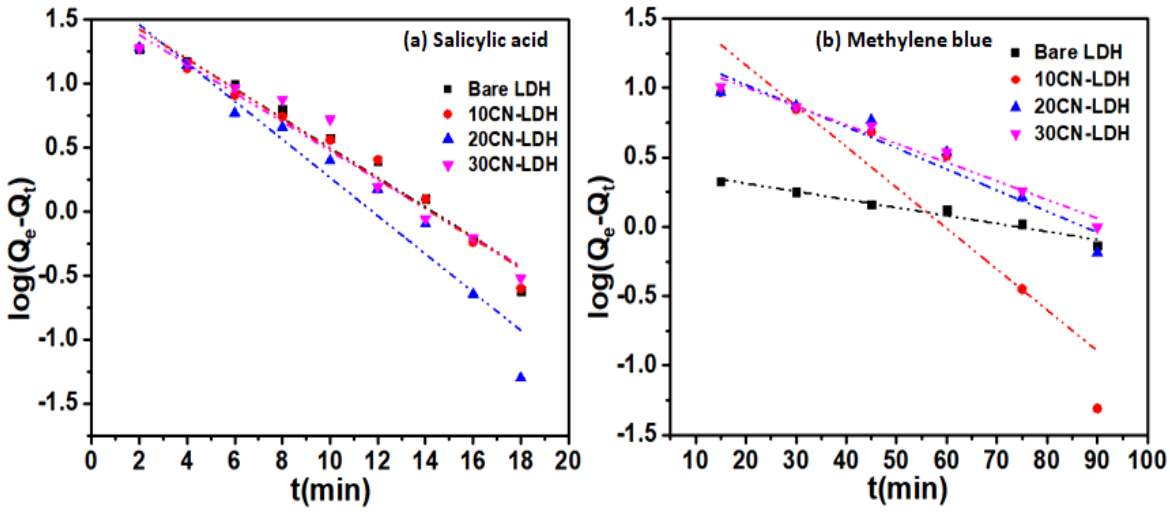

Fig.2.14. Kinetics of adsorption of salicylic acid (a) and methylene blue (b) over Ni-Co LDH and (10-30) CN-LDH composites according to first order model.

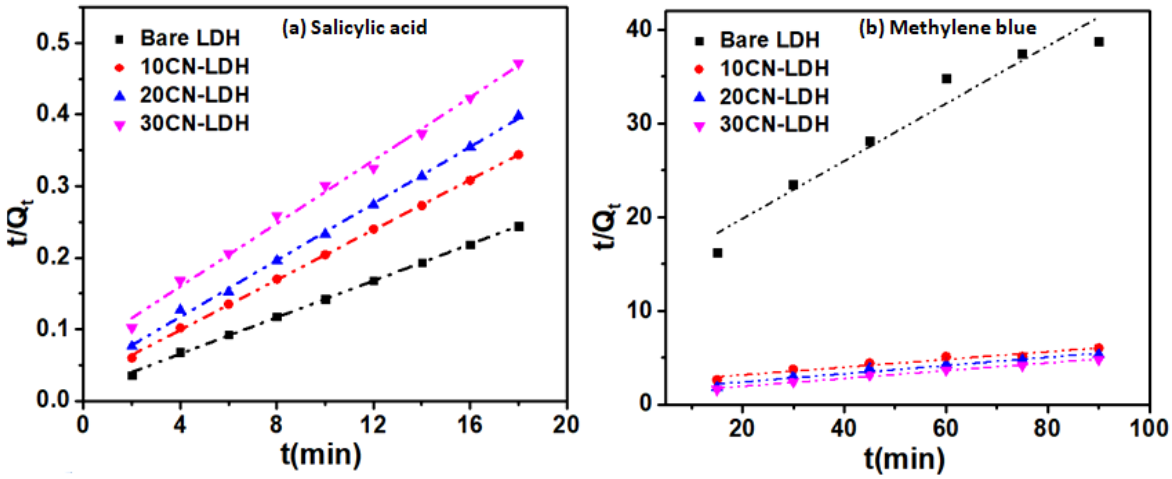

Fig.2.15. Kinetics of adsorption of salicylic acid (a) and methylene blue (b) by Ni-Co LDH and (10-30) CN-LDH composites according to second order model.

The slope and intercept obtained from the graphs were used to calculate the parameters of first and second order kinetics as mentioned in **Table-2.2.**

Table-2.2. The calculated parameters of first order kinetics and second order kinetics for the adsorption of (a) salicylic acid and (b) methylene blue over bare LDH and CN-LDH composites are as follows:

(a) Salicylic acid:

	First order kinetics			Second order kinetics		
Adsorbent	**Q_e**	**k_1**	**R^2**	**Q_e**	**k_2**	**R^2**
Bare LDH	45.19	0.266	0.9682	78.30	0.011	0.9995
10CN-LDH	40.24	0.260	0.9708	57.10	0.010	0.9995
20CN-LDH	57.05	0.343	0.9380	50.55	0.010	0.9982
30CN-LDH	45.45	0.268	0.9607	13.9	0.235	0.9936

(b) Methylene blue:

	First order kinetics			Second order kinetics		
Adsorbent	**Q_e**	**k_1**	**R^2**	**Q_e**	**k_2**	**R^2**
Bare LDH	2.67	0.013	0.9587	3.25	0.006	0.9384
10CN-LDH	56.65	0.067	0.8055	24.18	0.007	0.9370
20CN-LDH	21.22	0.035	0.9109	22.66	0.001	0.9507
30CN-LDH	18.75	0.031	0.9713	24.0	0.001	0.9903

For salicylic acid, the R^2 values of the second order kinetics were found higher and closer to unity than that for first order kinetics. It indicated that the salicylic acid was adsorbed on LDH and CN-LDH composites following second order kinetics. In the case of methylene blue, the R^2 values of the second order model were closer to unity than that of the first order model for CN-LDH composites except for bare LDH. The R^2 value of the second order model was lower than that of the first order model for bare LDH. The adsorption of methylene blue at the surface of bare LDH followed the first-order kinetics whereas followed second-order kinetics at the surface of CN-LDH composites.

2.4. Mechanistic understanding:

The Ni-Co LDH showed efficient adsorption towards salicylic acid, an anionic pollutant ascribed to the ionic interactions between salicylic acid molecules and the brucite like layers of LDH. To confirm the adsorption phenomenon, the zeta potential values of adsorbents after the adsorption of pollutants were analyzed (**Table-2.3**.).

Table-2.3. The analysis of zeta potential of bare LDH and (10-30) CN-LDH composites after the adsorption of salicylic acid and methylene blue:

Adsorbent	**Initial zeta potential (mV)**	**Zeta potential after salicylic acid adsorption (mV)**	**Zeta potential after methylene blue adsorption (mV)**
Bare LDH	+27.7	-0.41	+29.7
10CN-LDH	+10.6	-1.21	+12.3
20CN-LDH	+6.69	-2.94	+9.98
30CN-LDH	+3.36	-4.82	+8.46

The zeta potential value of bare LDH after the adsorption of salicylic acid changed from +27.7 to -0.41 mV suggesting the adsorption of salicylic acid at the surface of LDH through electrostatic interactions. Similarly, the zeta potential value for CN-LDH composites becomes more negative after the adsorption of salicylic acid. It may be due to the neutralization of the positive surface charge of LDH by adsorbed salicylic acid molecules and the presence of negatively charged g-C_3N_4. The surface zeta potential of bare LDH after contact with methylene blue increased from +27.7 to +29.7 mV. It can be due to the presence of adsorbed methylene blue molecules at LDH. Similarly, the zeta potential value of CN-LDH composites becomes more positive after the adsorption of methylene blue. It could be due to electrostatic interactions of methylene blue molecules with nitrogen atoms and π-π interactions with sp^2 hybridized carbon atom of g-C_3N_4 loaded onto LDH [47]. The comparison study regarding the removal of pollutants depending upon the surface zeta potential of adsorbent is shown in **Fig. 2.16.**

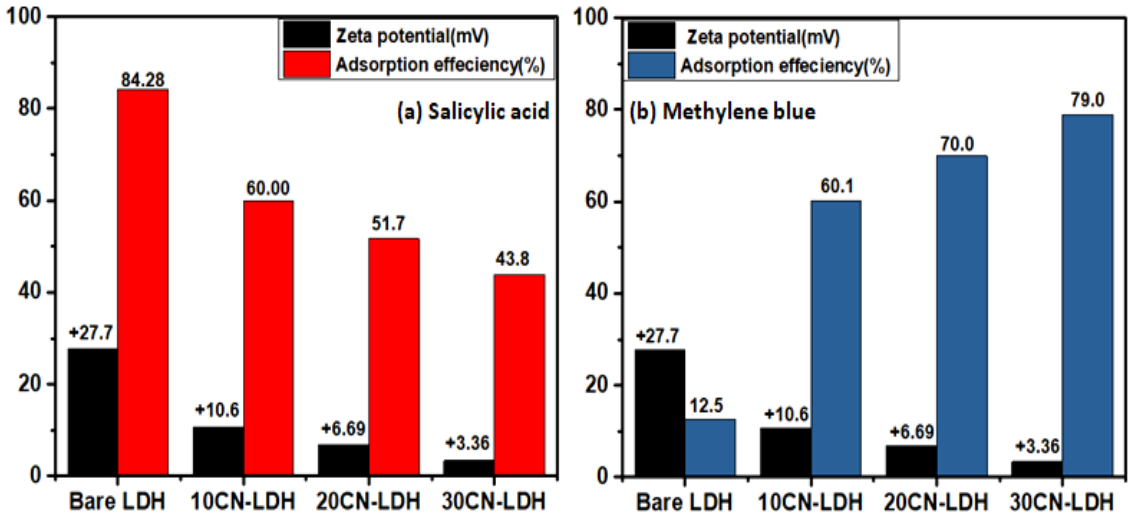

Fig.2.16. Comparison of adsorption efficiency (%) of (a) salicylic acid and (b) methylene blue by variation of zeta potential of Ni-Co LDH and (10-30) CN-LDH composites.

2.5. Conclusion:

This study explored that the bare LDH having a positively charged surface was an efficient adsorbent for anionic pollutants whereas showed poor affinity towards cationic pollutants. After g-C_3N_4 deposition, the adsorption behavior of LDH towards cationic pollutants improved as the coupling of LDH with negatively charged g-C_3N_4 nanosheets resulted in neutralizing its surface positive charge. Accordingly, by varying the amount of g-C_3N_4 loadings, the surface charge of the composite can be adjusted as desired to effectively adsorb the cationic and anionic pollutants. Hence, the formation of such hybrid materials can come out as a very beneficial strategy to design non-toxic, environment friendly, low cost, easily synthesized materials for wastewater treatment.

References:

[1] D.E. Helbling, Bioremediation of pesticide-contaminated water resources: The challenge of low concentrations, Curr. Opin. Biotechnol. 33 (2015) 142–148. https://doi.org/10.1016/j.copbio.2015.02.012.

[2] Y. Prabahkar, A. Gupta, A. Kaushik, Enhanced decolorization of Reactive Violet dye 1 by halo-alkaliphilic Nesterenkonia strain: Process optimization, short acclimatization and reusability analysis in batch cycles, Process Saf. Environ. Prot. 131 (2019) 116–126. https://doi.org/10.1016/j.psep.2019.09.004.

[3] M. Zubair, M. Daud, G. McKay, F. Shehzad, M.A. Al-Harthi, Recent progress in layered double hydroxides (LDH)-containing hybrids as adsorbents for water remediation, Appl. Clay Sci. 143 (2017) 279–292. https://doi.org/10.1016/j.clay.2017.04.002.

[4] I. Levchuk, J.J. Rueda Márquez, M. Sillanpaa, Removal of natural organic matter (NOM) from water by ion exchange – A review, Chemosphere. 192 (2018) 90–104. https://doi.org/10.1016/j.chemosphere.2017.10.101.

[5] N. Baliarsingh, K.M. Parida, G.C. Pradhan, Effects of Co, Ni, Cu, and Zn on photophysical and photocatalytic properties of carbonate intercalated M^{II}/Cr LDHs for enhanced photodegradation of methyl orange, Ind. Eng. Chem. Res. 53 (2014) 3834–3841. https://doi.org/10.1021/ie403769b.

[6] A. Talaiekhozani, M.R. Talaei, S. Rezania, An overview on production and application of ferrate (VI) for chemical oxidation, coagulation and disinfection of water and wastewater, J. Environ. Chem. Eng. 5 (2017) 1828–1842. https://doi.org/10.1016/j.jece.2017.03.025.

[7] R. Juanga, Y. Yei, C. Liao, K. Lind, H. Lue, S. Wange, A. Sun, Synthesis of magnetic Fe3O4/activated carbon nanocomposites with high surface area as recoverable adsorbents, J. Taiwan Inst. Chem. Eng. 90 (2018) 51-60. https://doi.org/10.1016/j.jtice.2017.12.005.

[8] C. Fonseca Couto, L.C. Lange, M.C. Santos Amaral, A critical review on membrane separation processes applied to remove pharmaceutically active compounds from water and wastewater, J. Water Process Eng. 26 (2018) 156–175. https://doi.org/10.1016/j.jwpe.2018.10.010.

[9] S. Daniel, S. Thomas, Layered double hydroxides: fundamentals to applications, Elsevier Ltd, 2020. https://doi.org/10.1016/b978-0-08-101903-0.00001-5.

[10] G. Zhang, X. Zhang, Y. Meng, G. Pan, Z. Ni, S. Xia, Layered double hydroxides-based photocatalysts and visible-light driven photodegradation of organic pollutants: A review, Chem. Eng. J. 392 (2020) 123684. https://doi.org/10.1016/j.cej.2019.123684.

[11] G. Arrabito, A. Bonasera, G. Prestopino, A. Orsini, A. Mattoccia, E. Martinelli, B. Pignataro, P.G. Medaglia, Layered Double Hydroxides : A Toolbox for Chemistry and Biology, (2019).

[12] A. Baruah, S. Mondal, L. Sahoo, U.K. Gautam, Ni-Fe-layered double hydroxide/N-doped graphene oxide nanocomposite for the highly efficient removal of Pb(II) and Cd(II) ions from water, J. Solid State Chem. 280 (2019) 120963. https://doi.org/10.1016/j.jssc.2019.120963.

[13] M. Zubair, N. Jarrah, M.S. Manzar, M. Al-Harthi, M. Daud, N.D. Mu'azu, S.A. Haladu, Adsorption of eriochrome black T from aqueous phase on MgAl-, CoAl- and NiFe-calcined layered double hydroxides: Kinetic, equilibrium and thermodynamic studies, J. Mol. Liq. 230 (2017) 344–352. https://doi.org/10.1016/j.molliq.2017.01.031.

[14] P. Chakraborty, R. Nagarajan, Efficient adsorption of malachite green and Congo red dyes by the surfactant (DS) intercalated layered hydroxide containing Zn^{2+} and Y^{3+} ions, Appl. Clay Sci. 118 (2015) 308–315. https://doi.org/10.1016/j.clay.2015.10.011.

[15] Y. Zheng, B. Cheng, W. You, J. Yu, W. Ho, 3D hierarchical graphene oxide-NiFe LDH composite with enhanced adsorption affinity to Congo red, methyl orange and Cr(VI) ions, Elsevier B.V., 2019. https://doi.org/10.1016/j.jhazmat.2019.02.013.

[16] Y. Long, J. Yu, F. Jiao, W. Yang, Preparation and characterization of MWCNTs/LDHs

nanohybrids for removal of Congo red from aqueous solution, Trans. Nonferrous Met. Soc. China. 26 (2016) 2701–2710. https://doi.org/10.1016/S1003-6326(16)64398-4.

[17] D. Huang, C. Liu, C. Zhang, R. Deng, R. Wang, W. Xue, H. Luo, G. Zeng, Q. Zhang, X. Guo, Cr(VI) removal from aqueous solution using biochar modified with Mg/Al-layered double hydroxide intercalated with ethylenediaminetetraacetic acid, Bioresour. Technol. 276 (2019) 127–132. https://doi.org/10.1016/j.biortech.2018.12.114.

[18] D. Bin Jiang, C. Jing, Y. Yuan, L. Feng, X. Liu, F. Dong, B. Dong, Y.X. Zhang, 2D-2D growth of NiFe LDH nanoflakes on montmorillonite for cationic and anionic dye adsorption performance, J. Colloid Interface Sci. 540 (2019) 398–409. https://doi.org/10.1016/j.jcis.2019.01.022.

[19] B. Zhang, Z. Dong, D. Sun, T. Wu, Y. Li, Enhanced adsorption capacity of dyes by surfactant-modified layered double hydroxides from aqueous solution, J. Ind. Eng. Chem. (2017) 1–11. https://doi.org/10.1016/j.jiec.2017.01.029.

[20] X. Cai, J. He, L. Chen, K. Chen, Y. Li, K. Zhang, Z. Jin, J. Liu, C. Wang, X. Wang, L. Kong, J. Liu, A 2D-g-C3N4 nanosheet as an eco-friendly adsorbent for various environmental pollutants in water, Chemosphere. 171 (2017) 192–201. https://doi.org/10.1016/j.chemosphere.2016.12.073.

[21] B. Ou, J. Wang, Y. Wu, S. Zhao, Z. Wang, Efficient removal of Cr (VI) by magnetic and recyclable calcined CoFe-LDH/g-C_3N_4 via the synergy of adsorption and photocatalysis under visible light, Chem. Eng. J. 380 (2020) 122600. https://doi.org/10.1016/j.cej.2019.122600.

[22] Z. Sun, H. Wang, Z. Wu, L. Wang, g-C_3N_4 based composite photocatalysts for photocatalytic CO_2 reduction, Catal. Today. 300 (2018) 160–172.

https://doi.org/10.1016/j.cattod.2017.05.033.

[23] X. Chen, Y. Li, L. Li, Facet-engineered surface and interface design of WO_3/Bi_2WO_6 photocatalyst with direct Z-scheme heterojunction for efficient salicylic acid removal, Appl. Surf. Sci. 508 (2020) 1–10. https://doi.org/10.1016/j.apsusc.2019.144796.

[24] X. Chen, W. Zhang, L. Zhang, L. Feng, J. Wen, J. Yang, C. Zhang, J. Jiang, H. Wang, Effective photocatalytic salicylic acid removal under visible light irradiation using Ag_2S/AgI-Bi_2S_3/BiOI with Z-scheme heterojunctions, Appl. Surf. Sci. 481 (2019) 1335–1343. https://doi.org/10.1016/j.apsusc.2019.03.214.

[25] Z. Ezzeddine, I. Batonneau-Gener, Y. Pouilloux, H. Hamad, Removal of methylene blue by mesoporous CMK-3: Kinetics, isotherms and thermodynamics, J. Mol. Liq. 223 (2016) 763–770. https://doi.org/10.1016/j.molliq.2016.09.003.

[26] P.M.K. Reddy, P. Verma, C. Subrahmanyam, Bio-waste derived adsorbent material for methylene blue adsorption, J. Taiwan Inst. Chem. Eng. 58 (2016) 500–508. https://doi.org/10.1016/j.jtice.2015.07.006.

[27] T. Wang, X. Liu, C. Ma, Y. Liu, H. Dong, W. Ma, 3D Ag/NiCo-layered double hydroxide with adsorptive and photocatalytic performance, J. Taiwan Inst. Chem. Eng. 0 (2018) 1–8. https://doi.org/10.1016/j.jtice.2018.07.031.

[28] S. Megala, M. Sathish, S. Harish, M. Navaneethan, S. Sohila, B. Liang, R. Ramesh, Enhancement of photocatalytic H_2 evolution from water splitting by construction of two dimensional g-C_3N_4/NiAl layered double hydroxides, Appl. Surf. Sci. 509 (2020) 144656. https://doi.org/10.1016/j.apsusc.2019.144656.

[29] S. Tonda, S. Kumar, M. Bhardwaj, P. Yadav, S. Ogale, g-C_3N_4/NiAl-LDH 2D/2D Hybrid Heterojunction for High-Performance Photocatalytic Reduction of CO_2 into Renewable

Fuels, ACS Appl. Mater. Interfaces. 10 (2018) 2667–2678. https://doi.org/10.1021/acsami.7b18835.

[30] S. Nayak, L. Mohapatra, K. Parida, Visible light-driven novel g-C_3N_4/NiFe-LDH composite photocatalyst with enhanced photocatalytic activity towards water oxidation and reduction reaction, J. Mater. Chem. A. 3 (2015) 18622–18635. https://doi.org/10.1039/c5ta05002b.

[31] T. Li, G.H. Li, L.H. Li, L. Liu, Y. Xu, H.Y. Ding, T. Zhang, Large-Scale Self-Assembly of 3D Flower-like Hierarchical Ni/Co-LDHs Microspheres for High-Performance Flexible Asymmetric Supercapacitors, ACS Appl. Mater. Interfaces. 8 (2016) 2562–2572. https://doi.org/10.1021/acsami.5b10158.

[32] H. Hu, J. Liu, Z. Xu, L. Zhang, B. Cheng, W. Ho, Hierarchical porous Ni/Co-LDH hollow dodecahedron with excellent adsorption property for Congo red and Cr(VI) ions, Appl. Surf. Sci. 478 (2019) 981–990. https://doi.org/10.1016/j.apsusc.2019.02.008.

[33] S.J. Xia, F.X. Liu, Z.M. Ni, J.L. Xue, P.P. Qian, Layered double hydroxides as efficient photocatalysts for visible-light degradation of Rhodamine B, J. Colloid Interface Sci. 405 (2013) 195–200. https://doi.org/10.1016/j.jcis.2013.05.064.

[34] Z. Peng, Y. Xin, X. Dong, Z. Quan, Facile synthesis of CoAl-LDH/MnO_2 hierarchical nanocomposites for high-performance supercapacitors, Ceram. Int. 40 (2014) 2115–2120. https://doi.org/10.1016/j.ceramint.2013.07.127.

[35] Y. Ao, D. Wang, P. Wang, C. Wang, J. Hou, J. Qian, Enhanced photocatalytic properties of the 3D flower-like Mg-Al layered double hydroxides decorated with Ag_2CO_3 under visible light illumination, Mater. Res. Bull. (2016). https://doi.org/10.1016/j.materresbull.2016.03.033.

[36] P. Wang, D.H.L. Ng, M. Zhou, J. Li, Freely standing MgAl-layered double hydroxides nanosheets and their derived metal oxides on g-C_3N_4 thin-layer designed for obtaining synergic effect of adsorption and photocatalysis, Appl. Clay Sci. 178 (2019) 105131. https://doi.org/10.1016/j.clay.2019.105131.

CHAPTER- 3

Plasmonic metal (Cu, Ag, and Au) loaded LDH composites for efficient degradation of tetracycline under LED light

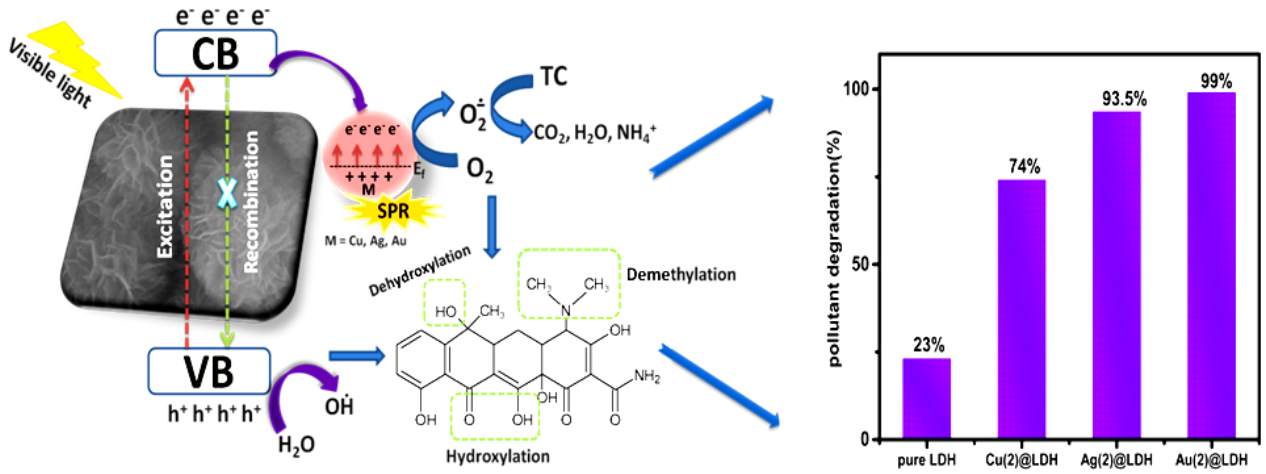

Schematic outline:

The Mg-Al LDH is a stable and durable photocatalyst with a wide band gap greater than 3 eV lying in UV region. The plasmonic metal deposition extended its optical response in the visible region, enhanced surface active sites, and decreased the rejoining of photoinduced charge carriers. Under LED lamp (λ_{max} > 360 nm), the plasmonic nanocomposites showed enhanced photocatalytic degradation of tetracycline. The nature and size of the metal played important roles in the degradation efficiency of metal-loaded composites.

3.1. Introduction:

Antibiotics have become widely used in recent years for the counteraction and treatment of irresistible illnesses in humans and animals. Tetracycline (TC) is a broad-spectrum antibiotic delivered in enormous amounts. It broadly utilizes in curing contaminations bring about by most Gram-positive and negative bacteria, chlamydia, intracellular mycoplasma, and rickettsia. Investigations have discovered that these antibiotics have stable chemical structures and antibacterial properties. Therefore, these remained unretained and transformed by humans and animals after utilization. Subsequently, these enter the environment as metabolites, putting human and animal health at risk. Therefore, the efficient removal of TC antibiotic residues from the environment has become fundamental for the ecological environment and human well-being [1-2]. The way to control the antibiotics entering the environment is to treat the wastewater containing antibiotics. As of now, photocatalysis has arisen as a green and cost-effective technique to eliminate them from water bodies. Besides, it can transform antibiotics into less harmful organic molecules and effectively biodegradable compounds, thus reducing or eliminating their antibacterial activity [3-4]. Therefore, the fabrication of a stable and proficient photocatalyst has become a central issue for the degradation of tetracycline.

Layered double hydroxides, typical two-dimensional layered structured inorganic materials, stand out in the field of photocatalysis. Many researchers have proved that these exhibit better performance than many of the metal oxide semiconductors credited to their appealing features like layered and mesoporous structure, large surface area, surface hydroxyl groups, highly dispersed MO_6 octahedrons, etc. [5-6]. The Mg-Al LDH showed advantages over other LDH photocatalysts that have been reported in the literature, in terms of structural durability, low cost, easy synthesis, and long-term sustainability. [7-8]. But due to its wide bandgap (> 3 eV), its

photocatalytic performance has not been explored well. Only a few reports for the photo degradation of harmful organic pollutants by highly stable and durable Mg-Al LDH are available. In this manner, it is essential to research such LDH in the interest of photocatalysis. However, the challenge is to adjust its wide band gap in the visible region and reduces the recombination of electron-hole pairs.

Recently, the approach of plasmonic nanoparticles such as Cu, Ag, and Au with localized surface plasmon resonance has made a unique way for the smooth procedure of photocatalysis in gentle and harmless circumstances. Compared with bare semiconductors, the plasmonic photocatalysts can extend the light absorption in the visible region due to the collective oscillations of conduction electrons at the surface of plasmonic nanoparticles. Additionally, Schottky barriers formed at the metal-semiconductor interface allow photoexcited electrons in the semiconductor's conduction band to migrate to metal nanoparticles acting as electron sinks. [9-10]. Thus, coupling semiconductors with plasmonic nanoparticles is a promising way to achieve dual advantages of improved optical response in the visible region and enhanced generation and separation of photogenerated electrons and holes. Considering this phenomenon, the photocatalytic activity of Mg-Al LDH can enhance by depositing plasmonic nanoparticles on its surface. However, the impact of different plasmonic nanoparticles modification on the photocatalytic behavior of LDH has not been investigated extensively.

This work aimed at assessing the photoactivity of LDH and different plasmonic nanocomposites. In this work, we have synthesized Mg-Al LDH through an easy and cost-effective solvothermal method. The prepared LDH was further modified by loading Cu, Ag, and Au metals with varying wt% contents (1, 2, and 3 wt%) through the photochemical reduction method. The electron trapping efficiency from the conduction band strongly depends on the type of metal because Cu,

Ag, and Au have quite different work functions. Meanwhile, the influence of different plasmonic metals with varying weight percentages on the surface, physicochemical and optical properties of LDH was discussed. It was found that the size of plasmonic nanoparticles varied according to their nature and followed the order Cu < Ag < Au that subsequently affects the photocatalytic activity. All the plasmonic composites showed better degradation of tetracycline than bare Mg-Al LDH under LED light. The possible mechanistic understanding of enhanced photoactivity and the role of different plasmonic metals were examined based on characterization results and photodegradation experiments. This study provides a better approach to designing photocatalysts having unique features of the layered structure and visible light harvesting properties of plasmonic metals.

3.2. Experimental Section:

3.2.1. Chemical and Reagents:

Magnesium nitrate hexahydrate ($Mg(NO_3)_2.6H_2O$), aluminium nitrate nonahydrate ($Al(NO_3)_2.9H_2O$), and urea (CH_4N_2O) were acquired from Loba chemicals, India. Silver nitrate ($AgNO_3$), cupric nitrate ($CuNO_3$), and tetrachloroauric (III) acid trihydrate ($HAuCl_4 \cdot 3H_2O$) were purchased from Sigma Aldrich India. Ethylene glycol, methanol, and ethanol were obtained from SD Fine Ltd. All the chemicals were used as they received without any further purification. Triple deionized water was obtained from Organo Biotech Laboratories Pvt. Ltd.

3.2.2. Synthesis of Mg-Al LDH:

The Mg-Al LDH was synthesized via an ethylene glycol mediated solvothermal method followed by hydrothermal treatment. $Mg(NO_3)_2.6H_2O$ (8 mmol), $Al(NO_3)_2.9H_2O$ (4 mmol), and urea (60 mmol) were added into a mixed dispersant of ethylene glycol (45 ml) and water (5ml) and the mixture was stirred for approximately 30 minutes at room temperature. The

homogeneous solution was then transferred to a stainless steel autoclave lined with Teflon, sealed, and heated for six hours at 160^{o}C. After cooling down naturally to room temperature, the obtained gel of Mg-Al LDH was collected and washed several times with distilled water and ethanol. The as-prepared gel was then dried at 100^{o}C to obtain a white powder.

3.2.3. Preparation of plasmonic composites:

The different plasmonic metal (Cu, Ag, and Au) loaded Mg-Al LDH composites were fabricated through the photochemical deposition method. 50 mg of the as-prepared LDH sample was added into a conical flask containing 25 ml water-methanol (4:1) solution and sonicated for about an hour to obtain dispersion. A calculated amount of metallic salt solution corresponding to a different weight percentage (1, 2, and 3 wt%) of Cu, Ag, and Au was added to the prepared dispersion. An inert atmosphere was created by purging the conical flask with argon gas for 10 to 15 minutes under continuous magnetic stirring followed by sealing with a rubber septum. Further, the solution was illuminated with UV light (Hg arc, 125 W, 300–390 nm, 10.4 mW cm^{-2}) under continuous stirring for 2 hours. The deposition of plasmonic metals was indicated by the change in the color of solution from white to colored (light sky blue, grey, and purple in the case of Cu, Ag, and Au loading, respectively) [50]. The solution was then centrifuged and washed with distilled water and ethanol followed by drying at 60^{o}C. The plasmonic metal-loaded Mg-Al LDH composites comparing to various weight percentages were named Cu(1)@LDH, Cu(2)@LDH, Cu(3)@LDH; Ag(1)@LDH, Ag(2)@LDH, Ag(3)@LDH; Au(1)@LDH, Au(2)@LDH, Au(3)@LDH. Here (1), (2), and (3) demonstrate the 1, 2, and 3 wt% of plasmonic metals, individually.

As Mg-Al LDH was photoexcited after the absorption of UV light, the electrons generated in its conduction band induced the selective deposition of plasmonic metals. The conduction band

potential of Mg-Al LDH was calculated to be -0.158 eV (discussed in section 3.4) and the photogenerated electrons in its CB were capable of performing the electrochemical reactions described in equations:.

$Cu^{2+}(aq) + 2e^- \rightarrow Cu(s), E^o = +0.34$ V vs NHE…… (3.1)

$Ag^{+}(aq) + e^- \rightarrow Ag(s), E^o = +0.799$ V vs NHE…….. (3.2)

$Au^{3+}(aq) + 3e^- \rightarrow Au(s), E^o = +1.498$ V vs NHE…….. (3.3)

3.2.4. Photocatalytic activity:

Herein, tetracycline (TC) was targeted as a model toxic pharmaceutical drug to analyze the photocatalytic properties of Mg-Al LDH and its plasmonic composites. A set of test tubes containing 10 mg of photocatalysts and 5 ml of TC solution with an initial concentration of 50 ppm was analyzed for photocatalytic degradation. All the experiments were performed at room temperature. In order to achieve equilibrium between adsorption and desorption prior to the reactions, the suspensions were kept in darkness for thirty minutes while being continuously stirred. After that, the test tubes were exposed to LED light irradiations (Wipro Garnet B22 50-watt LED bulb (wavelength >360 nm) for degradation analysis at pre-fixed intervals of time. The catalysts were removed by centrifugation and the concentration of TC in respective solutions was analyzed using a UV-visible spectrophotometer. As the pollutant volume was less, it was not possible to observe the degradation efficiency of a catalyst with only a single sample. Therefore, we prepared different test tubes for each time interval with the same amount of pollutant solution and catalyst. For each catalyst, the same procedure was performed. The decontamination percentage of TC was examined as follow:

The degradation efficiency of TC (%) = $\frac{C_o - C_t}{C_o} \times 100$……. (4)

where, C_o and C_t are the initial and residual concentrations of TC (mg/L), respectively [11].

Further, the mineralization of the pollutant during degradation was determined by measuring the total oxygen chemical demand (TOC) using the chemical method. In addition, the catalyst was separated from the reaction and dried for a recyclability test. The intermediates and end products were investigated through the LC-MS analysis.

3.3. Results and discussion:

3.3.1. Crystallographic and structural studies:

The phase structures of the samples were revealed by the XRD diffraction patterns. **Fig.3.1 (A)** represents the XRD patterns for Mg-Al LDH and its plasmonic metal (2 wt%) loaded composites. All the diffraction patterns exhibited peaks at 2θ values of 11.7°, 23.4°, 34.9°, 39.4°, 46.8°, 53.1°, 60.9°, 62.3°, 75.0°, and 80.8° indexed as (0 0 3), (0 0 6), (0 0 9), (0 1 5), (0 1 8), (1 0 10), (1 1 0), (1 1 3), (0 0 18), and (1 1 12) planes, respectively, of pure crystal phase of Mg-Al LDH [24-25]. The sharp peaks at 11.7° and 23.4° are characteristic of a layered structure. The existence of peaks at 60.9° and 62.3° indicates that the intercalated anions present in the interlayer spacing of hydrotalcite were carbonate anions [26]. The XRD patterns of Ag(2)@LDH (b), Cu(2)@LDH (c), and Au(2)@LDH (c) composites showed all the peaks of pure Mg-Al LDH suggested that the loading of plasmonic metals does not change the crystallinity of hydrotalcite materials. However, the intensity of diffraction peaks was found lower than bare Mg-Al LDH due to the deposition of plasmonic metals at LDH's surface. In the pattern of Ag(2)@LDH composite, three additional peaks at 2θ values of 38.0°, 44.3°, and 64.5° were detected correspond to (1 1 1), (2 0 0), and (2 2 0) planes, respectively, of pure silver metal with face-centered cubic symmetry [27]. For Au(2)@LDH composite, the XRD pattern showed two new peaks at 2θ values of 38.2° and 44.5° assigned to the diffraction lines of metallic gold's face-centered cubic planes (1 1 1) and (2 0 0), respectively [28, 55]. Thus, XRD patterns confirmed the presence of Ag and Au in

Ag(2)@LDH and Au(2)@LDH composites. However, no characteristic peak related to Cu NPs was observed in XRD patterns of Cu(2)@LDH composite. It could because of the very small size of Cu NPs as analyzed from HRTEM studies discussed in the next section.

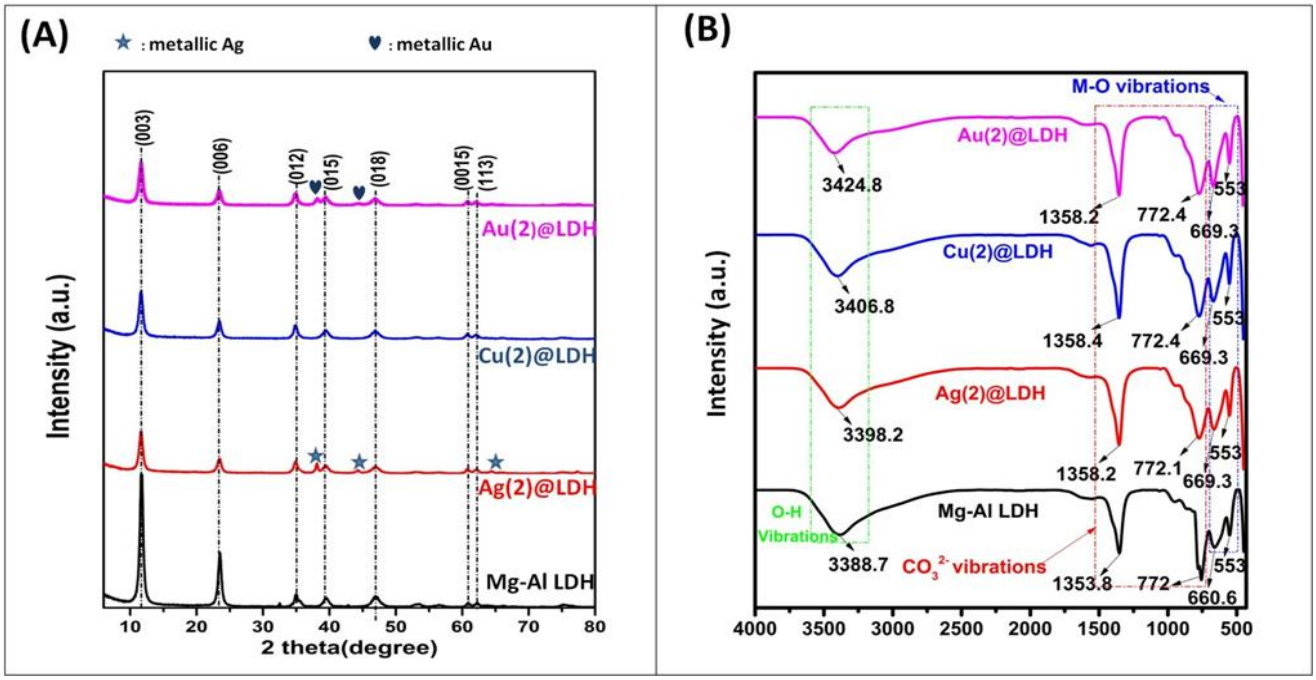

Fig.3.1. XRD diffraction patterns (A) and FTIR patterns (B) of Mg-Al LDH and Ag(2)@LDH, Cu(2)@LDH, and Au(2)@LDH composites.

Fig.3.1 (B) represents the FTIR patterns of LDH and its plasmonic composites. A broad band at 3389 cm^{-1} in spectra of all the samples was due to the vibrations of the O-H group of both the brucite like layers's hydroxides and the intercalated water molecules. Two intense peaks at 1353 cm^{-1} and 772 cm^{-1} correspond to the symmetric stretching vibrations and deformation of intercalated carbonate anions. The absorption bands in the range 500-800 cm^{-1} were due to vibrational transitions of M-O, M-O-M, and O-M-O (M= Mg^{2+}, Al^{3+}) [29-30]. However, no notable change in the FTIR pattern was noticed after the deposition of plasmonic metal NPs over LDH for Cu(2)@LDH, Ag(2)@LDH, and Au(2)@LDH composites. The observations suggested

that the samples had been properly prepared and that the structure of Mg-Al LDH was unaffected by the deposition of plasmonic metal NPs.

3.3.2. Structural/morphological and surface studies:

The morphology and elemental composition of LDH and its plasmonic composites were studied using FESEM-EDS analysis. The FESEM images of Mg-Al LDH showed flower-like microspheres with randomly grown flakes assembled like petals of flowers oriented in non-uniform directions (**Fig.3.2 (A)**). The EDS spectra of the prepared samples were examined to confirm the atomic and mass wt% of various elements present in them. The EDS spectrum of bare Mg-Al LDH showed that the sample contained Mg, Al, O, and C elements (**Fig.3.2 (B)**). In the case of Cu(2)@LDH (**Fig.3.2. (C and D**)), Ag(2)@LDH (**Fig.3.3 (A and B)**), and Au(2)@LDH composites (**Fig.3.3 (C and D)**), spherical micro flowers were observed similar to that observed in bare LDH. The EDS spectrum of Cu(2)@LDH, Ag(2)@LDH, and Au(2)@LDH also contained Cu, Ag, and Au, respectively along with Mg, Al, O, and C elements that confirmed the successful synthesis of plasmonic composites. Moreover, the content of Cu, Ag, and, Au was 1.5%, 1.71%, and 1.88%, respectively, close to the theoretical value of 2%.

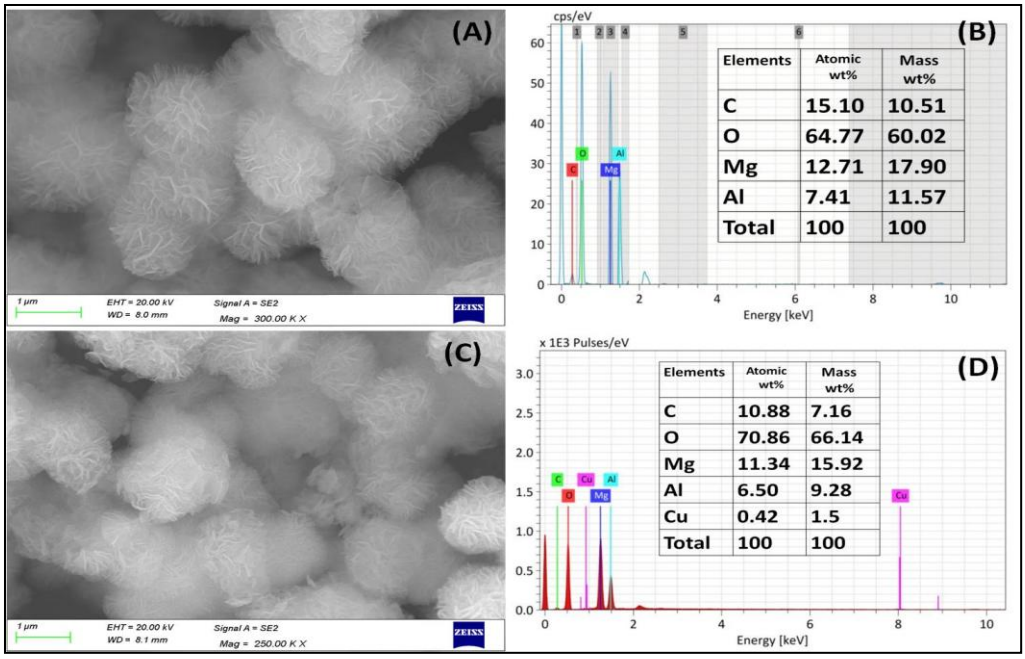

Fig.3.2. FESEM image (A), EDS pattern and elemental compositon (B) of Mg-Al LDH; FESEM image (C), EDS pattern and elemental compositon (D) of Cu(2)@LDH composite.

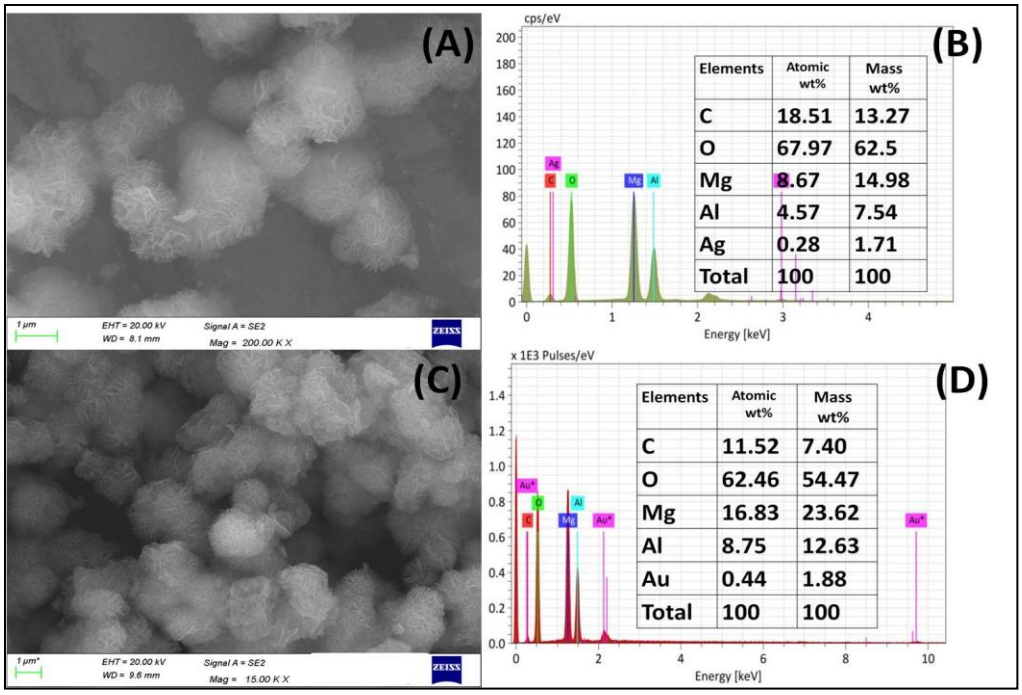

Fig.3.3. FESEM image (A), EDS pattern and elemental compositon (B) of Ag(2)@LDH composite; FESEM image (C), EDS pattern and elemental compositon (D) of Au(2)@LDH

composite.

Further, the topographical characteristics, deposition, and size of plasmonic NPs at Mg-Al LDH's surface were represented by HR-TEM analysis.. As shown in **Fig.3.4 (a)**, bare LDH consists of non-uniform and randomly oriented flakes consistent with the FESEM results. The SAED pattern represented the (1 0 10), (1 1 0), (0 0 18), and (1 1 12) planes corresponding d-spacing value of 0.172 nm, 0.152 nm, 0.126 nm, and 0.118 nm, respectively, of the pure phase of LDH (**Fig.3.4 (b)**). Moreover, the HRTEM image **(Fig.3.4 (c and d))** represents the lattice fringes with an interplanar distance of 0.172 nm and 0.15 nm ascribed to the (1 0 10) and (1 1 0) planes, respectively.

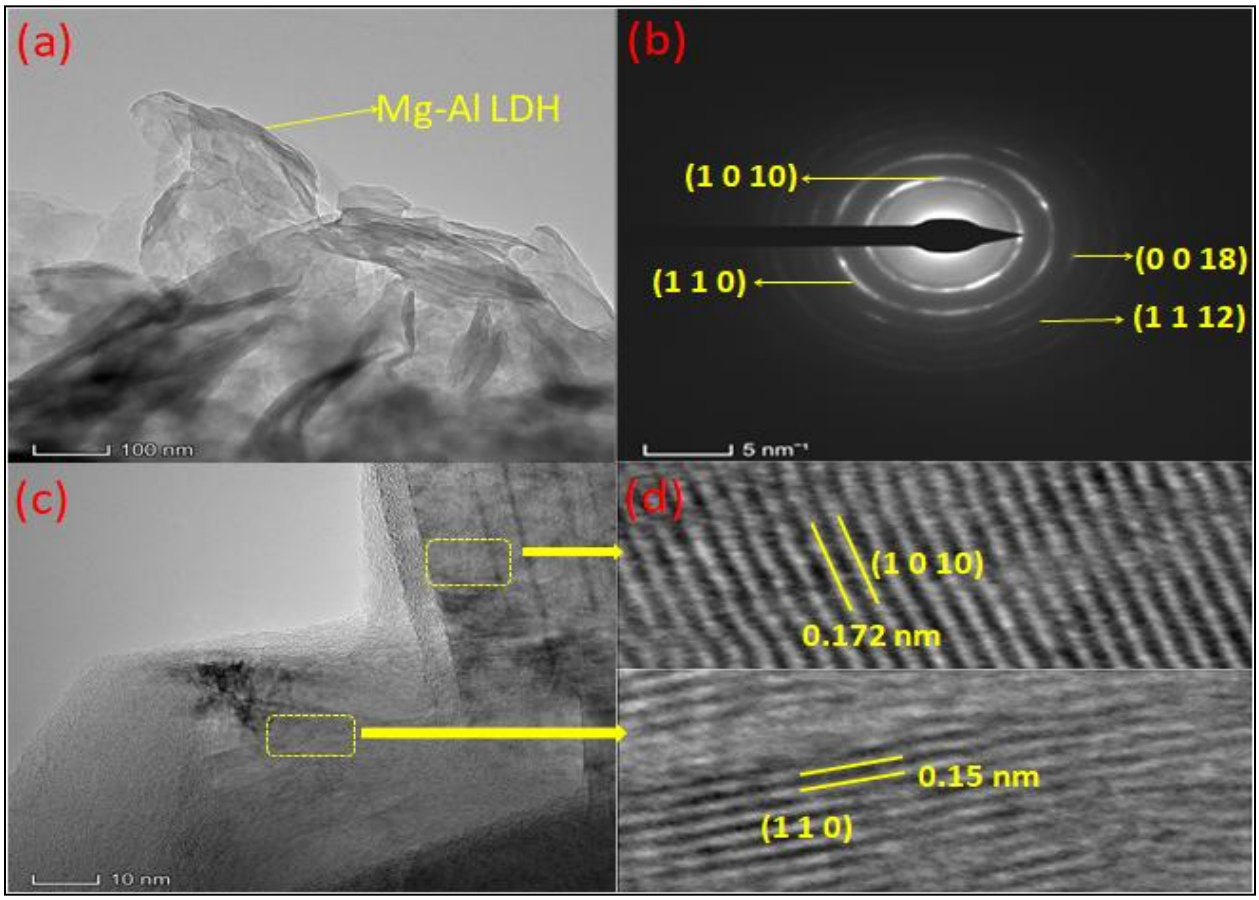

Fig.3.4. HRTEM image (a), SAED pattern (b), and lattice fringes (c and d) of Mg-Al LDH.

Fig.3.5 (a) shows the TEM image of Cu(2)@LDH composite in which we can find the small dark dots representing Cu NPs (circled by red color) over the light grey colored Mg-Al LDH surface. The results demonstrated that the Cu NPs with almost spherical morphology were deposited over the surface of LDH. The size of Cu NPs was found in the range ~2 - 7 nm. The plane (1 2 1) in the SAED pattern **(Fig.3.5 (b))** assigned to the d-spacing value of 0.21 nm of the crystal face of Cu along with the (1 0 10) and (0 0 18) planes ascribed to the d-spacing of 0.17 nm and 0.12 nm, respectively of Mg-Al LDH. Further, the HRTEM **(Fig.3.5 (c and d))** indicated the lattice fringes with 'd' value of 0.21 nm and 0.228 nm ascribed to (1 2 1) and (0 1 5) planes of Cu and Mg-Al LDH, respectively [19-20].

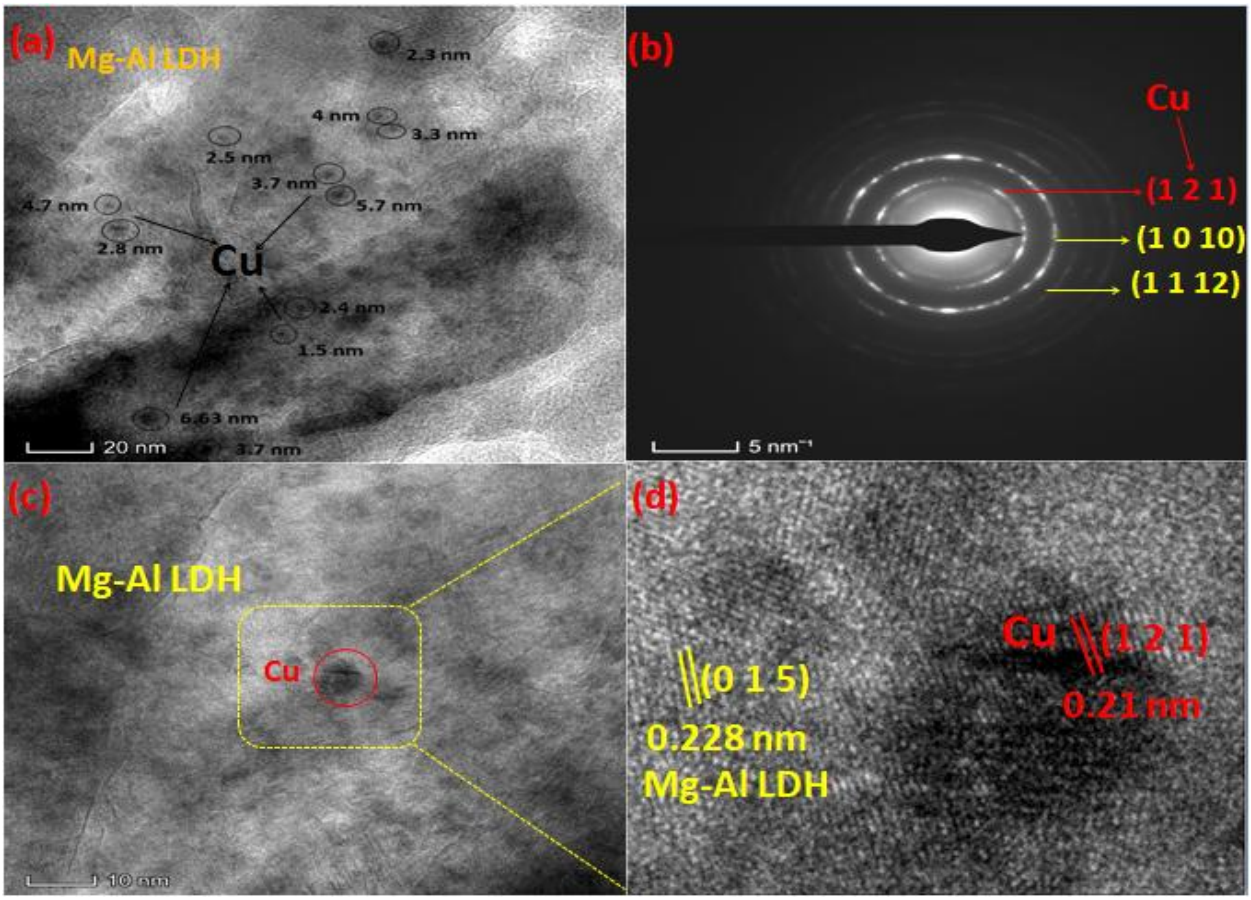

Fig.3.5. HRTEM image (a), SAED pattern (b), and lattice fringes (c-d) of Cu(2)@LDH composites.

The TEM-HRTEM analysis for Ag(2)@LDH composite is mentioned in **Fig.3.6.** The small Ag NPs (circled by dark yellow color) were deposited at Mg-Al LDH. The Ag NPs had a uniform distribution and were almost spherical in shape with varying sizes in the range of ~ 3-12 nm (**Fig.3.6 (a)**). The plane (0 0 4) in the SAED pattern (**Fig. 3.6 (b)**) ascribed to the d-spacing value of 0.248 nm of Ag NPs and the planes (1 0 10), (1 1 0), (0 0 18), and (1 1 12) planes correspond to Mg-Al LDH. **Fig.3.6 (c and d)** represented the high-resolution image of Ag deposited over the LDH surface and fringes with a lattice spacing of 0.25 nm and 0.231 nm assigned to the (0 0 4) and (1 1 0) crystal face of Ag, respectively, and lattice spacing of 0.124 nm and 0.22 nm correspond to the (0 0 18) and (0 1 5) planes of Mg-Al LDH, respectively [21-22].

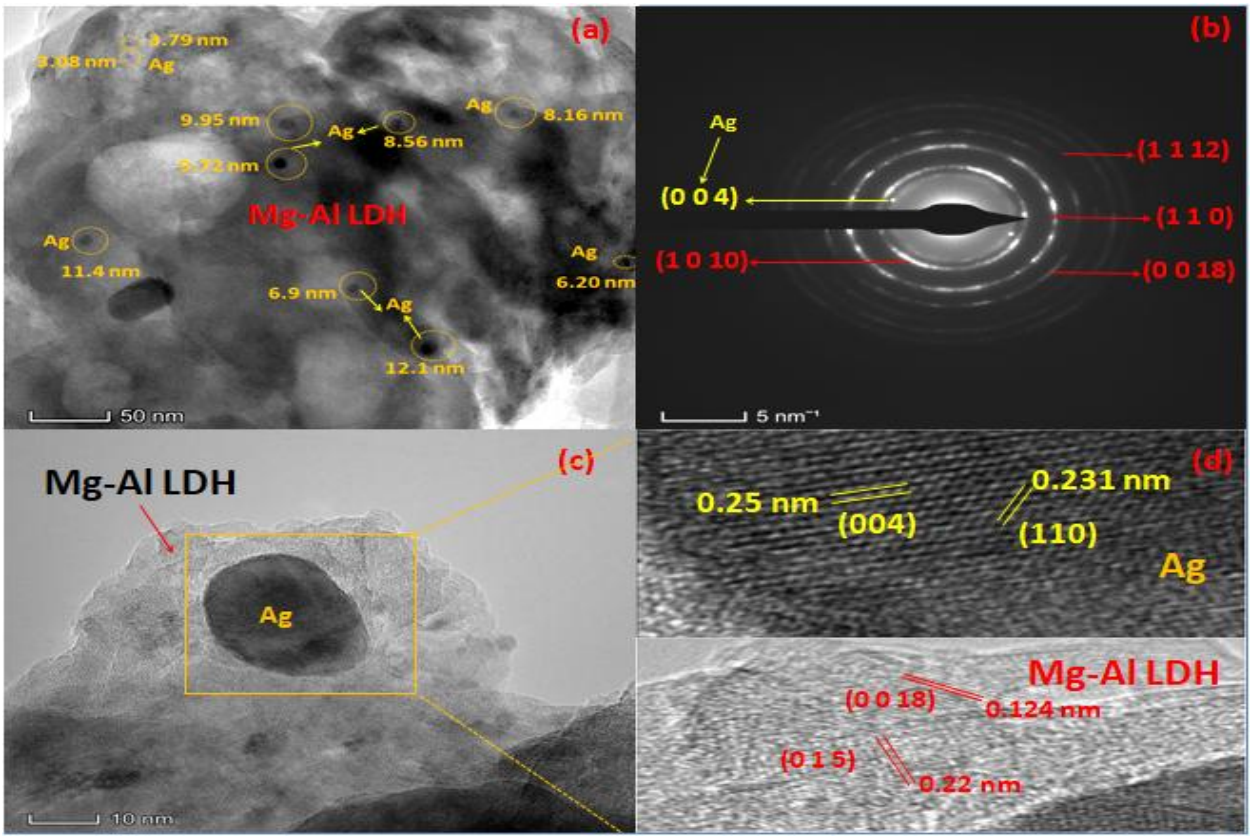

Fig.3.6. HRTEM image (a), SAED pattern (b), and lattice fringes (c-d) of Ag(2)@LDH composites.

Fig.3.7 represents the HRTEM analysis of Au(2)@LDH composite. As shown in **Fig.3.7 (a)**, the Au NPs (circled by yellow color) were found in the size range of ~ 4-25 nm larger than that of Cu and Ag NPs. The plane (1 1 1) in the SAED pattern **(Fig.3.7 (b))** assigned to the d-spacing value of 0.23 nm of Au NPs. The high-resolution image (**Fig.3.7 (c and d)**) demonstrates the lattice fringes of 0.23 nm and 0.171 nm correspond to (1 1 1) and (1 0 10) crystal face of Ag and Mg-Al LDH, respectively [23].

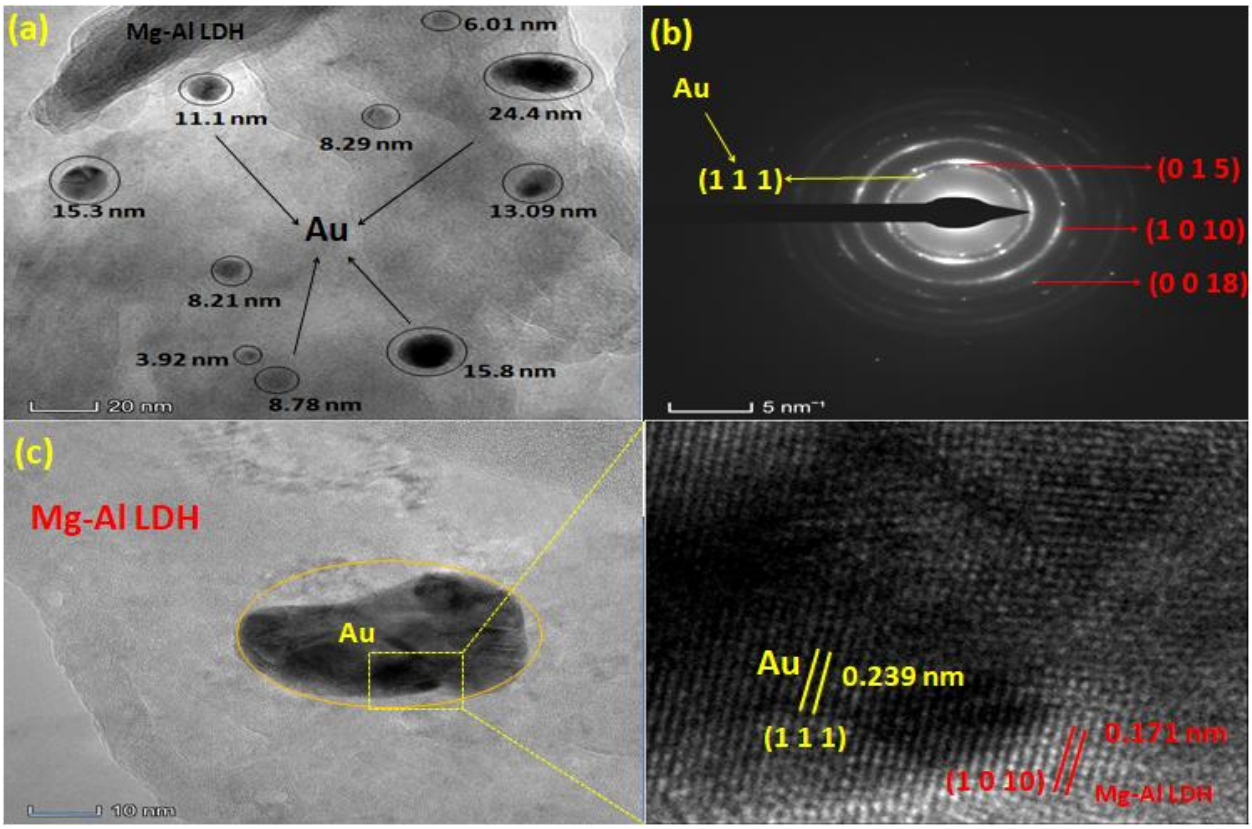

Fig.3.7. HRTEM image (a), SAED pattern (b), and lattice fringes (c-d) of Au(2)@LDH composites.

To understand the influence of metal NPs on the surface area of Cu@LDH, Ag@LDH, and Au@LDH nanocomposites, the N_2 adsorption-desorption isotherms and pore size distribution of catalysts were investigated. As shown in **Fig.3.8**, all of the catalysts exhibited a type IV isotherm

with a typical H3 hysteresis loop indicating their mesoporous nature. Also, the specific surface area slightly increased upon loading of metal NPs from 56.0 m^2/g for Mg-Al LDH to 58.9, 63.5, and 66.5 m^2/g for Cu@LDH, Ag@LDH, and Au@LDH composites, respectively. The values of the specific surface area, pore volume, and pore diameter are mentioned in **Table-3.1**. The increase in surface area and pore volume in plasmonic composites was due to metal impregnation.

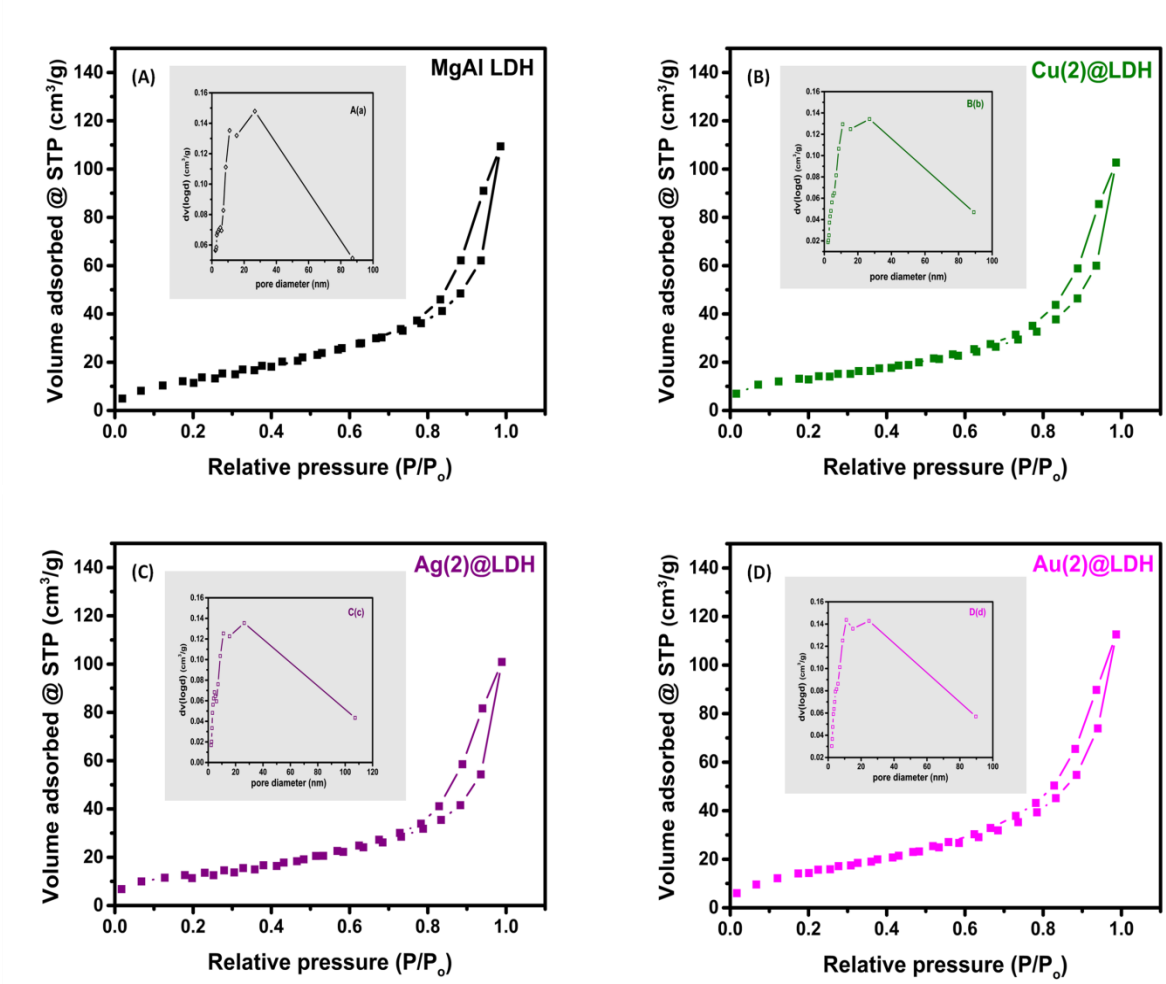

Fig.3.8. The N_2 adsorption-desorption curves and pore size distribution curves (inset) of Mg-Al LDH (A) and M(2)@LDH composites (M= Cu, Ag, Au) (B-D).

Table-3.1. BET surface area analysis of Mg-Al LDH and its metal loaded composites.

S.No.	Sample	Surface area (m^2/g)	Pore volume (cc/g)	Pore diameter (nm)
1.	Mg-Al LDH	57.0	0.159	4.490
2.	Cu(2)@LDH	58.9	0.160	4.524
3.	Ag(2)@LDH	63.6	0.176	3.143
4.	Au(2)@LDH	66.5	0.178	2.206

As shown in **Fig.3.9 (a)**, the hydrodynamic size of Mg-Al LDH was 487 nm, which increased to 533 nm, 634 nm, and 761 nm for Cu(2)@LDH, Ag(2)@LDH, and Au(2)@LDH composites, respectively. The increment in hydrodynamic size after loading metal NPs confirmed their successful deposition on Mg-Al LDH.

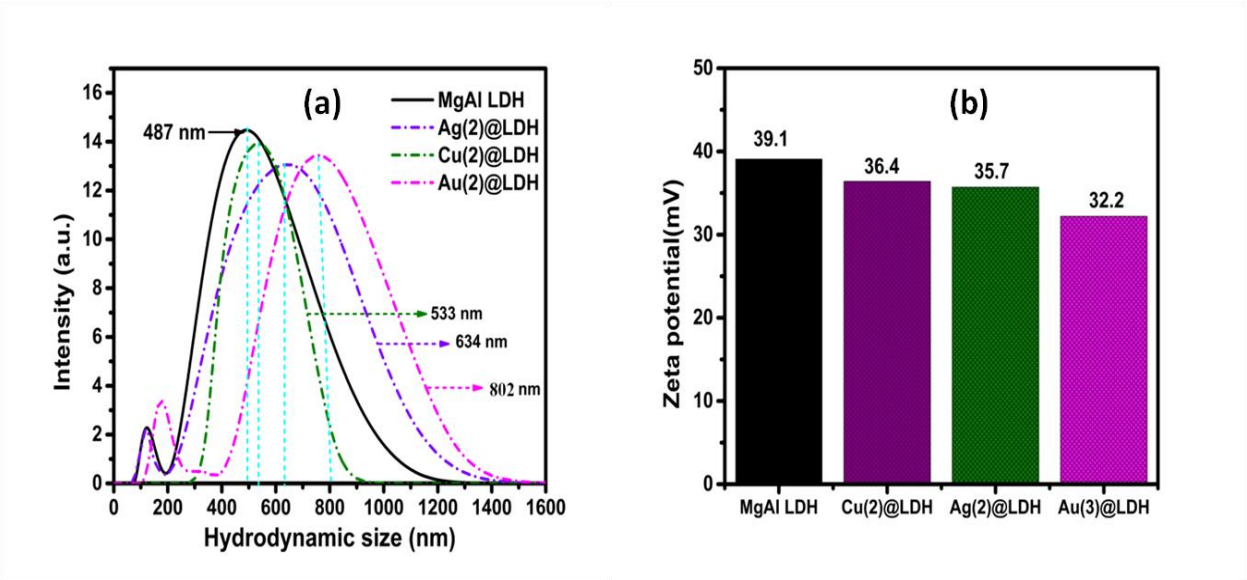

Fig.3.9. Hydrodynamic size (a) and zeta potential (b) of Mg-Al LDH and Cu(2)@LDH, Ag(2)@LDH, and Au(2)@LDH composites.

Further, the zeta potential **(Fig.3.9 (b))** of Mg-Al LDH was +39.1 mV due to its positively charged surface attributed to the partial substitution of Mg^{2+} by Al^{3+} ions. For plasmonic composites, the zeta potential value decreased to +36.4 mV, +35.7 mV, and +32.2 mV after

loading Cu, Ag, and Au NPs, respectively. Moreover, the variation in hydrodynamic size and zeta potential values in plasmonic composites was consistent with HRTEM results as the results of both the parameters were directly related to the size of metal NPs.

The elemental composition and elemental states of bare Mg-Al LDH, Cu(2)@LDH, Ag(2)@LDH, and Au(2)@LDH composite was further confirmed by X-ray photoelectron spectroscopy. The survey XPS spectrum **(Fig.3.10)** confirmed the signals of Mg, Al, C, and O elements in bare Mg-Al LDH. The binding energy peaks of Mg 2p observed at 50.1 eV proved the presence of $Mg(OH)_2$ and the peak at 73.29 eV of Al 2p revealed the presence of $Al(OH)_3$ in brucite layers of Mg-Al LDH [47]. The peak originated at 529.1 eV in the O 1s spectrum credited to the hydroxyl groups of brucite-like layers at the surface of LDH [48]. The C 1s spectrum fitted with peaks at 284.6 eV and 288.3 eV correspond to the binding energy of C-C and O-C=O bonds, respectively, confirming the presence of carbonate anions as interlayer anions [49].

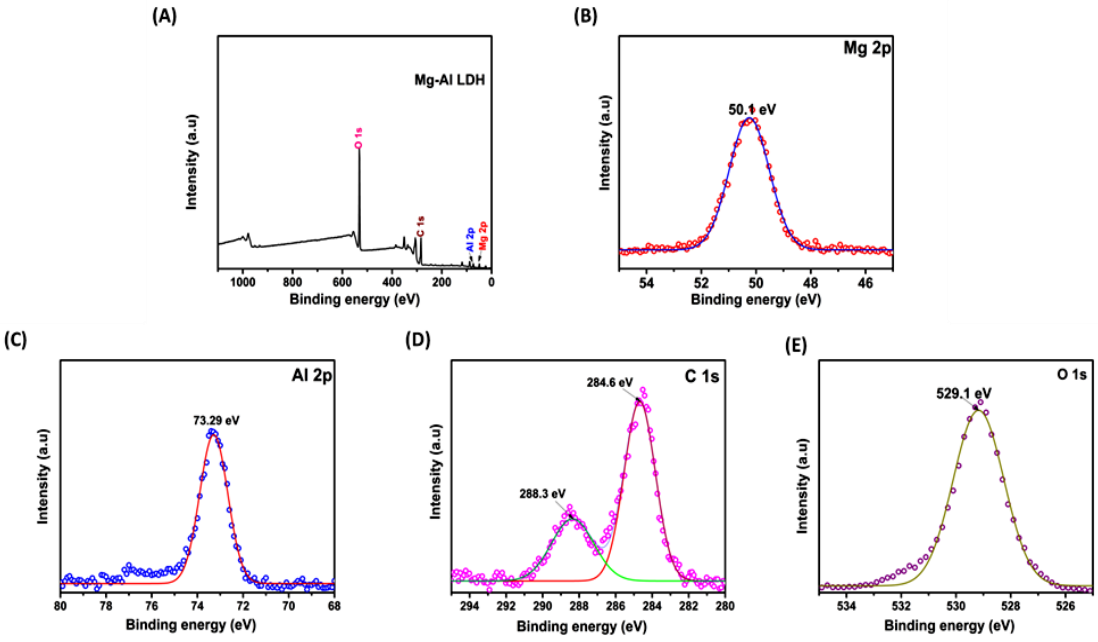

Fig.3.10. XPS spectrum of bare Mg-Al LDH; Survey (A), Mg 2p (B), Al 2p (C), C 1s (D), and O

1s (E).

The survey spectrum of Cu(2)@LDH, Ag(2)@LDH, and Au(2)@LDH composites shown in **Fig. 3.11** indicate the presence of Cu, Ag, and Au, respectively in plasmonic composites along with elements corresponding to Mg-Al LDH. In the spectrum of plasmonic composites, a significant increase in the binding energies of the peaks in O 1s and C 1s spectrum was observed. This slight rise in binding energies of Mg, Al, C, and O elements in the Cu(2)@LDH, Ag(2)@LDH, and Au(2)@LDH composites ascribed to the strong interactions between LDH and plasmonic NPs due to quick charge transfer from LDH to plasmonic NPs. In the case of Cu@LDH, the presence of Cu in the 0 (Cu^0) and +1 oxidation states (Cu_2O) is indicated by the two intense peaks at 932.3 eV and 952.2 eV, respectively. Moreover, a small peak deconvoluted at 933.8 eV highlighted the presence of Cu^{2+} species (CuO) [51]. In the spectrum of Ag 3d, the peaks observed at binding energy value of 368.2 eV and 374.0 eV correspond to Ag $3d_{5/2}$ and Ag $3d_{3/2}$, individually confirming the presence of metallic Ag in Ag(2)@LDH composite [52]. The peaks observed at 82.67 eV and 88.7 eV in the Au 4f spectrum were related to Au $4f_{5/2}$ and Au $4f_{7/2}$, respectively, in Au(2)@LDH composite [53].

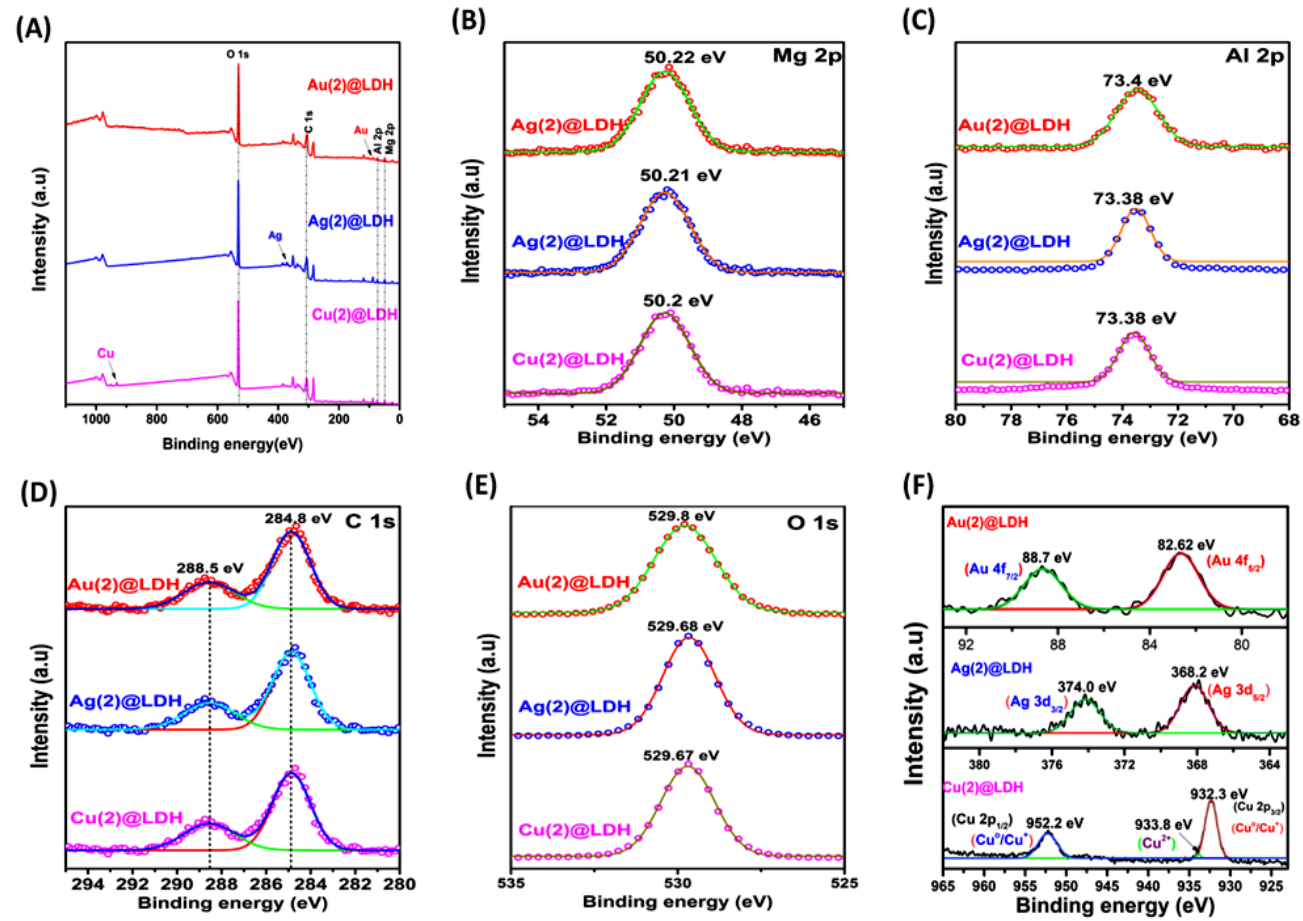

Fig.3.11. XPS spectra of Cu(2)@LDH, Ag(2)@LDH, and Au(2)@LDH composites: Survey spectra (A); Mg 2p (B); Al 2p (C); C 1s (D); O 1s (E); and Cu 2p, Ag 3d, and Au 4f (F).

3.3.3. Optical Studies:

Fig.3.12 displays the absorbance spectra of Mg-Al LDH and different weight %ge loaded Cu, Ag, and Au @LDH composites. The Mg-Al LDH exhibited an intense peak at 210 nm in the UV domain with no significant absorbance edge in the visible region. Compared with pure LDH, plasmonic composites produced a red-shifted absorption edge in the visible region and a simultaneous hyperchromic shift due to the intense surface plasmon resonance of plasmonic NPs resulting from the collective oscillations of the electrons at the surface of the NPs. A significant absorption band appeared between 400 and 800 nm in the case of Cu@LDH composites

(**Fig.3.12 (B)**), was ascribed to the presence of Cu species at LDH. The bands in the visible region: (a) at 400-500 nm corresponds to Cu^{1+} in the CuO matrix caused by partial reduction of Cu^{2+}, (b) at 580 nm due to LSPR of Cu^{0}, and (c) at 600-800 nm and 740-800 nm due to $2E_g$ to $2T_{2g}$ interband transitions of Cu^{2+} clusters in a distorted or octahedral geometry, respectively [12-13]. However, despite the significant increase in absorbance, the SPR bands produced by Cu were not particularly intense. This may be attributable to the extremely small size of Cu NPs, as confirmed by HRTEM analysis.

In the case of Ag@LDH composites (**Fig.3.12 (C)**), a significant improvement in the absorption of light related to the SPR effect of Ag was observed. The Ag NPs showed surface plasmon resonances at 400-500 nm due to transfer of electrons between the d-electronic states of Ag metal and LDH, and the absorbance spectra became broad enough to reach up to 800 nm [14,15, 56]. **Fig.3.12 (D)** displays the UV-visible absorbance spectra of Au@LDH composites. All Au-loaded composites show a broad band between 500-600 nm corresponding to the SPR effect of well-dispersed Au NPs due to the intra-band excitation of electrons in the outer orbital (6sp) of the Au species. The SPR effect of NPs strongly depends on the shape and size of the particles corresponding to variation in SPR bands. The spectra of Au@LDH composites with different weight percentage loading of Au particles are quite different as SPR bands of Au appear at a different wavelength between 500-600 nm. It might be due to the mixed dispersion of spherical and elliptical-shaped Au NPs of varying sizes confirmed by HRTEM analysis. Due to different shape and size of Au NPs, the broad SPR bands between 500-600 nm were observed instead of sharp intense bands ascribed to a particular shape and size. A significant increment in the visible light absorption was noticed with an increase in the wt% loadings of Au. The existence of SPR bands in plasmonic composites confirmed the presence of metal NPs onto Mg-Al LDH [16-17].

Moreover, the intensities of plasmon bands were continuously enhanced with increase in the weight percentage of plasmonic metals from 1 to 3 wt%. Higher intensities with broader bands correspond to more deposition of NPs and greater optical response of as prepared composites.

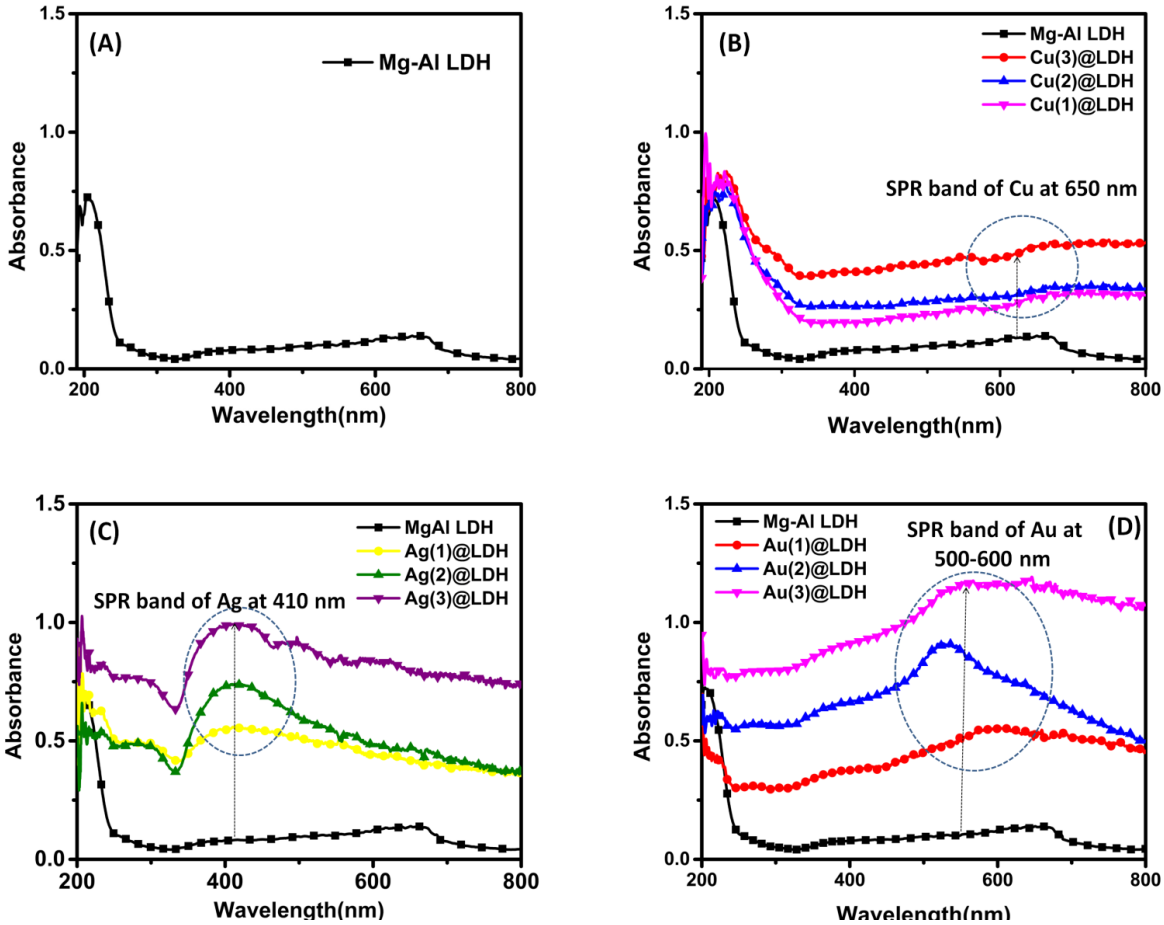

Fig.3.12. Diffuse reflectance spectra of MgAl LDH (A), Cu@LDH composites (B), Ag@LDH composites (C), and Au@MgAl LDH composites (D).

However, the plasmonic effect of NPs strongly depends on the size of the NPs. In the absorbance spectra of M@LDH composites, broad SPR bands were observed because the plasmonic NPs were not monodispersed, but different-sized particles were found at LDH as observed from HRTEM analysis. The different-sized particles could improve the photocatalytic performance as polydispersity in size and shape widens the light absorbance range in visible region. The photons

harvested by plasmons of different-sized NPs reduced the rejoining of electron-hole pairs and effectively enhanced the catalytic activity under visible light [54].

The bandgap energies of all prepared photocatalysts were calculated using Tauc's expression written as:

$$\alpha h\nu = A(h\nu - E_g)^n \ldots\ldots\ldots\ldots (3.5)$$

where, α is the absorption coefficient, hν is the energy of the photon, A is a constant, E_g is the bandgap energy of a photocatalyst, and n is the exponent coefficient depending upon the direct or indirect bandgap transitions (n = ½ and 2 for direct and indirect transitions, respectively) [18]. The bandgap values were found by extrapolating a straight line to the x-axis in the graph of $(\alpha h\nu)^{0.5}$ *vs* hν (as shown in **Fig.3.13** and **Fig.3.14**.).

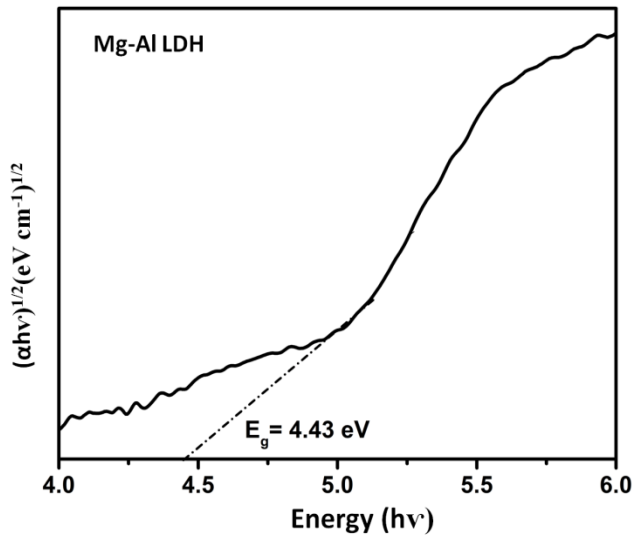

Fig.3.13. The Tauc's plot of bare Mg-Al LDH.

The bandgap value of the Mg-Al LDH was calculated as 4.43 eV. But in its plasmonic composites, it decreased gradually (< 3.1 eV) with the loading of Cu, Ag, and Au and their increased contents. Among all composites, the lowest band gap value was 2.43 eV for Au@ Mg-

Al LDH composites containing 2 wt% of Au.

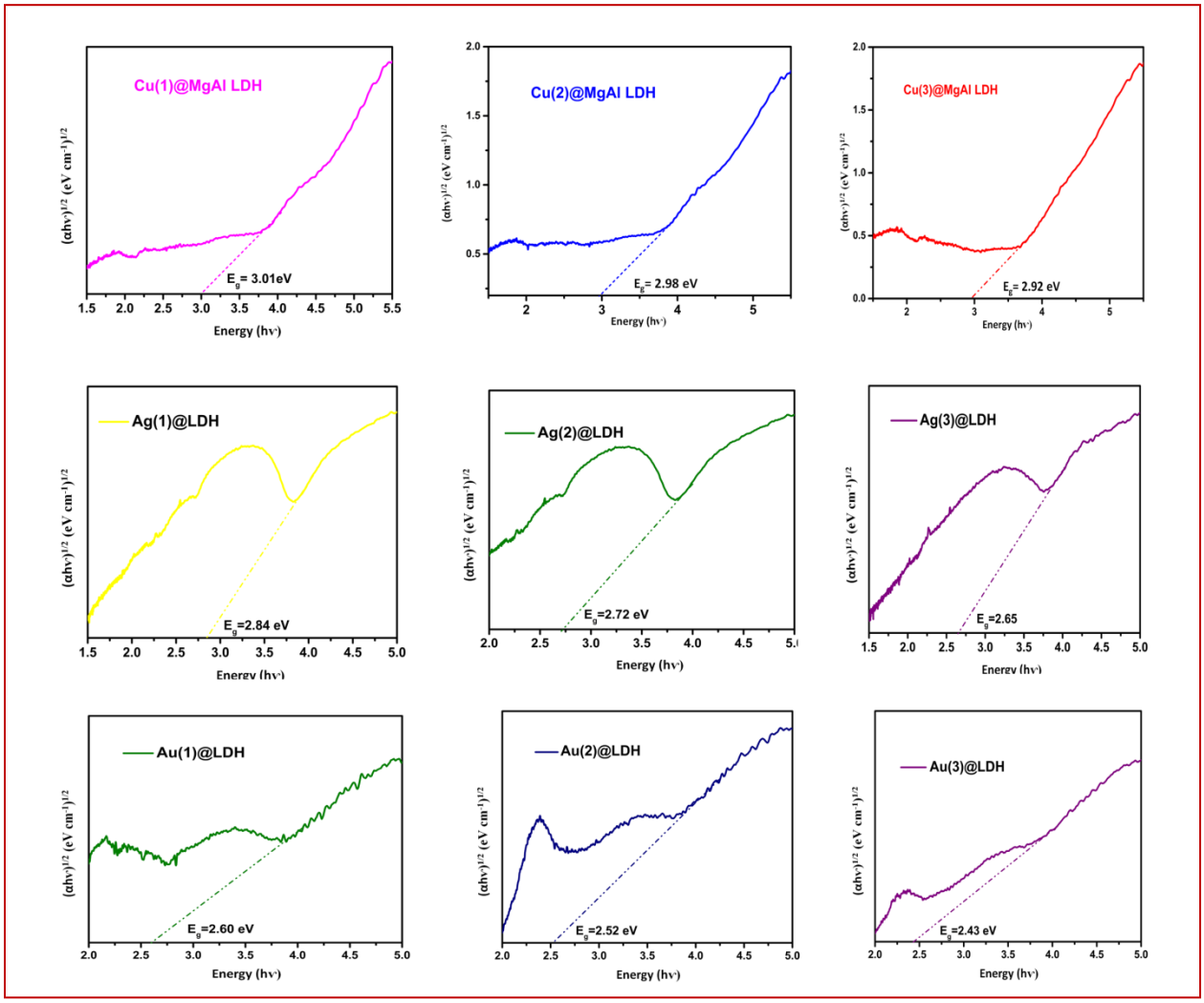

Fig.3.14. The Tauc's plots of plasmonic metal composites.

To explore the electron-hole separation efficiency of catalysts, photoluminescence studies were investigated through excitation of prepared catalysts at wavelength of 340 nm. The intensity of the PL signal determines the recombination rate of electron and holes; lower the intensity, higher the separation of charge carriers. As shown in **Fig.3.15**, the Mg-Al LDH showed emission peaks at 386 nm and 420 nm. When compared to bare Mg-Al LDH, the PL signal intensity of all plasmonic LDH composites was lesser. The lower intensity of the PL signal corresponds to

better electrical conductivity and induced SPR effect of plasmonic NPs. For all the plasmonic composites, M(3)@LDH composites showed a signal with a higher intensity as compared to M(1-2)@LDH composites (M= Cu, Ag, and Au) might be due to an excess amount of metal loading. Further, the quenching of signal followed the order Au@LDH > Ag@LDH > Cu@LDH corresponded to their reduction potential: Au (+1.49 eV) > Ag (+0.79 eV) > Cu (+0.34) favouring electron trapping efficiency [31].

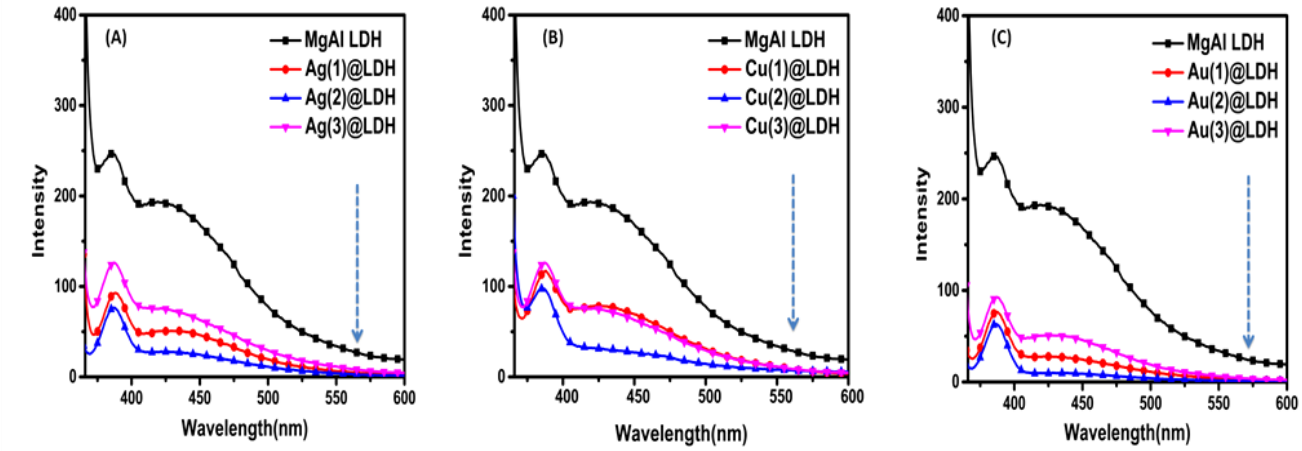

Fig.3.15. The comparative photoluminescence spectra of Mg-Al LDH and plasmonic composites.

3.3.4. Photodegradation studies:

The pharmaceutical drug, tetracycline hydrochloride (TC) was chosen as a model pollutant to demonstrate the photoactivity of prepared catalysts. First, the 5 ml of TC solution containing 10 mg of catalyst was kept in dark for half an hour under continuous stirring to achieve an equilibrium between adsorption and desorption, and afterward, the LED lamp was turned on to simulate photodegradation. **Fig.3.16** shows the adsorption and photodegradation curves of TC over different catalysts. The adsorption efficiencies of all the catalysts were witnessed in the following manner: Au@LDHs > Ag@LDHs > Cu@LDHs > bare Mg-Al LDH. This could be

explained based on their specific surface area (Au@LDH > Ag@LDH > Cu@LDH > bare LDH).

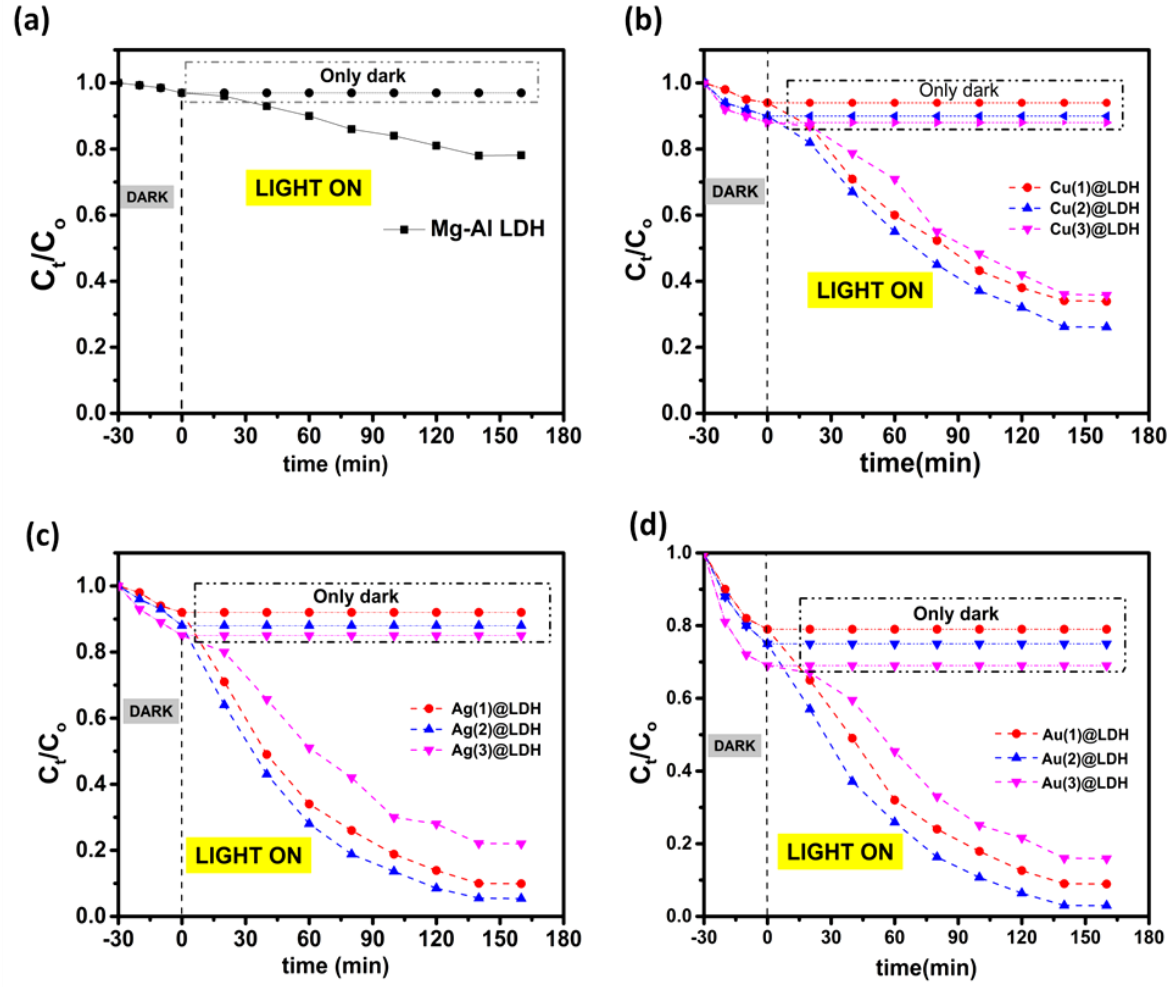

Fig.3.16. Adsorption (in dark) and photodegradation (in light) curves of tetracycline over Mg-Al LDH (A), Cu@LDH composites (B), Ag@LDH composites (C), and Au@LDH composites (D).

In the degradation process, Mg-Al LDH having a wide bandgap (Eg = 4.43 eV) showed very little photoactivity under LED irradiation. However, the loading of plasmonic metals (Cu, Ag, and Au) decreased the band gap values (< 3.1 eV) providing hyperchromic and bathochromic shifts to absorbance spectra in the visible region as discussed in optical properties. Therefore, the M@LDH composites (M = Cu, Ag, and Au) showed a remarkable degradation of tetracycline

within 140 minutes under LED light (**Fig.3.17**).

The bare Mg-Al LDH showed only 23% degradation efficiency, whereas composites exhibited higher photoactivity (63.6% to 99%). For Cu@LDH composites, the concentration of TC gradually decreased under LED light. After 140 min, about 66%, 74%, and 63.6% of TC were decomposed for the Cu(1)@LDH, Cu(2)@LDH, and Cu(3)@LDH, respectively. For Ag@LDH composites, the degraded percentage of TC was 89%, 93.5%, and 77.8% for Ag(1)@LDH, Ag(2)@LDH, and Ag(3)@LDH, respectively. For Au@LDH composites, about 92%, 99%, and 84% of TC was degraded for Au(1)@LDH, Au(2)@LDH, and Au(3)@LDH, respectively.

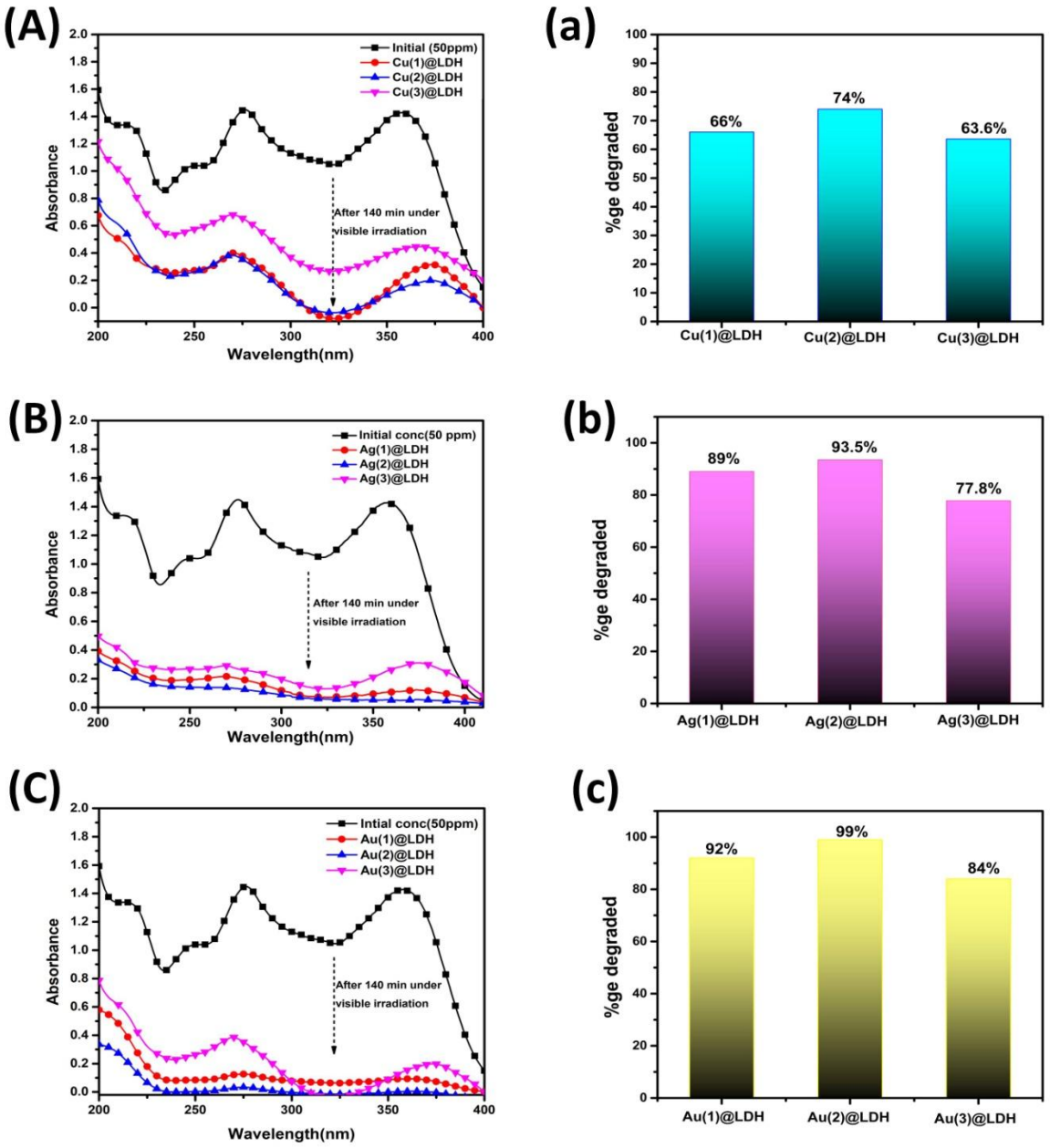

Fig.3.17. The absorbance spectra of tetracycline at initial concentration (50 ppm) and after degradation (a, c, and d); and their corresponding bar graphs showing percentage of tetracycline degradation.

The deposition of plasmonic metals had a positive effect on photocatalytic activity. It might be due to (i) the SPR effect of plasmonic metal NPs activated by the photons compared to their

plasmonic absorption band and (ii) the enhanced separation of electron-hole pairs due to the Schottky barrier created between metal NPs acting as electron sink and LDH surface [32, 33]. Among different plasmonic metal-loaded composites, the highest photoactivity was shown by Au@LDH composites. It credits to (i) the smaller bandgap value of Au@LDH than Cu and Ag@LDH prompting better visible light absorption, (ii) the larger size of Au NPs favoring more LSPR effect, and (iii) higher electronegativity and electron affinity of Au than Ag and Cu corresponding improved electron trapping efficiency [34, 35, 36]. Additionally, among all the M@LDH composites, the highest photoactivity was accomplished for M(2)@LDH composites which further decreased for M(3)@LDH composites. The optimum wt% of metal NPs increased the active sites and enhanced the charge migration but increased content could lead to the agglomeration of metal NPs and decrease the photo-efficiency. Herein, the optimum wt% of metal NPs came out as 2 wt% as the activity decreased with further loading content (3 wt%).

The following pseudo first order equation described the rate of heterogenous photocatalytic process:

$$\ln\left(\frac{C_0}{C_t}\right) = kt \quad \text{..... (3.6)}$$

where C_o is the initial concentration pollutant before irradiation, C is the concentration of pollutant as a function of irradiation time t, and k is the rate constant (min^{-1}) [37]. The linear curves shown in **Fig.3.18** indicated that first order reaction kinetics was applicable for all the prepared catalysts. All the plasmonic composites exhibited an enhanced degradation rate of TC than bare LDH due to an increment in visible light absorption accredited to the SPR effect of plasmonic NPs and inhibited rejoining of charge carriers credited to electron trapping efficiency of plasmonic NPs. The kinetic rate constant for Au(2)@LDH composite was 0.021 min^{-1}, which was almost 35 times higher than that of bare LDH, and was the highest among all the M@LDH

composites.

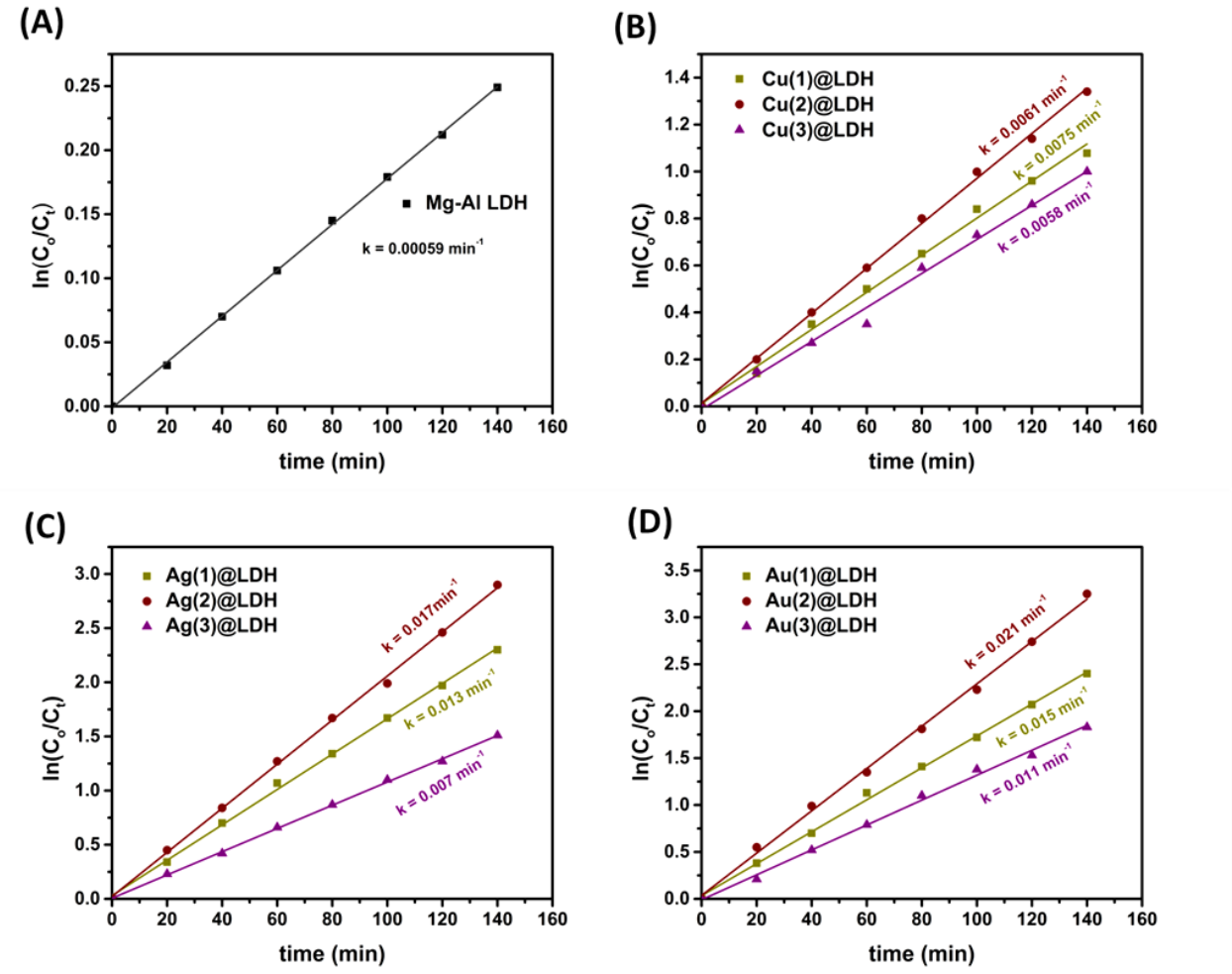

Fig.3.18. The observed reaction kinetics of degradation of tetracycline using Mg-Al LDH (A), Cu@LDH composites (B), Ag@LDH composites (C), and Au@LDH composites (D) at different intervals of time.

Moreover, among all the plasmonic nanocomposites, the degradation rate of tetracycline removal was highest with Au(2)@LDH composite. It could be due to (i) its larger surface area providing more active sites, (ii) maximum separation efficiency of photogenerated charge carriers witnessed with the highest quenching of PL signal, and (iii) better electron trapping capability due to higher reduction potential of Au (+1.49 eV) than Ag (+0.79 eV) and Cu (+0.34).

3.3.5. Scavanging experiments for investigating active species:

The role of active species like superoxide anion radicals ($O_2^{\cdot -}$), hydroxide radicals (OḢ), and holes (h^+) in the photodegradation process was investigated by the introduction of scavengers to the reaction system. $K_2Cr_2O_7$, isopropanol, and methanol were used in this experiment as scavengers for $O_2^{\cdot -}$, OḢ, and h^+, respectively. The scavenging experiments were conducted for the photodegradation of TC solution over Au(2)@LDH photocatalyst under the same experimental conditions as those used above. As shown in **Fig.3.19**, the degradation performance over Au(2)@LDH decreased most significantly with the addition of $K_2Cr_2O_7$ indicating that superoxide anion radicals were crucial to the degradation process. However, the degradation activity was suppressed using methanol and iso-propanol which demonstrated that OḢ and h^+ also played important role in the degradation process.

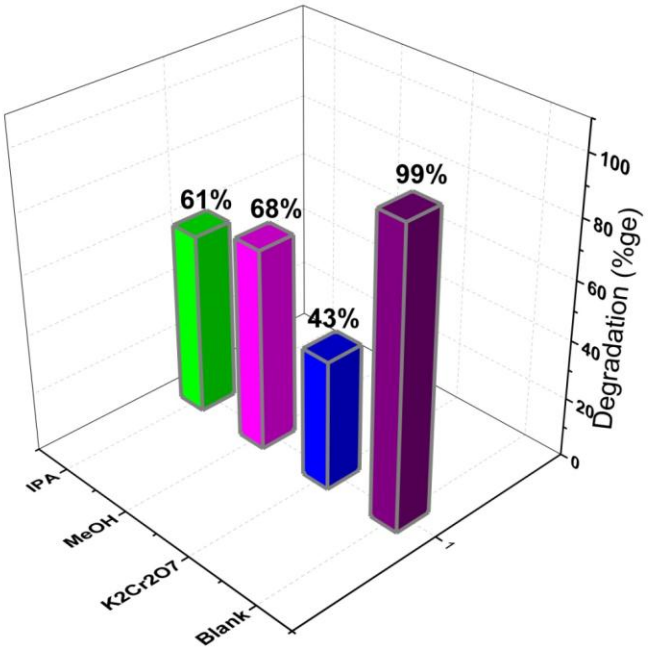

Fig.3.19. Effects of different scavangers on the degradation of tetracycline with Au(2)@LDH photocatalyst.

3.3.6. LC-MS studies:

For further investigation of photodegradation mechanism, LC-MS studies were analyzed to identify the intermediates in the degradation process of tetracycline. Based on the intermediated products found in LC-MS spectrum (**Fig.3.20 and Fig.3.21**), possible degradation pathways of tetracycline are depicted in **Fig.3.22.**

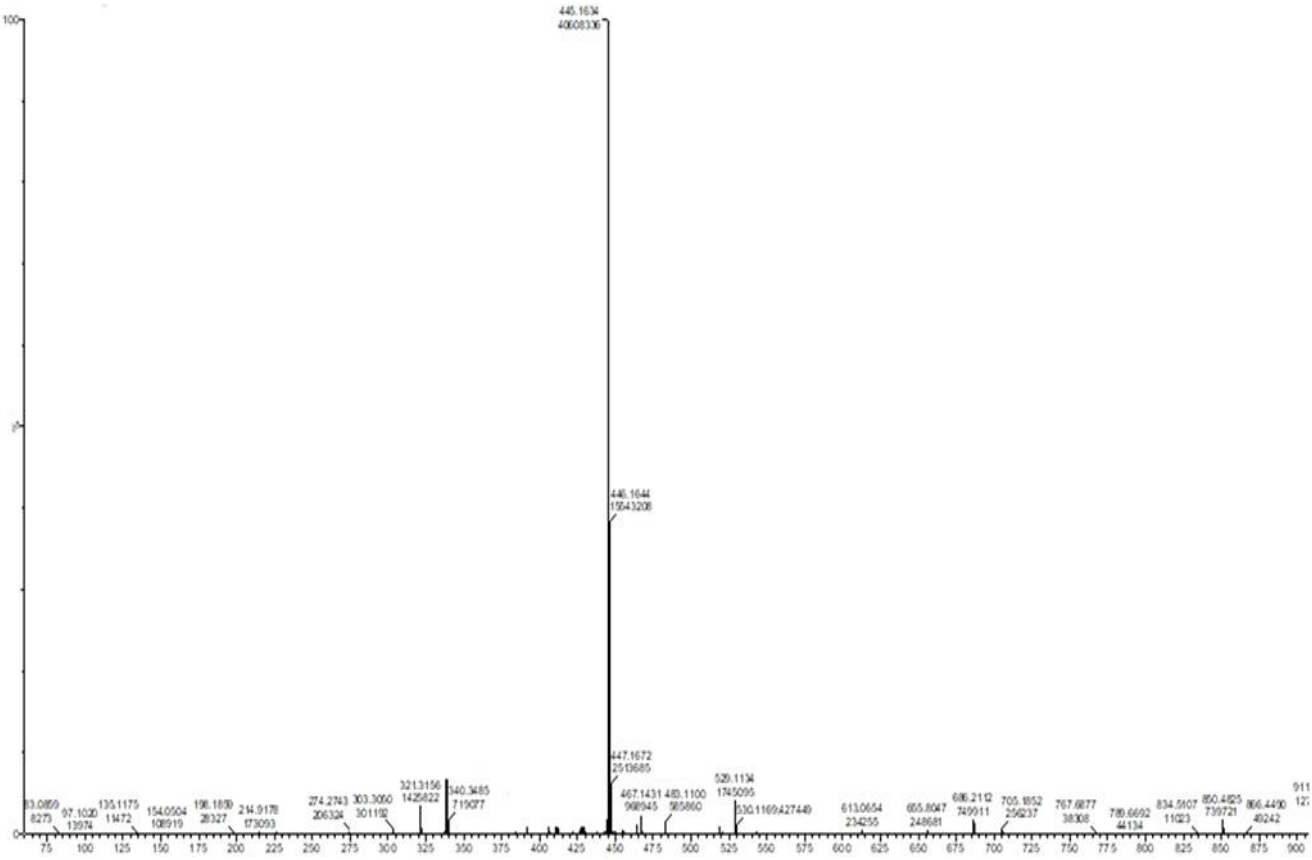

Fig.3.20. The LC-MS spectrum of tetracycline before degradation.

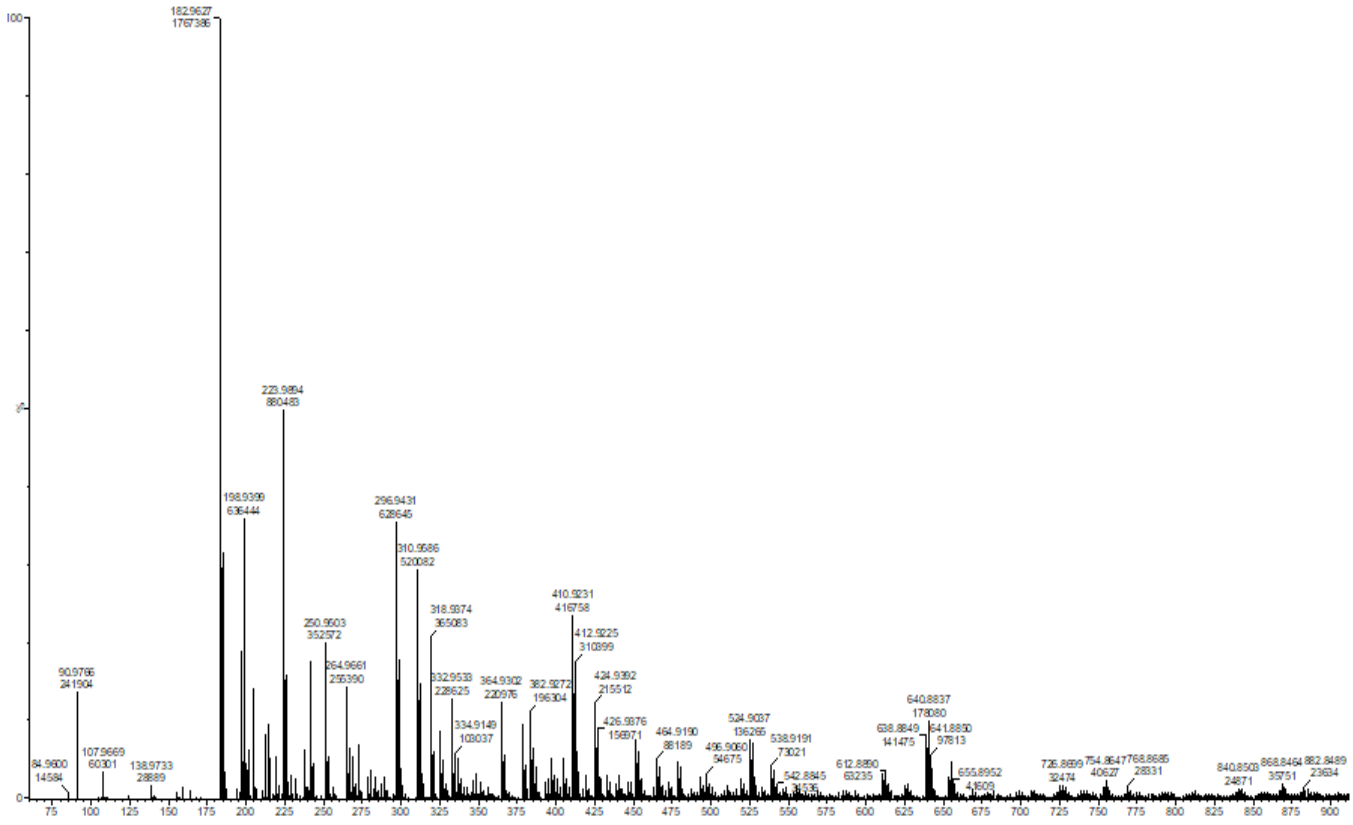

Fig.3.21. The LC-MS spectrum of tetracycline after degradation.

Various reactive species attacked tetracycline in four ways, including hydroxylation, functional group cleavage, and ring-opening reactions, to break it down. For the first degradation pathway, the TC got attacked by $O_2^{\cdot-}$ radicals and underwent deamination reaction to generate intermediate P1 (m/z = 392), which then oxidized by h^+ and produced P5 (m/z = 278). The resulting product further followed ring-opening reaction and generated P9 (m/z = 183) [41]. For the pathway two, TC underwent dehydroxylation and demethylation at C8 position to form P2 (m/z = 413) which then dehydrogenated and produced P6 (m/z = 411). Further, ring-opening and dehydroxylation reactions yielded P10 (m/z = 318) and P14 (m/z = 280) [42]. In the terms of third degradation pathway, P3 (m/z = 427) was formed by the dehydration of TC through the attack of OḢ radicals. The P3 produced P7 (m/z = 384) by the removal of N-dimethylation which eventually degraded into smaller product P11 (m/z = 224) [43]. For the fourth pathway of TC degradation,

P8 (m/z = 365), P12 (m/z = 219), P13 (m/z =139) were produced through ring opening process which then further degraded into smaller intermediate P15 (m/z =91) [46]. All by-products were then mineralized into small-molecule inorganic compounds like CO_2, H_2O, and NH^{4+}. Hence, LC-MS analysis revealed the participation of $O_2^{\cdot-}$, h^+, $O\dot{H}$ in the photodegradation of tetracycline molecules.

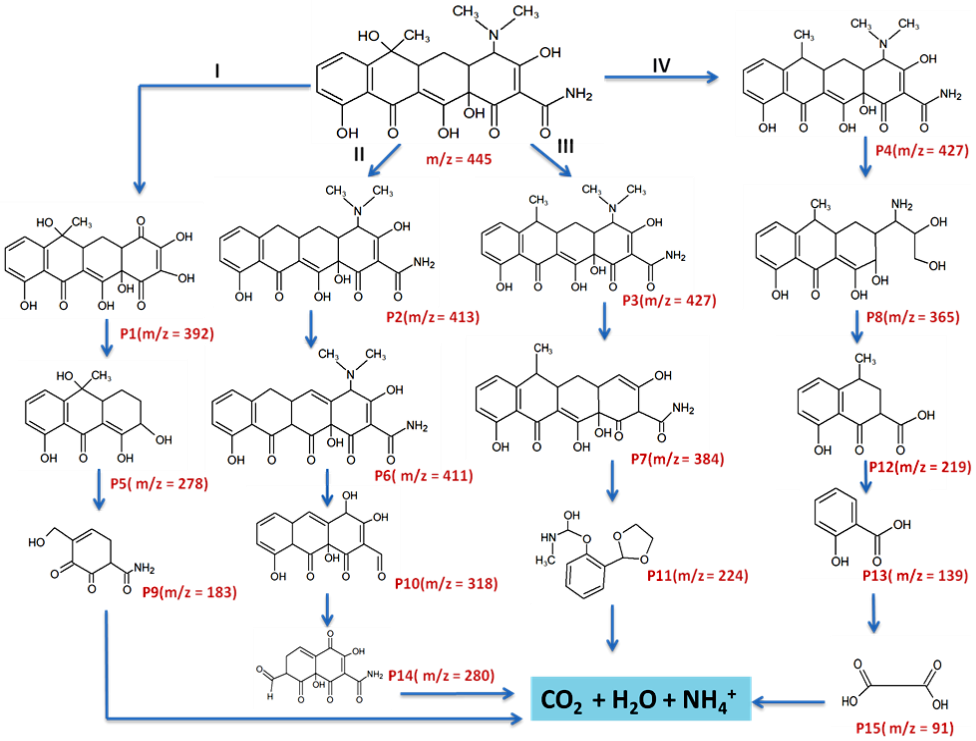

Fig.3.22. The proposed pathway of tetracycline degradation in Au(2)@LDH heterojunction photocatalytic reaction system.

3.3.7. Mineralisation (total organic carbon removal):

It is well-known that the degradation of a pollutant does not imply that it completely mineralizes into CO_2 and H_2O. Consequently, investigation of the mineralization process is crucial. The value of TOC, or total organic carbon, is related to the total amount of organic compound in the solution. A decrease in TOC value indicates how much mineralization has occurred toward the end of the photocatalytic process. The mineralization process of TC over Au(2)@LDH

photocatalyst at different time intervals was investigated in terms of TOC analysis. **Fig.3.23 (A)** shows the schematic representation of TOC analysis by chemical method and results are depicted in **Fig.3.23 (B)**.

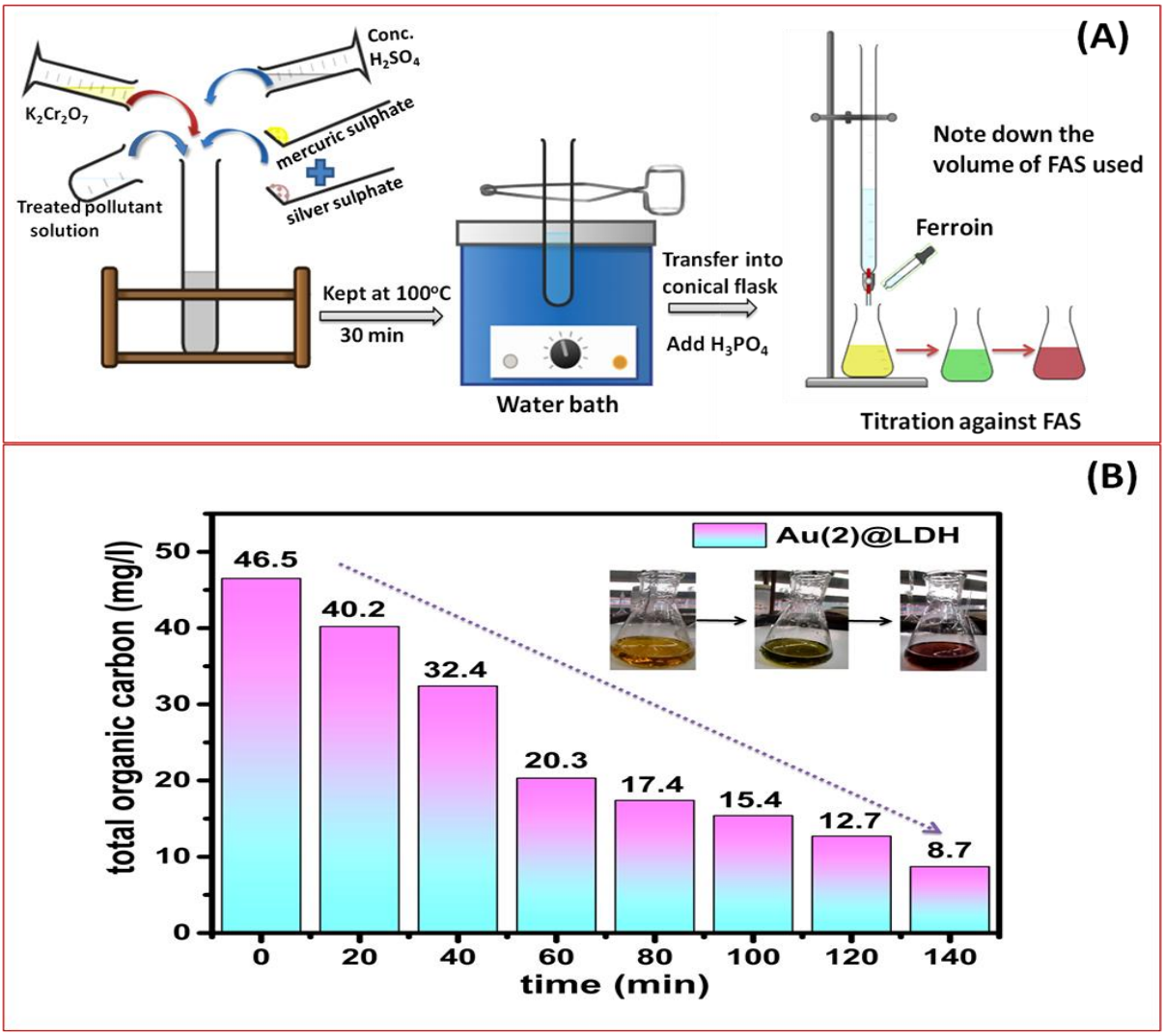

Fig.3.23. A schematic representation of TOC analysis by chemical method (A) and variation of TOC value over Au(2)@LDH composites at different intervals of time (B).

The TOC using distilled water as blank was determined using the following equation:

$$\text{TOC} = \frac{(\text{Blank}-\text{Sample})\times\text{Normality of FAS}\times 12000}{\text{Sample volume}\times 4} \quad \ldots\ldots\ldots\ldots\ldots (3.7)$$

The TOC (mg/L) removal efficiency indicated that with increase in time, there is gradual

decrease in TOC value from 46.5 mg/L to 8.7 mg/L after 140 min of reaction time. The mineralization at the end of the reaction was calculated as following [43]:

$$\text{Mineralization}(\%) = \frac{\text{TOC}_{\text{initial}} - \text{TOC}_{\text{final}}}{\text{TOC}_{\text{initial}}} \times 100 \ldots\ldots\ldots\ldots\ldots \quad (3.8)$$

The progressive mineralization of TC under light illumination was indicated by the constant decline in TOC values. At the end of the reaction, it was observed that about 84% of the organic pollutant molecules were mineralized.

3.3.8. Recyclibility and stability tests on Au(2)@LDH photocatalyst:

The recyclability and reusability of a catalyst are significant factors for evaluating its potential application. The reusability of Au(2)@LDH catalyst was explored by its photodegradation effectiveness and the results are depicted in **Fig.3.24 (A).** The reusable tests were performed for four cycles under LED irradiations with the same sample and experimental conditions. After reacting for 140 min, the powder catalyst was centrifuged from the treated solution, washed, dried, and reused in the subsequent experiment under similar conditions. The photodegradation efficiency of the catalyst declined by less than 10% in the fourth cycle compared to the initial use. The catalyst's weight loss during the separation and washing process from the degraded solution could be the cause of the decreased activity.

The XRD spectrum of the Au(2)@LDH composite was recorded before and after the photocatalytic experiment to ascertain the catalyst's stability. As shown in **Fig.3.24 (B)**, after photocatalysis, the catalyst's crystal structure remained nearly identical and was found to be stable by XRD. Thus, the above results showed that the Au(2)@LDH composite was an ideal material for the degradation of tetracycline.

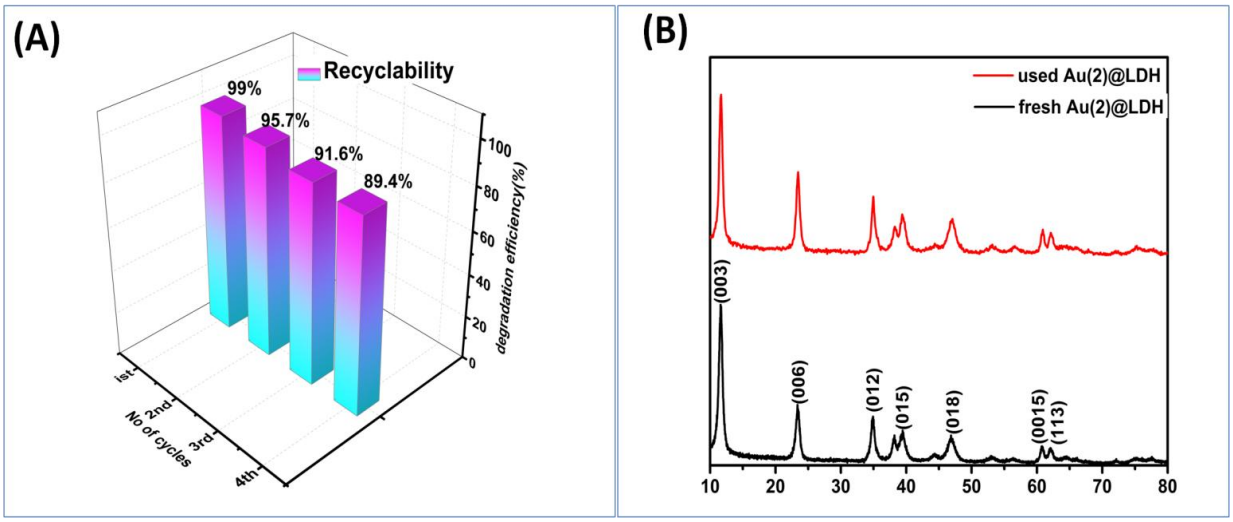

Fig.3.24. Recyclability of Au(2)@LDH photocatalyst for the degradation of tetracycline under LED light over four successive experimental runs (A) and XRD spectra of fresh and used Au(2)@LDH composite (B).

3.4. Proposed photocatalytic mechanism:

The photocatalytic mechanism of the system was proposed to explain the degradation process. A well-known Mulliken formula (written below) was applied to calculate the valence and conduction band edge potential of prepared catalyst at the point of zero charges [44]:

$$E_{VB} = \chi - E^{e} + 0.5E_{g} \quad \text{..... (3.9)}$$

$$E_{CB} = E_{VB} - E_{g} \quad \text{..... (3.10)}$$

where E_{CB} and E_{VB} were the conduction and valence band edge potential, χ was the absolute electronegativity of the photocatalyst (6.557 vs NHE for Mg-Al LDH), E_e was the potential energy of free electrons in the standard hydrogen electron (4.5 eV vs NHE), and E_g was the bandgap of photocatalyst. When the catalyst irradiates to light, the electrons excite to the conduction band, reach the surface of the catalyst through migration, and undergo reduction. The holes remaining in the valence band directly initiate the oxidation reactions. The available free radicals then break down the molecules of organic pollutants into smaller products. The CB and

VB edge positions of Mg-Al LDH were determined to be -0.158 eV and +4.272 eV, respectively. The electrons in the conduction band were able to reduce dissolved O_2 to $O_2^{\cdot-}$ radicals, as the conduction band was more negative than $Eo_2/o_2^{\cdot-}$ (-0.046 eV vs NHE). The holes in the valence band could oxidize H_2O into oxygen radicals because the E_{VB} was more positive than the $E_{OЙ/H2O}$ (+2.68 eV vs. NHE) [22]. But the photoactivity of Mg-Al LDH was limited to the UV region due to its large value of band gap (E_g = 4.43 eV) and exhibited a lower photoactivity under LED light (λ > 360 nm). The deposition of plasmonic NPs effectively enhanced the photoactivity of semiconductors in two possible ways: Schottky junction and Surface Plasmon resonance (SPR). The interfacial contact between metal NPs and semiconductors due to the flow of electrons leads to the generation of Schottky junction. The electron migration from the semiconductor to the metal NPs continued until it reached equilibrium with metal NPs generating a potential barrier. The metal NPs behave as electron sinks to capture electrons from the CB of the semiconductor and the potential barrier prevents the back flow of electrons to the semiconductor. Hence, the rejoining of electron-hole pairs successfully gets restricted. In this case, the electrons from LDH were successfully migrated to the metal via the formation of the Schottky barrier and thus, enhanced the separation of electron-hole pairs, consistent with PL results. In addition to acting as an electron sink, the metal loaded on the surface of LDH absorbed visible light. The SPR effect caused by collective oscillations of the spatially confined electrons in plasmonic metal NPs compelled the M@LDH composite to absorb more visible light, consistent with the findings of DRS. The photoinduced electrons may enter the CB of LDH, however, the Schottky barrier formed sent back the electrons to the metal itself, and these electrons directly reduced the dissolved oxygen to produce radicals. Also, the size of NPs directly affected the photocatalysis as the LSPR effect increased upon increasing the size. In this case, the photocatalytic trend

followed the order: Au@LDH > Ag@LDH > Cu@LDH which is directly related to the size of metal NPs followed the trend: Au > Ag > Cu. Thus, photogenerated charge carriers available due to the formation of Schottky junction had actively participated in redox reactions. The LSPR induced by plasmonic NPs was also highly responsible for the degradation of pollutant. Hence, the h^+, $O\dot{H}$, and $O_{2\cdot-}$ radicals caused the TC molecules to break down into mineralized products (**Scheme-3.1**).

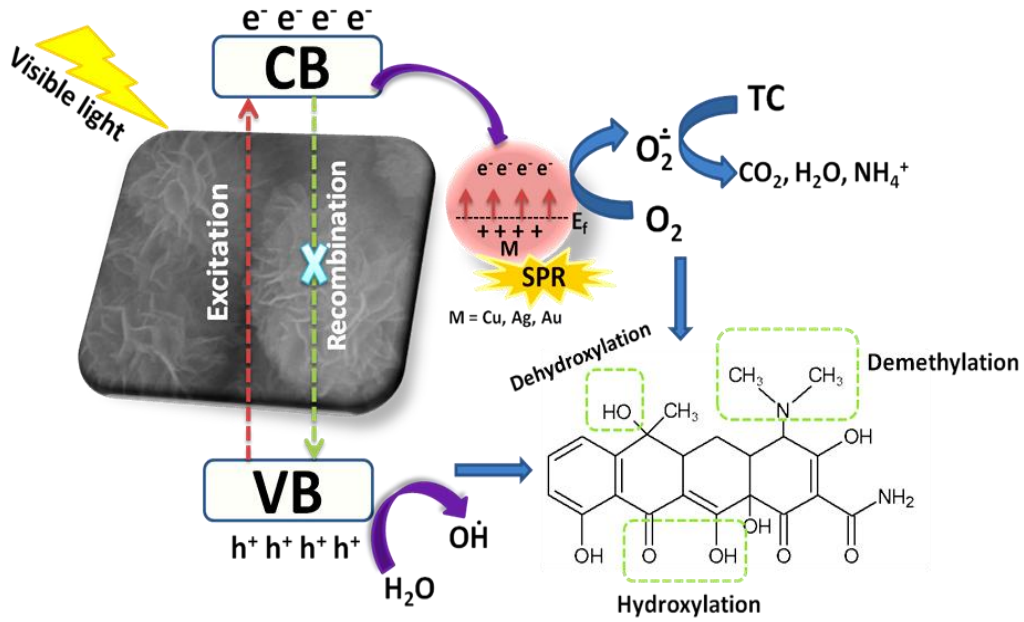

Scheme-3.1. The possible reaction mechanism of tetracycline degradation over M@LDH composite under LED irradiation.

3.5. Comparison with other photocatalysts:

Compared to other photocatalysts reported in literature, our synthesized Au(2)@LDH composite exhibited a high degradation efficiency of tetracycline, which is far better than most of the photocatalysts **(Table-3.2)**.

Table-3.2. A Comparative study of removal of tetracycline using different photocatalysts.

S.No	Photocatalyst	Tetracycline concentration (mg/L)	Light irradiations	Summary results	Reference
1.	Ni_2P/NiCo LDH	10	Visible light	46% degradation within 90 minutes	[38]
2.	Ag /g-C_3N_4	20	Visible light	77% degradation within 120 mintutes	[39]
3.	WO_3/Bi_2MoO_6	20	Visible light	85.9% degradation within 180 minutes	[40]
4.	$Bi_2O_2CO_3$/Ti_3C_2	20	Visible light	81% degradation within 120 minutes	[41]
5.	Ag_3VO_4/ZnTi LDH	50	Visible light	84.3% degradation within 100 minutes	[42]
6.	Au@Mg-Al LDH	50	LED light	99% degradation within 140 minutes	This work

3.6. Conclusion:

In this work, we had successfully improved the photocatalytic performance of wide band-gap Mg-Al LDH under LED irradiation by depositing plasmonic metal (M = Cu, Ag, and Au) and studied their comparative effect on its surface structural, physicochemical, and optical properties. The as-obtained metal-loaded composites provided a high optical response in the visible region, better charge separation, higher surface area, and superior degradation of tetracycline. The photo removal of tetracycline obeyed first-order kinetics with the highest rate constant value of 0.021 min^{-1} for Au(2)@LDH. A plausible mechanism and pathways of degradation had been proposed based on trapping experiments and LC-MS studies. By conducting TOC analysis, it was concluded that 84% of tetracycline was mineralized indicating that degradation had happened properly into smaller inorganic molecules which eventually degraded to CO_2 and H_2O. Thus, this research shed new light on the construction of highly effective photocatalysts for the promising application in wastewater decontamination.

References:

[1] S. Wu, H. Hu, Y. Lin, J. Zhang, Y.H. Hu, Visible light photocatalytic degradation of tetracycline over TiO_2, Chem. Eng. J. 382 (2020) 122842. https://doi.org/10.1016/j.cej.2019.122842.

[2] A. Zaher, M. Taha, R.K. Mahmoud, Possible adsorption mechanisms of the removal of tetracycline from water by La-doped Zn-Fe-layered double hydroxide, J. Mol. Liq. 322 (2021) 114546. https://doi.org/10.1016/j.molliq.2020.114546.

[3] P. Gholami, A. Khataee, R.D.C. Soltani, L. Dinpazhoh, A. Bhatnagar, Photocatalytic degradation of gemifloxacin antibiotic using Zn-Co-LDH@biochar nanocomposite, J. Hazard. Mater. 382 (2020) 121070. https://doi.org/10.1016/j.jhazmat.2019.121070.

[4] W.K. Jo, Y.G. Kim, S. Tonda, Hierarchical flower-like NiAl-layered double hydroxide microspheres encapsulated with black Cu-doped TiO_2 nanoparticles: Highly efficient visible-light-driven composite photocatalysts for environmental remediation, J. Hazard. Mater. 357 (2018) 19–29. https://doi.org/10.1016/j.jhazmat.2018.05.038.

[5] K. Abderrazek, F.S. Najoua, E. Srasra, Synthesis and characterization of [Zn-Al] LDH: Study of the effect of calcination on the photocatalytic activity, Appl. Clay Sci. 119 (2016) 229–235. https://doi.org/10.1016/j.clay.2015.10.014.

[6] H. Kaur, S. Singh, B. Pal, A brief review on modified layered double hydroxides for H_2 production through photoinduced H_2O splitting, Environ. Nanotechnology, Monit. Manag. 16 (2021) 100451. https://doi.org/10.1016/j.enmm.2021.100451.

[7] L. Wang, X. Gao, J. Su, Q. Zhang, K. Zheng, Z. Zhang, Synthesis of Ag/AgCl-modified TiO_2/MgAl-layered double hydroxide nanocomposite with enhanced photocatalytic

activity, J. Photochem. Photobiol. A Chem. 383 (2019) 111973. https://doi.org/10.1016/j.jphotochem.2019.111973.

[8] M. Zubair, N. Jarrah, M.S. Manzar, M. Al-Harthi, M. Daud, N.D. Mu'azu, S.A. Haladu, Adsorption of eriochrome black T from aqueous phase on MgAl-, CoAl- and NiFe-calcined layered double hydroxides: Kinetic, equilibrium and thermodynamic studies, J. Mol. Liq. 230 (2017) 344–352. https://doi.org/10.1016/j.molliq.2017.01.031.

[9] P. Subramanian, S. Szunerits, R. Boukherroub, Plasmon-induced photocatalytic transformations, INC, 2020. https://doi.org/10.1016/B978-0-12-817836-2.00009-0.

[10] M. Dinari, F. Dadkhah, Visible light photodegradation of 4-nitrophenol by new high-performance and easy recoverable Fe_3O_4/Ag_2O-LDH hybrid photocatalysts, Appl. Organomet. Chem. 35 (2021) 1–13. https://doi.org/10.1002/aoc.6355.

[11] A. Uheida, A. Mohamed, M. Belaqziz, W.S. Nasser, Photocatalytic degradation of Ibuprofen, Naproxen, and Cetirizine using PAN-MWCNT nanofibers crosslinked TiO_2-NH_2 nanoparticles under visible light irradiation, Sep. Purif. Technol. 212 (2019) 110–118. https://doi.org/10.1016/j.seppur.2018.11.030.

[12] G. Colón, M. Maicu, M.C. Hidalgo, J.A. Navío, Cu-doped TiO_2 systems with improved photocatalytic activity, Appl. Catal. B Environ. 67 (2006) 41–51. https://doi.org/10.1016/j.apcatb.2006.03.019.

[13] S.M. Park, A. Razzaq, Y.H. Park, S. Sorcar, Y. Park, C.A. Grimes, S. Il In, Hybrid Cu_xO-TiO_2 Heterostructured Composites for Photocatalytic CO_2 Reduction into Methane Using Solar Irradiation: Sunlight into Fuel, ACS Omega. 1 (2016) 868–875. https://doi.org/10.1021/acsomega.6b00164.

[14] M. Janczarek, Z. Wei, M. Endo, B. Ohtani, E. Kowalska, Silver- and copper-modified

decahedral anatase titania particles as visible light-responsive plasmonic photocatalyst, J. Photonics Energy. 7 (2016) 012008. https://doi.org/10.1117/1.jpe.7.012008.

[15] K. Saravanakumar, V. Muthuraj, Fabrication of sphere like plasmonic Ag/SnO_2 photocatalyst for the degradation of phenol, Optik (Stuttg). 131 (2017) 754–763. https://doi.org/10.1016/j.ijleo.2016.11.127.

[16] S. Thiripuranthagan, V. Rupa, Detoxification of Carcinogenic Dyes by Noble Metal (Ag, Au, Pt) Impregnated Titania Photocatalysts, Gold Nanoparticles - Reach. New Height. (2019) 1–26. https://doi.org/10.5772/intechopen.80467.

[17] S. Tonda, W.K. Jo, Plasmonic Ag nanoparticles decorated NiAl-layered double hydroxide/graphitic carbon nitride nanocomposites for efficient visible-light-driven photocatalytic removal of aqueous organic pollutants, Catal. Today. 315 (2018) 213–222. https://doi.org/10.1016/j.cattod.2017.12.019.

[18] S. Nayak, L. Mohapatra, K. Parida, Visible light-driven novel g-C_3N_4/NiFe-LDH composite photocatalyst with enhanced photocatalytic activity towards water oxidation and reduction reaction, J. Mater. Chem. A. 3 (2015) 18622–18635. https://doi.org/10.1039/c5ta05002b.

[19] X. Huang, X. Xu, R. Yang, X. Fu, Synergetic adsorption and photocatalysis performance of g-C_3N_4/Ce-doped MgAl-LDH in degradation of organic dye under LED visible light, Colloids Surfaces A Physicochem. Eng. Asp. 643 (2022) 128738. https://doi.org/10.1016/j.colsurfa.2022.128738.

[20] J. Han, H.Y. Zou, Z.X. Liu, T. Yang, M.X. Gao, C.Z. Huang, Efficient visible-light photocatalytic heterojunctions formed by coupling plasmonic $Cu_{2-x}Se$ and graphitic carbon nitride, New J. Chem. 39 (2015) 6186–6192. https://doi.org/10.1039/c5nj01010a.

[21] L. Yin, H. Zhang, J. Huang, X. Kong, H. Li, P. Bai, J. Song, Enhanced visible-light photocatalytic activity of Ag/In_2S_3 photocatalysts induced by Schottky contact and SPR of Ag, J. Mater. Sci. Mater. Electron. 31 (2020) 2089–2099. https://doi.org/10.1007/s10854-019-02730-x.

[22] T. Wang, X. Liu, C. Ma, Y. Liu, H. Dong, W. Ma, Z. Liu, M. Wei, C. Li, Y. Yan, 3D Ag/NiCo-layered double hydroxide with adsorptive and photocatalytic performance, J. Taiwan Inst. Chem. Eng. 93 (2018) 298–305. https://doi.org/10.1016/j.jtice.2018.07.031.

[23] M. Lu, W. Wang, W. Zhao, Q. Li, C. Du, J. Xu, X. Fan, H. Shi, Au-loaded porous g-C_3N_4 nanosheets for enhanced photocatalytic IPA degradation under visible-light irradiation, J. Phys. D. Appl. Phys. 52 (2019). https://doi.org/10.1088/1361-6463/aaf782.

[24] H. Kaur, S. Singh, B. Pal, Impact of g-C_3N_4 loading on NiCo LDH for adsorptive removal of anionic and cationic organic pollutants from aqueous solution, Korean J. Chem. Eng. 38 (2021) 1248–1259. https://doi.org/10.1007/s11814-021-0784-6.

[25] S. Das, K. Parida, Superior photocatalytic performance of CoAl LDH in the race of metal incorporated LDH: A comparison study, Mater. Today Proc. 35 (2021) 275–280. https://doi.org/10.1016/j.matpr.2020.05.759.

[26] E. Heraldy, K.D. Nugrahaningtyas, F.B. Sanjaya, D.S. Handayani, Influence of Variation (Ca-Mg)/Al Molar Ratios on Phase Composition of Ca-Mg-Al Hydrotalcite, Int. J. Adv. Chem. Eng. Biol. Sci. 1 (2014) 97–100. https://doi.org/10.15242/ijacebs.c1213057.

[27] T. Theivasanthi, M. Alagar, Silver Nanoparticle Synthesize, Nano Biomed. Eng. 4 (2012). http://nanobe.org/Data/View/194100.

[28] M. S. S. Mouli, A. Tamrakar, M. D. Pandey, A.K. Mishra, The nucleobase assisted pyrene functionalization of gold nanoparticles, New J. Chem 45 (2021) 9478-9482.

https://doi.org/10.1039/D1NJ00556A.

[29] K. Parida, M. Satpathy, L. Mohapatra, Incorporation of Fe^{3+} into Mg/Al layered double hydroxide framework: Effects on textural properties and photocatalytic activity for H 2 generation, J. Mater. Chem. 22 (2012) 7350–7357. https://doi.org/10.1039/c2jm15658j.

[30] B. Li, Y. Zhang, X. Zhou, Z. Liu, Q. Liu, X. Li, Different dye removal mechanisms between monodispersed and uniform hexagonal thin plate-like MgAl-CO_3^{2-}-LDH and its calcined product in efficient removal of Congo red from water, J. Alloys Compd. 673 (2016) 265–271. https://doi.org/10.1016/j.jallcom.2016.02.248.

[31] H.J. Kang, D. Il Won, Y. Lim, J. Kim, W.I. Lee, Remarkable variation of visible light photocatalytic activities of M/$Sn_{0.9}Sb_{0.1}O_2$/TiO_2 (M=Au, Ag, Pt) heterostructures depending on the loaded metals, Chemosphere. 265 (2021) 129160. https://doi.org/10.1016/j.chemosphere.2020.129160.

[32] Y. Zhu, R. Zhu, G. Zhu, M. Wang, Y. Chen, J. Zhu, Y. Xi, H. He, Plasmonic Ag coated Zn/Ti-LDH with excellent photocatalytic activity, Appl. Surf. Sci. 433 (2018) 458–467. https://doi.org/10.1016/j.apsusc.2017.09.236.

[33] K.H. Leonga, B.L. Gana, S. Ibrahima, P. Saravanan, Synthesis of surface plasmon resonance (SPR) triggered Ag/TiO_2 photocatalyst for degradation of endocrine disturbing compounds, Appl. Surf. Sci. 319 (2014) 128-135. http://dx.doi.org/10.1016/j.apsusc.2014.06.153

[34] J.E. Lee, S. Bera, Y.S. Choi, W.I. Lee, Size-dependent plasmonic effects of M and M@SiO_2 (M = Au or Ag) deposited on TiO_2 in photocatalytic oxidation reactions, Appl. Catal. B Environ. 214 (2017) 15–22. https://doi.org/10.1016/j.apcatb.2017.05.025.

[35] G. Liu, L. Wang, X. Chen, X. Zhu, B. Wang, X. Xu, Z. Chen, W. Zhu, H. Li, J. Xia,

Crafting of plasmonic Au nanoparticles coupled ultrathin BiOBr nanosheets heterostructure: Steering charge transfer for efficient CO_2 photoreduction, Green Chem. Eng. (2021). https://doi.org/10.1016/j.gce.2021.11.007.

[36] C. Zhang, Y. Zhang, W. Xie, Plasmonic metal/semiconductor hybrid nanomaterials for solar to chemical energy conversion, J. Energy Chem. 63 (2021) 40–53. https://doi.org/10.1016/j.jechem.2021.08.036.

[37] H. Tang, W. Zhang, Y. Meng, B. Xie, Z. Ni, S. Xia, Investigation onto the performance and mechanism of visible light photodegradation of methyl orange catalyzed by M/CeO_2 (M=Pt, Ag, Au), Mater. Res. Bull. 144 (2021) 111497. https://doi.org/10.1016/j.materresbull.2021.111497.

[38] Y. Sun, L. Wang, T. Wang, X. Liu, T. Xu, M. Wei, L. Yang, C. Li, Improved photocatalytic activity of Ni_2P/NiCo-LDH composites via a Co–P bond charge transfer channel to degrade tetracycline under visible light, J. Alloys Compd. 852 (2021) 156963. https://doi.org/10.1016/j.jallcom.2020.156963.

[39] Z. Ren, F. Chen, K. Wen, J. Lu, Enhanced photocatalytic activity for tetracyclines degradation with Ag modified g-C_3N_4 composite under visible light, J. Photochem. Photobiol. A Chem. 389 (2020) 112217. https://doi.org/10.1016/j.jphotochem.2019.112217.

[40] W. Han, T. Wu, Q. Wu, Fabrication of WO_3/Bi_2MoO_6 heterostructures with efficient and highly selective photocatalytic degradation of tetracycline hydrochloride, J. Colloid Interface Sci. 602 (2021) 544–552. https://doi.org/10.1016/j.jcis.2021.05.128.

[41] B. Tan, Y. Fang, Q. Chen, X. Ao, Y. Cao, Construction of $Bi_2O_2CO_3$/Ti_3C_2 heterojunctions for enhancing the visible-light photocatalytic activity of tetracycline

degradation, J. Colloid Interface Sci. 601 (2021) 581–593. https://doi.org/10.1016/j.jcis.2021.05.155.

[42] J. Xiong, H.Y. Zeng, C.R. Chen, S. Li, S. Xu, D.S. An, Ag_3VO_4 anchored ZnTi hydrotalcite microspheres with rosette-like structure for tetracycline degradation, Appl. Clay Sci. 208 (2021) 106118. https://doi.org/10.1016/j.clay.2021.106118.

[43] C. Hao, Z. Yan, K. Liu, J. Qiu, Degradation of Pharmaceutical Contaminant Tetracycline in Aqueous Solution by Coaxial-Type DBD Plasma Reactor, IEEE Trans. Plasma Sci. 48 (2020) 471–481. https://doi.org/10.1109/TPS.2020.2964612.

[44] G. Salehi, R. Abazari, A.R. Mahjoub, Visible-Light-Induced Graphitic-C_3N_4@Nickel-Aluminum Layered Double Hydroxide Nanocomposites with Enhanced Photocatalytic Activity for Removal of Dyes in Water, Inorg. Chem. 57 (2018) 8681–8691. https://doi.org/10.1021/acs.inorgchem.8b01636.

[45] L.G. Devi, R. Kavitha, A review on plasmonic metal-TiO_2 composite for generation, trapping, storing and dynamic vectorial transfer of photogenerated electrons across the Schottky junction in a photocatalytic system, Appl. Surf. Sci. 360 (2016) 601–622. https://doi.org/10.1016/j.apsusc.2015.11.016.

[46] F. Meng, W. Ma, Y. Wang, Z. Zhu, Z. Chen, G. Lu, A tribo-positive Fe@MoS_2 piezocatalyst for the durable degradation of tetracycline: degradation mechanism and toxicity assessment, Environ. Sci. Nano. 7 (2020) 1704–1718. https://doi.org/10.1039/d0en00284d.

[47] X. Li, J. Xue, S. Ma, P. Xu, C. Huang, M. Wang, Synthesis of MgAl LDH/Acidified g-C_3N_4 Heterojunction Photocatalyst for Improved Tetracycline Hydrochloride Degradation Activity, Nano. 14 (2019) 1–13. https://doi.org/10.1142/S1793292019500668.

[48] C. Chen, H. Zeng, J. Xiong, S. Xu, D. An, Z-scheme AgBr@Ag/CoAl layered double hydroxide heterojunction for superior photocatalytic Cr(VI) reduction under visible light, Appl. Clay Sci. 192 (2020) 105627. https://doi.org/10.1016/j.clay.2020.105627.

[49] X. fei Tan, Y. guo Liu, Y. ling Gu, S. bo Liu, G. ming Zeng, X. Cai, X. jiang Hu, H. Wang, S. mian Liu, L. hua Jiang, Biochar pyrolyzed from MgAl-layered double hydroxides pre-coated ramie biomass (Boehmeria nivea (L.) Gaud.): Characterization and application for crystal violet removal, J. Environ. Manage. 184 (2016) 85–93. https://doi.org/10.1016/j.jenvman.2016.08.070.

[50] I.S. Grover, R.C. Prajapat, S. Singh, B. Pal, Highly photoactive Au-TiO_2 nanowires for improved photo-degradation of propiconazole fungicide under UV/sunlight irradiation, Sol. Energy. 144 (2017) 612–618. https://doi.org/10.1016/j.solener.2017.02.001.

[51] W.T. Chen, Y. Dong, P. Yadav, R.D. Aughterson, D. Sun-Waterhouse, G.I.N. Waterhouse, Effect of alcohol sacrificial agent on the performance of Cu/TiO_2 photocatalysts for UV-driven hydrogen production, Appl. Catal. A Gen. 602 (2020) 117703. https://doi.org/10.1016/j.apcata.2020.117703.

[52] F. He, S. Wang, H. Zhao, Y. Wang, J. Zhang, Q. Yan, P. Dong, Z. Tai, L. Chen, Y. Wang, C. Zhao, Construction of Schottky-type Ag-loaded fiber-like carbon nitride photocatalysts for tetracycline elimination and hydrogen evolution, Appl. Surf. Sci. 485 (2019) 70–80. https://doi.org/10.1016/j.apsusc.2019.04.164.

[53] Q. Li, W. Zhao, Z. Zhai, K. Ren, T. Wang, H. Guan, H. Shi, 2D/2D Bi_2MoO_6/g-C_3N_4 S-scheme heterojunction photocatalyst with enhanced visible-light activity by Au loading, J. Mater. Sci. Technol. 56 (2020) 216–226. https://doi.org/10.1016/j.jmst.2020.03.038.

[54] J.L. Chansa, F. Wewers, T. Mthethwa, Plasmonic photocatalysts consisting of a mixture of

Au nanospheres and Au nanorods on TiO_2 support for improved visible light induced photocatalytic degradation properties, J. Photochem. Photobiol. A Chem. 401 (2020) 112740. https://doi.org/10.1016/j.jphotochem.2020.112740.

[55] S. S. Shendage, A. S. Singh, J. M. Nagarkar, One step electrochemical synthesis of bimetallic PdAu supported on nafion–graphene ribbon film for ethanol electrooxidation, Mater. Res. Bull. 70 (2015) 539-544. https://doi.org/10.1016/j.materresbull.2015.05.025.

[56] A. Zielinska-Jurek, Z. Wei, I. Wysocka, ´ P. Szweda, E. Kowalska, The effect of nanoparticles size on photocatalytic and antimicrobial properties of Ag-Pt/TiO_2 photocatalysts, Appl. Surf. Sci. 353 (2015) 317-325. https://doi.org/10.1016/j.apsusc.2015.06.065.

CHAPTER- 4

Construction of a novel ternary Ag@g-C_3N_4-Co-Al LDH heterostructure for efficient degradation of pharmaceutical drug under LED irradiations

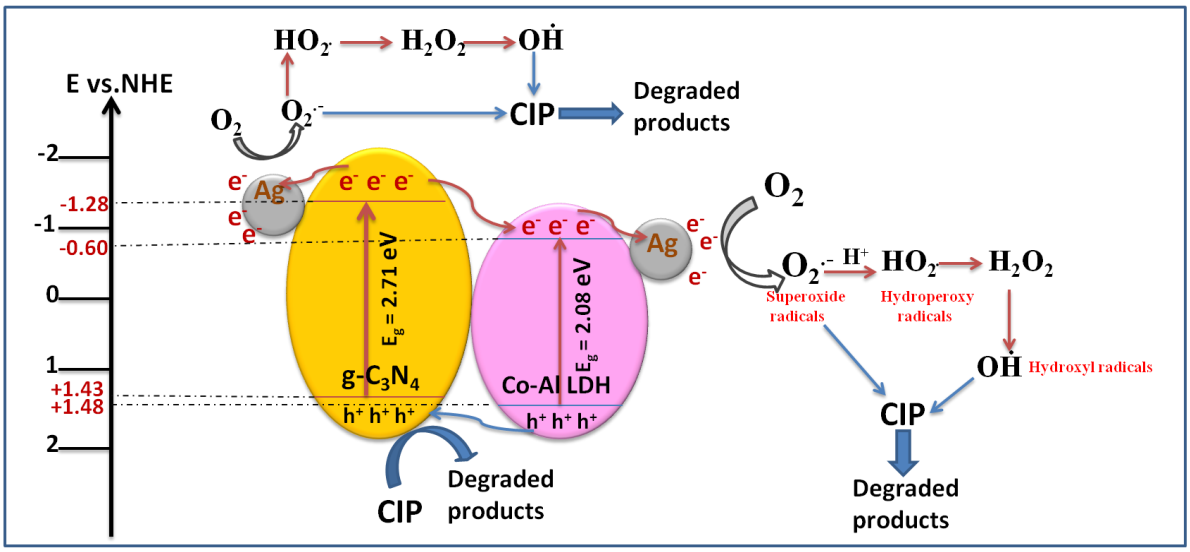

Schematic outline:

A series of highly efficient ternary Ag-deposited g-C_3N_4 coupled Co-Al LDH composites were constructed through multistep synthesis. The structural and physicochemical properties of LDH were examined in relation to the loadings of g-C_3N_4 and Ag nanoparticles. The enhanced photoactivity of Ag@CN-LDH composites was accredited to the increment in reactive sites, rapid charge transfer at the CN-LDH interface, and the SPR effect of NPs acting as electron acceptors.

4.1. Introduction:

The surplus production, immoderation use, and erroneous release of pharmaceutical wastes from their production plants into water resources have become significant issues of water contamination today. The tainting of water assets by pharmaceutical compounds, predominantly antibiotics, transformed into a major issue among environmental specialists considering the expansion in their production with population growth. Ciprofloxacin (CIP), an extensively utilized antibacterial medication is highly effective in the treatment of respiratory tract, urinary infections, and lung sicknesses. It is highly stable and difficult to decompose in the environment due to the presence of fluoride atoms in its structural composition. The introduction of ciprofloxacin into water resources due to its overuse and inadequate digestion causes dangers to human well-being and is an overall concern [1-3]. Subsequently, it is a natural need to terminate and decay such harmful compounds from the aquatic environment.

Photocatalysis using semiconductors has been regarded as a green, cost-effective, and efficient method for removing organic pollutants from water bodies among the various natural remediation methods. One of the prominent challenges to realizing such a strategy in its practical use is the development of an eco-friendly, cost-effective, visibly active, and efficient semiconductor photocatalyst having band edges suitable for targeted reactions. Recently, 2D layered double hydroxides possessing prominent features like tunable chemical composition, great stability, non-toxicity, minimal cost, simple preparation, surface hydroxyl group basicity, and apparent light response have gained great interest in the field of photocatalysis [4-6]. According to the literature reports, Co-Al LDH is a visible responsive catalyst with band energy of ~ 2.1 eV and reasonable band edge positions for redox reactions engaged in the photodegradation of harmful organic compounds. But the practical applications of such an

attractive photocatalyst have not been investigated well because of the lower separation proficiency of photoinduced charge carriers. As a consequence, there is a need to explore the photoactivity of such an exceptionally competent photocatalyst [7].

However, the photocatalytic performance of the bare LDH remains too low due to the slow charge carrier's portability and the quick recombination of photoinduced electrons and holes. Thus, it realized that only LDH component photocatalysts are deficient for photocatalytic reactions. The photocatalytic performance of a LDH can be strengthened by fabricating a hybrid system with another semiconductor having a lower or higher band gap, particularly in a 2D layered structure with matching band potentials prompting a stronger light response, more reactive sites, rapid charge transfer, effective charge partition, and expanded lifetime of electrons and holes. Recently, a well-known 2D material, g-C_3N_4, a visible responsive semiconductor (Eg ~ 2.71 eV) acquires matching band edge positions with Co-Al LDH required for efficient charge transfer. The CN sheets carries negative charge due to the amine group's deprotonation, whereas the surface of the LDH carries positive charge due to precisely organized cation layers [8, 9]. Therefore, the electrostatic interactions can firmly bond the two components and lead to a proficient charge transfer process. Consequently, constructing 2D-2D hybrid photocatalyst made of layered double hydroxide and g-C_3N_4 is a practical strategy for attaining better photocatalytic performance.

In addition to high charge separation efficiency, a photocatalyst must have a strong absorption response to visible light. Lately, a simple way for expanding the visible light response of a semiconductor is the deposition or doping of plasmonic metals. The plasmonic metals can provoke the collaborative oscillations of conducting electrons in resonance with incident light, named Surface Plasmon Resonance (SPR) which results in a noticeable increase in absorbance

response to visible range. The Schottky barriers framed at the metal-semiconductor interface cause electrons from the semiconductor to swiftly move to metal nanoparticles (NPs) serving as electron sinks. The electrons at the surface of metal NPs capture by suitable reactive species and go through photocatalytic action [10, 11]. As a consequence, introducing plasmonic metal NPs to the CN-LDH heterostructure is an effective approach to encourage charge carrier migration at the interface of LDH and CN and boost the capability of the material to absorb visible light.

This work reported the preparation of novel Co-Al LDH with two different kinds of morphologies ((i) micro flowers and (ii) hexagonal sheets) via a procedure combining urea hydrolysis and hydrothermal treatment. In the current study, a highly proficient plasmonic-metal-loaded ternary heterojunction system was constructed in a systematic way. First, the binary composites with different loadings (5-15 wt%) of CN over LDH were fabricated via the electrostatic self-assembly approach. To further improve the photocatalytic properties of CN-LDH heterostructure, the plasmonic Ag NPs with different loadings (0.5-2 wt%) were deposited on optimized CN-LDH composite through the photoreduction method.

Probably, this work is the first study providing beneficial information regarding the influence of CN and Ag loadings for the construction of ternary composite constituting Co-Al LDH, CN, and Ag. Moreover, a possible mechanism considering photodegradation of ciprofloxacin over Ag@CN-LDH ternary heterostructure was proposed in view of the consequences of photoluminescence, scavenging, and LC-MS experiments.

4.2. Experimental Section:

4.2.1. Chemical and Reagents:

Cobalt nitrate hexahydrate ($Co(NO_3)_2.6H_2O$), aluminium nitrate nonahydrate ($Al(NO_3)_2.9H_2O$), urea (CH_4N_2O), melamine ($C_3H_6N_6$), silver nitrate ($AgNO_3$) and potassium dichromate

($K_2Cr_2O_7$) were purchased from Loba chemie, India. Ammonium fluoride (NH_4F) was obtained from Sigma Aldrich. Ethanol, ethylene glycol, isopropanol and methanol were received from SD fine Ltd. Triple deionized water was obtained from Organo Biotech Laboratories Pvt. Ltd.

4.2.2. Synthesis of Co-Al LDH:

The Co-Al LDH was fabricated using the urea hydrolysis technique combining hydrothermal treatment as this strategy was simple, affordable, and provided significant yield. Typically, 0.227 g of cobalt salt and 0.0975 g of aluminium salt were added to 130 ml of distilled water. Subsequently, 0.312 g of urea and 0.0770 g of ammonium fluoride were added to the metallic solution under stirring for about 30 miniutes. The mixture was further transferred to an autoclave lined with Teflon, where it was heated to 120°C for 24 hours. The autoclave was allowed to chill off naturally to room temperature after completion of reaction. The pink product (Co-Al LDH) obtained was washed multiple times with distilled water and ethanol and dried at 60^oC.

4.2.3. Synthesis of g-C_3N_4 nanosheets:

The synthesis of g-C_3N_4 nanosheets (CN) is described in section **2.2.3**.

4.2.4. Preparation of CN-LDH composites:

The CN-LDH composites were fabricated via the self-assembly approach. The dispersion of LDH was prepared by dispersing a particular amount of LDH powder in water using a sonicator. Similarly, different CN dispersions (5-15 wt%) were fabricated by dispersing a particular appropriate amount of CN in distilled water. Then, a series of CN-LDH composites were constructed by mixing LDH dispersion with a particular CN dispersion and stirring for 24 hours. The different 5, 10, and 15 wt% CN loaded LDH composites were represented as 5CN-LDH, 10CN-LDH, and 15CN-LDH, respectively.

4.2.5. **Preparation of Ag deposited CN-LDH composites:**

To obtain a ternary Ag@CN-LDH composite, plasmonic Ag NPs were deposited onto the CN-LDH composite via photochemical deposition. 50 mg of a 10CN-LDH powder was dispersed in 25 ml of methanol (5 ml) and water (20 ml) solution, where methanol was a hole scavenger. The calculated amount of silver nitrate solution (0.01 M) according to varying weight percentages (0.5-2) of Ag was mixed with the above dispersion. The mixture was then cleansed with Argon gas for about 10 minutes to make inactive air and photoirradiated with a UV lamp for 2 hours under continuous stirring. The obtained brown-colored product was washed properly with deionized water and ethanol and kept at 50^{o}C for drying. A series of Ag@CN-LDH composites with different wt% (0.5-2) of Ag were prepared and designated as 0.5Ag@10CN-LDH, 1Ag@10CN-LDH, and 2Ag@10CN-LDH. **Scheme-4.1** represents the schematic illustration of the synthetic procedure of prepared catalysts. Upon illumination to UV light, both the CN and Co-Al LDH were photoexcited and produced electrons in their respective conduction bands. The electrons in their CB induced the deposition of Ag NPs on their surface by reducing the Ag^{+} ions in the metallic solution to Ag^{0}. The electrons generated in the conduction bands of both the CN and LDH were capable of performing the electrochemical reaction described as:

$$Ag^{+}(aq) + e^{-} \rightarrow Ag\,(s),\ E^{o} = +0.799\ V \text{ vs NHE} \ldots\ldots (4.1)$$

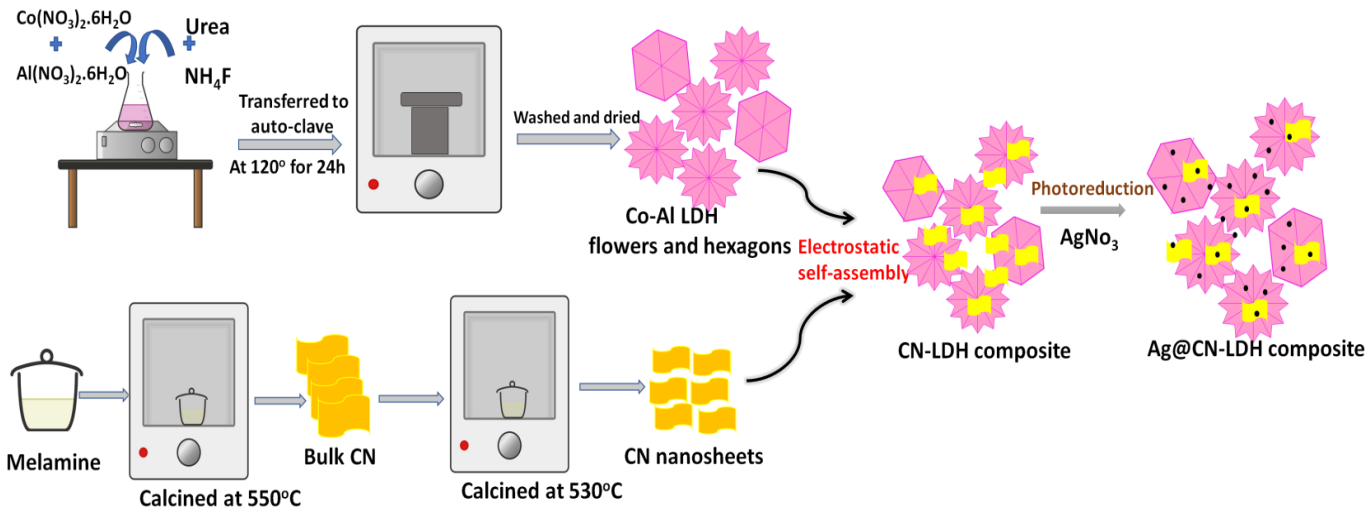

Scheme-4.1. A diagrammatic representation showing the preparation of Co-Al LDH, CN, CN-LDH composites, and Ag@CN-LDH composites.

4.2.6. Photocatalytic activity:

The photoactivity of LDH, CN-LDH composites, and Ag@10CN-LDH composites was investigated using ciprofloxacin as a model toxic pollutant with 20 ppm of its initial concentration. A set of test tubes, each test tube containing 5 ml of ciprofloxacin solution and 10 mg of the catalyst was prepared and stirred for about half an hour in dark to attain equilibrium between adsorption and desorption. Then, the photodegradation experiments were performed by irradiating each test tube with visible light irradiations (Wipro Garnet B22 50-watt LED bulb (Cool daylight, white)) under continuous stirring for different pre-fixed intervals (15, 30, 45, 60, 75, and 90 min) of time. After irradiating each test tube to light for a fixed time, the catalyst was separated from aqueous sample through centrifugation. The supernatant was analyzed with a UV-visible spectrophotometer to determine the remaining concentration of the pollutant. As the pollutant volume was less, it was not possible to observe the degradation efficiency of a catalyst with only a single sample. Therefore, we prepared different test tubes for each time interval with the same amount of pollutant solution and catalyst. For each catalyst, the same procedure was

performed.

The percentage of pollutant degraded was calculated as follows:

The pollutant degraded (%) = $\frac{C_o - C_t}{C_o} \times 100$……. …. (4.2)

where, C_o is the initial concentration of pollutant at time, t = 0 and C_t is residual concentration of the pollutant at time t [12,13].

4.3. Results and discussion:

4.3.1. Crystallographic and structural studies:

The XRD spectra were recorded to observe the phase structure of prepared catalysts. The XRD spectra of LDH, CN, CN-LDH composites, and Ag@CN-LDH composites are depicted in **Fig.4.1**. For LDH, the diffraction peaks located at 2θ = 11.7^o, 23.5^o, 34.6^o, 39.2^o, 46.6^o, 60.2^o, and 61.5^o indexed to the plane (003), (006), (012), (015), (018), (110), and (113), respectively, were well consistent with standard Co-Al LDH (JCPDS No. 51–0045). In the case of CN, a strong and sharp peak noticed at 2θ = 27.5^o was indexed to the (002) plane, a characteristic peak of g-C_3N_4, well consistent with standard g-C_3N_4 (JCPDS 87- 1526). In the spectra of CN-LDH composites, all the peaks related to LDH were present along with a weak peak originating at 2θ = 27.5^o. The intensity of the characteristic peak of CN got intensified upon increasing the CN loading (5-15 wt%), whereas, the intensity of LDH peaks slightly reduced indicating the strong interaction between CN and LDH responsible for the successful formation of the composites [13,14]. In the case of Ag@CN-LDH composites, a poor peak was observed at 2θ = 38.1^o indexed to the (111) plane of metallic Ag [15]. The diffraction peak corresponding to Ag was not much intensified attributable to its low concentration of only 0.5 to 2 wt%. The intensity of peak at 2θ = 27.5^o corresponding to CN got reduced and is not clearly visible in the XRD patterns of Ag@CN-LDH composites. The graphical representation zooming the 25-40^o region is shown in

Fig.4.2 to clearly observe the peak attributed to the presence of CN. The intensity of peaks was moderately reduced and peak position was slightly shifted in the spectra of CN-LDH composites and Ag@CN-LDH composites than that of bare Co-Al LDH, which might correspond to the strong interactions of CN and Ag NPs with LDH.

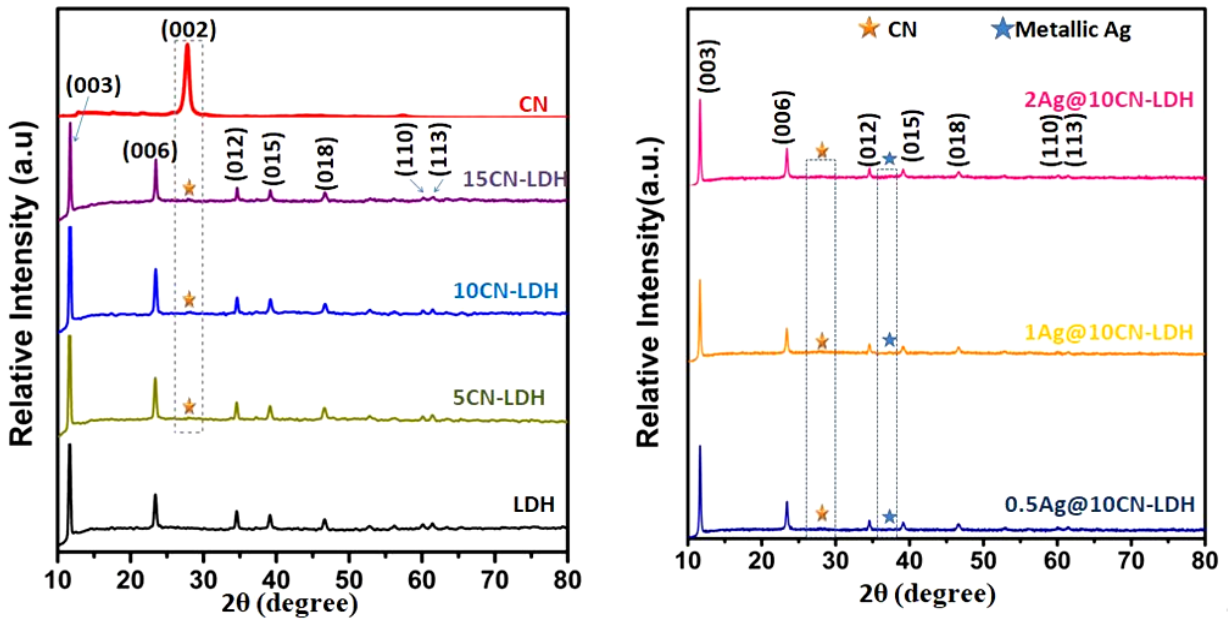

Fig.4.1. X-ray diffraction patterns of bare LDH, CN, CN-LDH composites, and Ag@10CN-LDH composites.

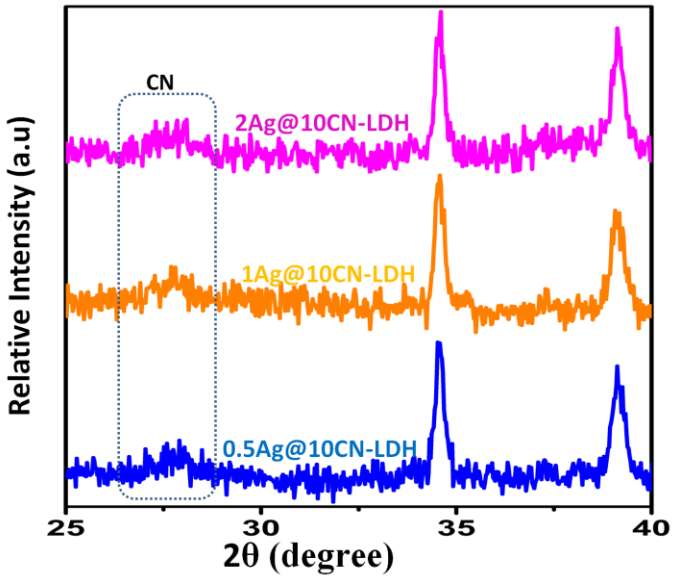

Fig.4.2. The zooming representation of 2θ values in the region 25-40^{o} for Ag@10CN-LDH composites.

To further demonstrate their structural properties, FTIR spectroscopy was conducted. **Fig.4.3 (a)** shows the FTIR spectra of LDH, 10CN-LDH, and 1Ag@10CN-LDH. In the case of bare LDH, broadband appearing at 3436 cm^{-1} indicated the vibrational modes of O-H bond related to brucite-like sheets of LDH and water molecules in the interlayer spacing. The peak at 1358 cm^{-1} associated with the carbonate anions intercalated between the adjacent brucite-like sheets of LDH. The other peaks found in the region 500-800 cm^{-1} attributed to stretching vibrations of M-O and M-O-M (M represents Co and Al) [13, 16, 17]. In the case of CN spectrum, the C-N and C=N vibrational modes were responsible for the emergence of peaks at 1635 cm^{-1} and 1239.5 cm^{-1}, respectively. The out-of-plane bending vibrations of six-member heptazine rings were attributed to a peak at 805.7 cm^{-1} [18]. The stretching vibration modes of the residual N-H bonds of the uncondensed amino groups were the cause of the band that appeared around 3300 cm^{-1} [14]. In the case of 10CN-LDH composite, all the peaks related to LDH were observed along

with some additional peaks related to CN at 1239.5 cm^{-1} and 1635 cm^{-1}. For 1Ag@10CN-LDH composite, all the peaks related to LDH and CN were observed and no significant change was observed in peak positions upon deposition of Ag NPs. The results suggested that the Co-Al LDH, CN, and CN-LDH composite were prepared successfully and the Ag NPs could not affect the structure of LDH and CN.

The zeta potential studies were analyzed to examine the electrokinetic properties of synthesized catalysts. **Fig.4.3 (b)** represents the variation in zeta potential. The zeta potential of bare LDH and CN was +32.3 mV and -19.2 mV, respectively. For CN-LDH composites, the zeta potential of LDH decreased as +25.8 mV, +15.3 mV, and +8.8 mV with an increase in the 5, 10, and 15 wt% loading of CN, respectively, indicated the neutralization of the positive surface charge of LDH by negatively charged CN nanosheets. Moreover, deposition of Ag further reduced the zeta potential of 10CN-LDH composite to +13.9 mV, +12.6 mV, and +10.3 mV due to coverage of its surface with 0.5, 1, and 2 wt% of Ag NPs, respectively. Hence, the variation in zeta potential values of LDH confirmed the successful formation of CN-LDH and Ag@10CN-LDH composites.

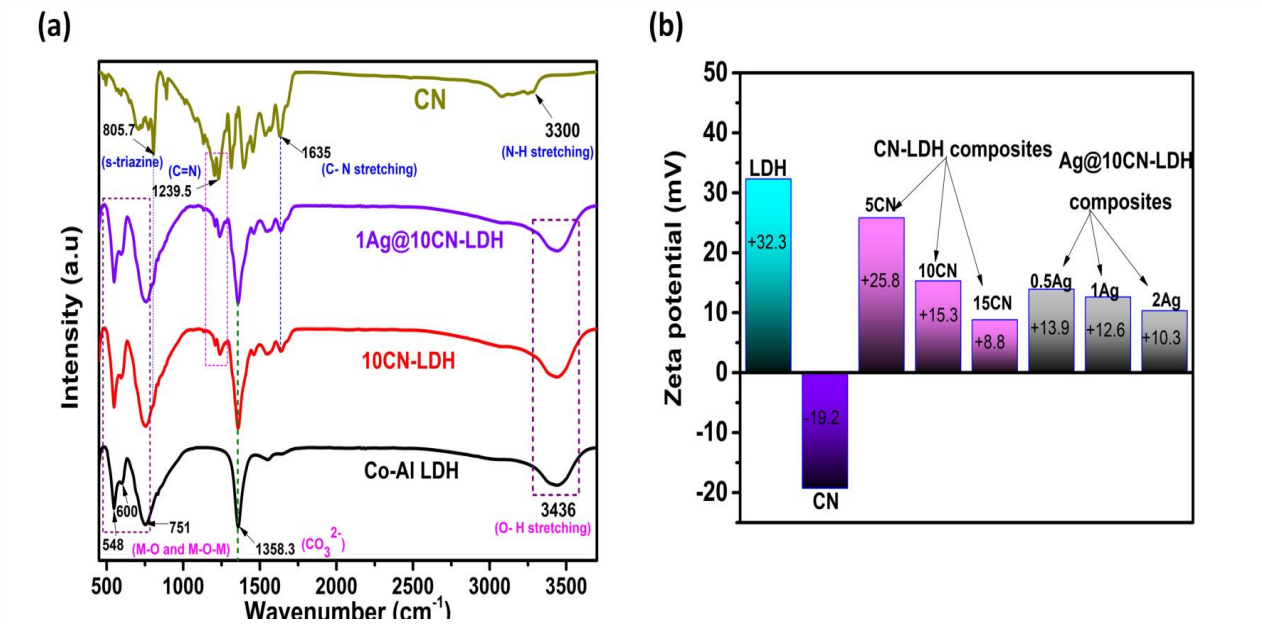

Fig.4.3. FTIR spectra of bare LDH, CN, 10CN-LDH composite, and 1Ag@10CN-LDH composite (a) and Zeta potential variation of bare LDH, CN, CN-LDH composites, and Ag@10CN-LDH composites (b).

The elemental composition and chemical states of elements found in the LDH, CN, 10CN-LDH composite, and 1Ag@10CN-LDH composite were examined using X-ray photoelectron spectroscopy (XPS). The charge correction of the spectra was done and the binding energy position was calibrated considering C1s peak at 284.8 eV as a reference. **Fig.4.4** exhibits the survey spectra of prepared catalysts. The survey spectra of prepared catalysts are depicted in Fig. 4.4. Co, Al, C, and O were found in LDH's survey spectrum, while C and N were found in CN's spectrum. The CN-LDH composite was successfully formed, as evidenced by the peaks associated with Co, Al, C, O, and N in the 10CN-LDH's survey spectrum. The 1Ag@10CN-LDH spectrum contained signals for Co, Al, C, O, N, and Ag, indicating that the ternary Ag@CN-LDH composite was fabricated successfully.

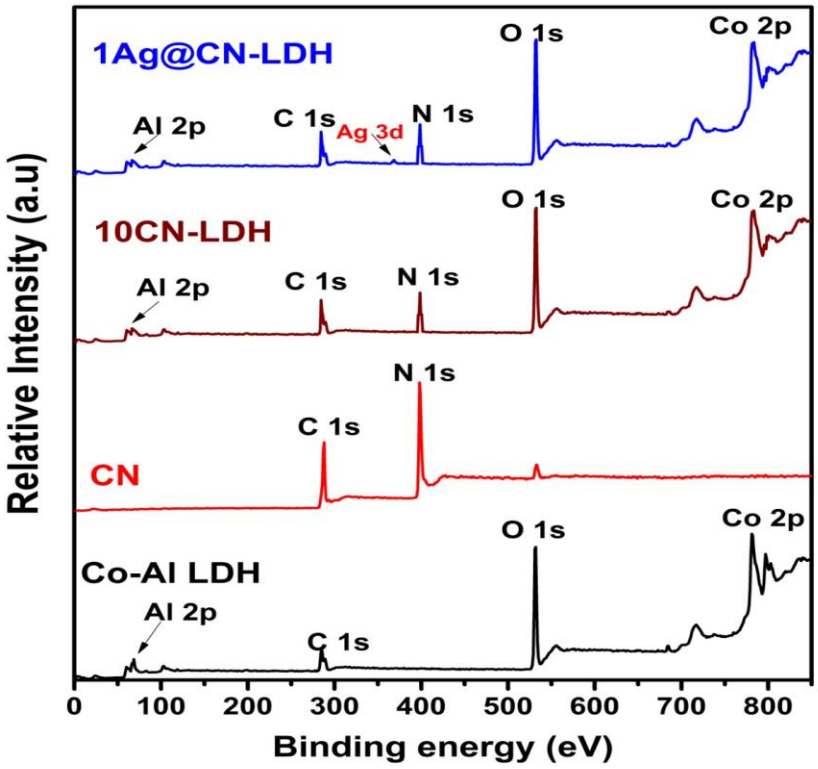

Fig.4.4. The survey spectra of LDH, CN, CN-LDH and 1Ag@10CN-LDH composite.

Co 2p (**Fig.4.5 (a)**): Due to $Co(OH)_2$ groups present in the LDH framework, the Co 2p spectrum of bare Co-Al LDH contained two peaks at 781.2 eV and 797.3 eV, which correspond to Co $2p_{3/2}$ and Co $2p_{1/2}$, respectively. The two satellite peaks ascribed to availability of high spin Co^{2+} in the LDH [19, 20]. In the case of the 10CN-LDH composite, the peak positions of Co 2p were slightly moved to higher binding energy relative to that of bare LDH. Furthermore, a little more shift in the peak positions of Co 2p was observed in the case of the 1Ag@10CN-LDH composite as compared to the 10CN-LDH composite.

Al 2p (**Fig.4.5 (b)**)**:** The Al 2p spectrum of LDH, 10CN-LDH, and 1Ag@10CN-LDH showed a peak at 73.7 eV, 73.76 eV, and 73.8 eV, respectively, which confirmed the presence of Al^{3+} in the LDH lattice [21].

O 1s (**Fig.4.5 (c)**): The O 1s spectrum of bare Co-Al LDH was deconvoluted to two peaks

positioned at 531.4 eV and 532.0 eV ascribed to O^{2-} species of intercalated carbonate anions and surface hydroxyl groups (O-H) of LDH, respectively [19]. In the case of 10CN-LDH and 1Ag@10CN-LDH, the binding energy of both the peaks of the O 1s spectrum was found to be slightly increased.

C 1s (**Fig.4.5 (d)**): The high-resolution C 1s spectrum of bare Co-Al LDH was fitted into peaks positioned at 284.68 eV, 285.7 eV, and 289.3 eV indicating the presence of C-C, C-OH, and O-C=O groups, respectively [14, 22]. In the case of CN, two peaks fitted at 284.8 eV and 287.8 eV were assigned to C-C/C=C units and sp^2 hybridized C-atoms in aromatic tri-s-triazine rings (N-C=N), respectively [23]. Moreover, a significant shift in the binding energy of peaks of the C 1s spectrum was detected for 10CN-LDH and 1Ag@10CN-LDH compared to LDH and CN.

N 1s (**Fig.4.5 (e)**): The N 1s spectrum of CN was fitted into three peaks. The two main peaks positioned at 398.2 eV and 398.6 eV evident the presence of sp^2 hybridized N- atoms in C-N=C coordination and bridged N-atoms in $N-C_3$ coordination, respectively, in tri-s-triazine rings [10]. The small intensity peak originated at 400.0 eV assigned to the amino functional groups (N-H) [14]. In the spectrum of 10CN-LDH and 1Ag@10CN-LDH composite, all the peaks in the N 1s spectrum were positioned at higher binding energies relative to CN.

Ag 3d (**Fig.4.5 (f)):** The peaks at binding energy values of 368.1 eV and 374.1 eV in the Ag 3d spectrum of 1Ag@10CN-LDH correspond to Ag $3d_{5/2}$ and Ag $3d_{3/2}$, respectively, which were are well-matched with the standard binding energies of metallic Ag [24].

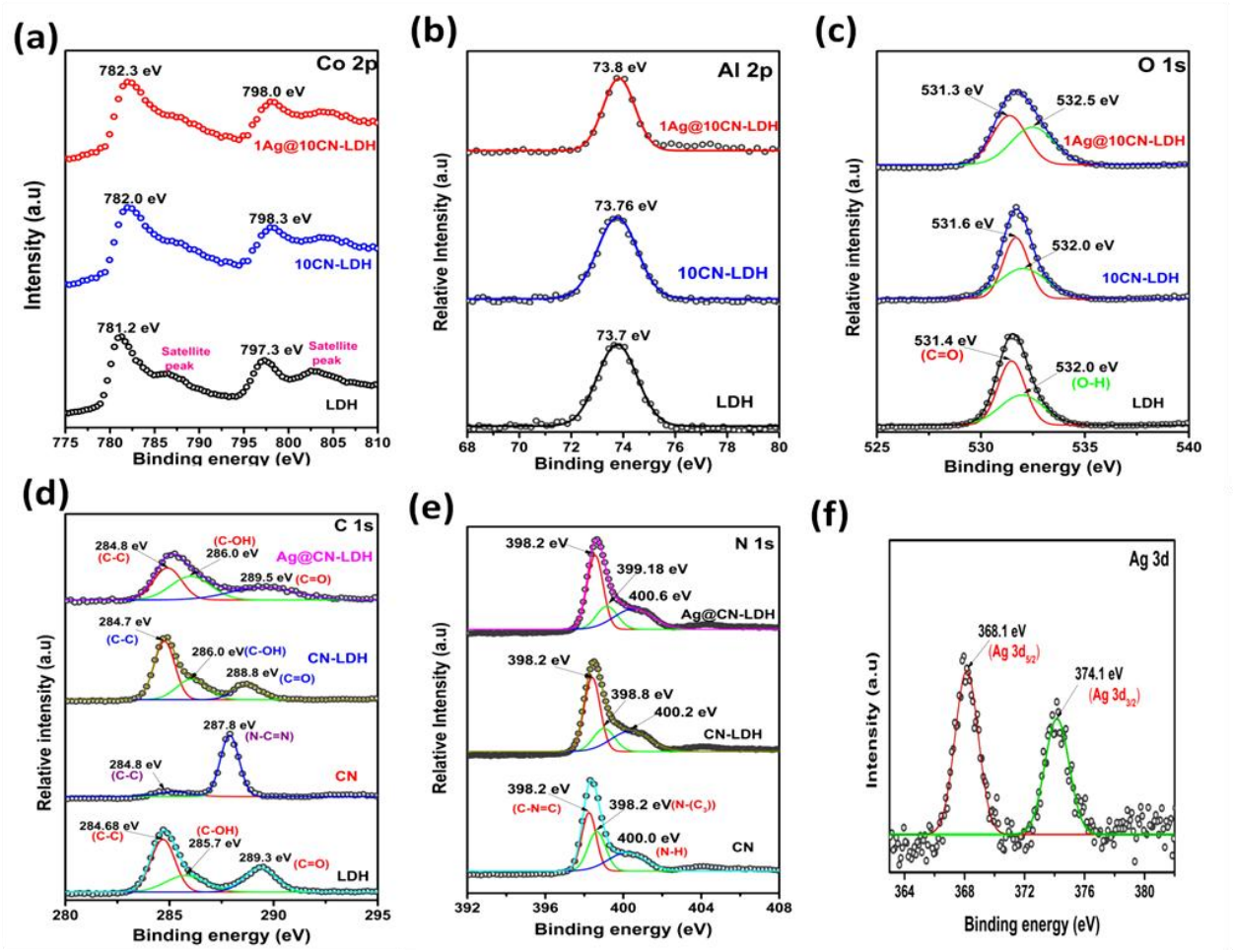

Fig.4.5. XPS spectra of the LDH, CN, 10CN-LDH and 1Ag@10CN-LDH composites; Co 2p (a), Al 2p (b), O 1s (c), C 1s (d), N 1s (e), and Ag 3d (f).

The strong interfacial and electronic interactions between bare LDH and CN were responsible for slight shifts observed in the binding energy values of elements Co, Al, C, O, and N in 10CN-LDH [12]. Further, the binding energies of corresponding elements in 1Ag@10CN-LDH composite were further shifted towards higher binding energy as compared to 10CN-LDH, which demonstrated the migration of electrons from LDH and CN to Ag NPs for quick charge transfer to enhance the photocatalytic performance [19, 25].

4.3.2. Surface and morphological studies:

During photocatalytic degradation, the pollutant molecules initially adsorbed on the surface of a

solid catalyst and afterward undergo the catalytic process. Therefore, one of the most important parameters for effective photocatalytic activity is the catalyst's surface area. **Fig.4.6 (a and b)** shows Brunauer–Emmett–Teller based nitrogen adsorption-desorption isotherms and pore size distribution of the LDH, 10CN-LDH, and 1Ag@10CN-LDH photocatalysts. According to the IUPAC classification of adsorption isotherms, all of the samples' isotherms were identical to a type IV isotherm with a type H3 hysteresis loop suggesting the presence of mesopores formed due to aggregation of plate like particles [26-28]. The BET surface area of LDH, 10CN-LDH composite, and 1Ag@10CN-LDH composite was measured as 44 m^2/g, 60 m^2/g, and 98 m^2/g, respectively. The specific surface area of LDH was improved after the loading of CN which was further increased by the deposition of Ag NPs due to their small particle size. The increment in the surface area of LDH after the deposition of CN and Ag could enhance the adsorption and consequently the photocatalytic execution.

The values of specific surface area, pore volume, and pore diameter are mentioned in **Table-1**. The diameter of pores lies within 2-50 nm indicating the presence of mesopores [28]. Therefore, the LDH samples synthesized in this work showed the characteristics of mesoporous materials. The results indicated that the pore diameter of samples decreased after compositing with Ag NPs, this might be ascribed due to the incorporation of some of the small metallic NPs into the pores [29].

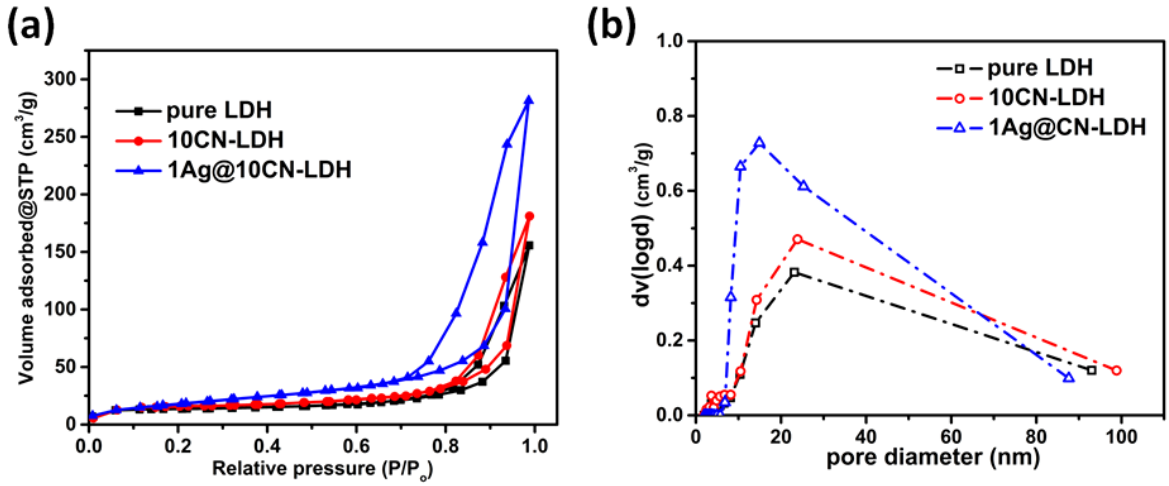

Fig.4.6. The N_2 adsorption-desorption curves (a) and pore size distribution curves (b) of bare LDH, 10CN-LDH and 1Ag@10CN-LDH.

Table-4.1. BET specific surface area analysis of LDH, CN-LDH, and Ag@CN-LDH composites.

S.No.	Sample	Specific Surface area (m^2/g)	Pore volume (cc/g)	Pore diameter (nm)
1.	Co-Al LDH	44	0.24	14.03
2.	10CN-LDH	60	0.29	14.26
3.	1Ag@10CN-LDH	98	0.46	10.48

The morphological and microstructural features of LDH, CN, 10CN-LDH, and 1Ag@10CN-LDH composites were investigated using the FESEM technique. The FESEM images of Co-Al LDH (**Fig.4.7 (a-c)**) revealed two kinds of morphologies: (i) self assemble of nano-flakes to form 3D hierarchical flower-like microspheres and (ii) hexagonal-shaped sheets. The FESEM image of CN displayed typical morphology with various crumpled sheets and folds over the entire surface (**Fig.4.7 (d)**). The FESEM image of 10CN-LDH and 1Ag@10CN-LDH clearly showed micro-flowers and a hexagonal sheet of LDH along with g-C_3N_4 (**Fig.4.7 (e and f)**). But the Ag NPs were not shown in FESEM images due to their very small size in the nano-range.

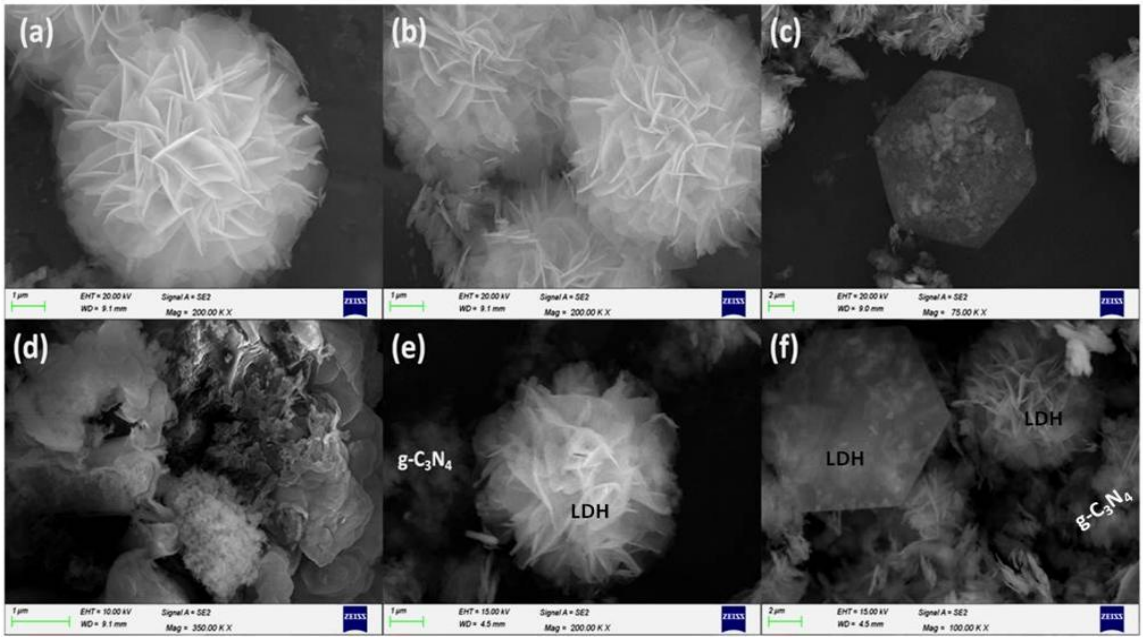

Fig.4.7. FESEM images of bare Co-Al LDH (a-c), CN (d), 10CN-LDH composite (e), 1Ag@10CN-LDH composite (f).

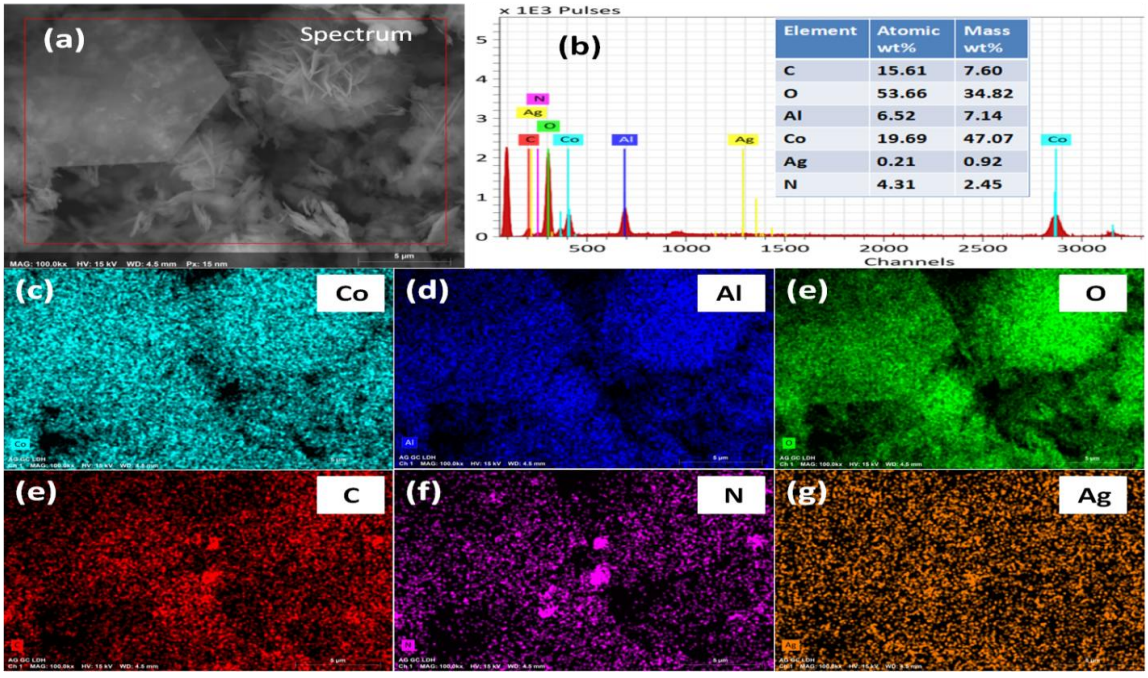

Fig.4.8. FESEM image (a) with its corresponding; the EDS spectrum and elemental composition (b); elemental mapping of elements (c-g) in 1Ag@10CN-LDH composite.

The energy dispersive spectroscopy (EDS) and elemental mapping analysis are shown in **Fig.4.8**.

The presence and precise distribution of the elements Co, Al, O, C, N, and Ag in the 1Ag@10CN-LDH composite were confirmed by the elemental mapping and the EDS spectrum. The TEM images of the 1Ag@10CN-LDH composite at different resolutions are showed **Fig.4.9 (a and b)**. It was observed that Ag NPs (black spherical dots) mostly in spherical shape were distributed almost over the whole surface of the 10CN-LDH composite. The Ag nanoparticles of different particle size in the range of 4-32 nm were observed. The results indicated that the Ag particles were in the nanometer range. The small size could provide more active sites to prompt photocatalytic activity. Moreover, the HRTEM images (**Fig.4.9 (c and d)**) showed the lattice fringes distanced by 0.227 nm, 0.33 nm, and 0.231 nm accredited to LDH (015), CN (002), and Ag (111), respectively [30-32].

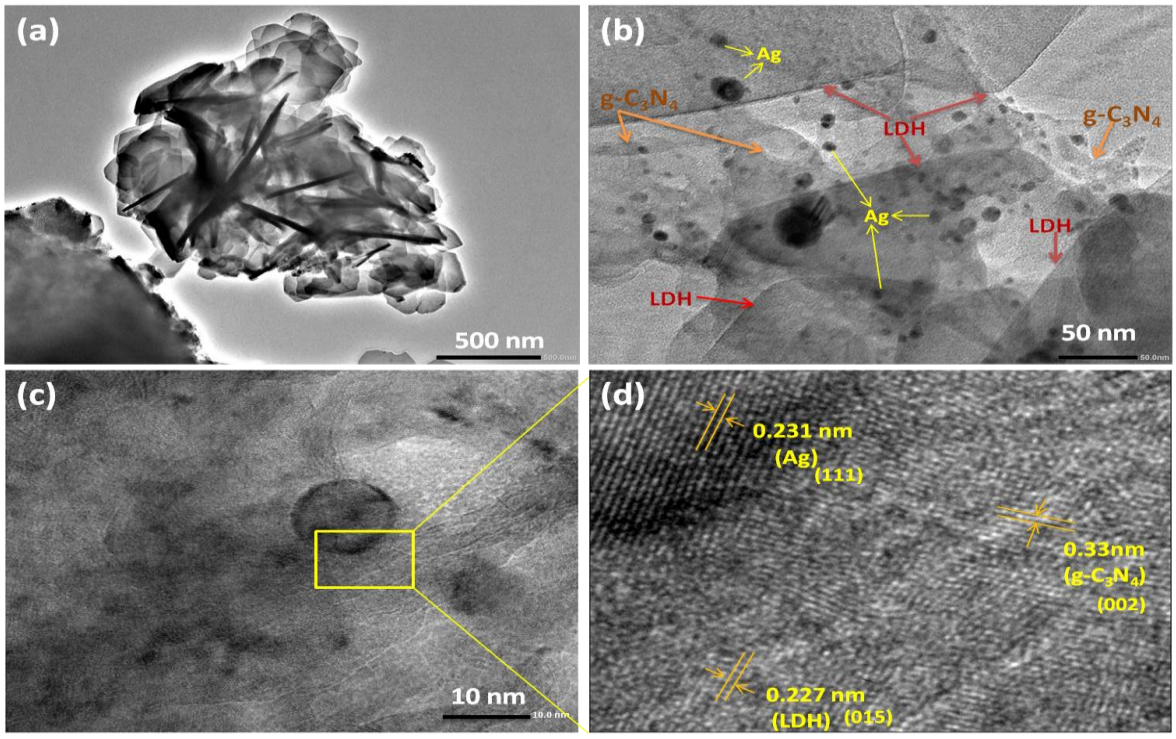

Fig.4.9. HRTEM images (a, b, and c) and lattice fringes (d) of 1Ag@CN-LDH composite.

4.3.3. Optical studies:

Fig.4.10 (a) represents the DRS spectra of prepared catalysts. In Co-Al LDH spectrum, the three bands located in the visible region at 450 nm, 490 nm and 520 nm were credited to the d-d transitions of Co^{2+} present in octahedral coordination geometry. No such absorption band related to Al^{3+} was found in DRS spectra because of its d^0 electronic configuration [20, 33]. The CN displayed an absorption edge at 457 nm having intrinsic semiconductor like properties assigned to n-Π* transitions occurring due to lone pairs on N atoms present in triazine/heptazine rings [10, 26]. For CN-LDH composites, the loading of CN affected the optical properties of LDH. With an increase in the wt% of CN on LDH, a significant decrease in visible light absorption and an increase in the UV-light absorption were observed. This change was attributed to the presence of CN in composites and strong interactions between CN and LDH affecting the absorption capability. In the case of Ag@10CN-LDH composites, a remarkable increase in absorbance over the visible region was observed after the deposition of Ag NPs due to their Surface Plasmon resonance (SPR) effect. The SPR peak of Ag NPs was found to merge with the absorption spectrum of LDH due to the large absorbance band of LDH. The intensity of absorption in the visible region increased with an increase in wt% loading (0.5, 1, and 2 wt%) of Ag NPs. The extended absorption would reap more photons to produce more photoinduced electrons and holes, resulting in improved photocatalytic performance.

The bandgap value of all the prepared catalysts was calculated using Tauc's expression written as:

$$\alpha h\nu = A(h\nu - E_g)^n \quad \text{..... (4.3)}$$

where, α is the absorption coefficient, hν is the energy of the photon, A is a constant, E_g is the bandgap energy of a photocatalyst, and n is the exponent coefficient that depends on the direct or

indirect bandgap transitions (n = ½ and 2 for direct and indirect transitions, respectively) [34]. The bandgap values were determined by extrapolating a straight line to the x-axis in the graph of $(\alpha h\nu)^{0.5}$ *vs* $h\nu$ (as shown in **Fig.4.10 (c and d)**). The bandgap value of the Co-Al LDH and g-C_3N_4 was calculated as 2.08 eV and 2.71 eV, respectively.

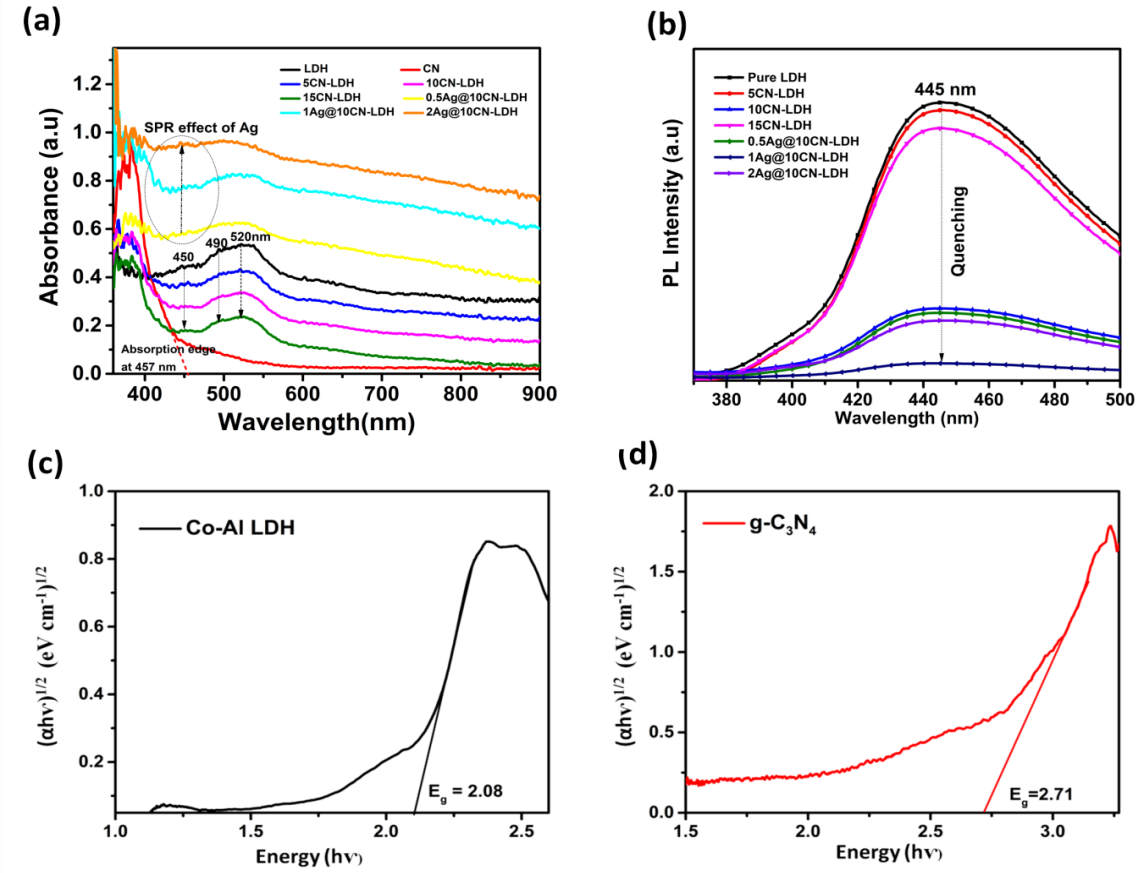

Fig.4.10. Diffuse reflectance spectra of all synthesized catalysts (a), photoluminescence spectra of bare LDH, CN-LDH composites, and Ag@CN-LDH composites (b), and Tauc's plot of Co-Al LDH and CN (c-d).

The prepared catalysts were excited at wavelength of 320 nm to record their photoluminescence spectra. As displayed in **Fig.4.10 (b)**, the bare LDH exhibited an emission peak at 445 nm related to the $^4T_{2g}$ (F) - $^4T_{1g}$ (F) transitions of ligand field splitting [17, 20]. Highest intensity of LDH's PL signal indicated a quick recombination of electrons and holes. In the case of CN-LDH

composites, a significant decrease in the PL intensity was observed due to the migration of electrons and holes between LDH and CN components leading to suppressed rejoining of electron and hole pairs. The intensity of 10CN-LDH signal was found lower than 5CN-LDH and 15CN-LDH composites indicating that optimum wt% of CN could efficiently enhance the separation of charge carriers. Especially, the PL signal of Ag@10CN-LDH composites was much less intensified than those of binary CN-LDH composites and bare LDH due to the electron-accepting capability of Ag NPs inhibiting the rejoining of electron and hole pairs. The maximum quenching was observed for Ag@CN-LDH with 10 wt% of CN and 1 wt% of Ag loading at LDH. Therefore, the optimal loading of CN and Ag on LDH and powerful collaboration between the Ag, CN, and LDH contributed to upgraded photocatalytic execution.

4.3.4. Photodegradation studies:

The ideal weight percentage of CN loading over LDH and Ag loading over CN-LDH composite for photocatalytic application was analyzed by photodegrading CIP (20 ppm) under LED light using all prepared catalysts. **Fig.4.11** displays the changes in concentration of CIP at various time spans in the presence of prepared catalysts under dark conditions and illumination of LED light. Before illuminating to light, the samples stirred in a dark chamber for 0-30 minutes possessed significant changes in the concentration of CIP due to its adsorption over prepared catalysts. The CN-LDH and Ag@CN-LDH composites displayed higher adsorption of CIP than the bare LDH. It might be due to the increment in the surface area of LDH composites with the deposition of CN and Ag NPs. After attaining adsorption-desorption equilibria, the photoactivity of catalysts was inspected under LED radiations for 0-90 minutes. The degradation efficiency of all the catalysts increased with irradiation time. Bare LDH exhibited the minimum photoactivity due to the quick rejoining of photoinduced electron and holes (**Fig.4.11 (a))**. With CN loading,

the degradation of CIP was increased with 5CN-LDH and 10CN-LDH composites and afterward decreased with 15CN-LDH composite (**Fig.4.11 (b)**). Herein, LDH was considered the main active material for photocatalysis and the purpose of CN loading was to improve the separation of photogenerated charge carriers. But, only an appropriate amount of CN loading could build photodegradation effectiveness. With an expansion in the wt% stacking of CN, the surface of LDH gets covered with CN, and exposure of active sites of LDH to photocatalytic interaction gets minimized. As a result, an excess amount of CN limited the migration of charge carriers and reduced the catalytic sites on the surface of LDH. Consequently, among CN-LDH composites, 10CN-LDH displayed the highest degradation efficiency and 10 wt% loading of CN was optimized for CN-LDH composites.

The 10CN-LDH composite was further loaded with 0.5-2 wt% of Ag. As shown in (**Fig.4.11 (c)**), all Ag@10CN-LDH composites showed noticeably higher degradation of CIP than LDH and CN-LDH composites. Also, the performance of Ag@10CN-LDH composites was influenced by the Ag contents. As the Ag content of the composites increased from 0.5-1 wt%, their photoactivity increased and then decreased with a further 2 wt% amount of Ag. The loading of Ag NPs extended the light absorbance response to visible region, accessed the exchange of electrons, and improved the reactive sites of the photocatalyst. But the amount of Ag must be optimized as the excess amount of Ag confined the access of light to reach the LDH due to more coverage of the surface of LDH by Ag particles and reduced its photoactivity. Among all, 1Ag@10CN-LDH composite with 1 wt% loading of Ag exhibited the highest photoactivity. **Fig.4.11 (d)** showed a decrease in absorbance value of CIP at 274 nm after irradiating the samples for 90 min under the LED lamp.

As shown in **Fig.4.12,** the photocatalytic proficiency of catalysts towards the degradation of CIP

followed the sequence: Bare LDH (13%) < 5CN-LDH (58.5%) < 15CN-LDH (63%) < 10CN-LDH (72.5%) < 2Ag@10CN-LDH (74%) < 0.5Ag@10CN-LDH (86.2%) < 1Ag@10CN-LDH (97%). The kinetics of photodegradation of CIP with prepared samples was further explored by first order kinetic equation written as follows:

$$\ln \frac{C_o}{C_t} = kt \ldots\ldots\ldots\ldots (4.4)$$

where C_o is the concentration of pollutant at time, t = 0 and C_t is the concentration of pollutant at irradiation time, t minutes and k is the first order rate constant of the photodegradation [13]. The rate constant of CIP degradation under LED light followed the order: Bare LDH (0.00152 min^{-1}) < 5CN-LDH (0.00985 min^{-1}) < 15CN-LDH (0.01079 min^{-1}) < 10CN-LDH (0.01407 min^{-1}) < 0.5Ag@10CN-LDH (0.01505 min^{-1}) < 2Ag@10CN-LDH (0.02115 min^{-1}) < 1Ag@10CN-LDH (0.0402 min^{-1}). Among all the samples, the composite of LDH loaded with 10 wt% of CN and 1 wt% of Ag attained the maximum reaction rate almost 26 times more than that of bare LDH. The synergetic effect between LDH, CN, and Ag was responsible for boosted photocatalytic efficiency of the 1Ag@10CN-LDH composite. Notably, an optimized amount of CN and Ag was effective for enhancing the photoactivity of LDH.

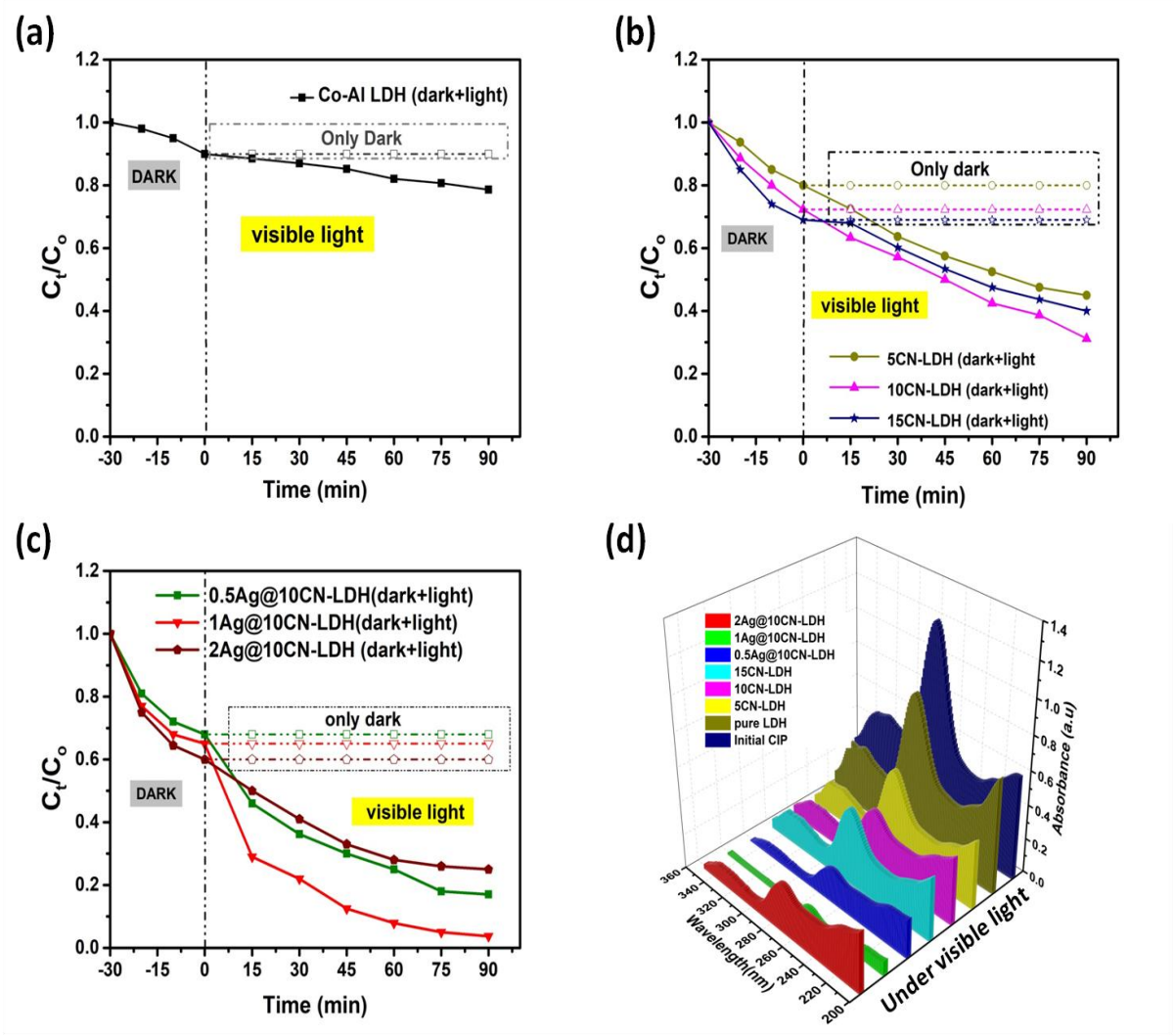

Fig.4.11. Adsorption (in dark) and photodegradation (in LED light) of CIP over bare LDH, CN-LDH composites, and Ag@CN-LDH composites (a-c) and the absorbance spectra of CIP at initial concentration (20 ppm) and after degradation under LED light using different prepared catalysts (d).

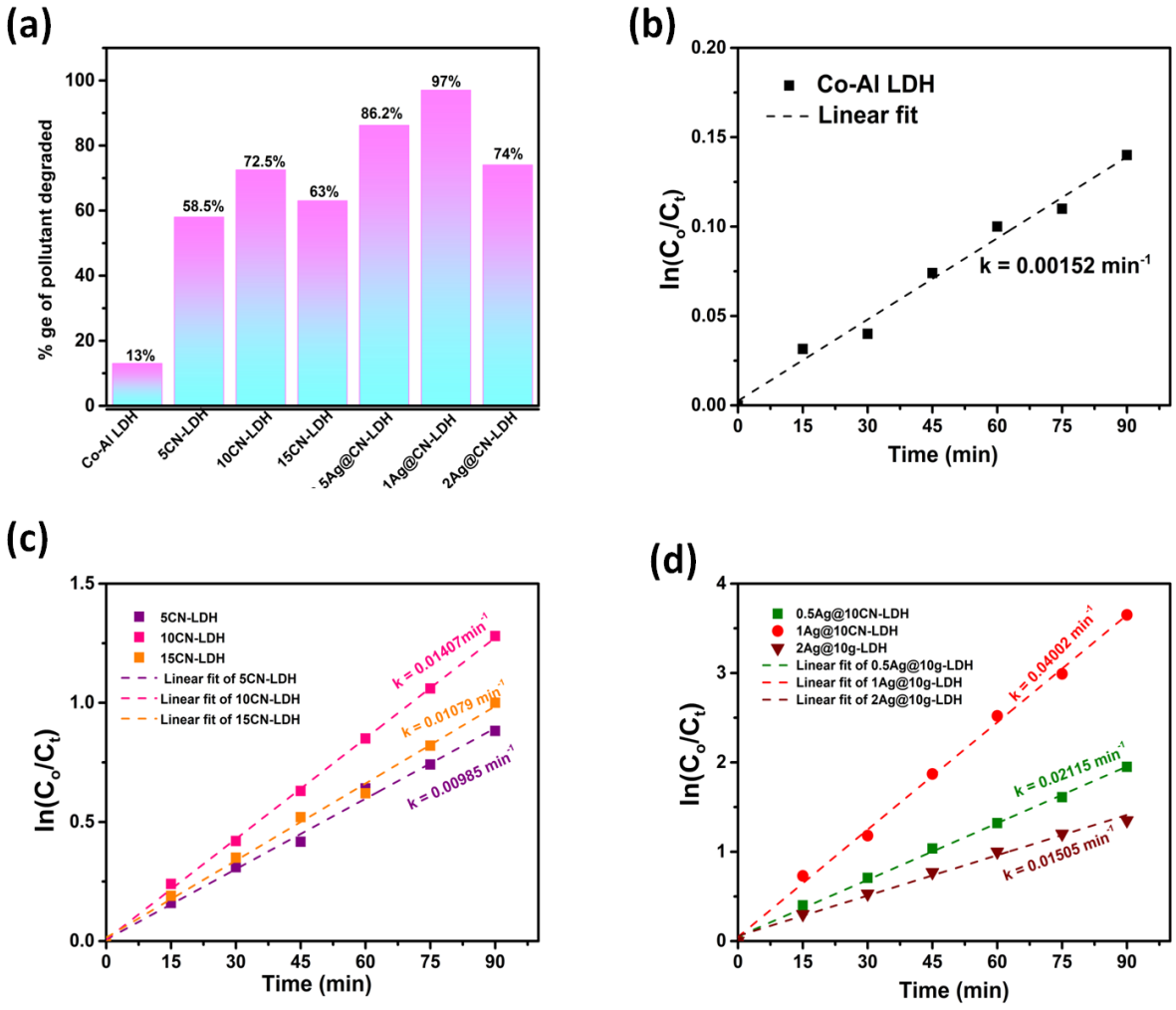

Fig.4.12. Bar graph showing percentage of CIP degraded using different catalysts (a) and the first order kinetic fit for degradation of CIP using bare LDH, CN-LDH, and Ag@10CN-LDH (b-d).

4.3.5. Scavanging experiments for investigating active species:

The role of different active species like superoxide anion radicals ($O_2^{\cdot-}$), hydroxyl radicals (O$\dot{H}$), and holes (h^+) in the degradation process of ciprofloxacin were investigated through a scavenging experiment. The scavenging experiment over 1Ag@10CN-LDH catalyst under similar conditions of degradation experiment was performed using $K_2Cr_2O_7$, isopropanol, and methanol as scavengers for $O_2^{\cdot-}$, O$\dot{H}$, and h^+, respectively. **Fig.4.13** shows the percentage of

ciprofloxacin degraded over 1Ag@10CN-LDH catalyst using none and different scavengers. The added $O_2^{\cdot-}$, OḢ, and h^+ scavengers suppressed the ciprofloxacin degradation to 65%, 86%, and 82.5%, respectively, whereas 97% of ciprofloxacin was degraded without addition of any scavenger. By comparison, after adding $K_2Cr_2O_7$, the degradation efficiency was most significantly decreased suggesting the main role of superoxide anion radicals in the degradation process. Moreover, the addition of isopropanol and methanol also suppressed the activity to a particular extent indicating that OḢ and h^+ also played significant roles in the degradation reaction.

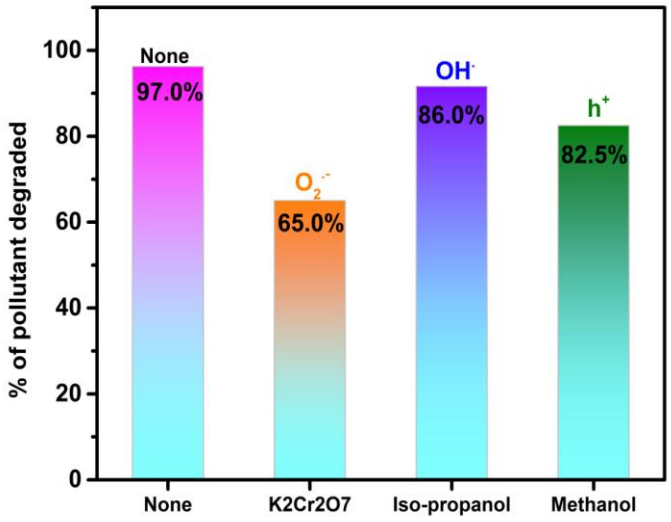

Fig.4.13. Effect of different scavangers on the degradation of CIP with 1Ag@10CN-LDH.

4.3.6. Recyclibility and stability test:

The reusability of the 1Ag@10CN-LDH composite was evaluated by utilizing the same catalyst for several times under similar experimental conditions. After the first cycle of the degradation of CIP, the catalyst was separated, washed, and dried. The photocatalyst was recycled and put into a fresh solution of CIP for the next experiment under the same conditions. A similar

procedure of reusing the catalyst was conducted up to five times. **Fig.4.14 (a)** shows the photodegradation of CIP under LED radiations during five photocatalytic cycles over 1Ag@10CN-LDH composite. The degradation efficiency remained practically similar up to five cycles and was diminished by just 2.33% in the fifth cycle contrasted with the first cycle. It proved that prepared photocatalyst possesses excellent reusability for its potential application in environmental remediation.

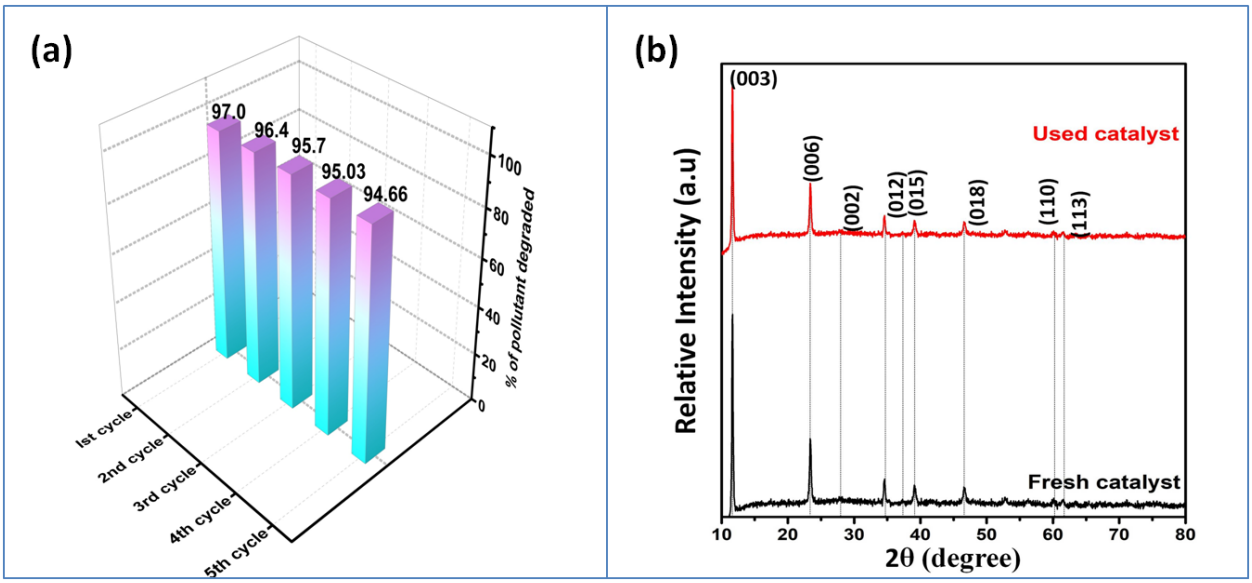

Fig.4.14. The photocatalytic efficiency of 1Ag@10CN-LDH for degradation of CIP over five cycle runs (a) and XRD spectra of fresh and used 1Ag@10CN-LDH for the degradation of CIP (b).

The stability of the 1Ag@10CN-LDH composite was further confirmed by analyzing its XRD spectrum before and after the photocatalytic reaction. As shown in **Fig.4.14 (b),** the XRD spectrum of the fresh catalyst is almost identical to that of the used catalyst confirming the conservation of crystal structure after photocatalytic application. It demonstrated that ternary 1Ag@10CN-LDH is an ideal and stable material towards removal of organic pollutants for water remediation.

4.3.7. LC-MS studies:

The possible pathways during degradation process were proposed based on the intermediates found during LC-MS analysis. The LC-MS spectra of CIP solution before and after degradation (**Fig.4.15** and **Fig.4.16)** showed that CIP molecules were almost degraded to other by-products. The peak of CIP molecule (m/z = 332) was absent in the spectrum of the treated sample while it was present for the untreated CIP solution.

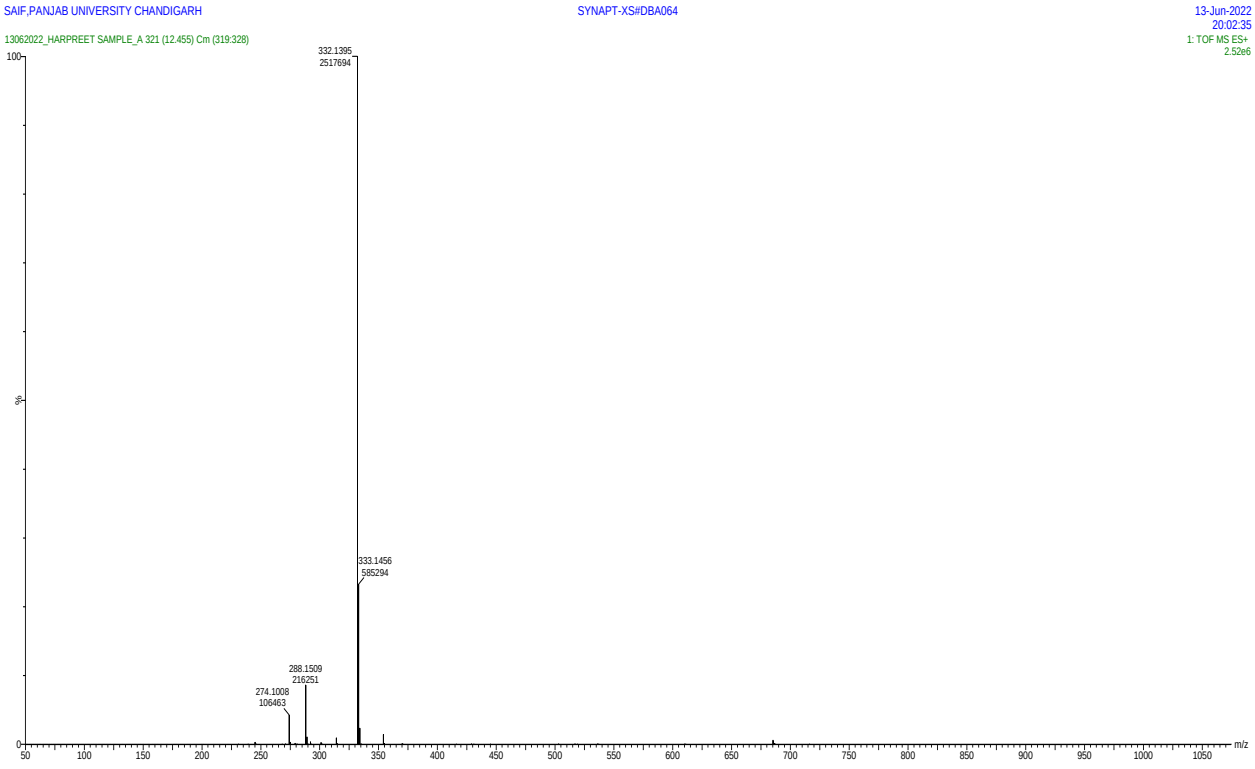

Fig.4.15. The LC-MS spectrum of initial ciprofloxacin solution before degradation.

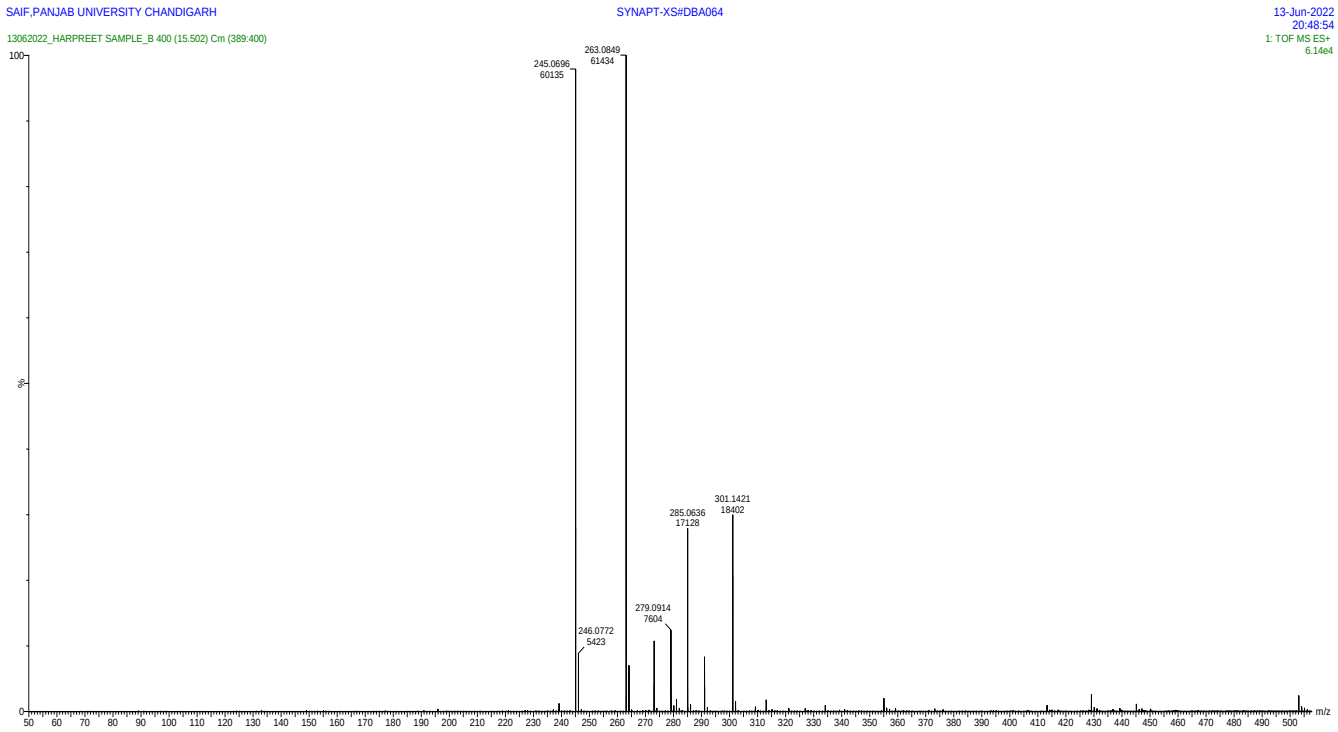

Fig.4.16. The LC-MS spectrum of initial ciprofloxacin solution after degradation.

Fig.4.17 shows the proposed degradation route of CIP via three possible pathways based on the intermediates found in the LC-MS spectrum. The $O_2^{\cdot-}$, OḢ, and h^+ radicals were liable to attack the piperazine and the quinoline rings in the CIP molecules. In the first pathway, the quinoline ring underwent a hydroxylation reaction by the attack of OḢ radicals. The OḢ radicals attacked the C2 atom and generated P1 (m/z = 348). Further, the piperazine ring got attacked by $O_2^{\cdot-}$ and OḢ radicals, while the fluorine atom remained attached and formed the product P2 (m/z = 279) [35].

In the second pathway, P3 (m/z = 362) was generated by the cracking of the piperazine ring and oxidation of the secondary amine group with the formation of two aldehyde groups, which then underwent decarboxylation to produce P4 (m/z = 334). The formaldehyde group was lost by the attack of h^+ and produced P5 (m/z = 306), which further underwent hydroxylation and generated P6 (m/z = 291). Further, loss of carbonyl group produced P7 (m/z = 263) [36, 37].

In the third pathway, the OḢ attacked the piperazine ring and produced P8 (m/z = 305) which further got converted into P9 (m/z = 278) via the process of hydroxylation and loss of the CH-NH_2 group. The P9 then underwent demethylation and generated P10 (m/z = 263) which further defluorinated to produce P11 (m/z = 245) [37, 38]. Hence, CIP molecules and the generated intermediated products would further be degraded into CO_2, H_2O, and other smaller intermediates.

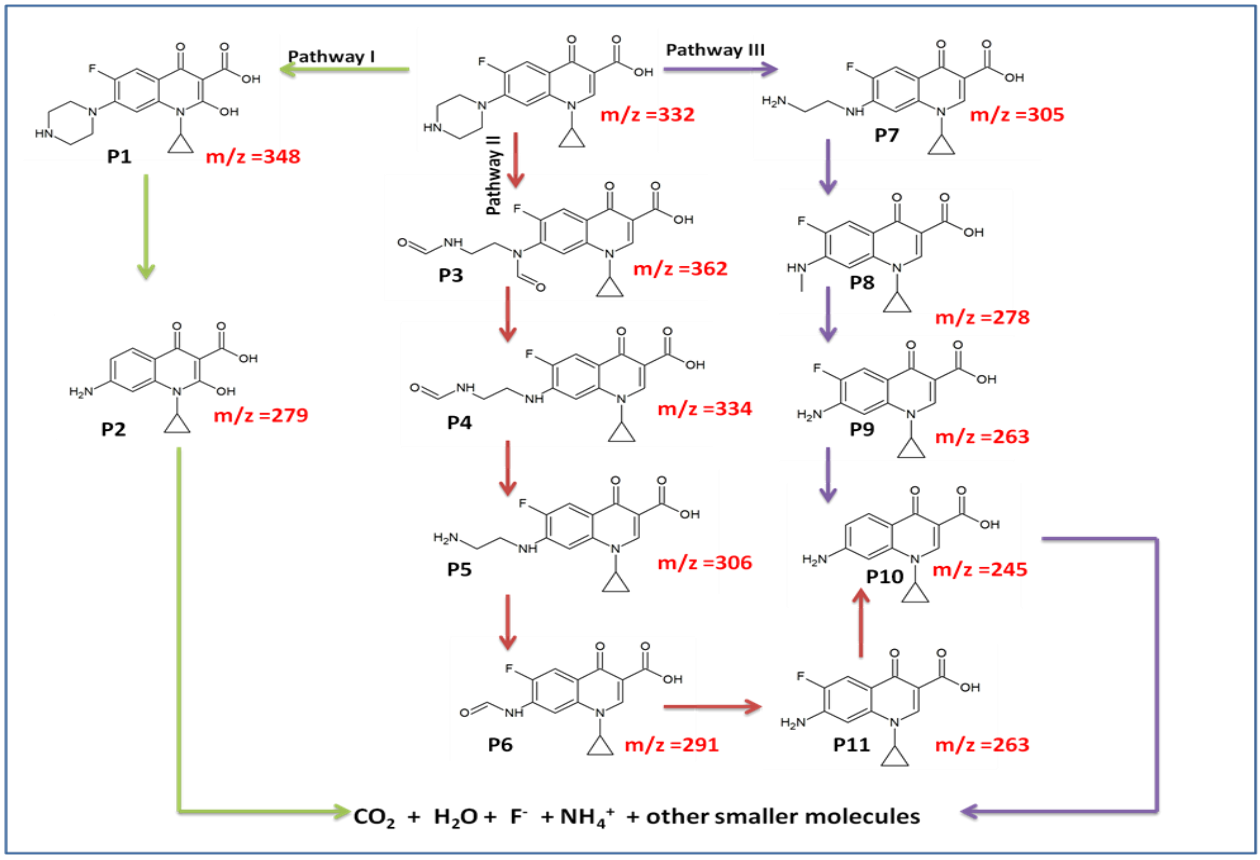

Fig.4.17. The possible degradation pathways of CIP degradation with 1Ag@10CN-LDH photocatalytic heterojunction.

4.4. Proposed photocatalytic mechanism:

To assess the band structures of LDH and CN, valence band XPS analysis was conducted. The

valence band potentials of bare LDH and CN, as depicted in Fig. 4.18, were determined to be +1.48 eV and +1.43 eV, respectively.

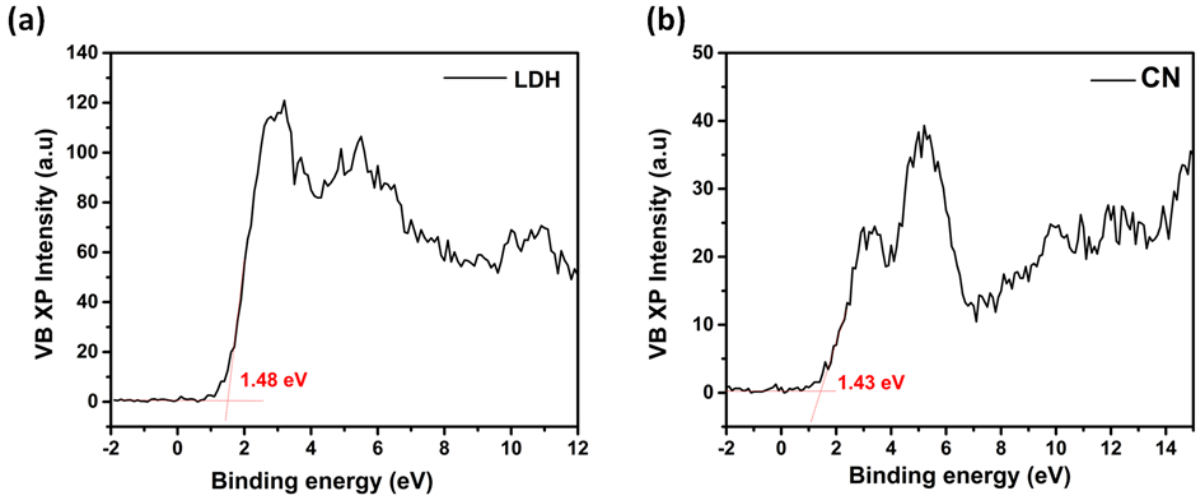

Fig.4.18. Valence band XPS spectra of Co-Al LDH (a) and CN (b).

The conduction band edge potential of the respective catalyst was calculated by the equation:

$E_{CB} = E_{VB} - E_g$ …….. (4.5)

Based on the band gap energy values i.e. 2.08 eV for LDH and 2.71 eV for CN, the conduction band edge potentials were determined as -0.6 eV and -1.28 eV of LDH and CN, respectively. As can be seen, the valence band potential of LDH is higher than that of CN, while the conduction band potential of CN is more negative than that of LDH. Consequently, the band potentials of LDH and CN composite were liable for the migration of electron and holes in the CN-LDH hybrid framework. Based on the above discussion, a possible mechanism for charge transfer and degradation of ciprofloxacin over ternary Ag@CN-LDH heterostructure under LED irradiations was proposed and schematically illustrated in **Scheme-4.2.**

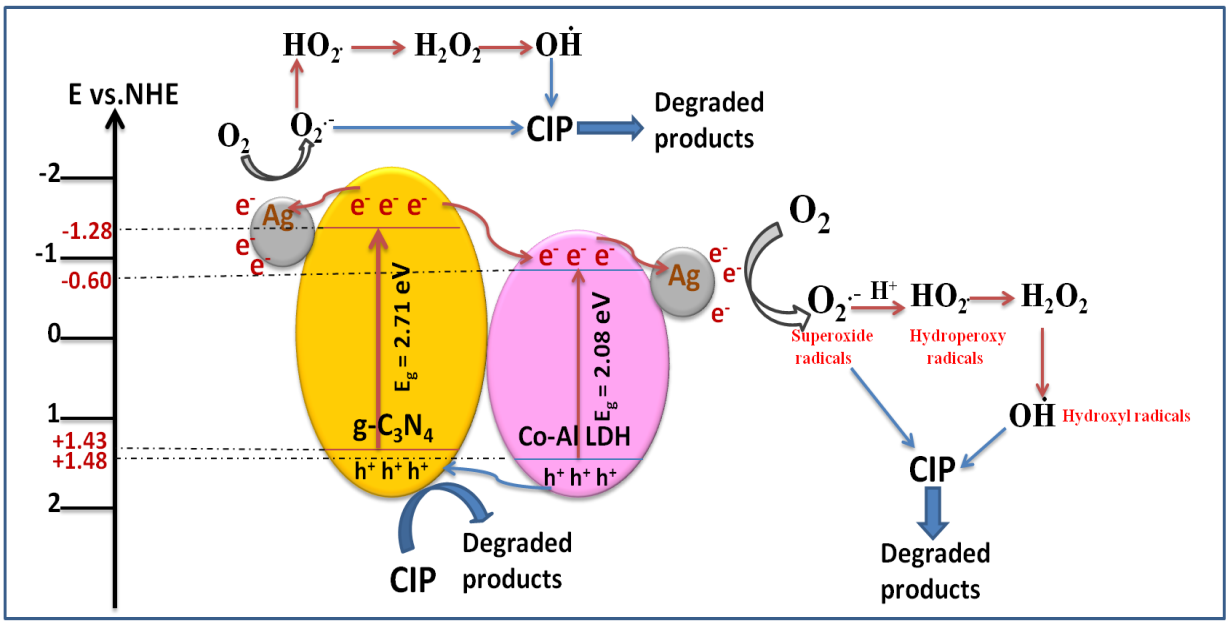

Scheme.4.2. A schematic illustration of charge transfer and separation in Ag@CN-LDH composite towards the degradation of CIP under light illumination.

When the ternary Ag@CN-LDH composite was illuminated to LED radiations, both the LDH and CN components got excited and generated electron and holes in conduction and valence band, respectively. pairs. As the conduction band edge potential of CN lied above that of LDH, the electrons from CN were easily migrated to the LDH. On the other hand, the valence band edge potential of LDH lied below that of CN, the holes from LDH were quickly transferred to CN. The appropriate band potentials of LDH and CN compelled an efficient migration and restricted the rejoining of electron-hole pairs across the CN-LDH heterojunction. This process resulted in the accumulation of electrons at LDH and holes at CN. Thusly, the electrons collected at LDH were caught by the Ag NPs attributable to the great electron-catching capacity of metallic Ag [25]. In addition, a portion of electrons at CN was directly caught by the Ag nanoparticles. In this manner, the loading of Ag nanoparticles further upgraded the separation efficiency of photogenerated electron-hole pairs.

Consequently, the electrons captured by Ag NPs reacted with dissolved oxygen (O_2) to produce

superoxide anion radicals ($O_2^{\cdot-}$) ($E_{O2}/E_{O2.-}$ = -0.046 eV). A few of the superoxide anion radicals reacted with H_2O to generate hydroxyl radicals and some of them directly attacked the CIP molecules in an aqueous solution to oxidize and degrade CIP into smaller molecules. Moreover, the potential of $H_2O/O\dot{H}$ ($E_{H2O}/E_{O\dot{H}}$ = +2.68 eV) was more positive than the CB potential of both the CN and LDH, therefore holes (h^+) oxidize water molecules to generate $O\dot{H}$ radicals [25]. Therefore, the photogenerated holes directly oxidized the CIP molecules in aqueous solution. Hence, the CIP molecules were degraded into mineralized products by the action of $O_2^{\cdot-}$, $O\dot{H}$, and h^+ radicals. The overall photocatalytic process involved in the degradation of CIP was as follows:

$$Ag@CN\text{-}LDH + h\nu \longrightarrow e^- + h^+$$

$$O_2 + e^- \longrightarrow O_2^{\cdot-}$$

$$O_2^{\cdot-} + CIP \longrightarrow degraded\ products$$

$$O_2^{\cdot-} + H^+ \longrightarrow HO_2^{\cdot}$$

$$2HO_2^{\cdot} \longrightarrow O_2 + H_2O_2$$

$$H_2O_2 + e^- \longrightarrow OH^- + O\dot{H}$$

$$O\dot{H} + CIP \longrightarrow degraded\ products$$

$$h^+ + CIP \longrightarrow \text{degraded products}$$

4.5. Conclusion:

In summary, the loading of CN and Ag was found to be decisive for the improvement of LDH's photocatalytic properties towards the degradation of ciprofloxacin. In this work, the heterojunction composed of Co-Al LDH and different wt% (5-15) CN loadings was fabricated. The 10CN-LDH showed a maximum of 72.5% degradation activity among different CN-LDH composites. Further, (0.5-2 wt%) Ag NPs were deposited over 10CN-LDH composite through

photochemical reduction and 1Ag@10CN-LDH was optimized which showed the highest 97% degradation rate. As proposed, the interfacial interactions and charge transfer between LDH, CN, and Ag altered several physicochemical and structural properties like UV-visible absorption, fluorescence, surface area, and increased active sites. Scavenging experiments confirmed the role of superoxide radical anions as the main active species, whereas h^+ and $O\dot{H}$ also played significant roles in the degradation process. Moreover, the Ag@CN-LDH composite was highly stable, even after five recyclable runs. The LC-MS analysis revealed the degradation of ciprofloxacin molecules into smaller products which further decomposed into CO_2, H_2O, and other smaller molecules.

References

[1] M. Li, J. Zhang, L. Wang, X. Cheng, X. Gao, Y. Wang, G. Zhang, Y. Qi, H. Zhai, R. Guan, Z. Zhao, Direct Z-Scheme Oxygen-vacancy-rich TiO_2/Ta_3N_5 heterojunction for degradation of ciprofloxacin under visible light: Degradation pathways and mechanism insight, Appl. Surf. Sci. 583 (2022) 152516. https://doi.org/10.1016/j.apsusc.2022.152516.

[2] M. Shi, W. Li, Q. Wang, H. Xu, Y. Zhao, G. He, Q. Meng, H. Chen, One-step hydrothermal synthesis of $BiVO_4/TiO_2$/RGO composite with effective photocatalytic performance for the degradation of ciprofloxacin, Opt. Mater. (Amst). 122 (2021) 111726. https://doi.org/10.1016/j.optmat.2021.111726.

[3] T.J. Al-Musawi, N. Mengelizadeh, K. Sathishkumar, S. Mohebi, D. Balarak, Preparation of $CuFe_2O_4$/montmorillonite nanocomposite and explaining its performance in the sonophotocatalytic degradation process for ciprofloxacin, Colloids Interface Sci. Commun. 45 (2021) 100532. https://doi.org/10.1016/j.colcom.2021.100532.

[4] H. Kaur, S. Singh, B. Pal, A brief review on modified layered double hydroxides for H_2

production through photoinduced H_2O splitting, Environ. Nanotechnology, Monit. Manag. 16 (2021) 100451. https://doi.org/10.1016/j.enmm.2021.100451.

[5] M. Daud, A. Hai, F. Banat, M.B. Wazir, M. Habib, G. Bharath, M.A. Al-Harthi, A review on the recent advances, challenges and future aspect of layered double hydroxides (LDH)–Containing hybrids as promising adsorbents for dyes removal, J. Mol. Liq. 288 (2019) 110989. https://doi.org/10.1016/j.molliq.2019.110989.

[6] C. Prasad, H. Tang, Q.Q. Liu, S. Zulfiqar, S. Shah, I. Bahadur, An overview of semiconductors/layered double hydroxides composites: Properties, synthesis, photocatalytic and photoelectrochemical applications, J. Mol. Liq. 289 (2019) 111114. https://doi.org/10.1016/j.molliq.2019.111114.

[7] S. Das, K. Parida, Superior photocatalytic performance of Co-Al LDH in the race of metal incorporated LDH: A comparison study, Mater. Today Proc. 35 (2021) 275–280. https://doi.org/10.1016/j.matpr.2020.05.759.

[8] Y. Zhang, J. Yuan, Y. Ding, B. Liu, L. Zhao, S. Zhang, Research progress on g–C_3N_4–based photocatalysts for organic pollutants degradation in wastewater: From exciton and carrier perspectives, Ceram. Int. 47 (2021) 31005–31030. https://doi.org/10.1016/j.ceramint.2021.08.063.

[9] H. Kaur, S. Singh, B. Pal, Impact of g-C_3N_4 loading on NiCo LDH for adsorptive removal of anionic and cationic organic pollutants from aqueous solution, Korean J. Chem. Eng. 38 (2021) 1248–1259. https://doi.org/10.1007/s11814-021-0784-6.

[10] S. Tonda, W.K. Jo, Plasmonic Ag nanoparticles decorated NiAl-layered double hydroxide/graphitic carbon nitride nanocomposites for efficient visible-light-driven photocatalytic removal of aqueous organic pollutants, Catal. Today. 315 (2018) 213–222.

https://doi.org/10.1016/j.cattod.2017.12.019.

[11] A. K. Chawla, S. Singhal, S. Nagar, H. O. Gupta, Study of composition dependent structural, optical, and magnetic properties of Cu-doped $Zn_{1-x}Cd_xS$ nanoparticles, J. Appl. Phys. 108 (2010) 123519. https://doi.org/10.1063/1.3524516

[12] S. Megala, M. Sathish, S. Harish, M. Navaneethan, S. Sohila, B. Liang, R. Ramesh, Enhancement of photocatalytic H_2 evolution from water splitting by construction of two dimensional g-C_3N_4/NiAl layered double hydroxides, Appl. Surf. Sci. 509 (2020) 144656. https://doi.org/10.1016/j.apsusc.2019.144656.

[13] G. Di, Z. Zhu, Q. Huang, H. Zhang, J. Zhu, Y. Qiu, D. Yin, J. Zhao, Targeted modulation of g-C_3N_4 photocatalytic performance for pharmaceutical pollutants in water using ZnFe-LDH derived mixed metal oxides: Structure-activity and mechanism, Sci. Total Environ. 650 (2019) 1112–1121. https://doi.org/10.1016/j.scitotenv.2018.09.134.

[14] D. Sun, D. Chi, Z. Yang, Z. Xing, J. Yin, Z. Li, Q. Zhu, W. Zhou, Mesoporous g-C_3N_4/Zn–Ti LDH laminated van der Waals heterojunction nanosheets as remarkable visible-light-driven photocatalysts, Int. J. Hydrogen Energy. 44 (2019) 16348–16358. https://doi.org/10.1016/j.ijhydene.2019.04.275.

[15] D. Gilea, T. Radu, M. Muresanu, G. Carja, Plasmonic photocatalysts based on silver nanoparticles – layered double hydroxides for efficient removal of toxic compounds using solar light, Appl. Surf. Sci. 444 (2018) 407–413. https://doi.org/10.1016/j.apsusc.2018.03.054.

[16] X. Li, Z. Yu, L. Shao, H. Zeng, Y. Liu, X. Feng, A novel strategy to construct a visible-light-driven Z-scheme (ZnAl-LDH with active phase/g-C_3N_4) heterojunction catalyst via polydopamine bridge (a similar “bridge” structure), J. Hazard. Mater. 386 (2020) 121650.

https://doi.org/10.1016/j.jhazmat.2019.121650.

[17] H. Zeng, H. Zhang, L. Deng, Z. Shi, Peroxymonosulfate-assisted photocatalytic degradation of sulfadiazine using self-assembled multi-layered CoAl-LDH/g-C_3N_4 heterostructures: Performance, mechanism and eco-toxicity evaluation, J. Water Process Eng. 33 (2020) 101084. https://doi.org/10.1016/j.jwpe.2019.101084.

[18] S. Nayak, L. Mohapatra, K. Parida, Visible light-driven novel g-C_3N_4/NiFe-LDH composite photocatalyst with enhanced photocatalytic activity towards water oxidation and reduction reaction, J. Mater. Chem. A. 3 (2015) 18622–18635. https://doi.org/10.1039/c5ta05002b.

[19] W.K. Jo, S. Kumar, S. Tonda, N-doped C dot/CoAl-layered double hydroxide/g-C_3N_4 hybrid composites for efficient and selective solar-driven conversion of CO_2 into CH_4, Compos. Part B Eng. 176 (2019) 107212. https://doi.org/10.1016/j.compositesb.2019.107212.

[20] S. Das, S. Patnaik, K.M. Parida, Fabrication of a Au-loaded $CaFe_2O_4$/CoAl LDH p-n junction based architecture with stoichiometric H_2 & O_2 generation and Cr(vi) reduction under visible light, Inorg. Chem. Front. 6 (2019) 94–109. https://doi.org/10.1039/c8qi00952j.

[21] C. Chen, H. Zeng, J. Xiong, S. Xu, D. An, Z-scheme AgBr@Ag/CoAl layered double hydroxide heterojunction for superior photocatalytic Cr(VI) reduction under visible light, Appl. Clay Sci. 192 (2020) 105627. https://doi.org/10.1016/j.clay.2020.105627.

[22] A. Kumaresan, S. Yang, K. Zhao, N. Ahmad, J. Zhou, Z. Zheng, Y. Zhang, Y. Gao, H. Zhou, Z. Tang, Facile development of CoAl-LDHs/RGO nanocomposites as photocatalysts for efficient hydrogen generation from water splitting under visible-light

irradiation, Inorg. Chem. Front. 6 (2019) 1753–1760. https://doi.org/10.1039/c9qi00307j.

[23] X. Huang, X. Xu, R. Yang, X. Fu, Synergetic adsorption and photocatalysis performance of g-C_3N_4/Ce-doped MgAl-LDH in degradation of organic dye under LED visible light, Colloids Surfaces A Physicochem. Eng. Asp. 643 (2022) 128738. https://doi.org/10.1016/j.colsurfa.2022.128738.

[24] C. Peng, W. Wang, W. Zhang, Y. Liang, L. Zhuo, Surface plasmon-driven photoelectrochemical water splitting of TiO_2 nanowires decorated with Ag nanoparticles under visible light illumination, Appl. Surf. Sci. 420 (2017) 286–295. https://doi.org/10.1016/j.apsusc.2017.05.101.

[25] T. Wang, X. Liu, C. Ma, Y. Liu, H. Dong, W. Ma, 3D Ag/NiCo-layered double hydroxide with adsorptive and photocatalytic performance, J. Taiwan Inst. Chem. Eng. 0 (2018) 1–8. https://doi.org/10.1016/j.jtice.2018.07.031.

[26] X. Li, J. Xue, S. Ma, P. Xu, C. Huang, M. Wang, Synthesis of MgAl LDH/Acidified g-C_3N_4 Heterojunction Photocatalyst for Improved Tetracycline Hydrochloride Degradation Activity, Nano. 14 (2019) 1–13. https://doi.org/10.1142/S1793292019500668.

[27] D.R. Das, P. Kalita, A. K. Talukdar, Ti/Cr incorporated mesoporous MCM-48 for oxidation of styrene to benzaldehyde, J. Porous Mater. 27 (2020) 893-903. https://doi.org/10.1007/s10934-020-00868-2.

[28] K.S.W. Sing, R.T. Williams, Physisorption hysteresis loops and the characterization of nanoporous materials, Adsorpt. Sci. Technol. 22 (2004) 773–782. https://doi.org/10.1260/0263617053499032.

[29] R.A. Rather, S. Singh, B. Pal, A C_3N_4 surface passivated highly photoactive Au-TiO_2 tubular nanostructure for the efficient H_2 production from water under sunlight irradiation,

Appl. Catal. B Environ. 213 (2017) 9–17. https://doi.org/10.1016/j.apcatb.2017.05.002.

[30] W.K. Jo, Y.G. Kim, S. Tonda, Hierarchical flower-like NiAl-layered double hydroxide microspheres encapsulated with black Cu-doped TiO_2 nanoparticles: Highly efficient visible-light-driven composite photocatalysts for environmental remediation, J. Hazard. Mater. 357 (2018) 19–29. https://doi.org/10.1016/j.jhazmat.2018.05.038.

[31] M.S. Nasir, G. Yang, I. Ayub, S. Wang, L. Wang, X. Wang, W. Yan, S. Peng, S. Ramakarishna, Recent development in graphitic carbon nitride based photocatalysis for hydrogen generation, Appl. Catal. B Environ. 257 (2019) 117855. https://doi.org/10.1016/j.apcatb.2019.117855.

[32] Y. Zhang, T. Wang, M. Zhou, Y. Wang, Z. Zhang, Hydrothermal preparation of Ag-TiO_2 nanostructures with exposed {001}/{101} facets for enhancing visible light photocatalytic activity, Ceram. Int. 43 (2017) 3118–3126. https://doi.org/10.1016/j.ceramint.2016.11.127.

[33] C. Rudolf, B. Dragoi, A. Ungureanu, A. Chirieac, S. Royer, A. Nastro, E. Dumitriu, NiAl and CoAl materials derived from takovite-like LDHs and related structures as efficient chemoselective hydrogenation catalysts, Catal. Sci. Technol. 4 (2014) 179–189. https://doi.org/10.1039/c3cy00611e.

[34] M.K. Aulakh, B. Pal, Journal of Industrial and Engineering Chemistry Tuning the band energetics of size dependent titania nanostructures for improved photo-reductive effi ciency of aromatic aldehydes, J. Ind. Eng. Chem. 80 (2019) 325–334. https://doi.org/10.1016/j.jiec.2019.08.011.

[35] H. Liang, M. Yu, J. Guo, R. Zhan, J. Chen, D. Li, A novel vacancy-strengthened Z-scheme g-C_3N/Bp/MoS_2 composite for super-efficient visible-light photocatalytic

degradation of ciprofloxacin, Sep. Purif. Technol. 272 (2021) 118891. https://doi.org/10.1016/j.seppur.2021.118891.

[36] A. V Karim, A. Shriwastav, Degradation of cipro fl oxacin using photo, sono, and sonophotocatalytic oxidation with visible light and low-frequency ultrasound : Degradation kinetics and pathways, Chem. Eng. J. 392 (2020) 124853. https://doi.org/10.1016/j.cej.2020.124853.

[37] B. Gupta, A. Kumar, Photocatalytic performance of 3D engineered chitosan hydrogels embedded with sulfur-doped C_3N_4/ZnO nanoparticles for Ciprofloxacin removal : Degradation and mechanistic pathways, Int. J. Biol. Macromol. 198 (2022) 87–100. https://doi.org/10.1016/j.ijbiomac.2021.12.120.

[38] Y. Huang, L. Nengzi, X. Zhang, J. Gou, Y. Gao, G. Zhu, Catalytic degradation of ciprofloxacin by magnetic CuS/Fe_2O_3/Mn_2O_3 nanocomposite activated peroxymonosulfate : Influence factors, degradation pathways and reaction mechanism, 388 (2020). https://doi.org/10.1016/j.cej.2020.124274.

CHAPTER- 5

Fabrication of g-C_3N_4 coupled Mg-Al LDH binary heterojunction photocatalyst with boosted photocatalytic degradation of doxycycline under LED light

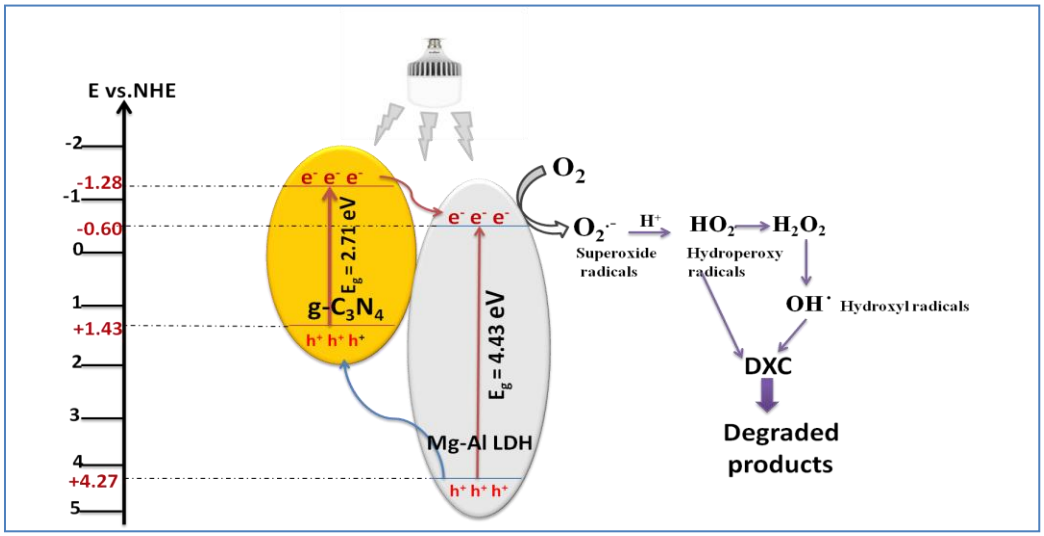

Schematic outline:

Mg-Al LDH, a UV-active photocatalyst possess band gap energy values greater than 3 eV. The coupling of Mg-Al LDH with visible active g-C_3N_4 (CN) came out as an effective strategy to improve its light absorbance response in the visible region, inhibit the rejoining of charge carriers, and enhance its specific surface area.

5.1. Introduction:

Doxycycline (DXC), a broad-spectrum antibiotic, is frequently used to cure infections in animals and humans that are caused by a variety of Gram-positive and Gram-negative bacteria. However, antibiotic resistance and water pollution occur when DXC is released into the natural environment without proper treatment [1-2]. To remove these harmful pollutants from the environment, it is, therefore, necessary to develop a technology that is both highly effective and safe. Various decontamination strategies like adsorption, coagulation, photocatalysis, biodegradation, and so on are being widely used worldwide. Among them, photocatalysis, an environment friendly technique with high degradation efficiency is an effective approach for water remediation [3-4].

Recently, layered double hydroxides, the 2D mesoporous inorganic materials are gaining much attention in the field of photocatalysis. Mg-Al LDH is a highly stable, durable, economical, and non-toxic photocatalyst. But, its light-absorbing properties are restricted in the UV region only due to wide band gap [5-6]. Researchers are currently very interested in a photocatalyst that absorbs light in the visible range. The formation of heterojunction via coupling of LDH with other semiconducting materials is becoming a powerful phenomenon which results in a stronger and wider visible light response, a greater number of reactive sites, increased lifetime and rapid transfer of charge carriers, and efficient charge separation.

Recently, graphitic carbon nitride (CN), a 2D organic polymer is a visible active semiconductor (E_g ~ 2.7 eV) [7]. Both Mg-Al LDH and g-C_3N_4 are two-dimensional materials; therefore, charge carriers' separation efficiency at their interface can be effectively improved by the 2D-2D electron channel. Moreover, the oppositely charged surface of LDH and CN permits them to incorporate through electrostatic interactions [8]. The present work aims to improve the

photoactivity of Mg-Al LDH via the formation of a heterojunction with g-C_3N_4. A series of CN-coupled LDH composites were fabricated via an in-situ hydrothermal approach with a varying weight percentage of CN (10 to 30 wt%). The photoactivity of prepared catalysts was determined towards degradation of doxycycline under LED light ($\lambda > 360$ nm). The as-prepared catalysts were characterized through various techniques to investigate the impact of CN coupling on the surface, structural, and electronic properties of LDH. The CN-LDH composites exhibited better adsorption and degradation efficiency than bare Mg-Al LDH due to enhanced specific surface area, increased reactive sites, and inhibited recombination of photoinduced charge carriers.

5.2. Experimental Section:

5.2.1. Chemical and Reagents:

Magnesium nitrate hexahydrate ($Mg(NO_3)_2.6H_2O$), aluminiun nitrate nonahydrate ($Al(NO_3)_2.9H_2O$), urea (CH_4N_2O), melamine ($C_3H_6N_6$) were purchased from Loba chemie, India. Ammonium fluoride (NH_4F) was obtained from Sigma Aldrich. Ethanol, iso-propanol and methanol were received from SD fine Ltd. Triple deionized water was obtained from Organo Biotech Laboratories Pvt. Ltd.

5.2.2. Synthesis of Mg-Al LDH:

The synthesis of Mg-Al LDH is described in section **3.2.2**.

5.2.2. Synthesis of g-C_3N_4 nanosheets:

The synthesis of g-C_3N_4 nanosheets is described in section **2.2.3**.

5.2.3. Preparation of CN-LDH composites:

The CN-LDH composites were prepared via one-step in situ hydrothermal method. First, an appropriate amount of CN (10. 20, and 30 wt%) was dispersed in 25 ml of dionized water using a sonicator for 60 minutes. On the other side, $Mg(NO_3)_2.6H_2O$ (8 mmol), $Al(NO_3)_2.9H_2O$ (4

mmol) were added into a mixed dispersant of ethylene glycol (45 ml) and water (5ml) and stirred for about 30 minutes at room temperature. Then, the metallic solution was dropwise added to the CN suspension and stirred for an hour for the electrostatic assembly of metal ions through CN. After that, 60 mmol of urea was added to the above mixture and allowed to dissolve completely. The obtained mixture was transferred into a Teflon-lined stainless steel autoclave, sealed, and heated at 160^{o}C for 6 hours. After cooling to room temperature naturally, the formed CN-LDH nanocomposites were collected and washed with distilled water and ethanol a few times. The as-prepared nanocomposites were kept at 100^{o}C for 12 hours for drying. The different 10, 20, and 30 wt% CN coupled with LDH composites were prepared and abbreviated as 10CN-LDH, 20CN-LDH, and 30CN-LDH.

5.2.4. Photocatalytic activity:

The photoactivity of LDH and CN-LDH composites were investigated using doxycycline (DXC) as a model toxic pollutant. A set of test tubes, each test tube with 10 ml of DXC solution (100 ppm) and 5 mg of the catalyst were prepared and stirred in the dark conditions for half an hour. The photo degradation experiments were then carried out by irradiating each test tube with LED light (Wipro Garnet B22 50-watt LED bulb (Cool daylight, white) (λ > 360 nm)) at predetermined intervals of time (10, 20, 30, 40, 50, and 60 min) while continuously stirring. Each test tube's aqueous sample was centrifuged to separate the catalyst after it had been exposed to light for a predetermined amount of time. To determine the remaining concentration of the pollutant, a Shimadzu-2600 UV-visible spectrophotometer was used to analyze the supernatant.

Using a trapping experiment similar to the one described above and the addition of various scavenging agents to the reaction mixture, the function of reactive species was demonstrated. The catalyst's reusability and stability were also evaluated.

5.3. Results and discussion:

5.3.1. Crystallographic and structural studies:

The XRD analysis of CN, Mg-Al LDH and various CN-LDH composites is depicted in **Fig.5.1** (left). The peak at $2\theta = 27.5^{o}$ found in the spectrum of CN ascribed to the (002) crystal plane of pure CN [9].The diffraction peaks corresponding to the planes (003), (006), (012), (015), (018), (0015), and (113) observed in the spectra of bare LDH as well as different CN-LDH composites were indexed to the pure crystal phase of Mg-Al LDH [10]. In the pattern of CN-LDH composites, an extra peak related to CN was emerged at $2\theta = 27.5^{o}$. The intensity of the CN peak gradually increased with an increase in weight percentages of CN confirming the presence and successful coupling of CN with LDH in CN-LDH composites.

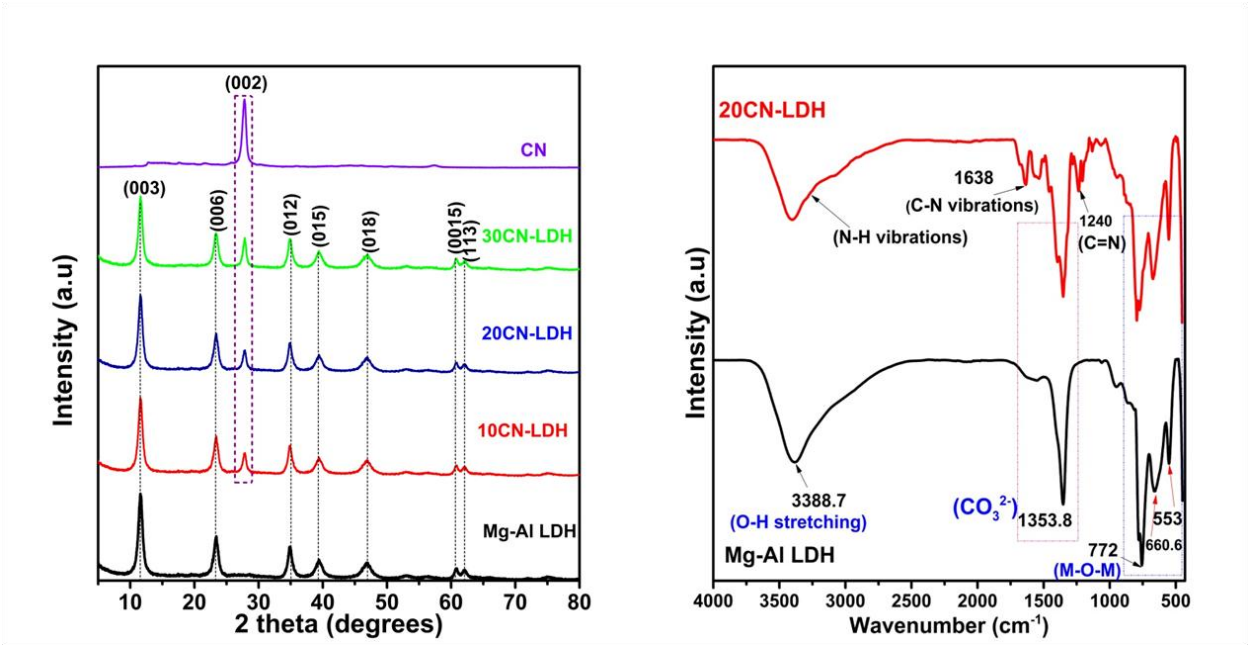

Fig.5.1. XRD diffraction patterns of Mg-Al LDH, CN, and CN-LDH composites (left) and FTIR spectra of Mg-Al LDH and 20CN-LDH composite (right).

Fig.5.1 (right) shows the FTIR spectra of Mg-Al LDH and 20CN-LDH composites. The broadband appeared around 3388 cm^{-1} ascribed to the stretching vibrations of O-H groups and

water molecules in LDH framework. An intense peak at 1353.8 cm^{-1} accredited to the carbonate anions intercalated in the interlayer region. The other peaks below 800 cm^{-1} were due to stretching vibrations of M-O and M-O-M linkages (M represents Mg and Al [11-12]. Due to the vibration modes of the uncondensed amino group N-H bonds, there was an additional peak in the 20CN-LDH composite's spectrum at approximately 3300 cm^{-1}. The C-N and C=N vibrational modes were attributed to the peak at 1638 cm^{-1} and 1240 cm^{-1}, respectively [13-14]. The characteristic peaks corresponding to CN were present in the 20CN-LDH composite confirming the successful formation of a heterostructure comprising CN and LDH.

In addition, X-ray photoelectron spectroscopy was used to ascertain the chemical species' compositions and oxidation states in the Mg-Al LDH and 20CN-LDH composites (**Fig.5.2**). The peaks associated with Mg, Al, C, and O elements related to LDH and C and N elements related CN were observed in their corresponding survey spectra. The successful coupling of CN and LDH during the formation of heterostructures was demonstrated by the peaks of Mg, Al, C, O, C, and N elements in the survey spectrum of the 20CN-LDH composite.

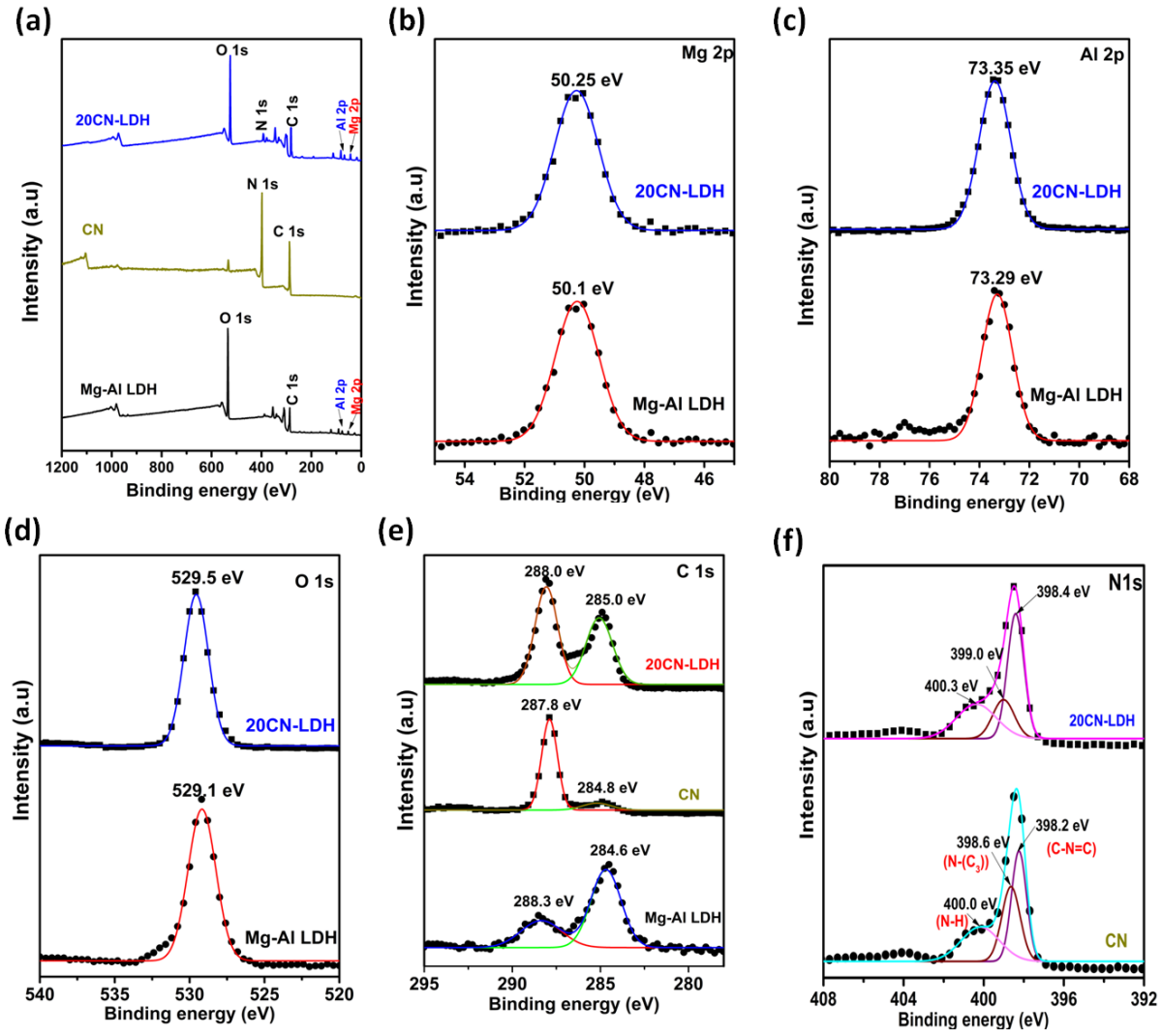

Fig.5.2. XPS spectra of the Mg-Al LDH, CN, and 20CN-LDH composite; Survey spectra (a) Mg 2p (b), Al 2p (c), O 1s (d), C 1s (e), and N 1s (f).

The Mg 2p spectrum of bare Mg-Al LDH exhibited a peak at 50.1 eV attributed to the presence of $Mg(OH)_2$ groups in the LDH framework. The binding energy peak at 73.29 eV confirmed the existence of $Al(OH)_3$ groups in brucite-like layers of LDH [6]. A peak originated at a position of 529.1 eV corresponds to the hydroxyl groups of brucite-like layers in LDH [15]. The slight shift observed in peak positions of elements in CN-LDH than that of bare LDH credited to the strong interactions between CN and LDH. The carbonate anions intercalated in the interlayer region

were identified by the deconvolution of the LDH C 1s spectrum into two peaks at 284.6 eV and 288.3 eV [16]. Two peaks at 284.8 eV and 287.8 eV in the C 1s spectrum of CN are attributed, respectively, to pure graphitic carbon units and sp^2 hybridized C-atoms in tri-s-triazine rings (N-C=N) [17]. The formation of C-N bonds in the CN-LDH composite was indicated by the rise in peak height at 288.0 eV in the CN-LDH spectrum. The sp^2 hybridized N atom in C-N=C coordination, bridged tertiary N atoms in N-C_3 coordination, and N-H groups in tri-s-triazine rings were all represented by three peaks in the N 1s spectrum of CN at 398.2 eV, 398.6 eV, and 400.0 eV, respectively [18]. In 20CN-LDH spectrum, the peaks in the N 1s spectrum shifted to higher binding energies relative to CN, credited to the electronic and chemical interactions between CN and LDH.

5.3.2. Surface and morphological studies:

The morphology and elemental composition of prepared photocatalysts were analysed using FESEM-EDS. **Fig.3.2 (A and B)** and **Fig. 5.3 (A and B)** shows the FESEM and the EDS spectrum of Mg-Al LDH and 20CN-LDH composite, respectively. The FESEM image of 20CN-LDH composites showed that micro-flowers of Mg-Al LDH were missing in CN-LDH composite. This distorted morphology attributed to the stacking of CN sheets with LDH brucite like layers due to strong electrostatic interactions. The EDS spectrum confirmed the presence of Mg, Al, C, O, and N elements in CN-LDH composites.

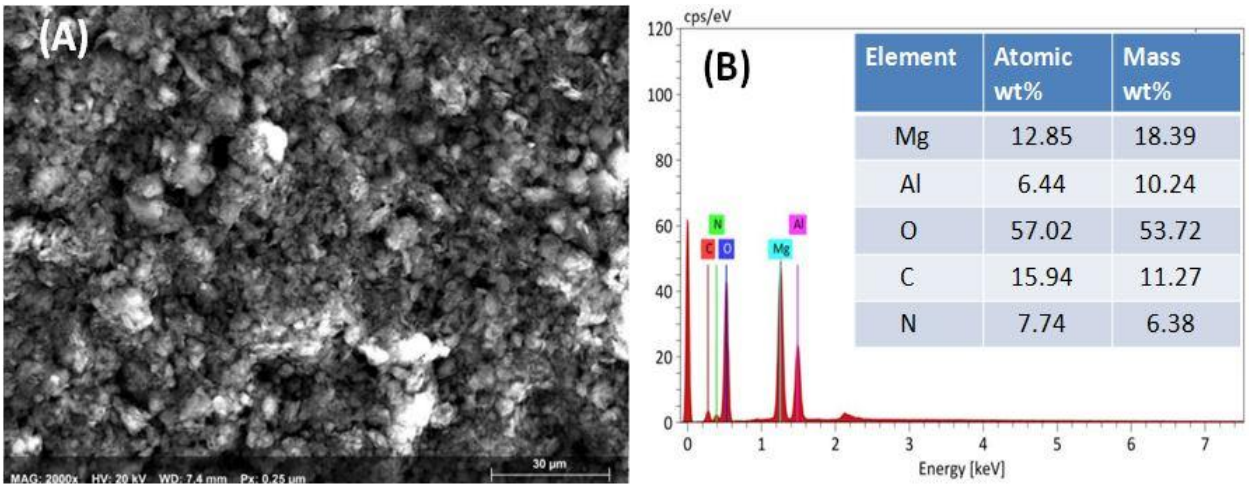

Fig.5.3. FESEM image (A) and EDS pattern with elemental compositon (B) of 20CN-LDH composite.

As shown in **Fig.5.4,** the nitrogen based isotherms of Mg-Al LDH and 20CN-LDH were of a type IV with a typical H3 hysteresis loop indicating their mesoporous nature. The specific surface area of bare LDH was found to be 57.0 m^2/g, which increased to 62.43 m^2/g after coupling with 20wt% of CN. The large surface area promoted the adsorption and degradation of pollutant by providing more active sites at the surface of catalyst. The values of the specific surface area, pore volume, and pore diameter are mentioned in **Table-5.1**.

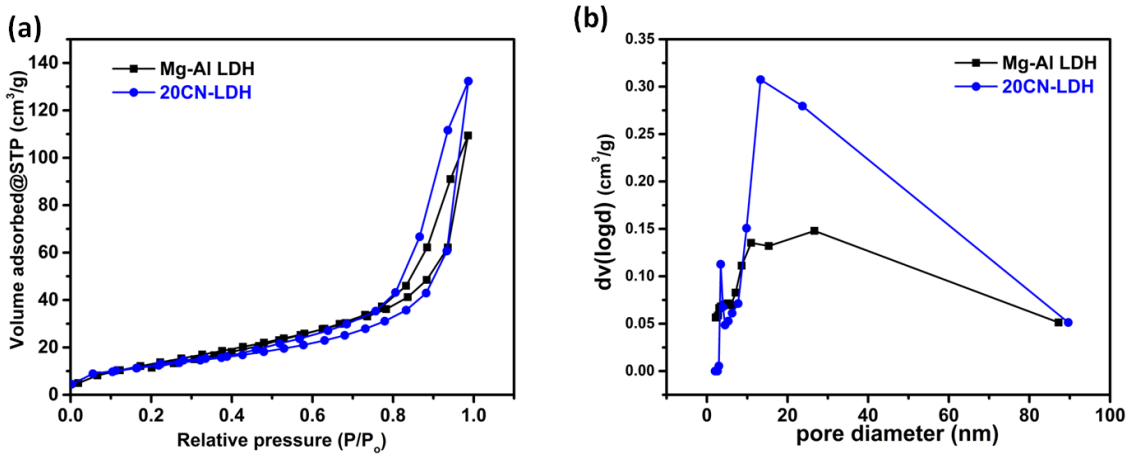

Fig.5.4. The N_2 adsorption-desorption curves (a) and pore size distribution curves (b) of bare

Mg-Al LDH and 20CN-LDH composite.

Table-5.1. BET specific surface area analysis of LDH and 20CN-LDH composite.

S.No.	Sample	Specific Surface area (m^2/g)	Pore volume (cc/g)	Pore diameter (nm)
1.	Mg-Al LDH	57.0	0.159	4.490
2.	20CN-LDH	62.43	0.214	3.412

5.3.3. Optical studies:

The optical absorbance of Mg-Al LDH, CN, and different CN-LDH composites was evaluated using diffuse reflectance spectroscopy. As shown in **Fig.5.5 (a)**, the bare LDH showed almost negligible response to visible light. The pure CN showed an intense peak at 380 nm in UV region with absorption edge at 470 nm. In the case of CN-LDH composites, the absorbance in the visible region enhanced after coupling LDH with CN and a peak emerged at 380 nm corresponding to the presence of CN in the composites. Moreover, the intensity of absorbance spectra in CN-LDH composites continuously increased with an increase in the weight percentage of CN.

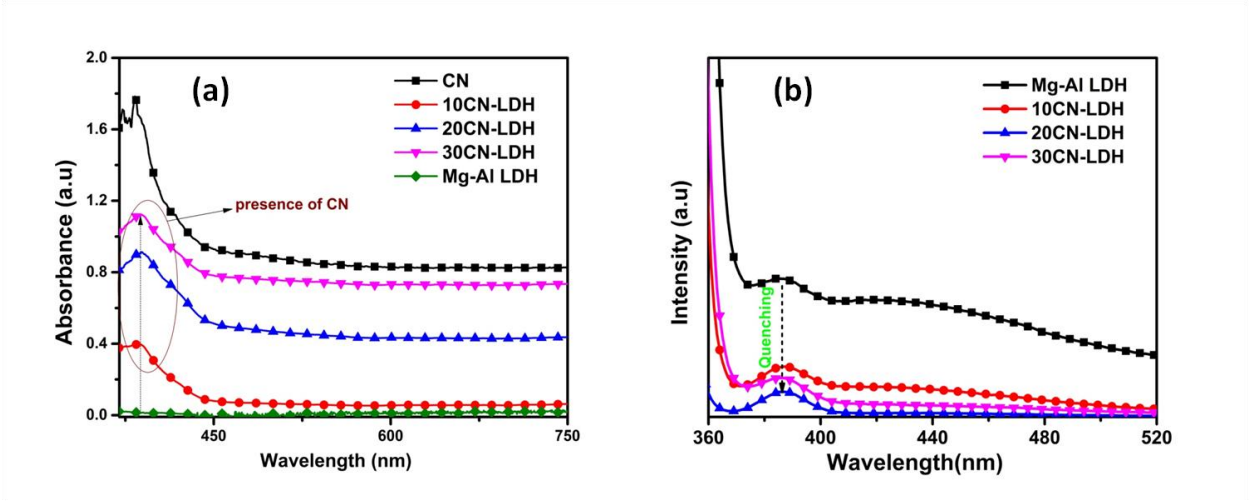

Fig.5.5. The comparative absorbance spectra of Mg-Al LDH, CN, and CN-LDH composites (a) and photoluminescence spectra (b) of Mg-Al LDH and CN-LDH composites.

The photoluminescence spectra of bare LDH and CN-LDH composites are shown in **Fig.5.5 (b)**. The Mg-Al LDH was excited at a wavelength of 340 nm and two emission peaks were observed at 386 nm and 420 nm. In the photoluminescence spectra of CN-LDH composites, the PL signal was quenched, as CN coupling reduced the recombination of the rate of charge carriers in CN-LDH heterojunction via migration of electron and holes at the interface of CN and LDH. The maximum quenching was observed in the 20CN-LDH composite with 20wt% of CN as a further increase in wt% of CN intensified the PL signal due to an excess amount of CN.

5.3.4: Photodegradation studies:

Doxycycline, a toxic pollutant with an initial concentration of 100 ppm, was used to evaluate the adsorption and photocatalytic performance of LDH and CN-LDH composites. The adsorption and degradation efficiency of catalysts over a variety of time spans is depicted in **Fig.5.6**. Due to the adsorption of DXC over prepared catalysts, the samples stirred in a dark chamber for 0 to 30 minutes experienced significant changes in concentration before being illuminated. The CN-LDH composites displayed higher adsorption of DXC than the bare LDH. It might be due to the hydrophobic and pi-pi interactions of DXC with CN and the increment in the surface area of LDH composites with the deposition of CN. The catalysts' photoactivity was examined under LED light for 0 to 60 minutes after achieving adsorption-desorption equilibrium. With increasing irradiation duration, the degradation efficiency of each catalyst increased.

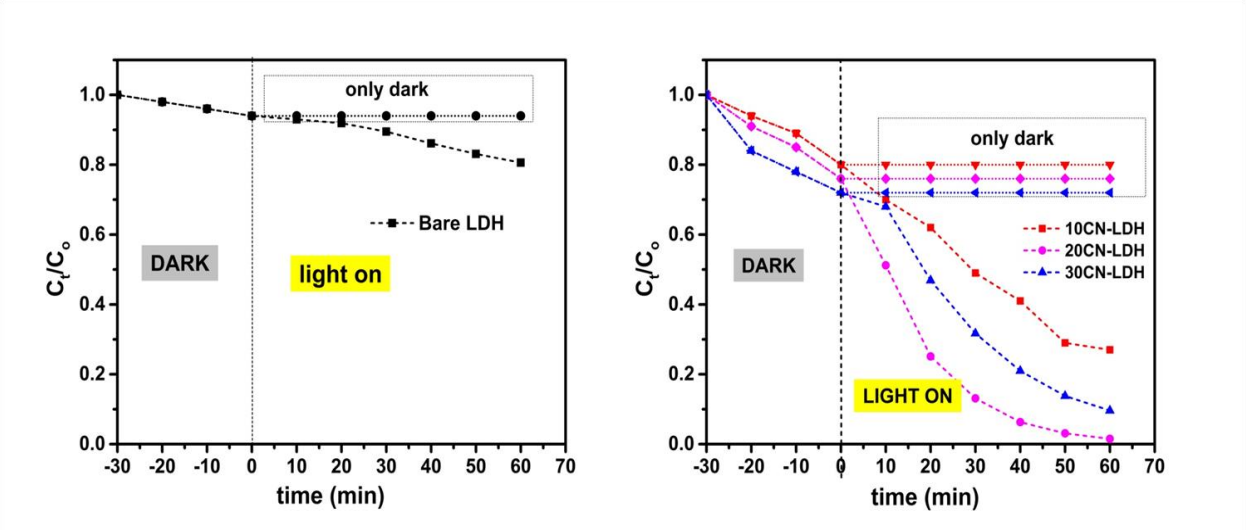

Fig.5.6. Adsorption (in dark) and photodegradation (in LED light) of DXC over bare LDH and CN-LDH composites.

The photocatalytic proficiency (**Fig.5.7)** of catalysts towards the degradation of DXC followed the sequence: Bare LDH (19.4%) < 10CN-LDH (73%) < 30CN-LDH (90.4%) < 20CN-LDH (98.5%). The kinetics of photodegradation of DXC with prepared samples was further explored by first order kinetic equation written as follows:

$$\ln \frac{C_o}{C_t} = kt \ldots\ldots\ldots\ldots (5.3)$$

where C_o is the concentration of DXC at time 0 and and C_t is the concentration of DXC at irradiation time t minutes, and k is the degradation rate constant [19]. The rate constant of photodegradation of DXC under light illumination followed the order: Bare LDH (0.0003 min^{-1}) < 10CN-LDH (0.0222 min^{-1}) < 30CN-LDH (0.0392 min^{-1}) < 20CN-LDH (0.0694 min^{-1}). The 20CN-LDH composite showed the maximum rate of reaction out of all the samples. The synergistic interaction between LDH and CN components were responsible for increment of photocatalytic efficiency of LDH with CN coupling.

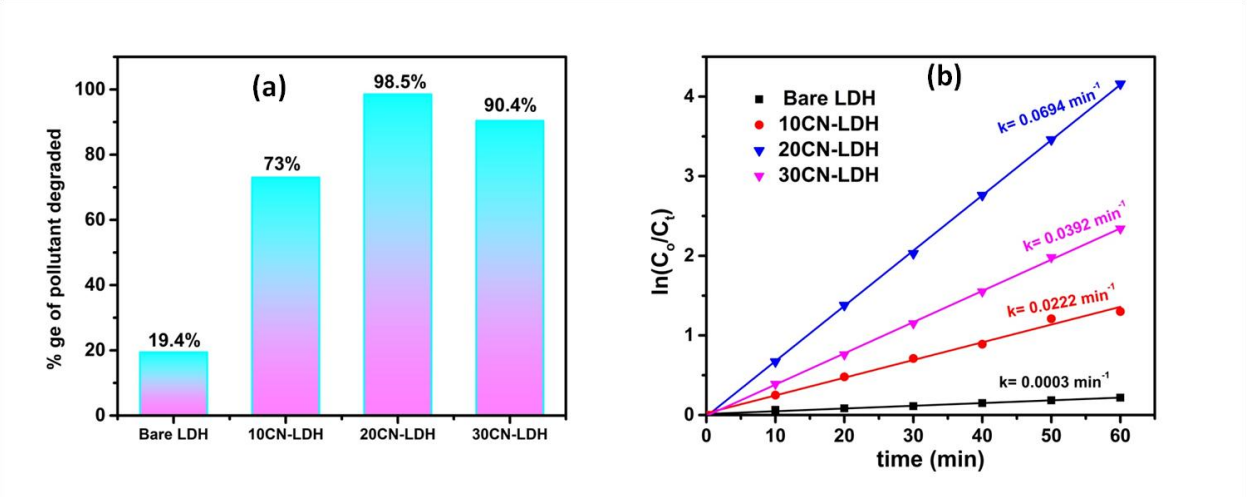

Fig.5.7. Bar graph showing percentage of DXC degraded using different catalysts (a) and the first order kinetic fit for degradation of DXC using bare LDH and CN-LDH composites (b).

5.3.5. Scavanging experiments for investigating active species:

$K_2Cr_2O_7$, isopropanol, and methanol were used as scavengers for $O_2^{\cdot-}$, OḢ, and h^+, respectively, in the scavenging experiment over 20CN-LDH catalyst. **Fig.5.8** shows the percentage of DXC degraded over 20CN-LDH catalyst using none and different scavengers. In contrast, the degradation efficiency was significantly reduced upon addition of $K_2Cr_2O_7$, indicating that superoxide anion radicals play the primary role in the degradation process. Additionally, the ddition of isopropanol and methanol reduced activity to a certain extent suggests that OḢ and h^+ also played a significant role in the degradation process.

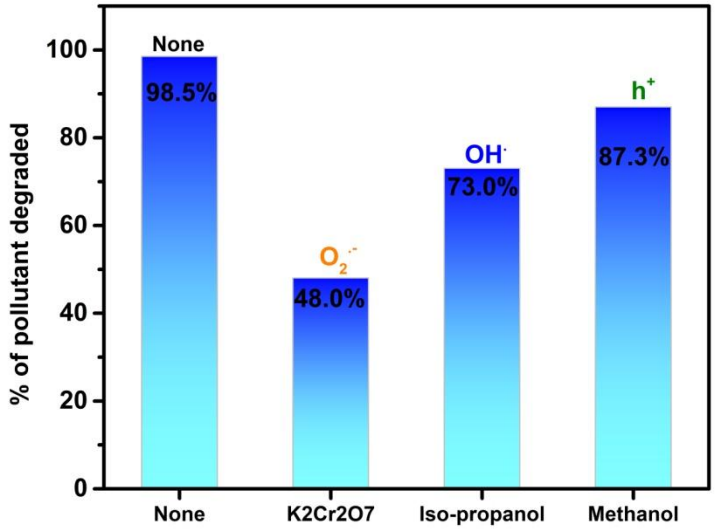

Fig.5.8. Effect of different scavangers on the degradation of DXC with 20CN-LDH.

5.3.6. Recyclability and stability test:

The reusability of the 20CN-LDH composite was assessed by utilizing the same catalyst multiple times under similar experimental conditions. During five photocatalytic cycles over 20CN-LDH composite, the photodegradation of DXC under LED radiation is depicted in **Fig.5.9 (a)**. The photocatalytic activity of 20CN-LDH changed to a little extent for the five cycles and only decreased by 3.7 percent in the fifth cycle in comparison to the first cycle. It demonstrated that prepared photocatalyst had excellent reusability for environmental remediation applications.

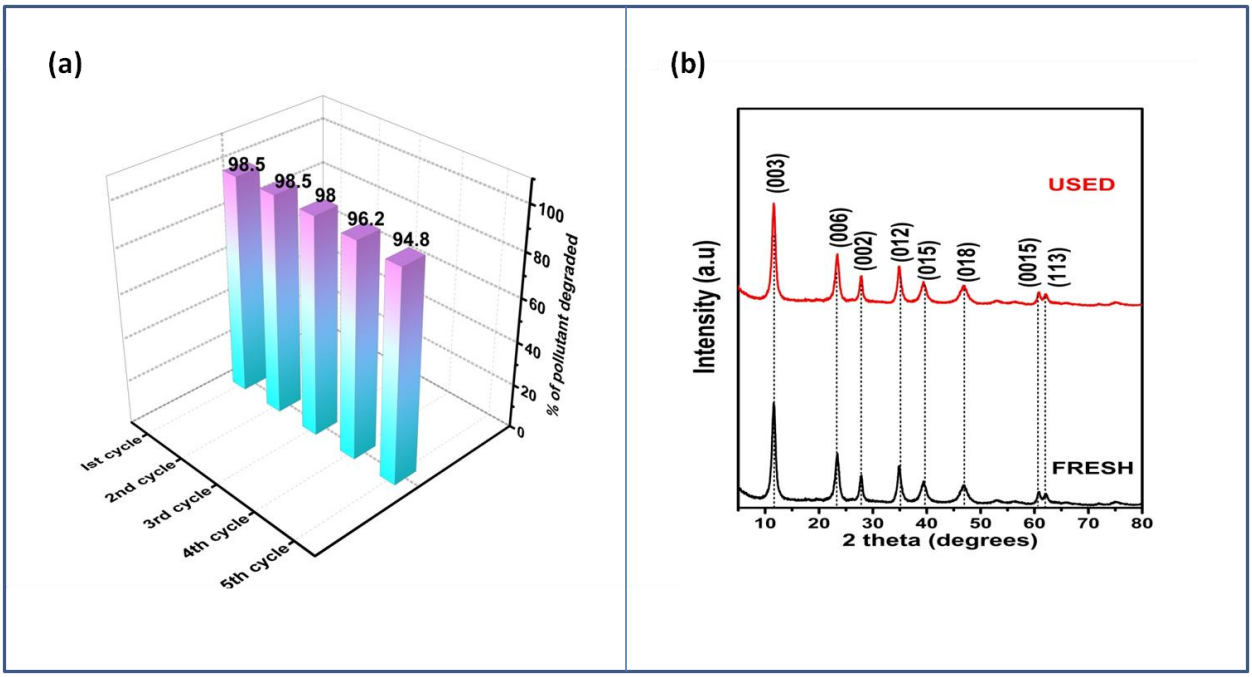

Fig.5.9. Recyclability of the 20CN-LDH for the degradation of DXC under LED irradiation (a); XRD spectra of fresh and used 20CN-LDH for the degradation of DXC (b).

The stability of the 20CN-LDH composite was further confirmed by analyzing its XRD spectrum before and after the photocatalytic reaction (shown in **Fig.5.9 (b)**). The XRD spectrum of used and fresh catalyst was nearly identical, indicating that the crystal structure remained unchanged following photocatalytic application. It demonstrated that binary 20CN-LDH was a suitable and stable substrate for the photocatalytic activities.

5.3.7. LC-MS studies:

LC-MS analysis was employed to investigate the process of doxycycline degradation by 20CN-LDH photocatalyst under LED irradiations. The LC-MS spectrum of DXC before and after degradation is shown in **Fig. 5.10** and **Fig.5.11**, respectively. The peak of DXC molecule (m/z = 445) was absent in the spectrum of the treated sample while it was present for the untreated DXC solution, which confirmed the successful degradation of doxycycline.

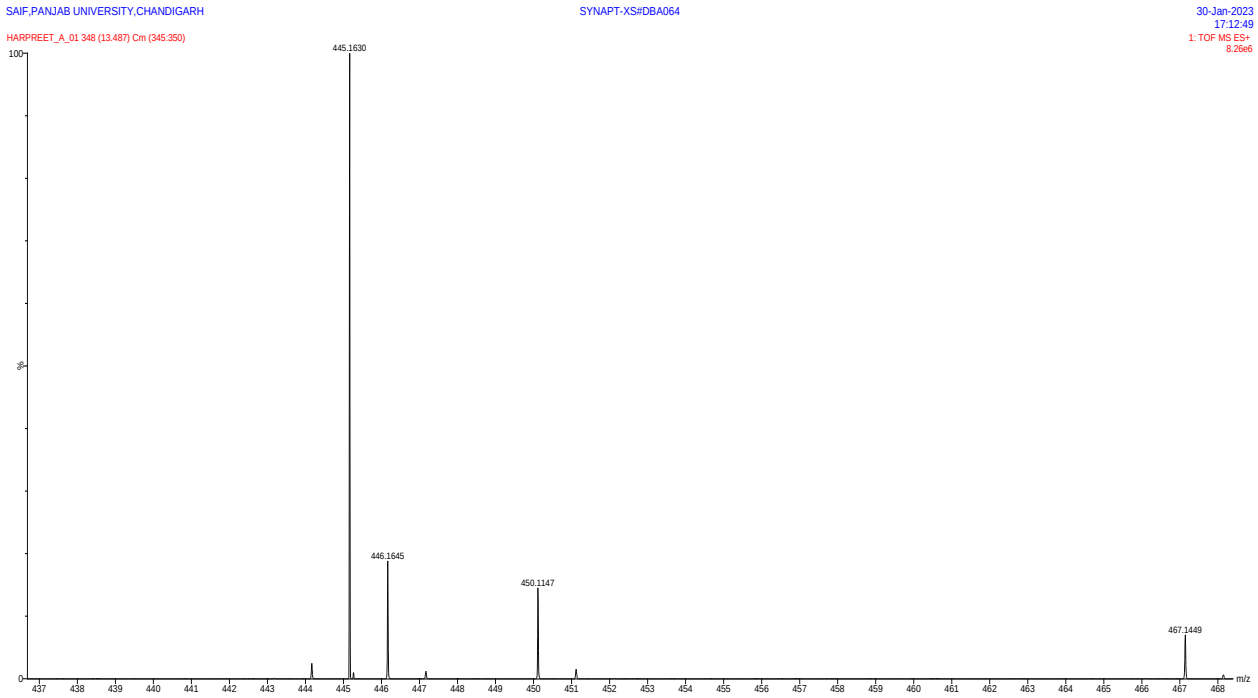

Fig.5.10. The LC-MS spectrum of initial doxycycline solution before degradation.

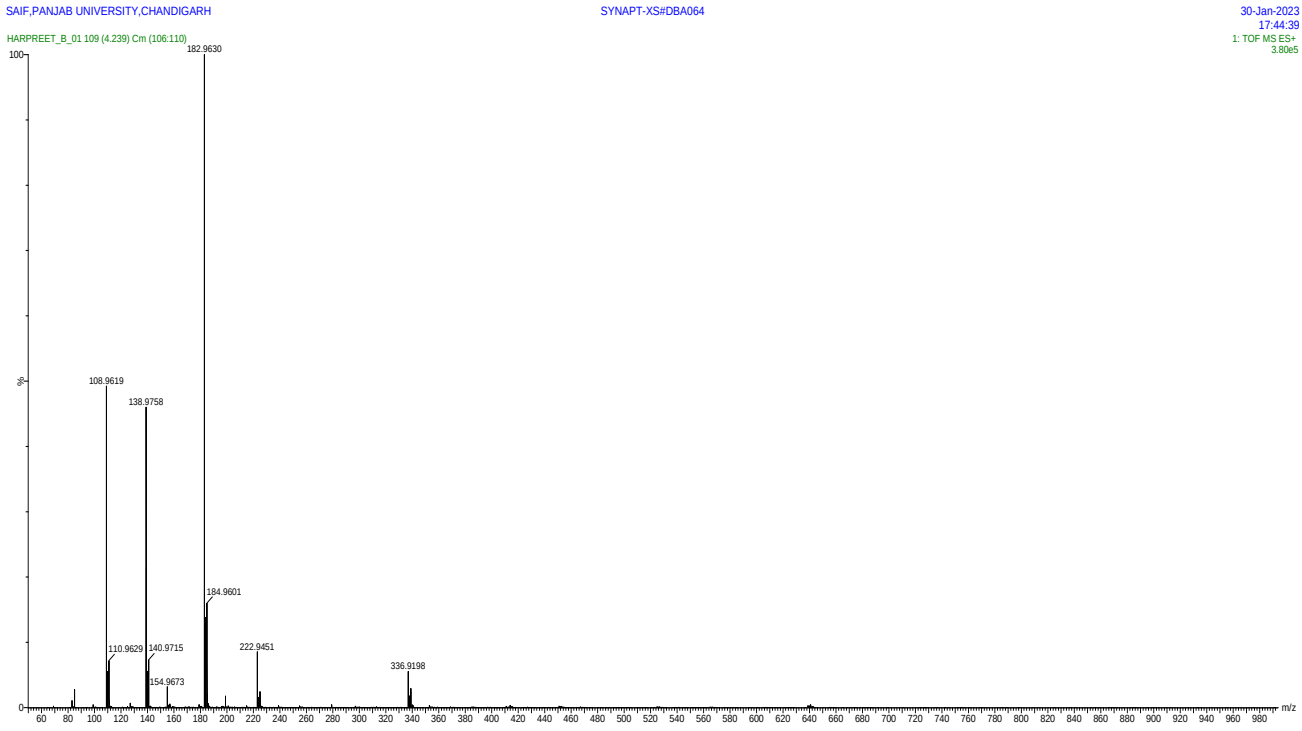

Fig.5.11. The LC-MS spectrum of initial doxycycline solution after degradation.

Fig.5.12 shows the proposed degradation route of DXC via two possible pathways based on the intermediates found in the LC-MS spectrum. In pathway 1, the DXC molecule was attacked by $O_2^{\cdot-}$ and OḢ radicals and undergone demethylation and generated P1 (m/z= 431). The P1 intermediate further undergone deamination and ring opening to produce P2 (m/z= 279). Further, P2 intermediate got attacked by radicals and undergone carbon cleavage and ring opening to produce P3 (m/z =183) and P4 (m/z= 155). In pathway 2, $O_2^{\cdot-}$ and OḢ radicals attacked the DXC molecule and caused ring opening and hydroxylation to produce P5 (m/z=113) and P6 (m/z= 110) [20].

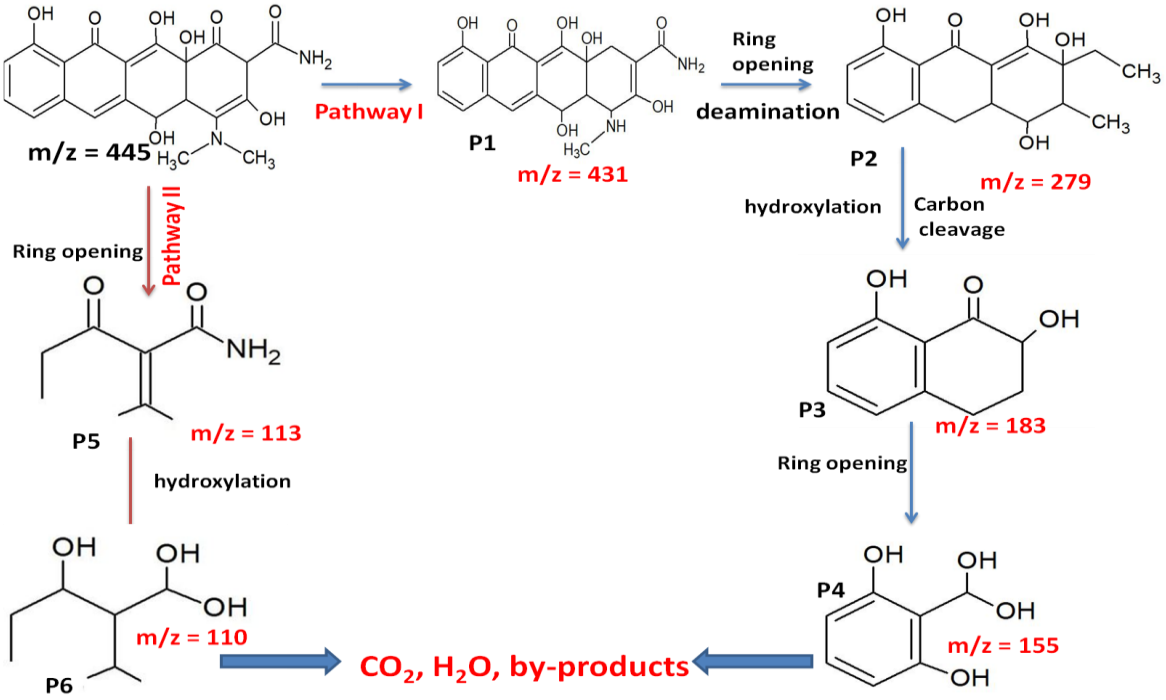

Fig.5.12. The possible degradation pathways of DXC degradation with 20CN-LDH photocatalytic heterojunction.

5.4. Proposed photocatalytic mechanism:

The band gap energy value of Mg-Al LDH and CN was found as 4.43 eV (discussed in section **3.3.3**) and 2.71 eV (discussed in section **4.3.3**), respectively. The conduction band edge

potential value of LDH and CN was determined as -0.158 eV and -1.28 eV, respectively. The valence band edge potential of LDH and CN was calculated as +4.272 eV and +1.43 eV, respectively (mentioned in sections **3.4** and **4.4**). The photogenerated electrons from CN were liable to migrate to LDH and holes migrated from LDH to CN. Thus, the recombination of electron-hole pairs was inhibited due to their transfer at CN-LDH heterojunction. Based on the above discussion, a possible mechanism for charge transfer and photocatalytic degradation of pollutant molecules was proposed and schematically illustrated in **Scheme 5.2**. The electrons accumulated at LDH reduced the dissolved oxygen (O_2) into superoxide anion radicals ($O_2^{\cdot-}$) ($E_{O2}/E_{O2.-}$ = -0.046 eV) [22]. Some of the superoxide anion radicals directly attacked the DXC molecules in an aqueous solution to oxidize and break down DXC into smaller molecules, while others reacted with H_2O to produce hydroxyl radicals. Additionally, because the potential of $H_2O/O\dot{H}$ ($E_{H2O}/E_{O\dot{H}}$ = +2.68 eV) was higher than the conduction band edge potential of CN, the accumulated holes (h^+) in VB of CN were unable to oxidize H_2O to generate $O\dot{H}$ radicals [23]. Also, some of the DXC molecules could directly by holes. As concluded, the action of the $O_2^{\cdot-}$, $O\dot{H}$, and h^+ radicals caused the DXC molecules to be broken down into mineralized products.

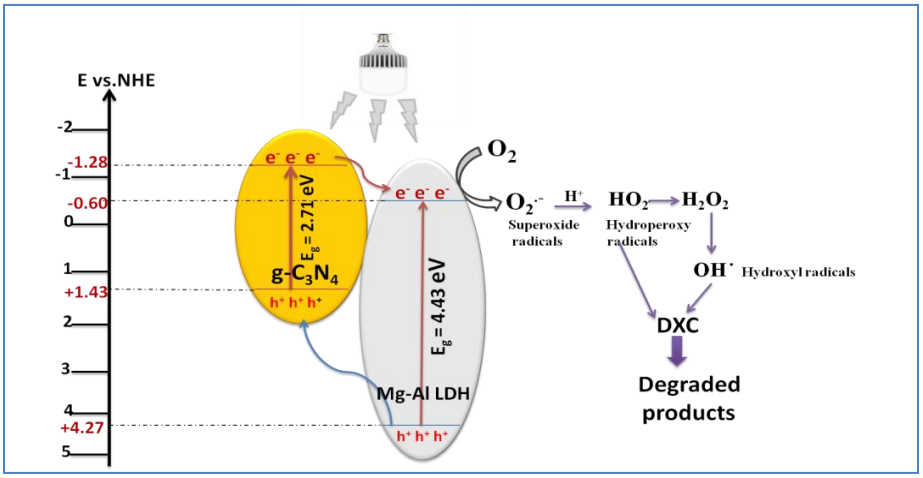

Scheme-5.1. A schematic illustration of charge transfer and separation in CN-LDH composite towards the degradation of DXC under LED light illumination.

5.5. Conclusion:

In conclusion, CN-coupled LDH composites of varying CN weight percentages were prepared using an in-situ hydrothermal method. Combining a UV-active Mg-Al LDH photocatalyst with a visible-active g-C_3N_4 photocatalyst was an efficient method for preventing charge carrier recombination, expanding surface area, and improving absorbance ability to visible light. The as-constructed CN-LDH composites exhibited better photocatalytic degradation of doxycycline, a model toxic pollutant under LED light (λ = 360 nm) compared with bare LDH. Also, an optimized amount of CN i.e. 20wt% was liable for effectively enhancing the photocatalytic properties of LDH as excess loading suppressed the activity of LDH by covering its surface. The 20CN-LDH composite degraded a maximum of 98.5% doxycycline in just 60 minutes. Further, LC-MS studies were analyzed to confirm the degradation process and to investigate the smaller by-products.

References:

[1] W. Liu, Z. Li, Q. Kang, L. Wen, Efficient photocatalytic degradation of doxycycline by coupling α-Bi_2O_3/ g-C_3N_4 composite and H_2O_2 under visible light, Appl. Surf. Sci. 197 (2021) 110925. https://doi.org/10.1016/j.envres.2021.110925.

[2] X. Yan, J. Qian, X. Pei, L. Zhou, R. Ma, M. Zhang, Y. Du, L. Bai, Enhanced photodegradation of doxycycline (DOX) in the sustainable $NiFe_2O_4$/MWCNTs/BiOI system under UV light irradiation, Environ. Res. 199 (2021) 111264. https://doi.org/10.1016/j.envres.2021.111264.

[3] P. Lovino, S. Chianese, S. Canzano, M. Prisciandaro, D. Musmarra, Ibuprofen photodegradation in aqueous solutions, Environ. Sci. Pollut. Res. (2016) 23:22993–23004. https://doi.org/10.1007/s11356-016-7339-0

[4] S. Singhal, R. Sharma, C. Singh, S. Bansal, Enhanced Photocatalytic Degradation of Methylene Blue Using $ZnFe_2O_4$/MWCNT Composite Synthesized by Hydrothermal Method, Indian J. Eng. Mater. Sci. (2013) 356025. http://dx.doi.org/10.1155/2013/356025.

[5] M. Zubair, N. Jarrah, M.S. Manzar, M. Al-Harthi, M. Daud, N.D. Mu'azu, S.A. Haladu, Adsorption of eriochrome black T from aqueous phase on MgAl-, CoAl- and NiFe-calcined layered double hydroxides: Kinetic, equilibrium and thermodynamic studies, J. Mol. Liq. 230 (2017) 344–352. https://doi.org/10.1016/j.molliq.2017.01.031.

[6] G. Gao, Z. Zhu, J. Zheng, Z. Liu, Q. Wang, Y. Yan, Ultrathin Magnetic Mg-Al LDH Photocatalyst for Enhanced CO_2 Reduction: Fabrication and Mechanism, J. Colloid Interface Sci. 555 (2019) 1-10. https://doi.org/10.1016/j.jcis.2019.07.025.

[7] M. Solehudin , U. Sirimahachai, G. A.M. Ali, K. F. Chong, S. Wongnawa, One-pot synthesis of isotype heterojunction g-C_3N4-MU photocatalyst for effective tetracycline hydrochloride antibiotic and reactive orange 16 dye removal, Adv. Powder Technol. 31 (2020) 1891-1902. https://doi.org/10.1016/j.apt.2020.02.020.

[8] L. Wang, X. Gao, J. Su, Q. Zhang, K. Zheng, Z. Zhang, Synthesis of Ag/AgCl-modified TiO_2/MgAl-layered double hydroxide nanocomposite with enhanced photocatalytic activity, J. Photochem. Photobiol. A Chem. 383 (2019) 111973. https://doi.org/10.1016/j.jphotochem.2019.111973.

[9] F. Li, Y. Huang, C. Gao, X. Wu, The enhanced photo-catalytic CO_2 reduction performance of g-C_3N_4 with high selectivity by coupling CoNiSx, Mater. Res. Bull. 144 (2021) 111488. https://doi.org/10.1016/j.materresbull.2021.

[10] S. Das, K. Parida, Superior photocatalytic performance of Co Al LDH in the race of metal incorporated LDH: A comparison study, Mater. Today: Proc. 35 (2021) 275-280.

https://doi.org/10.1016/j.matpr.2020.05.759.

[11] S. Zhai, J. Liu, J. Sheng, J. Xu, H. Jiang, Novel morphology-controlled three-dimensional flower-like magnetic $CoFe_2O_4$/CoFe-LDHs microsphere for high efficient removal of Orange II, Chem. Eng. J. 421 (2021) 130403. https://doi.org/10.1016/j.cej.2021.130403.

[12] B. Li, Y. Zhang, X. Zhou, Z. Liu, Q. Liu, X. Li, Different dye removal mechanisms between monodispersed and uniform hexagonal thin plate-like MgAl-CO_3^{2-}-LDH and its calcined product in efficient removal of Congo red from water, J. Alloys Compd. 673 (2016) 265-271. https://doi.org/10.1016/j.jallcom.2016.02.248.

[13] Y. Li, X. Xing, J. Pei, R. Li, Y. Wen, S. Cui, T. Liu, Automobile exhaust gas purification material based on physical adsorption of tourmaline powder and visible light catalytic decomposition of g-C_3N_4/$BiVO_4$, Ceram. Int. 46 (2020) 12637-12647. https://doi.org/10.1016/j.ceramint.2020.02.029.

[14] O. Fontelles-Carceller, M. J. Muñoz-Batista, M. Fernandez-Garcia, A. Kubacka, Interface effects in sunlight driven Ag/g-C_3N_4 composite catalysts: Study of the toluene photo-degradation quantum efficiency, Appl. Mater. Interfaces. (2016) 2617–2627. https://doi.org/10.1021/acsami.5b10434.

[15] X. fei Tan, Y. guo Liu, Y. ling Gu, S. bo Liu, G. ming Zeng, X. Cai, X. jiang Hu, H. Wang, S. mian Liu, L. hua Jiang, Biochar pyrolyzed from MgAl-layered double hydroxides pre-coated ramie biomass (Boehmeria nivea (L.) Gaud.): Characterization and application for crystal violet removal, J. Environ. Manage. 184 (2016) 85–93. https://doi.org/10.1016/j.jenvman.2016.08.070.

[16] Z. Lin, R. Guo, Y. Yuan, X. Ji , L. Hong, W. Pan, Fabrication of flower spherical-like Z-scheme $FeWO_4$/NiAl-LDH photocatalysts with excellent activity for CO_2 photoreduction

under visible light, Appl. Surf. Sci. 567 (2021) 150805. https://doi.org/10.1016/j.apsusc.2021.150805.

[17] A. Kumaresan, S. Yang, K. Zhao, N. Ahmad, J. Zhou, Z. Zheng, Y. Zhang, Y. Gao, H. Zhou, Z. Tang, Facile development of CoAl-LDHs/RGO nanocomposites as photocatalysts for efficient hydrogen generation from water splitting under visible-light irradiation, Inorg. Chem. Front. 6 (2019) 1753–1760. https://doi.org/10.1039/c9qi00307j.

[18] X. Huang, X. Xu, R. Yang, X. Fu, Synergetic adsorption and photocatalysis performance of g-C_3N_4/Ce-doped MgAl-LDH in degradation of organic dye under LED visible light, Colloids Surfaces A Physicochem. Eng. Asp. 643 (2022) 128738. https://doi.org/10.1016/j.colsurfa.2022.128738.

[19] S. Sreeja, V. Shetty K, Photocatalytic water disinfection under solar irradiation by Ag@TiO2 core-shell structured nanoparticles, Sol Energy. 157 (2017) 236-243. http://dx.doi.org/10.1016/j.solener.2017.07.057.

[20] Z. Pan, L. Qian, J. Shen, J. Huang, Y. Guo, Z. Zhang, Construction and application of Z-scheme heterojunction In_2O_3/Bi_4O_7 with effective removal of antibiotic under visible light, Chem. Eng. J. 426 (2021) 130385. https://doi.org/10.1016/j.cej.2021.130385.

Summary and Future Outlook

This work reported the viable synthesis of layered double hydroxides constituting variable divalent and trivalent metal cations. The Ni-Co LDH, Mg-Al LDH, and Co-Al LDH were prepared via different synthetic methods and characterized accordingly. Furthermore, g-C_3N_4, one of the most stable allotropes of carbon is a non-toxic, cost-effective, and promising material found in the area of adsorption and photocatalysis. Based on the research that was done, it was found that coupling g-C_3N_4 (CN) with LDH was a good way to improve the adsorption and photocatalytic properties of layered double hydroxides. It was observed that coupling of CN with LDH improved its adsorption properties towards cationic pollutants and also enhanced its photocatalytic properties via enhancing the surface active sites, inhibiting recombination of charge carriers, and widening the light absorption capabiltiy. Moreover, the deposition of plasmonic metal nanoparticles onto LDH and CN coupled LDH composites was emphasized in this work, which showed that plasmonic nanocomposites exhibited better photocatalytic performance towards the degradation of organic pollutants through enhancing the absorption of light in the visible region and separating the photogenerated electron-hole pairs. The prepared photocatalysts were highly effective in degrading harmful organic pollutants under cost-effective LED bulbs available in our homes. The LC-MS analysis proved that harmful organic pollutant molecules were broken down into smaller byproducts. In extension to this work, the CN-LDH nanocomposites and plasmonic nanocomposites could be employed for demonstrating hydrogen production through water splitting and dehydrogenation of waste alcohols under light radiations.

List of Publications

1. **Harpreet Kaur**, Satnam Singh, and Bonamali Pal (2021) Impact of g-C_3N_4 loading on NiCo LDH for adsorptive removal of anionic and cationic organic pollutants from aqueous solution, **Korean Journal of Chemical Engineering** 38(6), 1248-1259. **(I.F=3.3)** https://doi.org/10.1007/s11814-021-0784-6
2. **Harpreet Kaur**, Satnam Singh, and Bonamali Pal (2021) A brief review on modified layered double hydroxides for H_2 production through photoinduced H_2O splitting, **Environmental Nanotechnology, Monitoring and Management** 16, 100451. **(I.F=5.95)** https://doi.org/10.1016/j.enmm.2021.100451
3. **Harpreet Kaur**, Satnam Singh, and Bonamali Pal (2022) Effect of plasmonic metal (Cu, Ag, and Au) loading over the physicochemical and photocatalytic properties of Mg-Al LDH towards degradation of tetracycline under LED light, **Applied surface science** 609, 155455. **(I.F=7.392)** https://doi.org/10.1016/j.apsusc.2022.155455
4. Harpreet Kaur, Satnam Singh, and Bonamali Pal, Construction of Ag deposited g-C_3N_4 loaded Co-Al LDH ternary composites with aim of pharmaceutical wastewater treatment: pathways and mechanism for ciprofloxacin degradation, **Applied Clay Science** 238, 106922 (**I.F=5.9)** https://doi.org/10.1016/j.clay.2023.106922
5. Harpreet Kaur, Satnam Singh, and Bonamali Pal, Highly efficient g-C_3N_4 coupled Mg-Al LDH binary heterojunction photocatalyst for excellent photocatalytic degradation of doxycycline under LED light **(Manuscript under preparation)**

Other Publications

1. Manpreet Kaur Aulakh, **Harpreet Kaur**, Mehak Bansal, Bonamali Pal, and Satnam Singh (2022) Utilization of Waste and Renewable Material-HCM as an Efficient Adsorbent for Heavy Metal Ions Removal: A Study of Adsorption Isotherms and Kinetics, **Chemistry Select** 7, 28. **(I.F= 2.3)** https://doi.org/10.1002/slct.202200659
2. Jasmine Kaur, Bonamali Pal, Satnam Singh, and **Harpreet Kaur** (2022) Fabrication of highly efficient Au and layered double hydroxide modified g-C_3N_4 ternary composites for degradation of pharmaceutical drug: Pathways and mechanism, **Surfaces and Interfaces** 36, 102583. **(I.F= 6.1)** https://doi.org/10.1016/j.surfin.2022.102583
3. **Harpreet Kaur**, Satnam Singh, and Bonamali Pal, A review on noble metal loaded LDH based heterojunctions for boosted photocatalysis **(Manuscript under preparation)**

Conferences and Workshops

1. Harpreet Kaur, Satnam Singh, and Bonamali Pal, participated in 12th National conference on "Chemical and Environmental Sciences: Advanced Innovations-2020" **(CESAI-2020)**, Punjabi University, Patiala, 19th - 20th Feb, 2020.
2. Harpreet Kaur, Satnam Singh, and Bonamali Pal, participated in **SCI-FEST 2022** held at Thapar Institute of Engineering and Technology, 7th June, 2022.
3. Harpreet Kaur, Satnam Singh, and Bonamali Pal, presented paper in International Conference on "Emerging Trends in Science and Technology" **(ICETST-2022)** organized by department of Applied Sciences, Punjab Engineering College, Chandigarh,

10^{th} - 11^{th} June, 2022 (Oral presentation).

4. Harpreet Kaur, Satnam Singh, and Bonamali Pal, presented paper in National conference on Environment, Food Security and Health with reference to Climate Change" held at Sri Guru Granth Sahib World University, Fatehgarh Sahib, 7^{th}-9^{th} Feb, 2023 (Oral Presentation)

5. Harpreet Kaur, Satnam Singh, and Bonamali Pal, presented paper in International conference on "Recent Advances in Chemistry-2023" (CRAC-2023), held at Punjabi University, Patiala, 23^{rd}-24^{th} Feb, 2023 (Poster presentation).

thesis

ORIGINALITY REPORT

13%	8%	10%	3%
SIMILARITY INDEX	INTERNET SOURCES	PUBLICATIONS	STUDENT PAPERS

PRIMARY SOURCES

1	pubs.rsc.org Internet Source	1%
2	Wee-Jun Ong, Lling-Lling Tan, Yun Hau Ng, Siek-Ting Yong, Siang-Piao Chai. " Graphitic Carbon Nitride (g-C N)-Based Photocatalysts for Artificial Photosynthesis and Environmental Remediation: Are We a Step Closer To Achieving Sustainability? ", Chemical Reviews, 2016 Publication	1%
3	coek.info Internet Source	1%
4	idr.nitk.ac.in Internet Source	1%
5	Tao Wang, Xiqing Liu, Changchang Ma, Yang Liu, Hongjun Dong, Wei Ma, Zhi Liu, Maobin Wei, Chunxiang Li, Yongsheng Yan. "3D Ag/NiCo-layered double hydroxide with adsorptive and photocatalytic performance", Journal of the Taiwan Institute of Chemical Engineers, 2018	<1%

Korean J. Chem. Eng., 38(6), 1248-1259 (2021)
DOI: 10.1007/s11814-021-0784-6

pISSN: 0256-1115
eISSN: 1975-7220

Impact of g-C_3N_4 loading on NiCo LDH for adsorptive removal of anionic and cationic organic pollutants from aqueous solution

Harpreet Kaur, Satnam Singh, and Bonamali Pal†

School of Chemistry and Bio-Chemistry, Thapar Institute of Engineering and Technology, Patiala, 147004, India
(*Received 15 December 2020 • Revised 24 February 2021 • Accepted 13 March 2021*)

Abstract–Layered double hydroxides are traditional positively charged inorganic materials generally considered as efficient and low-cost adsorbents for the removal of anionic organic molecules. In this study, we prepared a series of g-C_3N_4@NiCo LDH composites by loading 10-30 wt% of g-C_3N_4 onto the LDH through the electrostatic self-assembly method. The bare LDH and g-C_3N_4 loaded LDH composites were characterized by XRD, SEM-EDS, Zeta, DLS, and FTIR techniques. Results revealed that extra peak corresponds to g-C_3N_4 originating in the XRD patterns, distorted morphology of LDH, reduction in positive surface zeta potential, and enhancement in hydrodynamic size after loading of g-C_3N_4 affirmed the successful formation of the composite. The adsorption performance of as-modified LDH was evaluated by removing the most commonly used salicylic acid and methylene blue as anionic and cationic model pollutant, respectively, from aqueous solution. The adsorption mechanism for both the pollutants by as-synthesized samples follows Langmuir isotherm. The results demonstrated that the bare LDH exhibited maximum adsorption efficiency of 75.16 mg/g and only 3.66 mg/g for salicylic acid and methylene blue, respectively. With 30 wt% loading of g-C_3N_4, the adsorption capacity for methylene blue increased to 25.16 mg/g almost 6-7 times higher than that of bare LDH. On the other hand, the opposite effect on adsorptive removal of salicylic acid was observed with increase in the wt% loading of g-C_3N_4. With 30 wt% loading of g-C_3N_4, the adsorption capacity for salicylic acid decreased to 38..37 mg/g, almost half that of bare LDH. A possible mechanism has been proposed. The kinetics for adsorption of salicylic acid onto bare LDH obeys the second-order model aside from the methylene blue adsorption which follows first-order kinetics. On the other hand, the kinetics of adsorption for both the pollutants onto (10-30) CN- LDH composites follows second order kinetics.

Keywords: g-C_3N_4@NiCo LDH Composite, Adsorptive Removal, Interactions Of Ionic Pollutants, Electro-kinetic Studies, Adsorption Isotherms, Surface Charge Variation

INTRODUCTION

Water contamination has become a most serious issue in the public arena causing several medical problems. One of the main reasons is the release of organic pollutants as effluents from industries into water sources [1-3]. To get rid of such kind of pollution, various techniques such as ion exchange [4], photocatalytic degradation [5], coagulation [6], adsorption [7], membrane separation [8] are used for water purification. Among them, adsorption is considered an easy, simple, economic, and highly effective method that is being extensively adopted worldwide to remove organic pollutants from water.

For the last few years, layered double hydroxides (LDH), mesoporous inorganic compounds commonly known as hydrotalcite or anionic clays are receiving incredible consideration in the adsorption research field. Their chemical composition is described as $[M^{2+}_{(1-x)}M^{3+}_{(x)}(OH)_2]^{x+}(A^{n-})_{x/n}\cdot mH_2O$, where M^{2+} and M^{3+} represents bivalent and trivalent metal ions, respectively, while A^{n-} are intercalated anions, and x is the stoichiometric ratio of $M^{3+}/(M^{2+}+M^{3+})$, having value within 0.2-0.33 range. They consist of positively charged hydroxide layers known as brucite layers and exchangeable anions in the interlayer region between two brucite layers [9-11]. Owing to low cost, high surface area, porous structure, non-toxicity, and excellent anion exchange capability, they are serving as efficient adsorbents capable of adsorbing toxic metal cations and anions, harmful organic dyes, herbicides, pesticides, toxic gases, pharmaceutical wastes, and various other pollution causing compounds [3,12,13]. Adsorption is a surface phenomenon that usually occurs due to certain kinds of intermolecular interactions between the adsorbate and adsorbent. Because of the positively charged surface, LDHs are highly effective adsorbents for the adsorption of harmful anionic organic compounds, whereas have low affinity towards cationic organic species due to ionic repulsions. Several modifications such as the intercalation of surfactants into their interlayer gallery [14], coupling with other adsorbing materials (graphene oxide [15], multiwalled carbon nanotubes [16], biochar [17], etc.) are being adapted to LDHs for improving their adsorption activity towards anionic as well as cationic organic compounds.

Recently, Zhang et al. fabricated NiFe LDH-montmorillonite composite consisting of the positively charged LDH nanoflakes on the negatively charged surface of montmorillonite. They investigated the adsorption performance of the composite towards both the anionic and cationic dye [18]. Li et al. modified the surface of MgAl LDH from hydrophilic to hydrophobic by intercalating organic surfactant for efficient removal of non-ionic, anionic, and cationic

†To whom correspondence should be addressed.
E-mail: bpal@thapar.edu

Environmental Nanotechnology, Monitoring & Management 16 (2021) 100451

Contents lists available at ScienceDirect

Environmental Nanotechnology, Monitoring & Management

journal homepage: www.elsevier.com/locate/enmm

A brief review on modified layered double hydroxides for H_2 production through photoinduced H_2O splitting

Harpreet Kaur, Satnam Singh, Bonamali Pal *

School of Chemistry and Bio-Chemistry, Thapar Institute of Engineering and Technology, Patiala, 147001, India

ARTICLE INFO

Keywords:
Layered double hydroxides
Photocatalysis
Modified LDHs
H_2O splitting
H_2 production

ABSTRACT

Layered double hydroxides (LDH), two dimensional (2D) layered nanostructured materials usually known as hydrotalcites, anionic clays, or host-guest compounds have attracted significant research interest in the photocatalysis field. Their photocatalytic behavior is attributable to their large specific surface area, high surface to volume ratio, tunable electronic and structural composition, highly dispersed metal (divalent, trivalent, or tetravalent) octahedrons linked to one another through metal oxo-bridge linkage undergoing certain transitions like d-d transitions, metal to metal charge transfer and ligand to metal charge transfer. Their photoactive response can be further improved through certain modifications like doping of particular cation, specific anion intercalation, calcination, heterostructure formation with other semiconductors, and noble metal loading generally providing a wider light response, inhibited recombination and longer lifetime of electron-hole pairs, shorter charge transfer distance, and increased specific surface area in some cases. Among various photocatalytic applications, hydrogen production through water splitting is an emerging area of research on account of rising energy crises with growing civilization. LDHs with highly attractive features are not at the backfoot for such pivotal zone, but are being extensively utilized as bare or modified for the reduction of water under light illumination. This review is aimed to illustrate the photocatalytic performance of LDHs with several adapted modifications to their structural and electronic properties and focused on their execution towards hydrogen production through photoinduced water splitting. To start with, brief information is provided about their commonly used synthetic methods, composition, structure, and key characteristics. Then, their photocatalytic properties are discussed with some specific examples for different applications and individual discussion with mechanistic approach is carried out that how certain modification to their original structure can bring improvement in their photoactivity. At last, all the past and recent progress of LDHs is provided with proper mechanistic understanding for photocatalytic hydrogen production.

1. Introduction

Layered double hydroxides belong to an important class of mesoporous inorganic compounds of basic nature having natural as well as synthetic origin. These are two-dimensional layered structured materials composed of positively charged mixed metal hydroxide layers generally constituting two kinds of metal cations (divalent and trivalent or tetravalent) along with anionic species and water molecules adapted in the interlayer space between the two metal hydroxide layers. These are regularly known as hydrotalcites because of their unique layered structure like that of naturally occurring mineral "hydrotalcite, a white hydrous mineral possessing rhombohedral crystallinity and structural properties indistinguishable from that of brucite $Mg(OH)_2$ like structure. This naturally occurring mineral was first found in 1842 having the chemical formula $[Mg_6\ Al_2\ (OH)_{16}]CO_3.\ 4H_2O$ constituting assembly of positively charged infinite brucite like layers containing Mg^{2+} partially replaced by Al^{3+} ions octahedrally coordinated to hydroxyl groups (OH^-), and carbonate anions (CO_3^{2-}) intercalated in the interlayer spacing along with few water molecules (Forano et al., 2013; Chubar et al., 2017; Mohapatra and Parida, 2016). Since then, in similar to that of hydrotalcite, numerous LDH materials have been synthesized constituting a wide range of divalent (e.g. Co^{2+}, Cu^{2+}, Ni^{2+}, Zn^{2+}, etc.)

Abbreviations: LDH, layered double hydroxides; MMO, mixed metal oxides; HOMO, highest occupied molecular orbital; LUMO, lowest occupied molecular orbital; CB, conduction band; VB, valence band; DRS, diffuse reflectance spectra; UV, ultra- violet.

* Corresponding author at: Thapar Institute of Engineering and Technology, Patiala, 147004, India.
E-mail address: bpal@thapar.edu (B. Pal).

https://doi.org/10.1016/j.enmm.2021.100451
Received 29 October 2020; Received in revised form 22 February 2021; Accepted 28 February 2021
Available online 9 March 2021

Applied Surface Science 609 (2023) 155455

Contents lists available at ScienceDirect

Applied Surface Science

journal homepage: www.elsevier.com/locate/apsusc

Full Length Article

Effect of plasmonic metal (Cu, Ag, and Au) loading over the physicochemical and photocatalytic properties of Mg-Al LDH towards degradation of tetracycline under LED light

Harpreet Kaur, Satnam Singh, Bonamali Pal *

School of Chemistry and Bio-Chemistry, Thapar Institute of Engineering and Technology, Patiala 147004, India

ARTICLE INFO

Keywords:
Mg-Al LDH
Plasmonic metal
Photocatalysis
Mineralization
Degradation pathways

ABSTRACT

This work focused on the enhancement of the photocatalytic activity of solvothermal synthesized $Mg_{0.667}Al_{0.333}(OH)_2(CO_3)_{0.167}(H_2O)_{0.5}$ layered double hydroxide (LDH) by plasmonic metal (Cu, Ag, and Au) photodeposition (1-3 wt%). HRTEM analysis confirmed the successful loading of plasmonic nanoparticles with varying sizes (Au (~4-25 nm) > Ag (~3-12 nm) > Cu (~2-7 nm)) on the surface of LDH. The effect of different plasmonic metals and their size on the surface structural, optical, electrokinetic, and photocatalytic properties of LDH was investigated. The prepared catalysts were evaluated for the degradation of tetracycline under LED irradiation for 140 min and the photoactivity trend followed the order: pristine LDH < Cu@LDH < Ag@LDH < Au@LDH. The LC-MS studies revealed that the degradation occurred by the attack of various reactive species ($O_2^{\cdot-}$, h^+, $^{\cdot}OH$) via four paths mainly including hydroxylation, functional group cleavage, and ring-opening reaction. A possible mechanism was proposed for the appreciable enhancement in performance caused by the formation of Schottky barriers and surface plasmon resonance of plasmonic nanoparticles. The results of total organic carbon (TOC) indicated the acceptable mineralization of about 84 %. Less than a 10 % fall in degradation efficiency was observed within four recycle runs.

1. Introduction

In recent years, antibiotics have been used worldwide for the counteraction and treatment of irresistible illnesses in humans and animals. Tetracycline (TC) is a broad-spectrum antibiotic delivered in enormous amounts. It broadly utilizes curing contaminations bring about by most Gram-positive and negative bacteria, chlamydia, intracellular mycoplasma, and rickettsia. Investigations have discovered that these antibiotics have stable chemical structures and antibacterial properties. Therefore, these remained unretained and transformed by humans and animals after utilization. Subsequently, these enter the environment as metabolites and cause serious harm to human and animal health. Therefore, the efficient removal of TC antibiotic residues from the environment has become fundamental for the ecological environment and human well-being [1–2]. The way to control the antibiotics entering the environment is to treat the wastewater containing antibiotics. As of now, photocatalysis has arisen as a green and cost-effective technique to eliminate them from water bodies. Besides, it can transform antibiotics into less harmful organic molecules and effectively biodegradable compounds, thus reducing or eliminating their antibacterial activity [3–4]. Therefore, the fabrication of a stable and proficient photocatalyst has become a central issue for the degradation of tetracycline.

Layered double hydroxides (LDHs), typical two-dimensional layered structured inorganic materials, stand out in the field of photocatalysis. Many researchers have proved that these exhibit better performance than many of the metal oxide semiconductors credited to their appealing features like layered and mesoporous structure, large surface area, surface hydroxyl groups, highly dispersed MO_6 octahedrons, etc. [5–6]. Among different LDH photocatalysts reported in the literature, the Mg-Al LDH showed the advantages of easy and low-cost synthesis, structural

Abbreviations: LDH, Layered double hydroxide; TC, Tetracycline; EG, Ethylene glycol; NPs, Nanoparticles; CB, Conduction band; VB, Valence band; FESEM, Field emission scanning electron microscopy; HRTEM, High resolution transmission electron microscopy; PL, Photoluminiscence; BET, Brunauer Emmett Teller; BJH, Barrett-Joyner-Halenda; DRS, Diffuse reflectance spectroscopy; XPS, X-ray photoelectron spectroscopy; EDS, Energy dispersive X-ray spectroscopy; DLS, Dynamic light scattering technique; LC-MS, Liquid chromatography mass spectroscopy; TOC, Total organic carbon.

* Corresponding author at: Thapar Institute of Engineering and Technology, Patiala 147004, India.
E-mail address: bpal@thapar.edu (B. Pal).

https://doi.org/10.1016/j.apsusc.2022.155455
Received 25 July 2022; Received in revised form 16 October 2022; Accepted 22 October 2022
Available online 28 October 2022
0169-4332/

Surfaces and Interfaces 36 (2023) 102583

Contents lists available at ScienceDirect

Surfaces and Interfaces

journal homepage: www.sciencedirect.com/journal/surfaces-and-interfaces

Fabrication of highly efficient Au and layered double hydroxide modified g-C_3N_4 ternary composites for degradation of pharmaceutical drug: Pathways and mechanism

Jasmine Kaur, Bonamali Pal, Satnam Singh, Harpreet Kaur *

School of Chemistry and Bio-Chemistry, Thapar Institute of Engineering and Technology, 147001, Patiala 147004, India

ARTICLE INFO

Keywords:
Graphitic carbon nitride
Pharmaceutical drug
Photocatalytic degradation
Visible light
Layered double hydroxides
Surface plasmon resonance

ABSTRACT

Graphitic carbon nitride (CN), a conjugated polymer widely recognized as a chemically stable and low toxic catalyst for the degradation of organic molecules. But it acquires certain limitations like a limited visible light response, high recombination rate of charge carriers, and lower charge density. To overcome such drawbacks, we synthesized a series of Ni-Al layer double hydroxide (LDH)/CN composites by loading 5–15 wt% of Ni-Al LDH onto CN by electrostatic self-assembly method. Further, Au nanoparticles were deposited photochemically on LDH/CN nanocomposites. The Au/LDH/CN nanocomposites exhibited enhanced photocatalytic degradation of tetracycline (TCH) under visible light. Particularly, the Au/LDH/CN nanocomposite with LDH and Au contents of 10 and 1 wt%, sequentially, displayed the highest degradation, which was much better than that for pure CN. The face-to-face interface between LDH and CN and the electron-accepting capability of Au nanoparticles in Au@LDH/CN boosts the separation and transfer efficiencies of photogenerated charge carriers. The intermediate products formed after the degradation of TCH were detected by LCMS and possible degradation pathways were shown. Based on photoluminescence, scavenging experiments, and LC-MS analysis, a possible mechanism for degradation of TCH on Au@LDH/CN nanocomposite was proposed.

1. Introduction

Both emerging and developed countries worldwide struggle daily with the significant issue of environmental pollution. Anthropogenic contamination of the air, water, and solid waste contribute significantly to the overall imbalance of the environment. Organic contaminants come in a wide variety of various forms in water. These pollutants can divide into many categories: pesticides, pharmaceutical drugs, phenolic compounds, surfactants, organohalides, dyes, and hydrocarbons. Some of these contaminants are resistant to decomposing in water, chemically stable, poisonous, and even carcinogenic [1,2,48].

Tetracycline is one such compound that has low solubility because it has a free tertiary amine structure. Tetracycline hydrochloride (TCH, $C_{22}H_{24}N_2O.8HCl$), which has a stable four-ring structure, would become a water-soluble and alkyl-substituted ammonium salt after being neutralized by hydrochloric acid. Therefore, looking for a novel, highly effective method to degrade its intricate structure and eliminate its biotoxicity is vital [3,38].

Photocatalytic technology is a "green" and successful environmental cleanup solution. Photocatalysts can degrade organic contaminants in wastewater to water, carbon dioxide, or other tiny nontoxic molecules [4,5,50]. Various semiconductor materials, such as TiO_2, Fe_2O_3, ZnO, $BiVO_4$, Ag_3PO_4, and their nanostructured assemblies are widely used as photocatalysts for pollutant degradation. The metal-free conjugated polymer semiconductor graphitic carbon nitride (g-C_3N_4) has recently come to light as a possible replacement for conventional metal-containing photocatalysts such oxides, sulfides, and oxynitrides because of its band gap energy (2.7 eV), visible light absorption, non-toxicity, outstanding thermal and chemical stability, easy method of preparation, abundance, and environmental friendliness [6,42–44].

However, pure g-C_3N_4's low specific surface area, low visible light utilization, and rapid charge carrier recombination result in its poor

Abbreviations: LDH, Layered double hydroxide; TCH, Tetracycline; CN, Graphitic carbon nitride; FESEM, Field emission scanning electron microscopy; HRTEM, High resolution transmission electron microscopy; PL, Photoluminiscence; DRS, Diffuse reflectance spectroscopy; XPS, X-ray photoelectron spectroscopy; EDS, Energy dispersive X-ray spectroscopy; LC-MS, Liquid chromatography mass spectroscopy.

* Corresponding author.
E-mail address: hkaur61_phd18@thapar.edu (H. Kaur).

https://doi.org/10.1016/j.surfin.2022.102583
Received 27 October 2022; Received in revised form 4 December 2022; Accepted 13 December 2022
Available online 14 December 2022

Catalysis

Utilization of Waste and Renewable Material-HCM as an Efficient Adsorbent for Heavy Metal Ions Removal: A Study of Adsorption Isotherms and Kinetics**

Manpreet K Aulakh,[a, b] Harpreet Kaur,[a] Mehak Bansal,[a] Bonamali Pal,*[a] and Satnam Singh[a]

This work describes the method of extraction and characterization of hardness causing materials (HCM) from boiling tap water via distillation assembly. The obtained white colored powered material was then calcined at different temperatures. It was revealed that powder residue was mainly consisted of calcium carbonate at room temperature and decomposed majorly to CaO, confirmed using XRD, when calcined at 900°C for about 4 h. Moreover, thermogravimetric analysis (TGA) showed single-step decomposition in case of HCM-900°C whereas two-step decomposition was observed for both HCM-400°C and HCM without calcination which can attributed to release of CO_2 from $CaCO_3$ and then decomposition of CaO in later cases. The SEM images showed crumbled type structure, flaked structure and disintegrated small-sized round shaped agglomerated particles for HCM-25°C, HCM-400°C and HCM-900°C. In addition, the impact of adsorption of different heavy metal ions (Mn^{2+}, Cr^{6+} and Ni^{2+}) over HCM with different time intervals was studied. The Langmuir adsorption isotherm is the best fit adsorption isotherm for this work. The kinetics studies follow the second order reaction. The results revealed that the Mn^{2+} adsorbs at higher efficiency among all the metal ions at negatively charged surface of HCM- 900°C due to higher oxidation state of Mn^{2+}.

Introduction

The contamination of water has become a critical global issue with the development of industries. Thus, water remediation is considered as a significant approach for its recycling. However, it is reported[1] that just 10% of total produced water is being remediated and rest residual amount as well as industrial waste is disposed as such into different water bodies like seas, rivers, seas and ultimately into groundwater reservoirs.[2] Most importantly, the origin of heavy metals (Cr, Cd, Mn, Ni, Pb, Ar, Cu, etc.) contamination is mainly due to discharge of effluents from mining, tanneries, metal plating, fertilizers used in agricultural practices.[2,3] Once these toxic metal ions enter human body through food chain, it can cause severe damage to organs and nervous system,[4–6] a great threat to living organisms which is serious matter of concern. For that reason, it is mandatory to treat effluents containing heavy metal ions prior to their discharge to large water sources.

In this respect, various treatment methods have been utilized in order to eliminate heavy metals including chemical precipitation,[7] reverse osmosis,[8] reduction,[9,10] ion exchange,[11] membrane filtration,[12] adsorption,[13–15] etc. Most of these mentioned methods are costly, consume high amount of energy, low efficacy and also produce toxic waste.[16,17] Among all techniques, adsorption is a method of choice owing to its convenience, cost-effective, high removal efficiency and simplicity.[18] However, more insight investigation is needed to choose an appropriate adsorbent, typically its abundant local availability for dealing with environmental applications for removing heavy metals potentially. Literature reveals that a variety of adsorbents had been used such as activated carbon,[19] silica gel,[20] metal oxides,[21] inorganic materials, resins,[22] etc. Nevertheless, it is still challenging to find economical with higher efficiency adsorptive materials.

Carbonate minerals are reported to show adsorption properties effectively suggested mechanism for their adsorption is ion-exchange and precipitation.[23,24] On the brighter side, $CaCO_3$ is cheapest material found it has been used for the removal of heavy metals,[25–27] but mainly for dye pollutants by opting various modifications which is also very tedious and energy or materials consuming. Zhang et al.[28] showed the monolayer process for mineralization of methylene blue and congo red dye with $CaCO_3$ modified with bentonite. Also, oxides of calcium act as low cost adsorbent[29] for toxic dyes/organic pollutants removal in various pharmaceutical and textile industries but still needs to be explored for heavy metals

[a] Dr. M. K Aulakh, H. Kaur, M. Bansal, Prof. B. Pal, Prof. S. Singh
School of Chemistry and Biochemistry,
Thapar Institute of Engineering and Technology,
Patiala (Punjab)
India-147004
Tel: 91-175-2393443
Fax: 91-175-2364498
E-mail: bpal@thapar.edu
[b] Dr. M. K Aulakh
Department of Chemistry,
University Institute of Sciences,
Chandigarh University, Gharuan,
Mohali, India-140413

[**] HCM - hardness causing materials

Supporting information for this article is available on the WWW under https://doi.org/10.1002/slct.202200659